Friedrich-Schiller-Universität Jena

Chemisch-Geowissenschaftliche Fakultät

Synthesis and self-assembly of plasmonic nanoparticles

Dissertation

zur Erlangung des akademischen Grades

doctor rerum naturalium (Dr. rer. nat.)

vorgelegt dem Rat der Chemisch-Geowissenschaftlichen Fakultät der

Friedrich-Schiller-Universität Jena

vorgelegt von Diplom-Chemiker Florian Kretschmer

geboren am 27.06.1986 in Saalfeld/Saale

Gefördert durch das Bundesministerium für Bildung und Forschung (PhoNa Projekt, 03IS2101A).

Gutachter:

1. Prof. Dr. Ulrich S. Schubert (Universität Jena)
2. Prof. Dr. Thomas Pertsch (Universität Jena)

Tag der öffentlichen Verteidigung: 17.12.2014

Table of contents

Documentation of authorship

This section contains a list of individual authors' contributions to the publications reprinted in this thesis.

P1) F. Kretschmer,[1] S. Mühlig,[2] S. Hoeppener,[3] A. Winter,[4] M. D. Hager,[5] C. Rockstuhl,[6] T. Pertsch,[7] U. S. Schubert[8]
"Survey of Plasmonic Nanoparticles: From Synthesis to Application"
Part. Part. Syst. Char. **2014**, *31*, 721-744.

Autor	1	2	3	4	5	6	7	8
Conception of the manuscript	X	X						
Preparation of the manuscript	X	X						
Correction of the manuscript			X	X	X	X		X
Supervision of F. Kretschmer			X		X			X
Supervision of S. Mühlig						X		
Vorschlag Anrechnung Publikationsäquivalente	0.5							

P2) M. Fruhnert,[1] F. Kretschmer,[2] R. Geiss,[3] I. Perevyazko,[4] D. Cialla-May,[5] Michael Steinert,[6] Norik Janunts,[7] Dmitry Sivun,[8] S. Hoeppener,[9] M. D. Hager,[10] U. S. Schubert,[11] T. Pertsch,[12] C. Rockstuhl[13]
"Synthesis, Separation, and Hypermethod Characterization of Gold Nanoparticle Dimers Connected by a Rigid Rod Linker"
In preparation

Autor	1	2	3	4	5	6	7	8	9	10	11	12	13
Simulations	X												
Preparation of the linker/dimers; UV-Vis spectroscopy		X											
Sample preparation FIB			X			X							
Setup far-field measurements							X	X					
Ultracentrifugation				X									
SERS measurements					X								
TEM measurements									X				
Preparation of the manuscript	X	X	X	X	X								
Correction of the manuscript									X	X	X	X	X
Supervision of M. Fruhnert													X
Supervision of F. Kretschmer								X	X	X			
Supervision of R. Geiss, M. Steinert, N. Janunts, D. Sivun												X	
Supervision of I. Perevyazko											X		
Vorschlag Anrechnung Publikationsäquivalente		0.5											

P3) F. Kretschmer,[1] A. Wild,[2] M. Hager,[3] U. S. Schubert[4]
"Synthesis of a Rigid Tetrahedral Linker with Thioether End Groups"
Synthesis **2014**, *46*, 475-478.

Autor	1	2	3	4
Synthesis of the linker	X			
Synthesis of tetrakis(4-iodophenyl)methane		X		
Preparation of the manuscript	X			
Correction of the manuscript			X	X
Supervision F. Kretschmer			X	X
Vorschlag Anrechnung Publikationsäquivalente	1.0			

P4) F. Kretschmer,[1] M. D. Hager,[2] U. S. Schubert[3]
"Synthesis of Functional Tripodal Thioacetates"
Synthesis, DOI: 10.1055/s-0034-1378497.

Autor	1	2	3
Synthesis and characterization of the thioacetates	X		
Preparation of the manuscript	X		
Correction of the manuscript		X	X
Supervision F. Kretschmer		X	X
Vorschlag Anrechnung Publikationsäquivalente	1.0		

P5) T. Rudolph,[1] M. J. Barthel,[2] F. Kretschmer,[3] U. Mansfeld,[4] S. Hoeppener,[5] M. D. Hager,[6] U. S. Schubert,[7] F. H. Schacher[8]
"Poly(2-vinyl pyridine)-*block*-poly(ethylene oxide) Featuring a Furan Group at the Block Junction – Synthesis and Functionalization"
Macromol. Rapid Commun. **2014**, *35*, 916-921.

Autor	1	2	3	4	5	6	7	8
Conceptual contribution	X	X						
Functionalization of the polymers and nanoparticles	X							
Synthesis of the polymers		X						
Synthesis and functionalization of gold nanoparticles			X					
DLS, UV-Vis, Zeta-potential measurements	X							
Preparation of the manuscript	X	X	X					
TEM measurements				X	X			
Correction of the manuscript						X	X	X
Supervision T. Rudolph								X

Supervision M. Barthel							X	
Supervision F. Kretschmer					X			X
Vorschlag Anrechnung Publikationsäquivalente			0.25					

P6) F. Kretschmer,[1] U. Mansfeld,[2] S. Hoeppener,[3] M. D. Hager,[4] U. S. Schubert[5]
"Tunable Synthesis of Poly(ethylene imine)-gold Nanoparticle Clusters"
Chem. Commun. **2014**, *50*, 88-90.

Autor	1	2	3	4	5
Conceptual contribution	X				
Synthesis and UV-Vis spectroscopy of the nanoparticles	X				
TEM measurements		X	X		
Preparation of the manuscript	X				
Correction of the manuscript			X	X	X
Supervision F. Kretschmer			X		X
Vorschlag Anrechnung Publikationsäquivalente	1.0				

P7) F. Kretschmer,[1] M. Fruhnert,[2] R. Geiss,[3] U. Mansfeld,[4] C. Höppener,[5] S. Hoeppener,[6] C. Rockstuhl,[7] T. Pertsch,[8] U. S. Schubert[9]
"Plasmonic Nanoparticle Clusters with Tunable Plasmonic Resonances in the Visible Spectral Region."
J. Mater. Chem. C **2014**, *2*, 6415-6422.

Autor	1	2	3	4	5	6	7	8	9
Synthesis and UV-Vis spectroscopy of the particles	X								
Simulations		X							
FIB slices			X						
TEM measurements				X		X			
Dark field microscopy					X				
Preparation of the manuscript	X	X	X						
Correction of the manuscript						X	X	X	X
Supervision F. Kretschmer						X			X
Supervision M. Fruhnert							X		
Supervision R. Geiss								X	
Vorschlag Anrechnung Publikationsäquivalente	1.0								

P8) F. Kretschmer,[1] S. Stumpf,[2] U. Mansfeld,[3] F. H. Schacher,[4] S. Hoeppener,[5] U. S. Schubert[6]
"Tunable PS-*b*-P2VP Plasmonic Nanostructures *via* a Cyclic Complexation-Reduction Approach"
J. Mater. Chem. C, submitted.

Autor	1	2	3	4	5	6
Preparation of the nanostructures, AFM measurements, UV-Vis spectroscopy, Photos	X					
TEM measurements		X	X		X	
Preparation of the manuscript	X					
Correction of the manuscript			X		X	X
Supervision F. Kretschmer					X	X
Vorschlag Anrechnung Publikationsäquivalente	1.0					

1 Introduction

Over hundreds of years metal salts have been utilized for coloring glass or porcelain.[1-2] In many cases, small nanoparticles, produced during the heating procedure, can be considered as the origin of, *e.g.*, beautifully colored cathedral windows (**Figure 1.1**). The Lycurgus cup is certainly one of the most famous examples of ancient nanotechnology. Metallic gold and silver nanoparticles embedded in the glass lead to a red color when irradiated from the inside, whereas the cup appears green in reflected light.[3] The origin of these optical properties lies in the localized surface plasmon resonance (LSPR) of the colloids where the electron cloud is shifted against the atom rumps under irradiation of light. Depending on the metal, particle size, geometry or direct surrounding, the resonance can be tuned.[4] Additionally, when brought into close vicinity further electromagnetic interactions arise between the particles.[5]

Figure 1.1: Top: Internal window of Notre Dame (Paris); Bottom: Lycurgus cup irradiated from the inside (left) and outside (right). (commons.wikimedia.org/WeEnterWinter/GFPL, © The Trustees of the British Museum)

Hence, plasmonic nanoparticle assemblies represent a powerful tool to further tune the optical properties in unprecedented ways. The variation of the parameters, *e.g.*, allows to adjust the absorption from the UV to the near IR region. Recently, these optical features gathered particular interest since they provide the possibility to create materials with a wide range of potential applications. Surface enhanced Raman spectroscopy (SERS) is probably one of the oldest analytical applications of plasmonic nanoparticles. The large field enhancement in the gap between two nanoparticles allows to detect even single molecules.[6] In solution the reaction of functionalized plasmonic nanoparticles enables the detection of minute amounts of analytes as well, *e.g.*, through large shifts of the LSPR upon aggregation.[7] By tuning the absorption of gold nanoparticles towards 800 nm they can be selectively heated, for instance, in body tissue. In combination with the resistance against photobleaching and the enhanced permeability and retention effect (EPR) this renders such structures versatile building blocks for medicinal applications like photothermal therapy or diagnostics.[8-10] Plasmonic nanoparticles also offer potential for increased power conversion efficiencies in solar cells[11-12] or for improved catalytic processes.[13] The most interesting features are obtained when large ordered plasmonic nanostructures are prepared. Thereby, materials with properties not existent in nature can be created. Such metamaterials could be utilized for light microscopy below the Abbe-limit or for the fabrication of cloaking devices.[14-16]

The aim of this thesis is to synthesize and characterize plasmonic nanoparticles as well as their assemblies. **Chapter 2.1** provides the physical background to understand the relationships between the structure and the optical properties of plasmonic nanoparticles as well as their assemblies. Moreover, general synthetic strategies to prepare particles with well-defined sizes and geometry are introduced in **Chapter 2.2**. **Chapter 2.3** discusses the formation of plasmonic nanoparticle assemblies *via* bottom-up and top-up approaches. The synthesis of small rigid-rod molecules of linear and tetrahedral structure as well as the formation of small gold nanoparticle clusters with these linkers is topic of **Chapter 3**. Moreover, a facile synthesis of tripodal thioacetates for the surface functionalization of gold nanoparticles is introduced. The preparation of gold particles bearing maleimide moieties and their reaction with a poly(ethylene oxide)-*block*-poly(2-vinyl pyridine) (PEO-*b*-P2VP) block copolymer bearing a single furan unit is demonstrated. The synthesis of large spherical clusters is reported in **Chapter 4**. Clusters with tunable size were prepared by the reaction of branched poly(ethylene imine) (bPEI) with $HAuCl_4$. Through the variation of the reaction parameters the elucidation of the factors responsible for the cluster formation could be performed. Seeded growth was conducted to increase the filling factor and to produce Au-Ag

core-shell clusters whereby the optical properties could be tuned. In **Chapter 5** the formation of plasmonic nanostructures on micrometer surface areas is demonstrated. Facilitated by phase separated polystyrene-*block*-poly(2-vinyl pyridine) PS-*b*-P2VP block copolymer films, metal ions could be selectively complexed and reduced in the P2VP phase. A cyclic approach is introduced which allows a step-wise increase of the metal content and adjustment of the optical response as well as the particle structure.

2 Theoretical background

Parts of this chapter have been published: P1) F. Kretschmer, S. Mühlig, S. Hoeppener, A. Winter, M. D. Hager, C. Rockstuhl, T. Pertsch, U. S. Schubert, *Part. Part. Syst. Char.* **2014**, *31*, 721-744.

2.1 Physical background

A general description for the interaction of electromagnetic waves with matter was first provided by James C. Maxwell[17] and later refined by Ludvig Lorenz[18] as well as Gustav Mie[19] for the optical regime and small metal colloids. When a metal is irradiated by light the negatively charged electron gas is shifted against the positive atom cores leading to localized charges (**Figure 2.1**). Attraction of the opposite charges leads to a restoring force, backshifting of the electron cloud and, hence, an oscillating behavior. Surface plasmon polaritons are thereby generated along the whole metal surface.[20] For small metal particles the propagation of these polaritons, however, is strongly limited. Resonance is achieved when the irradiated frequency matches the oscillating frequency of the particle, leading to the so-called localized surface plasmon resonance (LSPR). At this specific frequency a strong absorption of light takes place. The frequency strongly depends on the applied metal and ranges from the ultraviolet to the near IR region. For the visible region, gold and silver are the most important metals utilized because of their high environmental stability in contrast, *e.g.*, to alkali metals or copper. Moreover, the influence of structure, size, surrounding as well as assembly on the LSPR are easily visible with the naked eye (**Figure 2.2**).

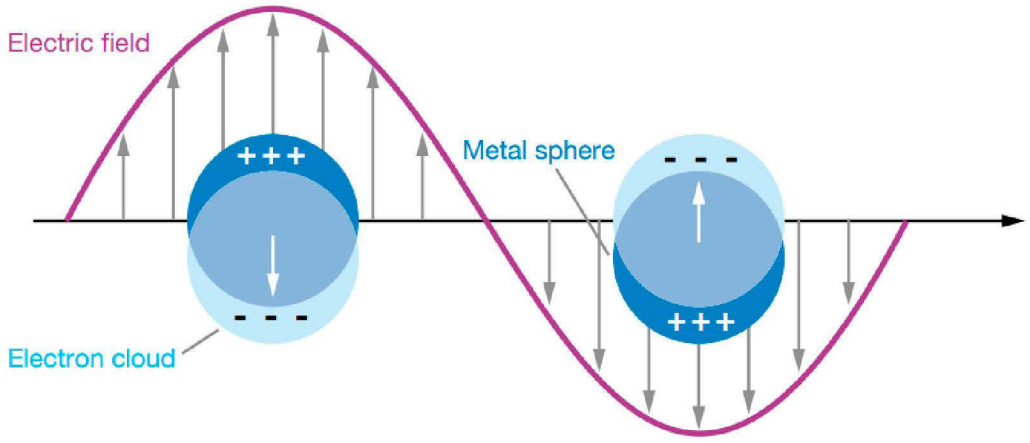

Figure 2.1: Schematic representation of the interaction between a metal nanoparticle and light.[21] Image reproduced with permission: Copyright 2007, Annual Reviews.

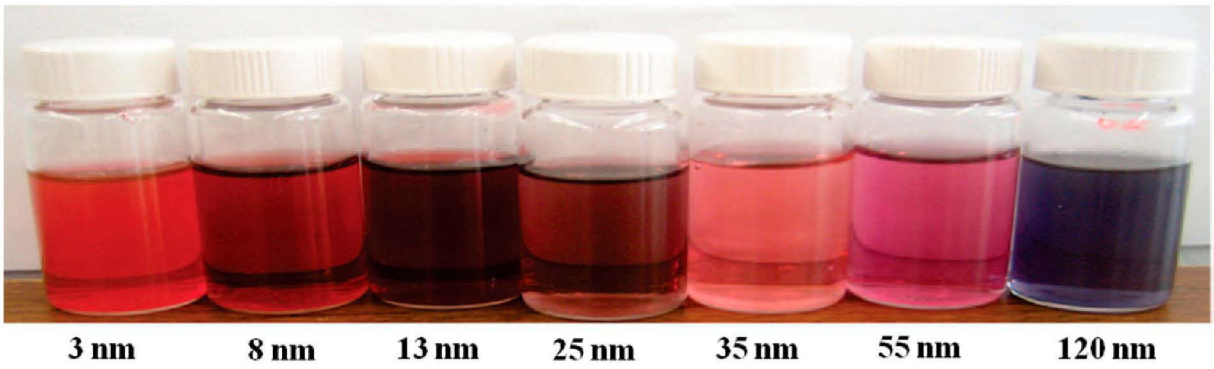

Figure 2.2: Solutions of gold nanoparticles of different diameter.[22] Image reproduced with permission: Copyright 2009, Wiley-VCH.

Due to the high cost and loss from absorption of gold also silicon[23] and certain metal oxides/nitrides[24-25] gathered attention recently. Initially, the Mie theory only allowed to predict the spectra of spherical particles but has nowadays been extended to nonspherical particles too which feature multiple LSPRs.[26] For instance, by elongation of a spherical particle along one axis a second resonance occurs. Oscillation along the long side of the rod leads to a bathochromically shifted resonance while oscillation along the short side occurs at a lower wavelength. Moreover, due to the anisotropic nature of nanorods and other nonsymmetrical structures, the optical response depends also on the angle and polarization of the irradiated light.[27] For spherical particles the resonance merely depends on the particle diameter increasing both in wavelength as well as intensity with up to a size of ~100 nm. Small nanoparticles (<< 5 nm) only show a negligible LSPR. For very large particles (>> 100 nm) scattering becomes a major factor contributing to the optical properties and, additionally, while a further redshift occurs, the overall intensity of the absorption starts to decrease.[19]

The presence of plasmons on the particle surface renders the LSPR also dependent on the direct surrounding. Absorption of molecules on the surface, changing the solvent and growth of a shell (*e.g.* SiO_2) can therefore influence the optical properties.[4, 28-29] While the overall shift of the wavelength is usually smaller compared to a change in particle structure the effect plays an important role for analytical applications.[7]

The preparation of nanoparticle assemblies allows to further fine-tune the optical properties. When plasmonic nanoparticles are brought together into close vicinity additional coupling arises resulting in new resonances.[5, 30] A common concept to describe this feature is plasmon hybridization.[31] By decreasing the distance between, *e.g.*, two spherical particles the two dipoles begin to interact generating four new modes. The in phase oscillations along the long

and the short axis creates two bright modes coupling into the far field, *i.e.*, they are observable as new peaks in the UV-Vis spectra. The out of phase oscillations are called dark modes and are not directly visible. However, they can lead to the occurrence of magnetic dipole moments which play an important role for the fabrication of metamaterials.[32-35] Likewise, the large field enhancement in the gap between the particles represents a key feature of SERS.

2.2 Synthesis of plasmonic nanoparticles

A plethora of different nanoparticle structures is enabled by utilizing different synthetic strategies to alter the size or shape of the colloids. In general, four approaches can be distinguished: a) *In-situ* synthesis, b) seeded growth, c) reshaping/etching and d) templated synthesis (**Figure 2.3**). Each approach has advantages and disadvantages and in many cases of particle synthesis more than one of these mechanisms plays an important role to yield the final particle structure.

The first approach involves the direct synthesis of plasmonic particles by a combination of solvent, metal salt, reducing agent and additives. In this case the metal ions are reduced to the elemental form in one reaction step. $HAuCl_4$ or $AgNO_3$ are the most commonly used sources for metal ions. In most cases the reactions are carried out in aqueous solution, but also organic solvents, in particular dimethylformamide[36] and polyols[37] are used. When organic solvents are utilized they often also act as reducing and structuring agents. In water sodium citrate, sodium borohydride or hydrazine are the most common reducing agents being applied. Certain additives, like poly(vinyl pyrrolidone) (PVP) or cetyltrimethylammonium bromide (CTAB), can be used to stabilize the particles against aggregation and/or to tune the particle structure. A classical and probably the most important example is the Turkevich/Frens method.[38-39] A $HAuCl_4$ solution is brought to boil and sodium citrate solution is added as reducing agent. The initial yellow solution immediately turns colorless, then blue after several seconds and shortly afterwards red indicating the formation of small spherical citrate stabilized gold nanoparticles.

A spherical shape is the most stable form of, *e.g.*, a gold or silver nanoparticle. However, additives,[40] solvents[41] and reducing agents as well as changing the temperature[42] and overall concentration/ratio[43] of the reactants can influence the shape of the particles and cause a deviation from the spherical structure. This can be caused by capping of the particles or certain crystal facets on the surface[44-47] as well as by changing electrochemical

potentials.[48] For instance lowering the reaction temperature or decreasing the amount of citrate in the Turkevich/Frens method yields larger particles but also the structure changes to more elongated particles or triangular as well as prism like structures.[43]

The second approach involves the seeded growth of nanoparticles. At least two reaction steps are required in this case. Mostly small seed particles are synthesized in the first step, *e.g.*, *via* the *in-situ* approach. Afterwards the seeds are added to a growth solution. By variation of the amount of initial seed particles or changing the growth solution, particles of different size or shape can be synthesized.[48-50] In this perspective also the structure of the seeds is of utmost importance. While at a first glance most seem to feature a spherical shape, high resolution TEM can reveal the presence of distinct crystal facets. Hence, seeds of high uniformity are required for growth into structures of high uniformity.[51] In the beginning seeded growth experiments were often unreliable and contradictory results were obtained. Over time, impurities in common chemicals which differed by the supplier and which were applied for the seeded growth could be elucidated as the origin of this peculiar behavior.[40] However, this can also be intentionally made use of. By tiny variations in the reaction conditions differently shaped particles can be synthesized from one batch of seeds. The most important reaction parameters for the synthesis of nanorods or multifaceted particles involve the amount of reducing agent[49, 52] and additives like silver ions or different halides.[51] But also isotope effects,[53] DNA[54] or light[55] can be used to tune the particle structure.

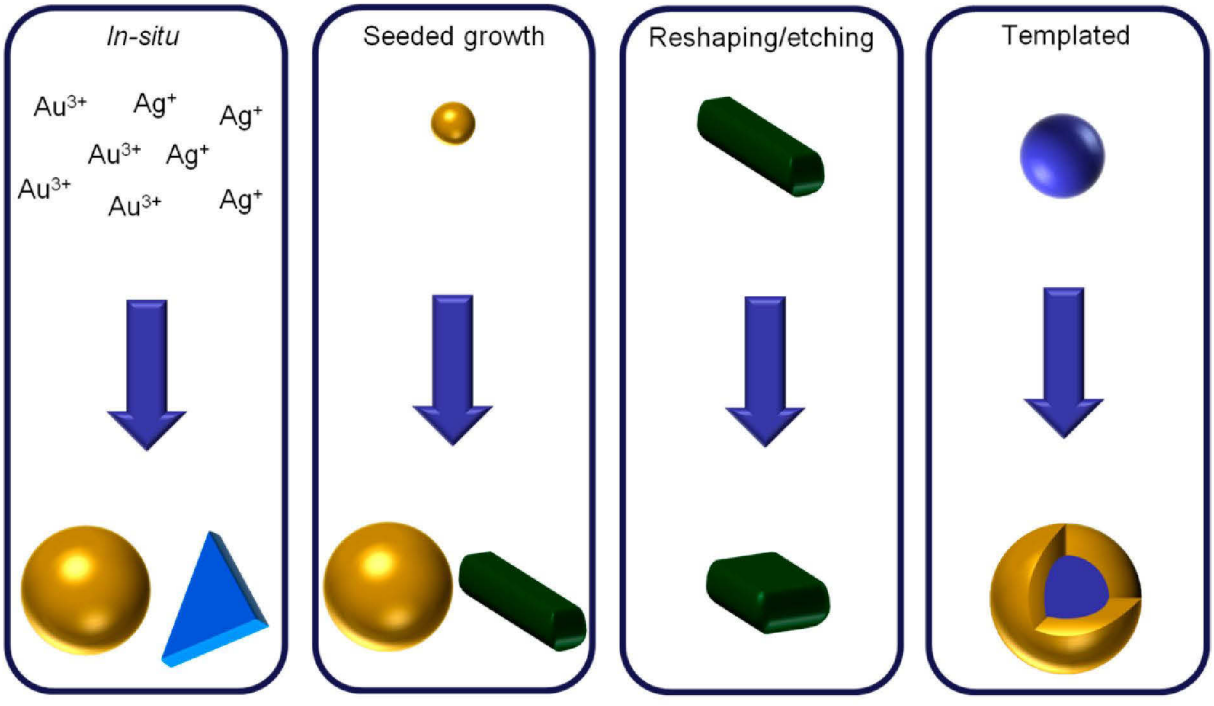

Figure 2.3: Overview of the different strategies to synthesize plasmonic nanoparticles.

By the seeded growth approach, also large spherical particles with a low size distribution can be prepared in contrast to the Turkevich/Frens method.[56] While in the beginning numerous synthesis steps were required, recently continuous methods have been developed which allow a faster synthesis and a higher concentration of the final particle solution.[57-58]

The reshaping/etching approach makes use of the intentional restructuring of nanoparticles after being synthesized by one of the introduced strategies. While being only rarely used, the processes involved are also important for the long term storage of the particles since they can lead to deterioration of the intended structure over time. Elevated temperatures, storage solution and oxygen (in case of Ag) can, *e.g.*, lead to reshaping of long nanorods into rods with a lower aspect ratio (AR) and finally spherical particles again.[59-60] Etching can be conducted by application of a cyanide solution to gold particles with protected facets yielding sophisticated nanostructures.[61]

The last strategy to synthesize plasmonic nanoparticles utilizes scaffolds consisting mostly of metals, metal oxides or polymers which determine the final structure.[62] These templates can be used to prepare particles which are impossible to be obtained by any of the other approaches since the growth direction is enforced by the template. Electrodeposition is an often applied strategy in this case, whereby, tubular[63-64] or chiral[65] structures can be obtained. However, the accessable amounts are generally lower compared to the other methods since the reaction is conducted on a surface. Also etching steps are often required to set free the final particles. In solution the templated approach represents a versatile way to synthesize core-shell particles,[66] nanoshells[67] or frames.[68]

2.3 Self-assembly of plasmonic nanoparticles

While isolated plasmonic nanoparticles already feature versatile optical properties, many potential applications rely on ordered structures of such nanoparticles. The fabrication of assemblies leads to additional resonances due to electromagnetic coupling between the particles. This enables completely new properties, like magnetic dipole moments, which are one important characteristic of metamaterials.

Three different approaches to generate plasmonic superstructures can be distinguished. In the top-down approach an area is patterned either by etching and/or cutting, *e.g.*, a layer of gold is ion milled at certain positions or is evaporated on a substrate with the desired structure.

Thereby, rather large plasmonic structures can be created, however, to the expense of long and expensive fabrication processes. The bottom-up approach relies on nanoparticles or metal salts which are utilized to form an assembly. This method is faster and a tremendous amount of structures can be synthesized at once, however, mostly only particle clusters with different structure and particle number can be prepared in this way. The top-up approach involves a combination of both approaches: A large patterned substrate is used to guide particle assembly or formation of particle structures on certain positions. With regard to this thesis mostly the bottom-up and top-up approach was utilized. Therefore, different methods to create particle assemblies by these means will be discussed. An overview on selected structures reported in literature is depicted in **Figure 2.4**.

Electrostatic interactions can be used to guide the assembly of nanoparticles, *e.g.*, by means of oppositely charged nanoparticles which are brought together or *via* a simple increase of the ionic strength of particle solutions.[69-70] But in this way in many cases only a mixture of structures can be prepared due to the reaction being merely a statistical process. This is also the case for chemical reactions between surface functionalized particles, like a click reaction of azide functionalized particles with alkyne functionalized particles. Therefore, clusters with a discrete number of particles cannot be synthesized in this way without additional purification steps.

Strategies to solve these issues involve the protection of one side of the particles which is mostly conducted *via* immobilization of the particle on a surface.[71] The unprotected site can then be functionalized. After redispersion the particles can then be reacted with a corresponding counterpart. Also particles with a discrete number of reactive moieties can be prepared. However, for large particles this synthesis is a statistical process too and requires a tedious removal of higher functionalized particles.[72] Though, in the case of small nanoparticles a discrete functionalization is easily possible by means of large chelating thiols which can wrap around a whole particle.[73] In this way, *e.g.*, particles with one or two alkyne groups could be prepared and assembled into a dimer *via* a Glaser reaction.[74] The LSPR of such small particles, however, is negligible and larger molecules have to be synthesized to make use of this strategy for potential applications.

DNA represents another versatile tool to direct the assembly of nanoparticles.[75] On the one hand DNA can be used to functionalize nanoparticles and complementary strands lead, for instance, to the formation of dimers or larger clusters.[76-77] On the other hand DNA itself can already form assemblies. DNA origami can be used to prepare all kinds of nanostructures with

a defined number of reactive positions, each reacting only with one type of complementary DNA. Brought together with respectively functionalized nanoparticles highly sophisticated plasmonic assemblies can be created.[78] Additionally, single DNA strands are able to absorb nanoparticles on the outside. Due to the helical nature this paves the way for chiral plasmonic nanostructures.[79] Also external triggers like light,[80] temperature[81] or magnetic fields[82] enable the formation of nanoparticle assemblies. For the preparation of assemblies on larger areas often a layer-by-layer approach is used. This can be facilitated either *via* the formation of layers electrostatically, *e.g.*, through polyelectrolytes,[83] or by mechanical preparation[84] of different layers.

Block copolymers (BCPs) are highly flexible tools for the fabrication of nanostructures.[85-86] On the one side small clusters can be formed, *e.g.*, through micelles or in BCP nanoparticles. The formation of long-range ordered nanostructures in thin films also allows to pattern large areas. Plasmonic nanostructures can then be formed through complexation and reduction of metal salts in certain blocks[87] (like P2VP) or *via* incorporation[88] of already formed nanoparticles in one of the blocks. Moreover, removal of one of the blocks in hexagonal or lamellar BCP films leads to the formation of deep grooves where nanoparticles can be assembled by capillary forces.[89]

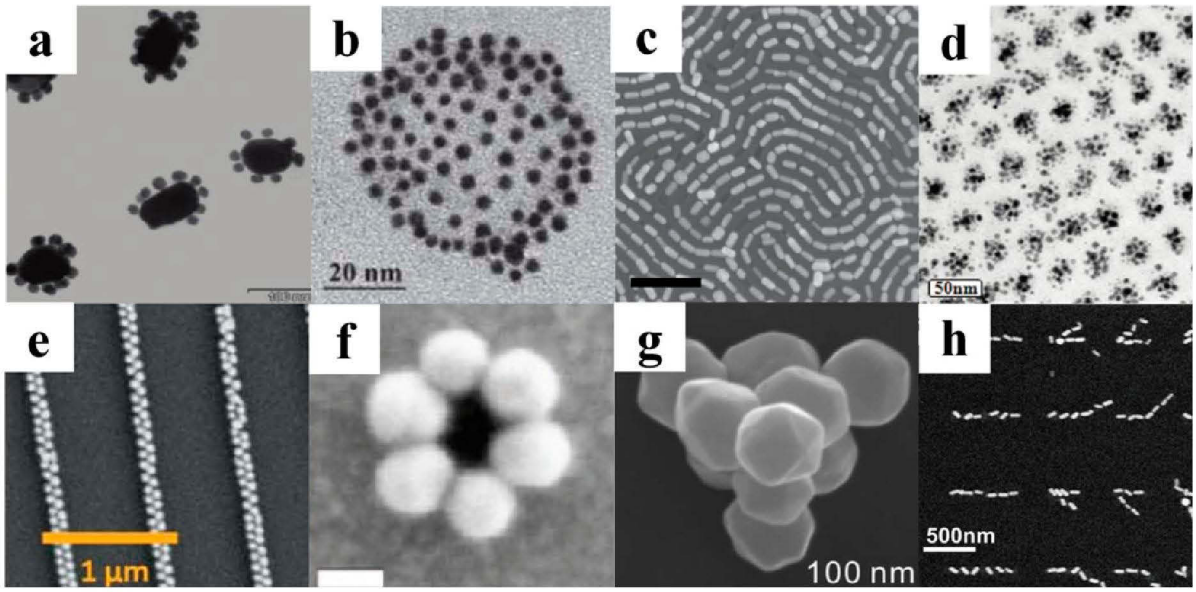

Figure 2.4: Nanoparticle assemblies obtained by different synthesis strategies. Scale bars: a) 100 nm, b) 20 nm, c) 200 nm, d) 50 nm, e) 1000 nm, f) 20 nm, g) 100 nm and h) 500 nm. Images reproduced with permission a), f), h).[76, 90-91] Copyright 2011, ACS. Image reproduced with permission b).[92] Copyright 2012, RSC. Image reproduced with permission c).[89] Copyright 2013, Wiley-VCH. Image reproduced with permission d).[93] Copyright 2012, ACS. Image reproduced with permission e).[94] Copyright 2010, RSC. Image reproduced with permission f).[95] Copyright 2012, ACS.

Top-up methods rely on the preparation of large patterned areas. Most often different lithography methods, like electron beam[96] or scanning probe lithography,[91] are utilized to write a structure either *via* chemical modification of the surface or through removal of parts of the substrate. Capillary forces or electrostatic as well as strong metal-thiol interactions then guide the deposition of plasmonic nanoparticles. Additionally, stamps can be used where a nanoparticle solution is forced into a superstructure and allowed to dry.[94]

3 Synthesis of nanoparticle dimers and multimers

Parts of this chapter have been published: P2) M. Fruhnert, F. Kretschmer, R. Geiss, I. Perevyazko, D. Cialla, S. Hoeppener, M. D. Hager, U. S. Schubert, T. Pertsch, C. Rockstuhl, *in preparation* P3) F. Kretschmer, A. Wild, M. Hager, U. S. Schubert, *Synthesis* **2014**, *46*, 475-478, P4) F. Kretschmer, M. Hager, U. S. Schubert, *Synthesis* DOI: 10.1055/s-0034-1378497, P5) T. Rudolph, M. J. Barthel, F. Kretschmer, U. Mansfeld, S. Hoeppener, M. D. Hager, U. S. Schubert, F. H. Schacher, *Macromol. Rapid Commun.* **2014**, *35*, 916-921.

A pivotal parameter for the optical response of a nanoparticle assembly is the interparticle distance as described in **Chapter 2.1**. In order to observe novel optical properties it is crucial to prepare clusters with defined gaps. Chemical reactions between complementary functionalized particles, *e.g.*, *via* esterification[97] or cycloadditions[98], can guide the formation of small clusters. However, additives required for the reactions like metal catalysts or coupling reagents might as well interact with the particles leading to aggregation. Such side reactions make the elucidation of the cluster forming mechanism considerably harder. Though, strong interactions of sulfur[99-100] and amine[101] containing moieties with gold can be utilized as well to synthesize clusters. α,ω-Alkane dithiols in principle allow to attach one gold particle at each end of the alkyl chain, however, the flexibility of the chain does not allow a stable interparticle distance.[102] Therefore, rigid rod linkers based on oligo(phenylene-ethynylenes) (OPEs) and -vinylenes were introduced as structural motive (**Figure 3.1**). Still, the exact binding mechanism remains elusive and contradictory results have been reported in literature.[103-105] From the perspective of a metal nanoparticle most synthesized linkers are flat compared to the spherical particle size. This makes binding of both ends (in case of a bifunctional linker) to one particle likely. Also the cluster is not necessarily stable on the long term and the gap formed by the linker might close overtime.

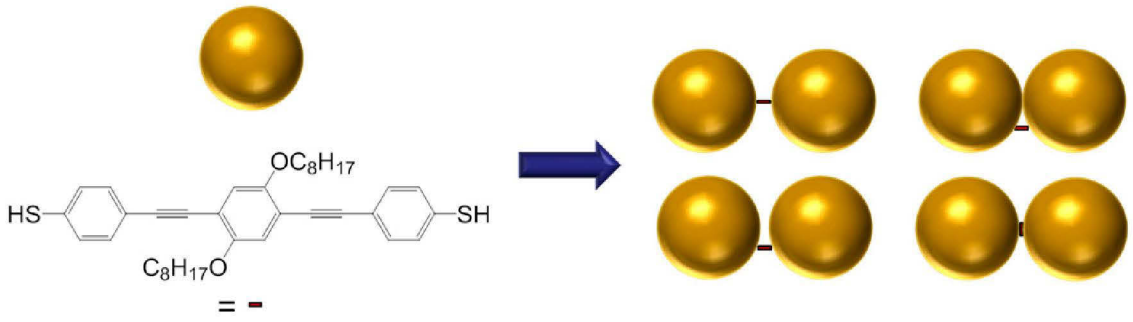

Figure 3.1: Schematic representation of different possible assembly modes of gold nanoparticles (d = 15 nm) with the deprotected linker molecule **3** (S-S = 2 nm).

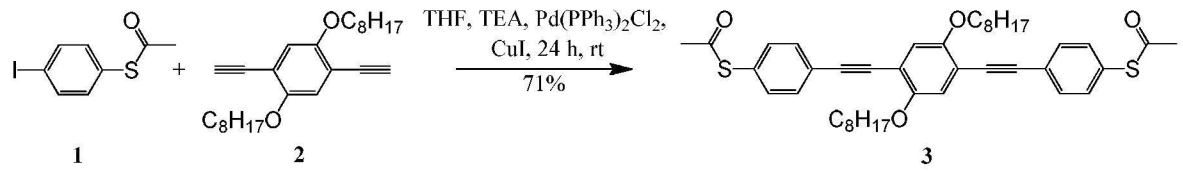

Scheme 3.1: Schematic representation of the linear linker synthesis.

Additionally, linking of the particles without a defined gap can just occur by substitution of the initially present stabilizing ligands (like citrate) with concomitant aggregation.

In order to investigate the particle assembly at first a rigid rod linker with a ~ 2 nm distance between the two thiol groups was prepared *via* a Sonogashira cross coupling reaction (**Scheme 3.1**). In the beginning, an acetyl protected thiol had to be used otherwise the reaction would fail and also the free thiols form disulfides over time leading to polymerization of the unprotected linker. Diazabicycloundecene (DBU) was utilized for removal of the acetyl group due to its easy miscibility with DMF where also **3** was readily soluble. Moreover, DBU leads to an accelerated cleavage compared to other reagents[106] and, hence, less side reactions like oxidation. Self-assembly could be achieved by adding increasing amounts of the deprotected solution of **3** in DMF to citrate stabilized gold nanoparticles (diameter ~ 15 nm). After one minute the reaction was stopped by addition of poly(acrylic acid) (PAA) which also stabilizes the clusters on the long term (**Figure 3.2**). The formation of particle clusters could easily be followed *via* UV-Vis spectroscopy revealing a redshift of the LSPR from 520 up to 550 nm with increasing linker concentration (**Figure 3.3**). The assembly of the particles also led to a broadening of the peaks caused by additional resonances from plasmon coupling. To exclude an influence of DBU on the particle stability itself,[69] a control reaction was performed with DBU only. The same amount of DBU was used as in case of the highest linker concentration, however, only a tiny redshift of the resonance could be observed. Therefore, the assembly process can be attributed to the presence of the linker. UV-Vis spectroscopy of the solutions itself, however, only reveals a sum of resonances comprising all kinds of structures like single particles, dimers, trimers etc. Also a TEM image of such a crude solution is hard to be interpreted. Artifacts can be generated through the sample preparation. Drying effects, caused by evaporation of the solvent, lead to cluster formation too, even if the initial solution consists of single particles. Hence, it was crucial to purify the clusters prior to a more detailed investigation. This was performed by density gradient centrifugation (**Figure 3.4**).[107]

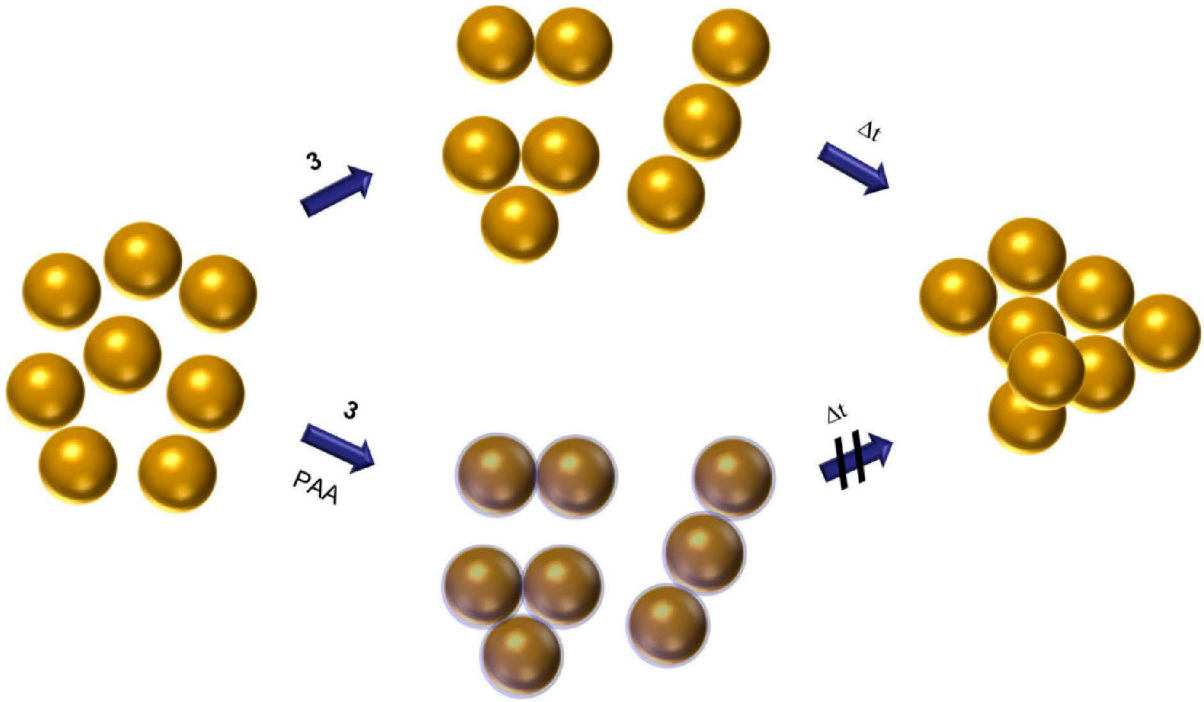

Figure 3.2: Schematic representation of the linking process: Assembly of particles with long term aggregation (top) and assembly of particles with long term stabilization *via* PAA (bottom).

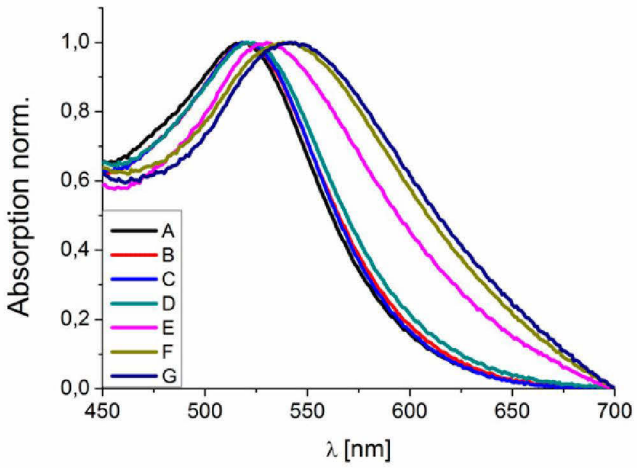

Figure 3.3: UV-Vis spectra of single gold nanoparticles, gold nanoparticles with only DBU and gold nanoparticles with different amounts of the linker solution. A - Au NP solution, B - Au NP control solution with only DBU (100 µg/mL), C to G - Au NP solutions with increasing amounts of **3** and DBU (20, 40, 60, 80, 100 µg/mL), respectively.

The crude particle solution was placed on top of a sucrose gradient and centrifugal force was applied. Thereby, separation of the particles according to the size and shape took place. Larger particles as well as assembled structures move faster to the bottom. The particle sizes

were determined by the Svedberg equation. Fraction I consisted of smaller single particles mixed with unbound linker, therefore, the average diameter is low. In contrast, fraction II fits well with the particle size obtained *via* TEM.

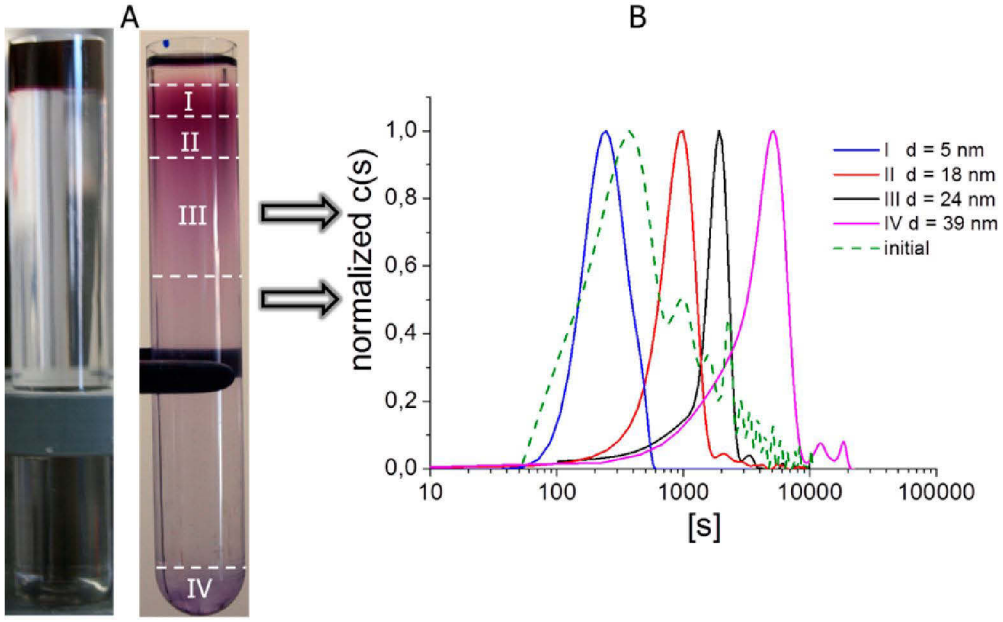

Figure 3.4: Density gradient centrifugation of gold nanoparticles. (A) Images of a centrifuge vial with the sample applied, before and after centrifugation. (B) Corresponding distributions of intrinsic sedimentation coefficients of the fractions collected.

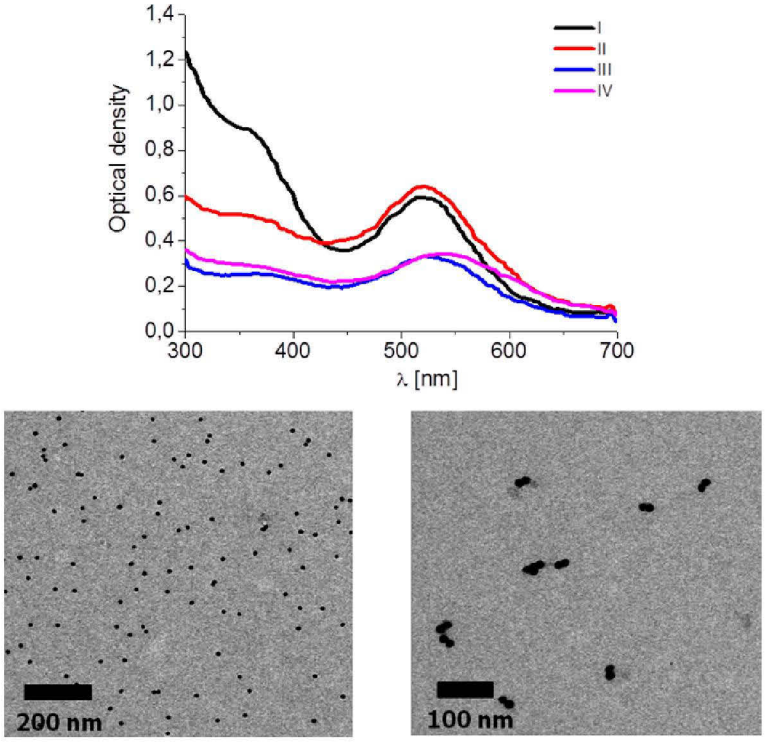

Figure 3.5: UV-Vis spectra of the separated fractions (top), TEM images of the fractionated particles, fraction I (bottom left) and fraction IV (bottom right).

Fraction III contained the largest particles, though the intensity of this band is much weaker compared to fractions I and II. The separation of the first three fractions is rather arbitrary since they still comprise only one band. However, the fourth fraction is clearly separated and also shows a different color. In combination with a particle size of 39 nm this already indicated the presence of particle clusters. This finding was finally corroborated by TEM imaging which clearly revealed the presence of single particles for the top fraction and particle clusters for the bottom fraction (**Figure 3.5**).

Binding of both ends to the linker is the most probable case for nanoparticles of this size, however, a rather high amount of linker was added to the particle solutions which can lead to a perpendicular reorientation of the linker at the surface. Luckily, the strong field enhancement in the particle gap allowed to analyze the binding mode of the linker in more detail *via* SERS (**Figures 3.6 and 3.7**). Numerical calculations of the electric field in the vicinity of a gold dimer with a distance of 2 nm and a nanoparticle radius of 7 nm revealed an almost tenfold increase of the electric field intensity in the gap between the particles. The measured spectrum of the pure compound features distinct peaks on top of a fluorescent background. They correspond to the C≡C stretching vibration (2200 cm^{-1}), C=C stretching vibration (1581cm^{-1}, 1543 cm^{-1}), CH_3 deformation vibration (1332 cm^{-1}), CH_2 twisting (1243 cm^{-1}), C-C stretching vibration (1177 cm^{-1}) and ring breathing vibration (1078 cm^{-1}), respectively.[108]

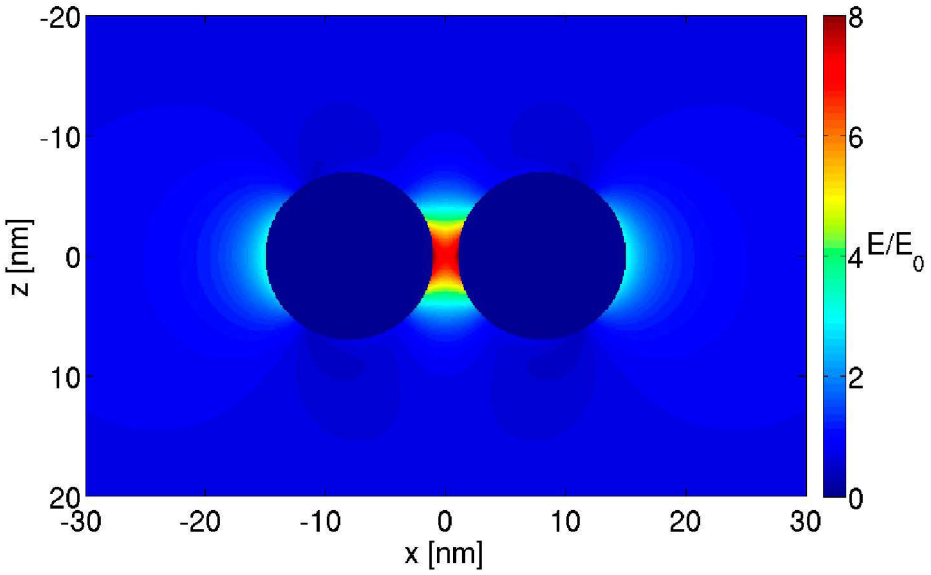

Figure 3.6: Absolute value of the electric field normalized with the amplitude of the incident field E_0

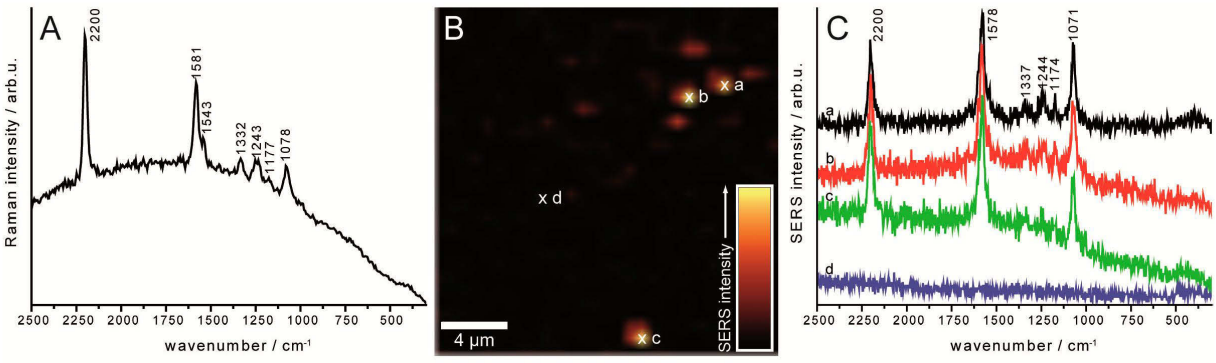

Figure 3.7: SERS-based characterization of gold nanoparticle cluster. (A) Reference Raman spectrum of the linker molecule **3**. (B) SERS intensity map with bright spots indicating the presence of nanoparticle cluster. (C) Related SERS spectra (a-c) and background signal of the substrate (d).

SERS analysis of fraction IV revealed bright spots indicating the presence of clusters. Spectra taken from some of these spots reveal two important details. At first, the fluorescence background is much smaller or not present at all which can be attributed to quenching stemming from absorption of the linker at the metal surface. Second, some Raman modes, in particular the ring breathing vibrations are enhanced. Based on surface selection rules this occurs when molecules are absorbed perpendicular to the surface.[109-110] Hence, it can be concluded that the linker is standing in an upright or slightly tilted orientation on the gold particle surface.

In order to perform the optical investigation of a single dimer, a diluted solution of the particles was placed on a SiO_2 substrate and allowed to dry. A single dimer was isolated by etching other particles and assemblies in the vicinity *via* focused ion-beam milling. The sample was transferred to the optical far-field setup which utilizes a spatial modulation technique and a lock-in amplifier to reduce the large noise stemming from the background (**Figure 3.8**). The dimer was scanned by a laser beam while moving the substrate along the x- and y-axis. A photon multiplier tube (PMT) was utilized for the detection of the scattered light. The obtained extinction images for irradiation at 532 nm are depicted in **Figure 3.9**. Due to the fivefold intensity of the dimer signal (green) compared to the signal of the etched particles (red) the characterization of a single dimer is unambiguously possible. The values obtained for the extinction by irradiation at 532 and 561 nm showed good agreement with simulated values.

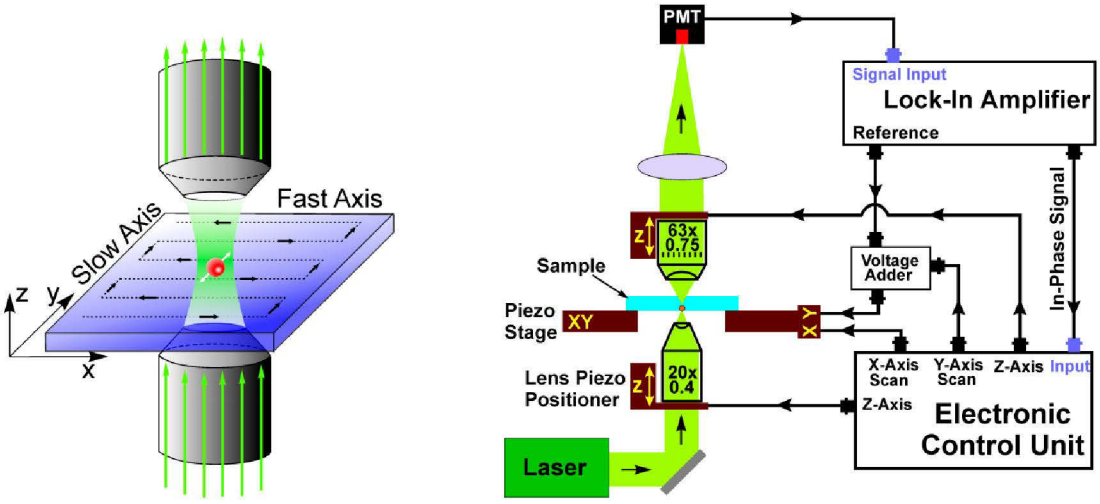

Figure 3.8: a) Illustration of the scanning regime. b) Schematic representation of the far-field detection setup consisting of a 2D scanning stage that modulates the position of the sample for lock-in detection while scanning.

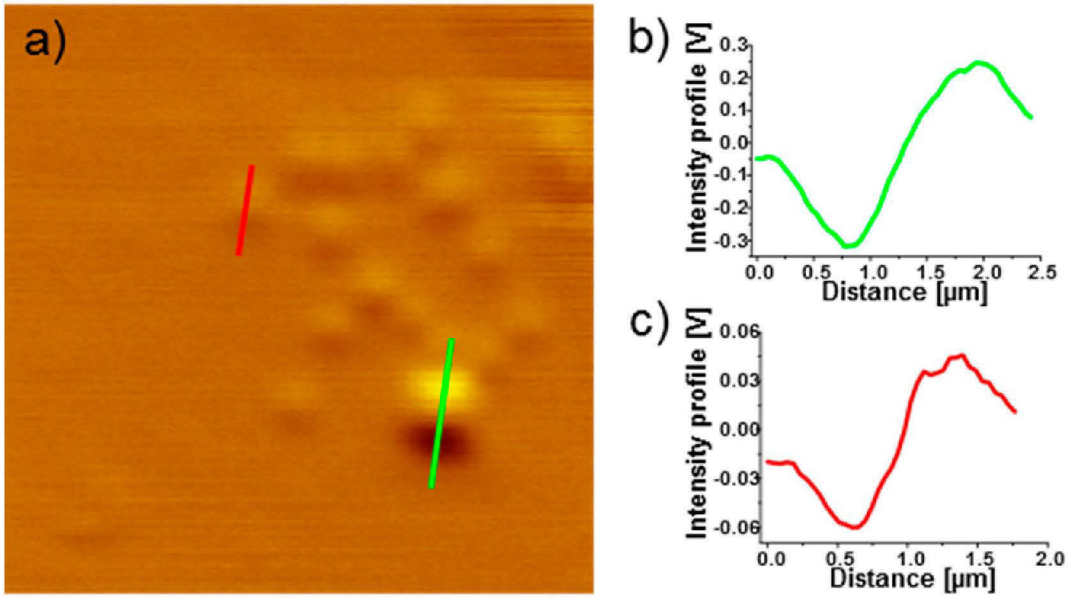

Figure 3.9: a) Recorded extinction image at a wavelength of 532 nm over an area of 12×12 µm². b) and c) Signal profiles along the lines indicated in the 2D plot. Green – nanoparticle dimer, red – etched gold nanoparticles.

The potential problem of binding of both ends of a rigid rod dithiol to one particle can be solved by increasing the number of arms and generating a 3D structure. This is most easily accomplished by a tetrahedral molecule. Depending on the size of the tetrahedron (*i.e.* arm length), the binding mode and the metal nanoparticle size, also the formation of a tetrahedral

particle cluster is possible. Such large rigid structures can be prepared by consecutive Sonogashira reactions.[111] The building blocks can be directly coupled onto a core followed by end capping of the arms with a thio-functionality. However, in order to synthesize arms of sufficient length multiple reaction steps are necessary, yet, the obtained product and potential byproducts become more and more similar in their physical properties. Separation *via* column chromatography of, *e.g.*, a tetrahedral OPE with three arms of the same length and one shorter arm becomes a daunting task the longer the arms get. Therefore, a convergent approach was chosen by coupling of the final arm to the core.

An iodo functionalized tetraphenylmethane core and the respective alkyne functionalized arm was utilized in order to prevent star-star coupling arising from a core bearing alkyne units (**Scheme 3.2**). Compound **4** was used as initial building block for the OPE arms. Due to the hexyloxy side chains the solubility is increased, otherwise such compounds become insoluble in common organic solvents after approximately four repeating units.[112] The reaction with the thioanisole derivative **5** followed by cleavage of the trimethylsilyl group with potassium fluoride afforded compound **7**.

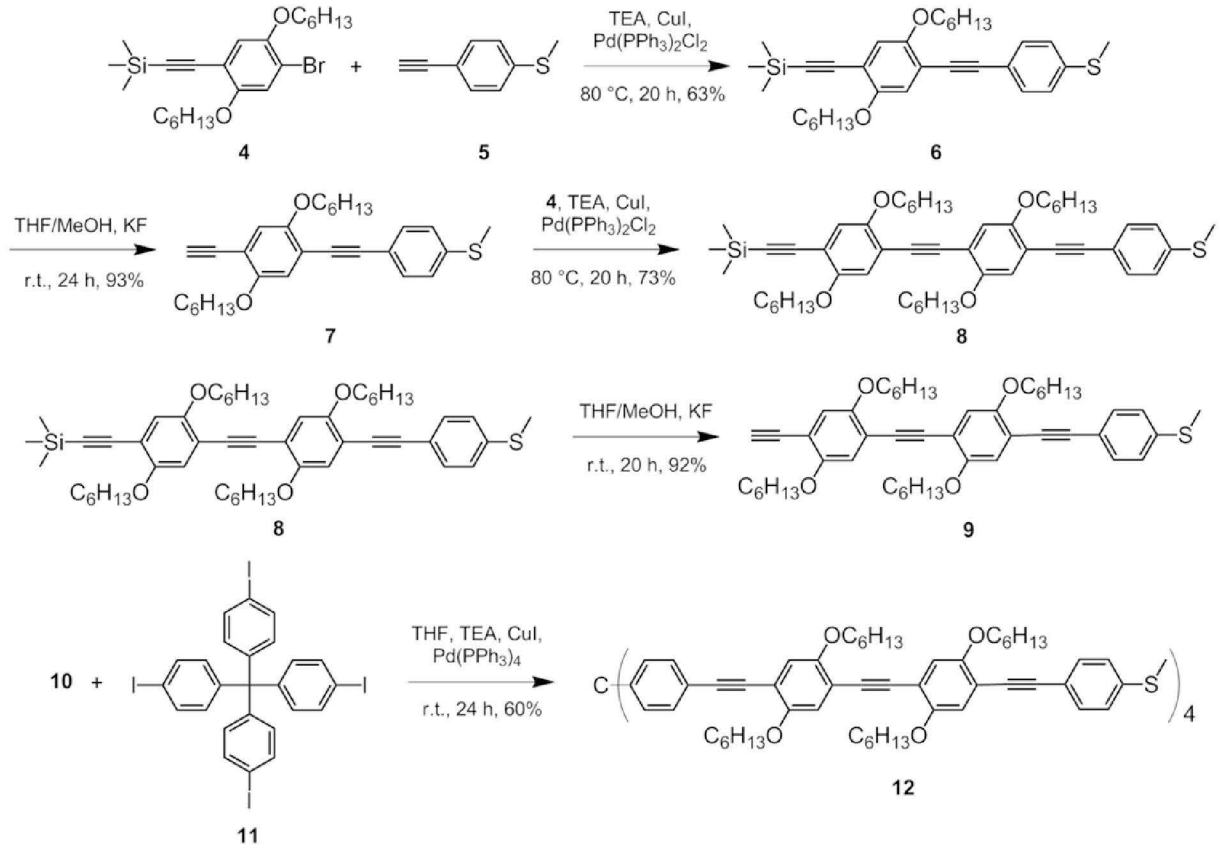

Scheme 3.2: Schematic representation of the tetrahedral linker synthesis.

Repeating these reactions yielded the final arm **9**. By a Sonogashira reaction with the core **11** the final tetrahedral compound **12** with a corresponding arm length of 2.6 nm could be obtained. In order to prepare assemblies with the tetrahedral linker citrate stabilized nanoparticles were transferred into chloroform *via* sodium oleate. Upon addition of the linker, however, no cluster formation could be observed. This could be explained by the utilization of a thioether moiety instead of a thiol. Multiple cross coupling reactions with the thioacetate would not have been possible due to cleavage during the reaction. But thioethers also have a lower affinity to the gold surface which might be the reason for their inability to efficiently induce the particle assembly.[113-115]

While such oligofunctional compounds can be used to synthesize clusters they do not differentiate between particles of different size, structure or composition. Mixing gold nanoparticles with silver nanoparticles of the same size followed by addition of a dithiol would lead to the formation of gold-silver dimers. Though, additionally gold-gold as well as silver-silver dimers are formed which would need to be separated. This adverse feature, however, can be attenuated by employing complementary functionalized particles. In this case, thiols with reactive end groups are utilized creating a self-assembled monolayer on the particle surface full of functional groups. A drawback of monothiols is their easy exchange between the particle surface and the solution which leads to mixed SAMs when batches of particles with different SAMs are mixed. Therefore, tripodal ligands were utilized who show a much stronger absorption on the metal surface due to the chelating effect of multiple thiol units.[71, 115-116] Up to now, the synthesis of such compounds often involved multiple reaction steps and harsh reaction conditions.[117-120] However, a much more versatile approach could be developed which enables the easy preparation of tripods with a variety of functional units (**Scheme 3.3**).

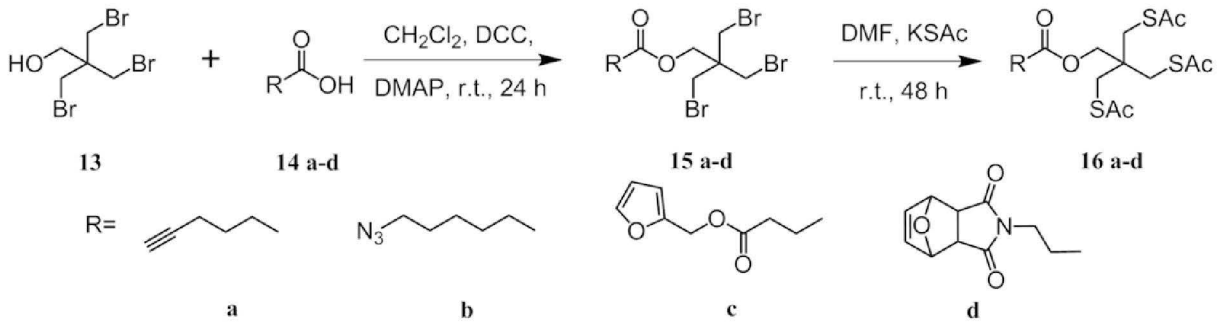

Scheme 3.3: Schematic representation of the tripodal thioacetate synthesis.

Pentaerythritol tribromide **13** was used as the main building block and Steglich esterification with alkyne, azide, furan as well as maleimide bearing carboxylic acids **14 a-d** provided the esters **15 a-d**. Since the maleimide moiety could possibly react with free thiols, it was protected with a furan unit by a Diels-Alder reaction prior to esterification. Conversion of the tribromide esters with potassium thioacetate in DMF resulted in the final thioacetates **16 a-d**.

Functionalized gold particles were prepared by addition of the compounds to gold nanoparticles in DMF. The free thiols are generated by hydrolysis of the thioacetates at the metal surface.[121] A click reaction between two batches of alkyne and azide functionalized particles, however, could not be achieved. Already the addition of the catalyst to one of the solutions led to aggregation of the particles. Also a respective Diels-Alder reaction was not possible probably due to reaction of free thiol groups instead of the furan moieties with the maleimide. Additionally, the reaction between tripods in solution (*e.g.* furan) with the ones on the particle surface (*e.g.* maleimide) could lead to capping of the particles rendering them unreactive towards the furan functionalized particles. Nevertheless, it could be demonstrated that maleimide functionalized particles are able to successfully form a shell with a polymer bearing a furan unit. A P2VP-*b*-PEO block copolymer was synthesized *via* sequential anionic polymerization. At the block junction a single furan moiety could be introduced. Deprotection of the protected maleimide particles was achieved by a retro-Diels-Alder reaction at 130 °C. To induce a Diels-Alder reaction the deprotected particles were subsequently treated with the polymer at 75 °C for two days in DMF. *Via* DLS investigations an increase in the particle diameter could be observed whereas uranyl acetate stained TEM images showed the formation of a shell (**Figure 3.10**). Additionally, retrotransfer of the original deprotected maleimide functionalized Au particles into water led to aggregation. In contrast, transfer of the BCP functionalized Au particles into water resulted in stable solutions due to the hydrophilic polymer shell.

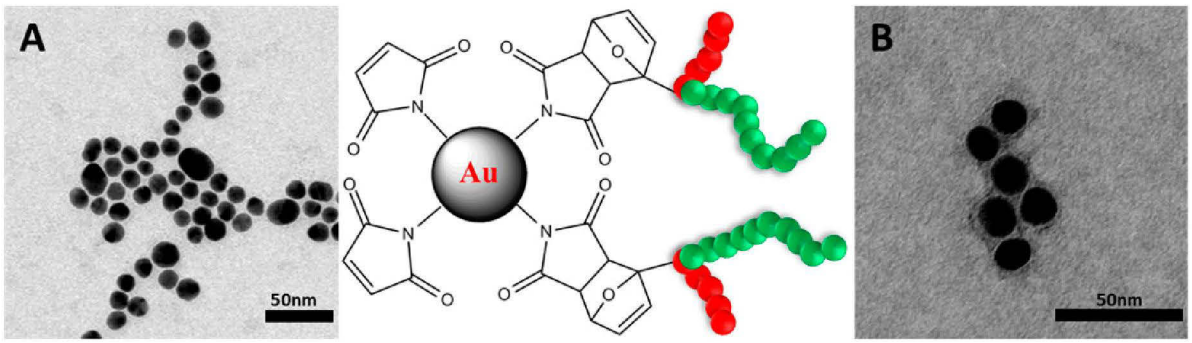

Figure 3.10: TEM image of the maleimide functionalized Au particles (A) and of the polymer functionalized particles (B).

In conclusion, it could be shown that rigid-rod linkers can be utilized to synthesize small nanoparticle clusters. Additionally, an improved synthetic access to tripodal thioligands was developed, providing versatile compounds to prepare particle surfaces with a multitude of reactive moieties. The synthesis of clusters with a large number of particles, however, requires other strategies which will be shown in **Chapter 4**.

4 Synthesis of PEI-nanoparticle clusters

Parts of this chapter have been published: P6) F. Kretschmer, U. Mansfeld, S. Hoeppener, M. D. Hager, U. S. Schubert, *Chem. Commun.* **2014**, *50*, 88-90, P7) F. Kretschmer, M. Fruhnert, R. Geiss, U. Mansfeld, C. Höppener, S. Hoeppener, C. Rockstuhl, T. Pertsch, U. S. Schubert, *J. Mater. Chem. C* **2014**, *2*, 6415-6422.

For small particle clusters the focus of potential applications is mostly on analytical issues.[107, 122-124] Moreover, the anisotropic nature of most of the smaller clusters can be utilized to determine orientations on the nanoscale. Yet, for creating a real 3D material this feature is rather disadvantageous. Instead, it is more convenient to employ large spherical clusters consisting of hundreds of individual particles. Such assemblies provide an inherent isotropic optical behavior and their properties hardly change when only a few more particles are added or are removed. Most importantly, however, they can exhibit a magnetic dipole moment which is a crucial parameter for metamaterials.[125-127] Two types of spherical clusters can be distinguished: Satellite structures consist of plasmonic particles assembled onto a spherical template, *e.g.*, a polymer or silica particle.[81, 92, 128] The second type involves spherical assemblies were also the interior is filled with particles. These can be formed, for instance, by encapsulation of pre-synthesized particles in a polymer shell or micelle.[129-130]

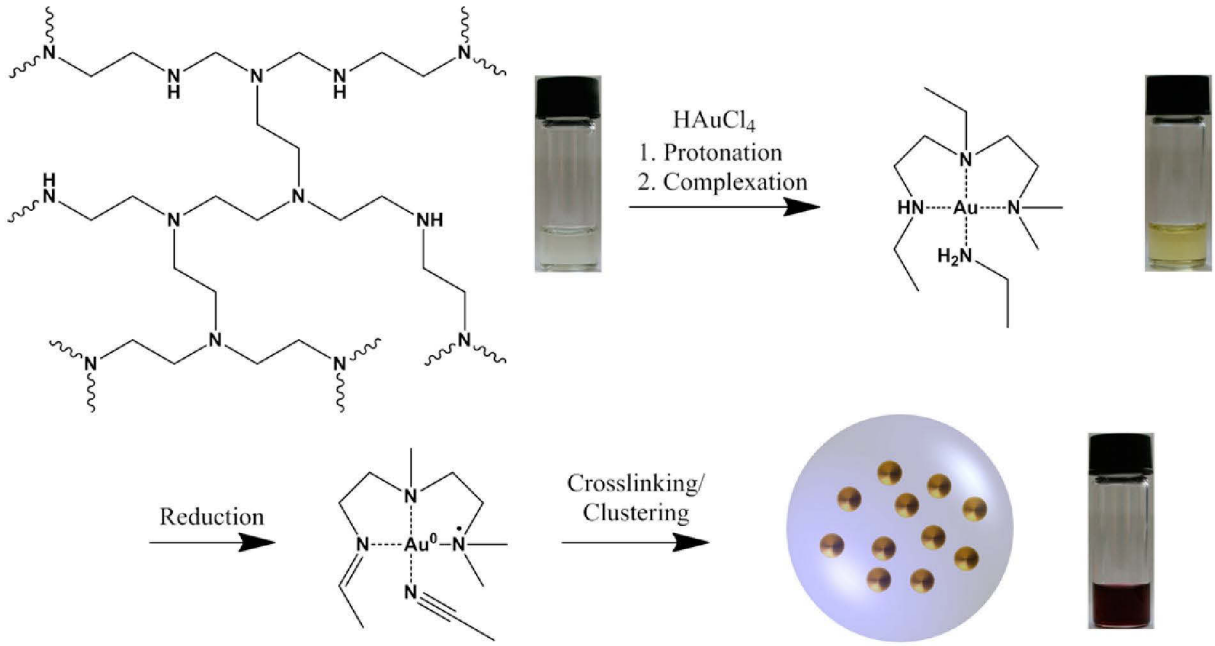

Scheme 4.1: Schematic representation of the cluster formation. Photographs depict the solutions at the different stages of the synthesis.

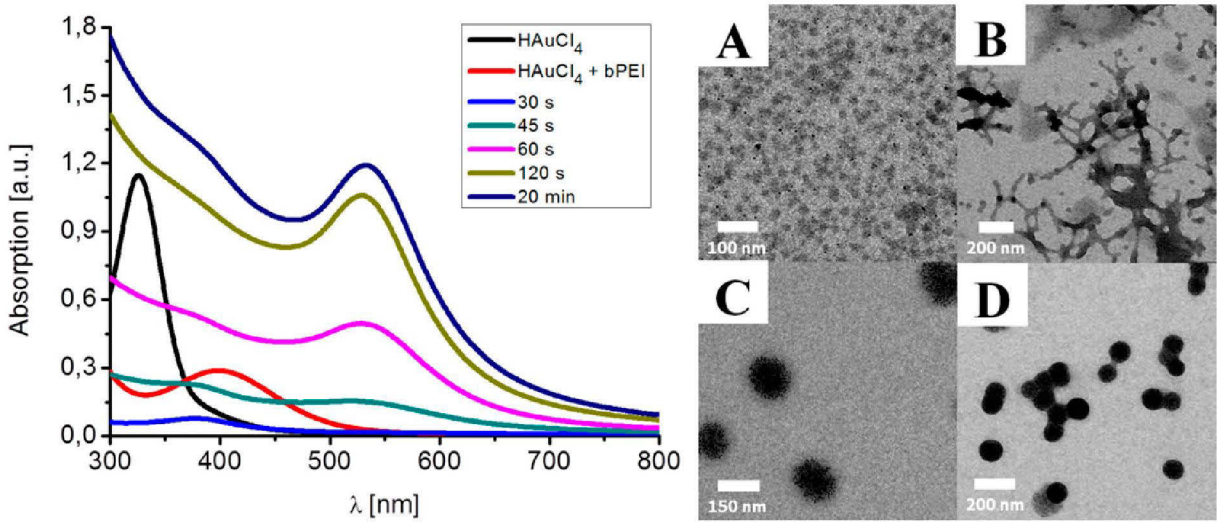

Figure 4.1: UV-Vis spectra and TEM images of the solutions at the different stages of the synthesis. After 30 sec (A), 45 sec (B), 1 min (C) and 2 min (D).

However, we could demonstrate that it is also possible to perform the synthesis of gold nanoparticles with a simultaneous formation of spherical clusters by the reaction of bPEI (25 kDa) with $HAuCl_4$ at a 1:1 mass ratio (**Scheme 4.1**). The reagents were mixed in DMF and the solution was immersed in an oil bath at 150 °C. The reaction was followed by UV-Vis spectroscopy which first showed a bathochromic shift due to the complex formation between the amine groups and the $AuCl_4^-$ anion (**Figure 4.1**). Afterwards a stepwise reduction took place where at first colorless Au^+ ions were formed followed by reduction to the elemental form. *Via* merging of the reduced Au atoms small gold nanoparticles were produced as indicated by an increase of the localized surface plasmon resonance over time. Additionally, TEM measurements were conducted revealing the presence of small polymer particles and occasionally gold particles after 30 sec. Fusion into larger aggregates (45 sec) and formation of more gold particles and a spherical shell takes place (1 to 2 min) over time. The final reaction time was set to 20 min for all further experiments. By prolonged heating only aggregation and precipitation took place.

In order to elucidate the cluster formation mechanism numerous reaction parameters were varied. It could be demonstrated that the utilized salt, temperature, reagent ratio and polymer as well as the solvent play a crucial role for the cluster synthesis.

By stirring the solution at room temperature several days were required to complete the reaction (**Figures 4.2 and 4.3**). Gold particles were formed and occasionally a polymer shell was visible, however, no clusters were generated. Utilization of water or ethanol in place of DMF resulted only in single spherical particles. Ethanol likely reduces Au^{3+} itself, whereas, in

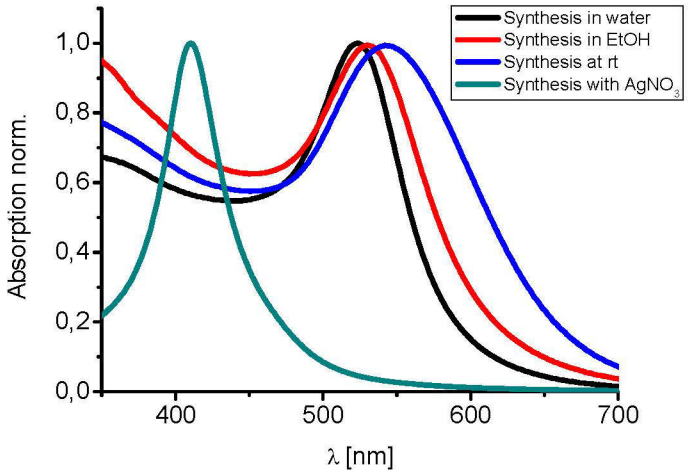

Figure 4.2: UV-Vis spectra of particles synthesized in water, ethanol, at room temperature (in DMF) and with silver nitrate (in DMF).

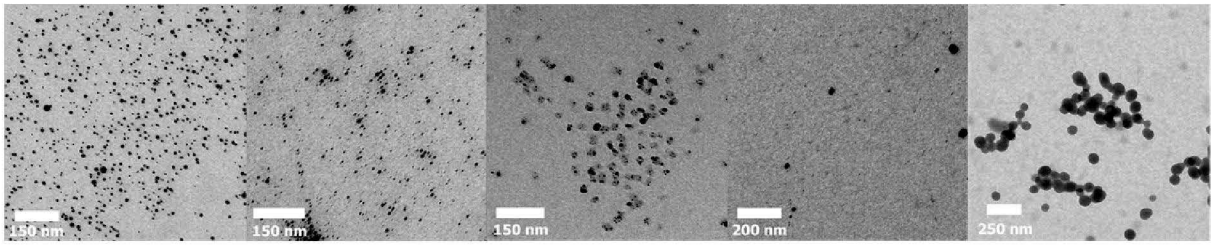

Figure 4.3: TEM images of particles synthesized in water, ethanol, at room temperature, with silver nitrate in DMF and with NH_4Cl in DMF (from left to right).

water it is reduced by PEI and the polymer only acts as capping agent. Dehydrogenative oxidation of the amine groups by Au^{3+} is the cause for the gold particle formation,[131-132] however, a similar reaction with $AgNO_3$ in DMF instead of $HAuCl_4$ revealed only single spherical Ag nanoparticles as observed by TEM. While DMF can hardly reduce Au^{3+} it is a good reducing agent for Ag^+ and the large excess of the solvents makes the reaction of silver ions with PEI unlikely.[36] Moreover, due the higher coordination number of Au^{3+} crosslinking of the polymer could be facilitated by complexation of more chains. When NH_4Cl was employed instead of $HAuCl_4$ also polymer particles were formed, however, no complexation or reduction could be expected in this case. The obtained particles, in contrast to the gold clusters, are instable in water and dissolve completely. The evolution of hydrochloric acid during heating was therefore deduced as a factor for the cluster formation. While PEI hydrochloride is readily soluble in water it is completely insoluble in DMF. The insolubility of the PEI-Au clusters in water furthermore supports a crosslinking mechanism.

The reaction of linear PEI (25 kDa) with $HAuCl_4$ only resulted in single particles, therefore, the cluster formation could be attributed to the branched structure of bPEI. However, when linear poly(allyl amine) was employed also clusters were formed. Thus, the presence of primary amine groups plays a pivotal role for the cluster formation. The molar mass of the bPEI is a less critical factor. Short bPEI (0.6 kDa) resulted in gold particle formation, however, precipitation occured during the reaction. With 1.8 kDa and 10 kDa bPEI already clusters were formed but still some aggregation took place as it is evident from the broadened LSPR (**Figures 4.4 and 4.5**). For large $HAuCl_4$:bPEI ratios (4:1; 3:1) no formation of stable particles occurred. By decreasing the ratio to 2:1 a stable red solution was obtained, but, instead of distinct clusters, TEM only revealed the presence of large aggregates of the crosslinked polymer and encapsulated gold nanoparticles. A valuable feature of this synthesis approach is the tunability of the cluster size. By keeping the reactant ratio at 1:1 but increasing the overall concentration clusters from 40 up to 230 nm could be synthesized (**Figure 4.6**).

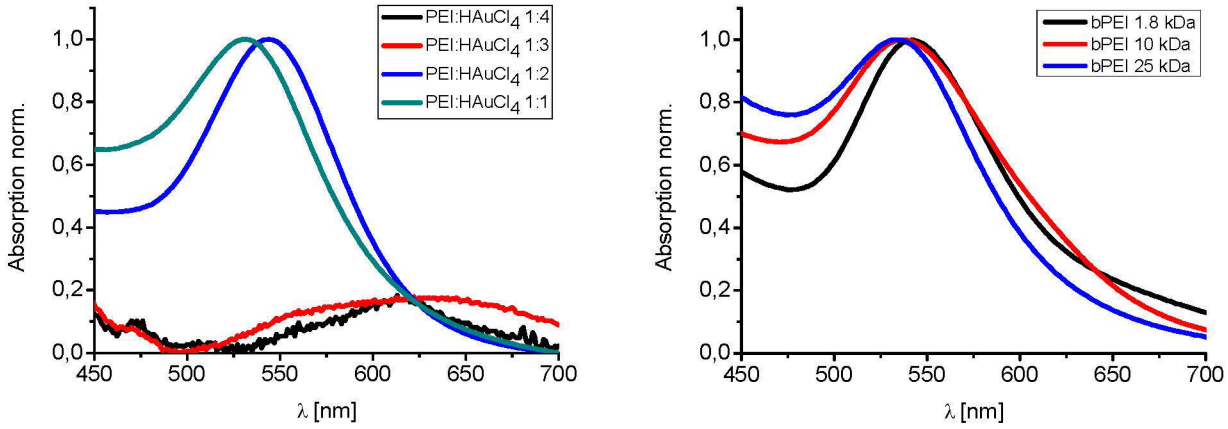

Figure 4.4: UV-Vis spectra of particles synthesized with different PEI/$HAuCl_4$ ratios (left), UV-Vis spectra of clusters synthesized with PEIs of different molar masses (right).

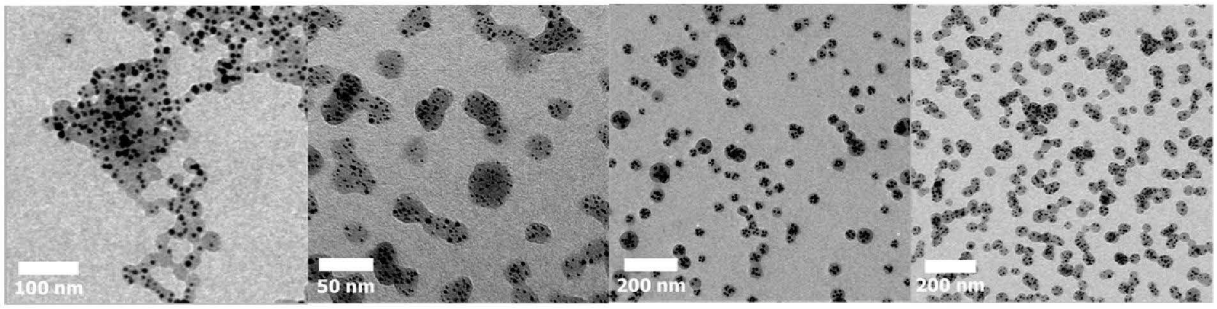

Figure 4.5: TEM images of particles synthesized with a 1:2 ratio, with PAAm, bPEI 1.8 kDa and bPEI 10 kDa (from left to right).

Decreasing the ratio led to the formation of large single particles with a plasmon peak at 561 nm (**Figure 4.7**). UV-Vis spectroscopy of the clusters showed a constant LSPR at ~530 nm except for the largest clusters. A small bathochromic shift was observed in this case which could be attributed to additional plasmon coupling.

It could also be demonstrated that pre-synthesized nanoparticles can be encapsulated in the clusters leading to an increased filling factor. For this purpose, citrate stabilized gold nanoparticles were transferred into DMF. Application of a low amount of initial particles resulted in secondary nucleation in particular for larger clusters and only small changes in the UV-Vis spectrum (**Figure 4.8**). By an increase to the tenfold concentration only seeded growth and encapsulation took place. Additionally, a significant redshift and broadening of the LSPR could be observed due to increased electromagnetic interactions between the particles. The optical properties of such cluster structures are largely dependent on the amount of metal in the cluster (*i.e.*, the filling factor), the employed metal and the size of the cluster as

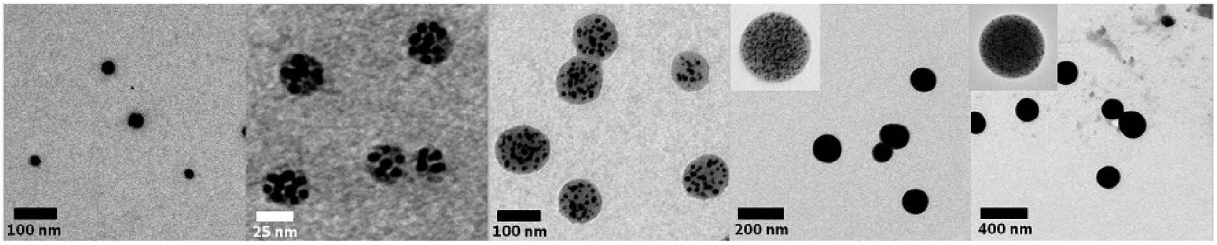

Figure 4.6: TEM images of single particles and clusters synthesized from bPEI 25 kDa and $HAuCl_4$ at a fixed ratio of 1:1. Concentrations of the reactants: 1, 10, 20, 50, 100 mg/mL (from left to right).

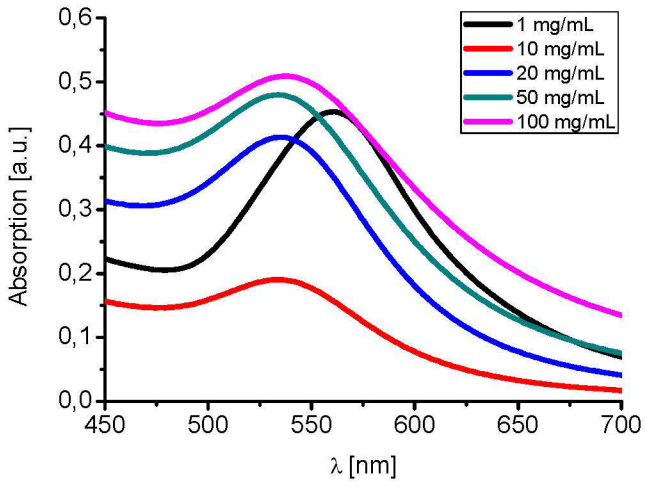

Figure 4.7: UV-Vis spectra of single particles and clusters synthesized at different concentrations of the reactants.

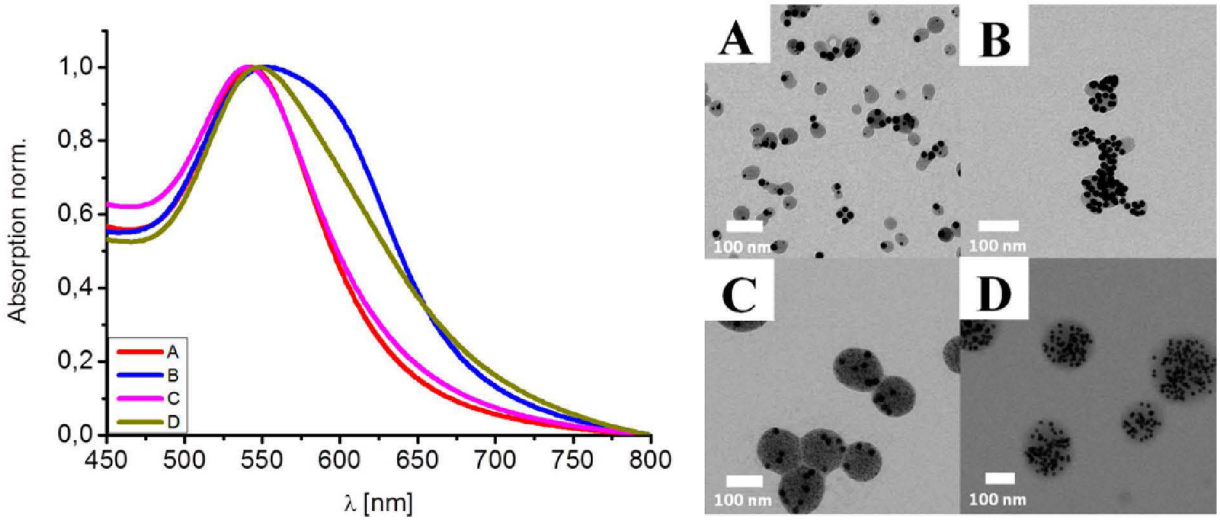

Figure 4.8: UV-Vis spectra and TEM images of clusters of different size and filling fractions: A - small clusters, low filling fraction; B - small clusters, high filling fraction; C - large clusters, low filling fraction; D - large clusters, high filling fraction.

well as of the individual nanoparticles. A low filling factor, as in case of the initial PEI-Au clusters, merely shows the LSPR of individual nanoparticles.

However, by an increase of the size of the embedded gold nanoparticles the filling factor increases with a concomitant decrease of the interparticle distance. A magnetic dipole moment can thereby be generated from plasmon coupling which, however, could not be determined experimentally in our case. As already shown, the filling factor in the PEI-Au clusters as well as the size of the gold particles can be increased by encapsulation of pre-synthesized gold nanoparticles. Though, thereby the initial gold content of 2.7% only doubles for the largest clusters even if the citrate stabilized particles are concentrated to tenfold of their original concentration. It could be demonstrated that the seeded growth of the clusters provides a versatile alterative to tune the optical properties of the clusters (**Scheme 4.2**). Clusters of 120 nm diameter were employed for the growth reactions. A growth solution consisting of a cetyltrimethylammonium bromide (CTAB)/$HAuCl_4$ complex and ascorbic acid was prepared.[133] At first Au^{3+} ions are only reduced to Au^{+}, but in the presence of elemental gold the reduction is catalyzed further to Au^{0}. Therefore, when a seed solution consisting of PEI-Au clusters was added to the Au(I) solution, growth of the initial gold particles took place. Decreasing volumes (20 µL, 10 µL, 5 µL) of seeds were added to 1 mL of the growth solution which led to a color change from an initial red over purple to a dark blue solution (**Figure 4.9**). UV-Vis spectroscopy of the samples revealed an increased intensity as well as a redshift and broadening of the plasmon resonance.

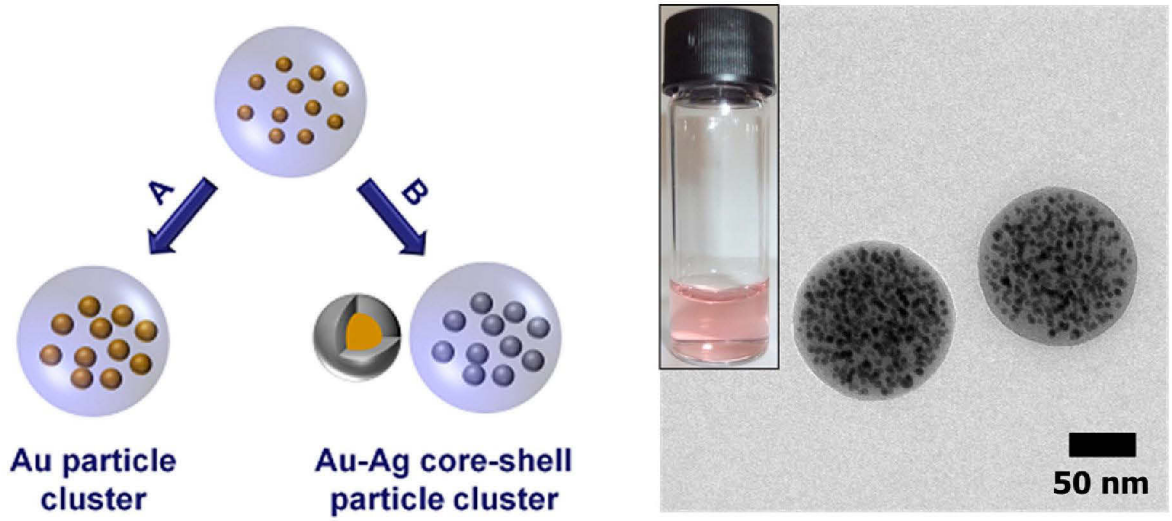

Scheme 4.2: Schematic representation of the nanoparticle growth inside of the clusters mediated by $HAuCl_4$/AA/CTAB (A) or $AgNO_3$, $NH_{3(aq)}$, $HCHO_{(aq)}$ (B) (left). TEM image and photograph of the seed clusters (right).

Since the change in particle size is not able to generate such large differences of the optical properties, the effects can be attributed to a decreased interparticle distance. TEM images disclosed an increased gold particle diameter from initial 5.4 to 8.1, 9.6 and 11.8 nm, respectively.

Silver is in general the material of choice for plasmonics in the visible region.[134] While the direct synthesis of Ag-PEI clusters was not possible, seeded growth could successfully be utilized to prepare Au-Ag-core-shell clusters (**Figure 4.10**). Tollens reagent was used for growth and the color of the solutions first changed to yellow and afterwards to purple and blue again by employing the same reaction volumes as in case of gold. Analysis of the clusters *via* TEM showed an increased particle size (9.8 nm, 12 nm, 14.8 nm) which corresponds to a shell thickness of 2.2 nm, 3.3 nm and 4.7 nm, respectively. In particular, for the lowest amount of seeds non-spherical core-shell particles were produced on the outside of the clusters which could be attributed to a slow diffusion of the growth solution to the inside and different growth kinetics of silver.[135-136] UV-Vis spectroscopy at first revealed a hypsochromic shift due to the lower LSPR of silver, with an increased size of the silver shell the LSPR shifts to higher wavelengths due the decreased interparticle distance.

In particular, for the lowest amounts of seeds a strong absorption in the near-IR region was observed due to the presence of non-spherical structures. Additionally, fusion of the individual particles into larger structures might occur.

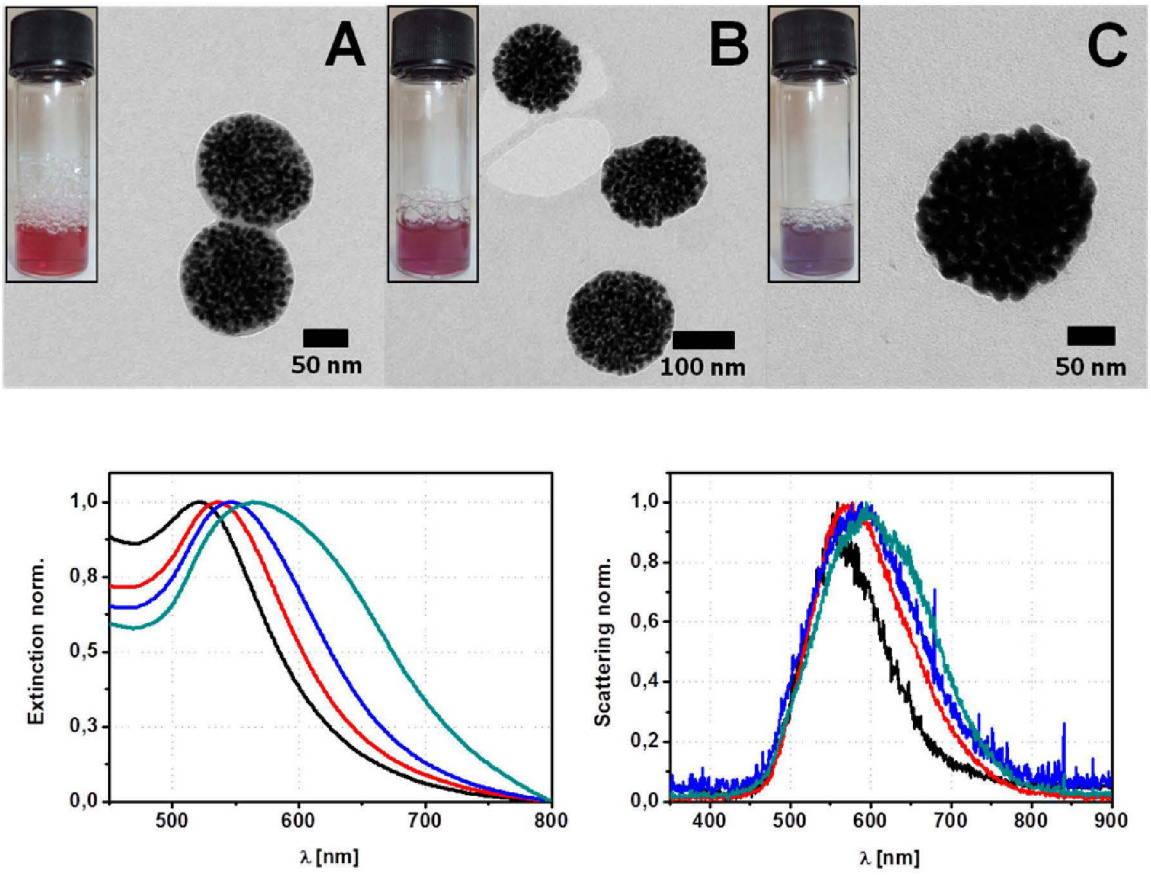

Figure 4.9: TEM images of the gold clusters synthesized with decreasing volumes of the seed solution (A 20 µL, B 10 µL, C 5 µL) (Top). UV-Vis spectra of the gold cluster solutions (bottom left) and scattering spectra of individual clusters (bottom right): Black – original clusters; red, blue, green – gold cluster solutions with increasing gold particle sizes/filling fractions. The seed concentration decreases from red to green.

Based on the amounts of the applied growth solutions filling factors of 9.2%, 15.4% and 28.5% for the gold clusters as well as 16.3%, 29.3% and 56.3% for the Au-Ag core-shell clusters, were calculated.

TEM investigations can only provide a 2D projection of the cluster structure. Therefore FIB milling was applied which allows to display the cross-section of the assembly (**Figure 4.11**). A platinum layer was deposited on the particles and cutting was performed with a gallium ion beam. The cross-section clearly revealed individual nanoparticles embedded in a spherical structure. A UV-Vis spectrum of such clusters represents the sum of both absorption as well as scattering. Hence, dark field microscopy was applied to elucidate the scattering spectra of individual clusters.[137-138] Yellow (blue) dots in the dark field images correspond to larger (smaller) clusters, since the scattering wavelength increases with increasing particle size (**Figure 4.12**).

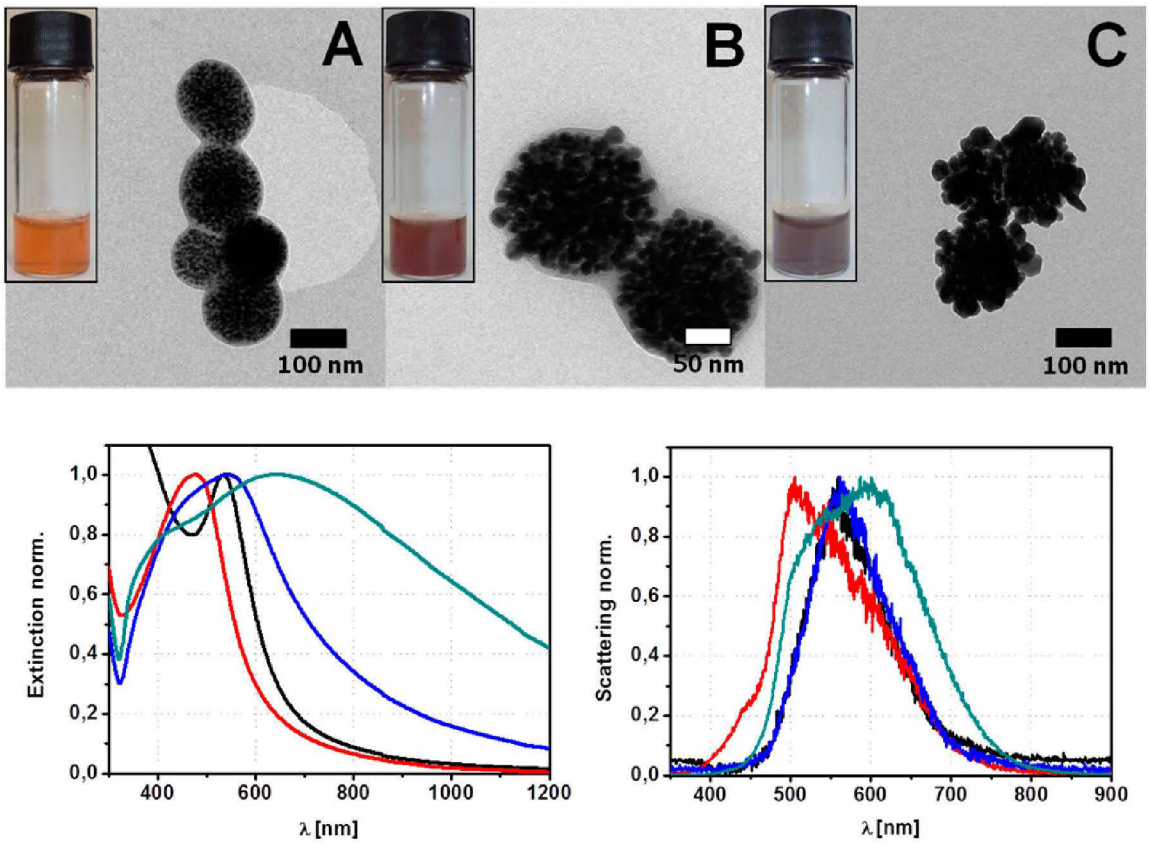

Figure 4.10: TEM images of the gold-silver core-shell clusters synthesized with decreasing volumes of the seed solution (A 20 µL, B 10 µL, C 5 µL) (Top). UV-Vis spectra of the gold-silver core-shell cluster solutions (bottom left) and scattering spectra of individual clusters (bottom right): Black – original clusters; red, blue, green – gold cluster solutions with increasing gold particle sizes/filling fractions. The seed concentration decreases from red to green.

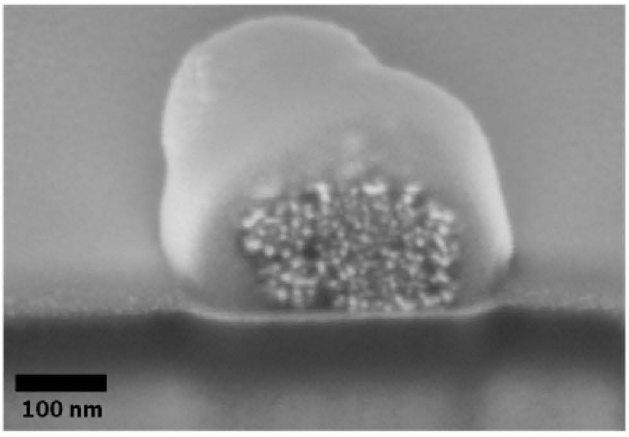

Figure 4.11: SEM image of a FIB prepared cross-section from a gold-PEI cluster with the highest filling factor. The area is covered by a 40 nm platinum layer, the substrate material is SiO_2 with a conductive layer of 10 nm ITO.

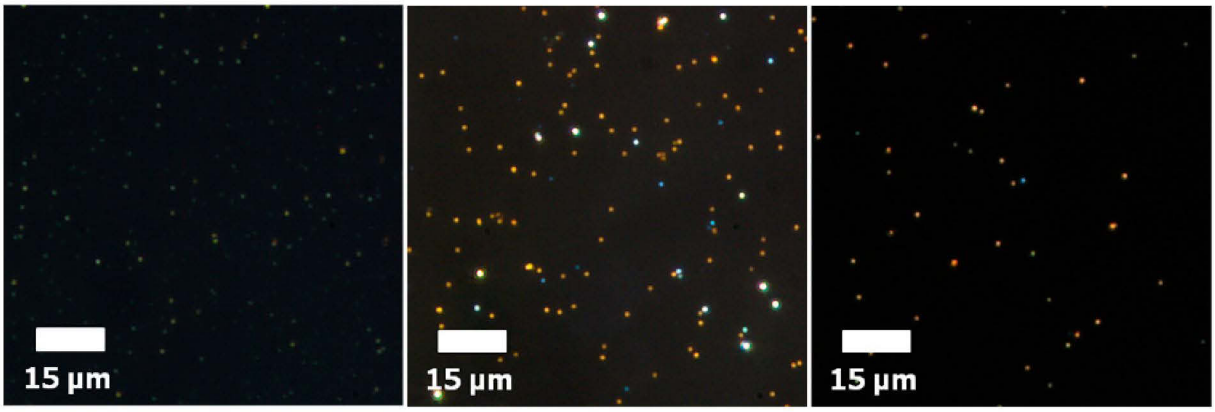

Figure 4.12: Dark field images of the seed solution (left), after gold growth with a medium amount of seeds (middle) and after silver growth with a medium amount of seeds (right).

The obtained scattering spectra showed a similar trend as the UV-Vis spectra. In case of the initial Au-PEI clusters the scattering maximum is shifted to 559 nm in comparison to 521 nm for the UV-Vis spectrum. With increasing filling factor a further shift to 578 nm, 588 nm and 595 nm occurred, respectively. For the Au-Ag core-shell clusters at first a hypsochromic shift to 505 nm followed by an increase of the scattering wavelength to 562 nm and 587 nm took place.

In order to compare the obtained optical properties with the theoretical predicted results, simulations based on an extended Mie theory[139-140] were carried out (**Figure 4.13**). The calculations were based on a cluster of 120 nm diameter consisting of 300 particles with increasing size. An initial LSPR maximum of 540 nm was calculated for the seed clusters consisting of 5.4 nm particles. In comparison to the experimental value (LSPR at 521 nm) this indicates a lower "real" particle size. More importantly, however, it corresponds only to the absorption of single particles, *i.e.*, no plasmon coupling is evident. With increasing filling factor of gold the interparticle distance decreases, whereby, coupling begins to emerge and the absorption is shifted towards higher wavelengths. In case of the Au-Ag core-shell clusters first a blueshift occurs due to the higher plasma frequency of silver. Additionally, a weak shoulder from the contribution of the gold plasmon resonance is still visible. Afterwards, the resonance is redshifted, similar to the experimental trend. The largest differences between predicted and experimental results were observed for the clusters with the highest amount of silver which could be attributed to the occurrence of non-spherical and fused particles. From the simulations the contribution of different dipole moments to the spectra can be established. It could be shown that the magnetic dipole moment contributes to only a small fraction of the

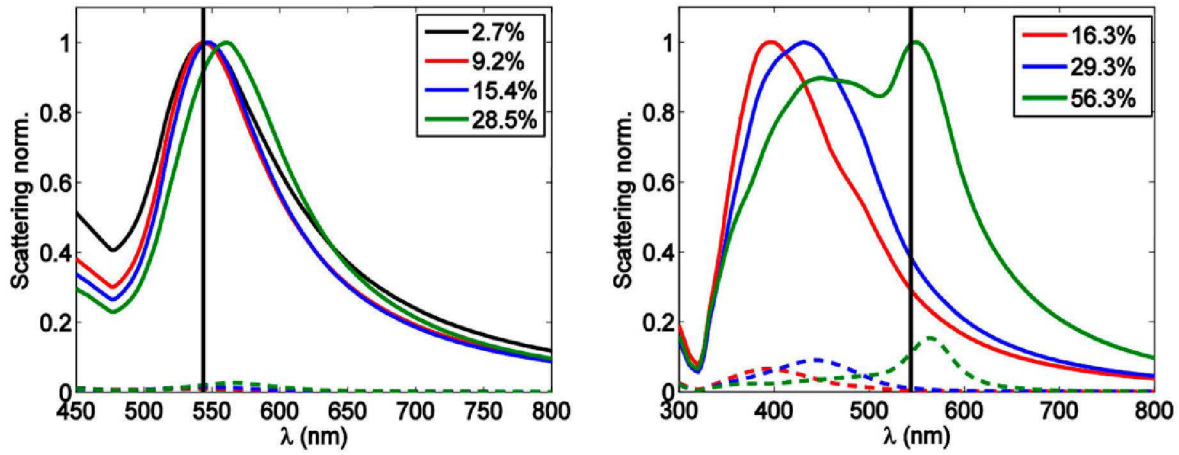

Figure 4.13: Simulated scattering cross-sections of gold nanospheres (left) and gold nanospheres with silver shells (right). Black – original particles; red, blue, green – gold particles with increasing diameter or silver shell thickness, respectively, where the colors correspond to different filling fractions of the cluster. Solid lines – total scattering cross-section; dashed lines – magnetic dipole contribution to the scattering cross-section. Black vertical line – resonance position of an isolated gold particle.

absorption in case of the Au-PEI clusters. Yet, for clusters with silver this contribution is considerably increased due to the lower intrinsic absorption of silver.

Summarizing, a versatile approach to synthesize gold nanoparticle clusters with a tunable size could be introduced. Additionally, the contribution of numerous factors responsible for the simultaneous formation of the gold particles and the spherical assembly structure could be elucidated. Moreover, it could be shown that the seeded growth of these clusters represents a versatile tool to tune the optical properties by an increased filling factor or through the generation of Au-Ag core-shell particle clusters. The experimental results are in good agreement with theoretical predictions. Therefore, these clusters might serve as valuable building blocks for metamaterials or functional polyamine–plasmonic particle composites.

5 Block copolymer assisted fabrication of plasmonic nanostructures

Parts of this chapter have been published: P8) F. Kretschmer, S. Stumpf, U. Mansfeld, F. H. Schacher, S. Hoeppener, U. S. Schubert, *J. Mater. Chem. C*, submitted

The synthesis of nanoparticle assemblies provides in most cases structure sizes well below the micrometer regime. Large areas covered with defined plasmonic nanostructures, however, could pave the way for the creation of 3D plasmonic materials. Available methods to pattern large nanostructures utilize top-down approaches like electron beam lithography.[141-142] Thereby, unique nanostructures can be written but long fabrication times and high costs are involved. Block copolymers (BCP) can be considered as a versatile alternative for the fabrication of ordered nanostructures on rather large areas. The covalent bond between two polymer blocks prohibits macroscopic demixing of the polymers, instead, nanophase separation takes place. Depending on the block length, ratio and composition, *e.g.*, a hexagonal, lamellar or gyroid phase separation can be achieved.[143-144] Incorporation of plasmonic nanoparticles into the BCP structure can be accomplished by several approaches. Pre-synthesized nanoparticles can be directly mixed with the polymer prior to the film formation but functionalization of the particles with one of the blocks is required in this case.[88] A second strategy employs removal of one of the blocks after phase separation, *e.g.*, through UV light or plasma treatment. In the generated voids particles can be deposited *via* capillary interactions.[89] Alternatively, metal salts can be incorporated into one of the blocks, for instance, through complexation with vinylpyridine units. By complexation in solution, micelles are formed. Deposition of the micelles on a substrate followed by reduction leads to a hexagonal lattice of plasmonic nanoparticle clusters.[87] However, also complexation in the film can be performed yielding well-ordered nanostructures depending on the phase separation.

As described in **Chapter 4**, high filling factors of nanoparticles are required to access novel optical properties. This cannot be achieved directly through the complexation approach since only relatively low amounts of metal ions are bound at once. Therefore, a novel strategy was developed to increase the metal content in phase-separated BCP films through a cyclic complexation-reduction approach. A PS-*b*-P2VP film (M_n = 230,000 g/mol, PS:P2VP 65:35, PDI 1.03) was prepared by spin-coating the polymer solution onto glass substrates. AFM

measurements revealed only disordered structures, hence, solvent vapor annealing was applied to obtain an ordered phase separation (**Figure 5.1**).[145-146] Hexane vapor only yielded small worm-like structures. By annealing with toluene a much more pronounced phase separation with elongated structures and dots was obtained. Annealing with ethanol resulted in porous structures due the selective dissolution/swelling of the P2VP phase.[147] Treatment with THF as well as with chloroform vapor already showed the formation of ordered lamellar structures but the obtained domain sizes were still rather small.

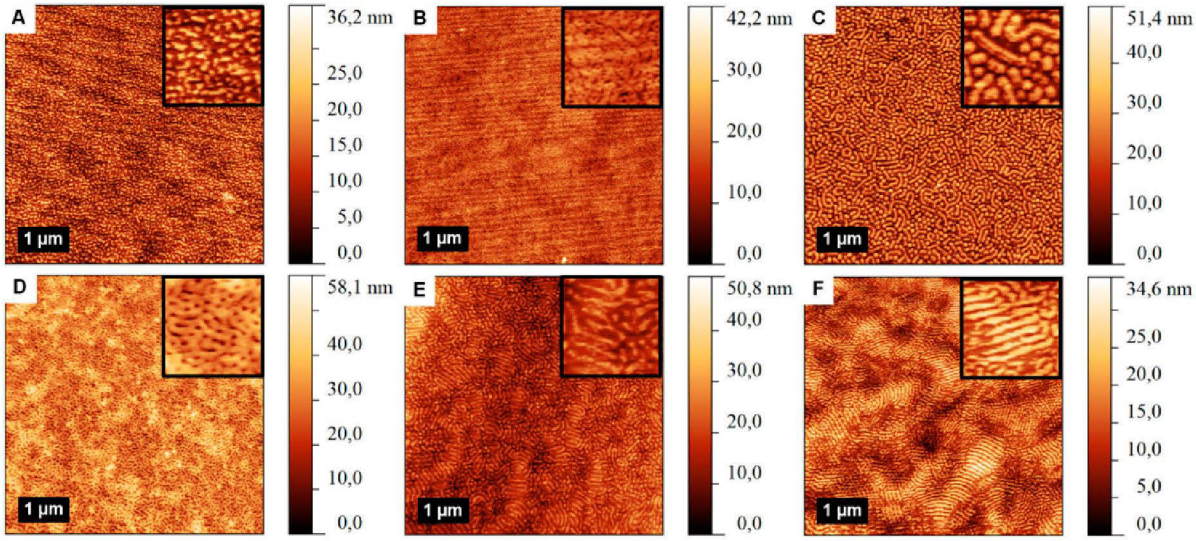

Figure 5.1: AFM height micrographs of PS-*b*-P2VP films annealed for 1 h in solvent vapor. A – as-cast, B – hexane, C – toluene, D – ethanol, E – tetrahydrofuran, F – chloroform. Images were acquired under hard-tapping conditions. Inset width is 630 nm in all cases.

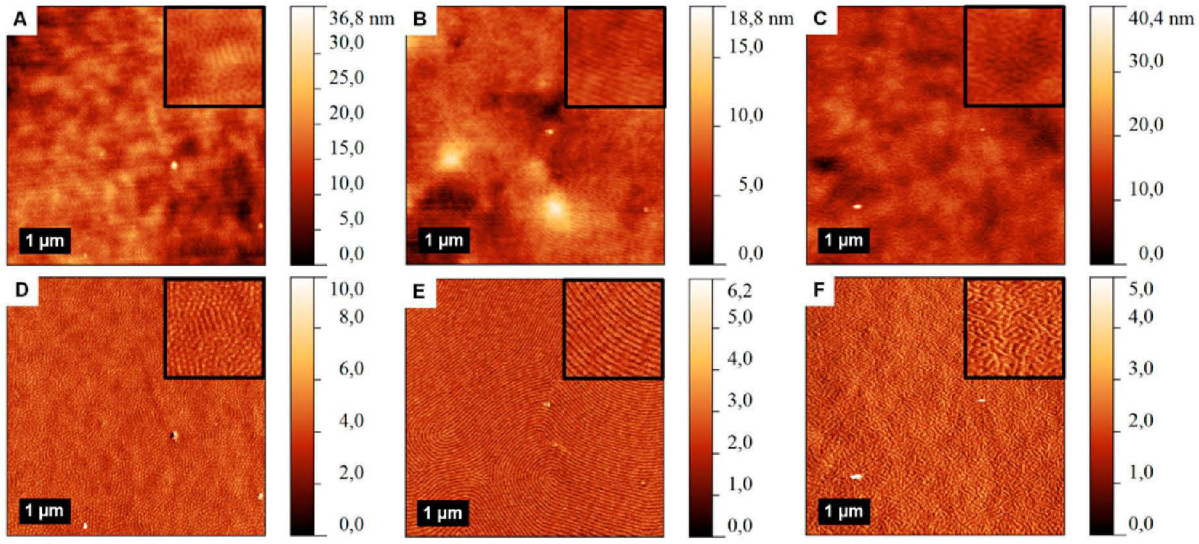

Figure 5.2: AFM height (A-C) and phase (D-F) micrographs of PS-*b*-P2VP films annealed for different times in dichlormethane vapor. A/D – 5 min, B/E - 1 h, C/F – 4 h. Inset width is 630 nm in all cases.

Finally, dichloromethane was identified as the solvent of choice (**Figure 5.2**). Short annealing times resulted mostly in a mixture of hexagonal and lamellar structures. The optimal formation of lamellar phases was obtained after one to two hours annealing. Longer times resulted in more disordered structures, again. For the complexation the films were immersed in a $HAuCl_4$ or $AgNO_3$ solution. After washing and drying, reduction was performed with hydrazine vapor. The color of the films changed to purple or yellow, respectively, which can be attributed to the nanoparticle formation (**Figure 5.3**). Seeded growth was conducted to obtain a higher filling factor but mostly secondary nucleation and overgrowth occurred. However, during the course of the reduction the ligand is released, and, as a consequence, the P2VP units are able to complex new metal ions. Therefore, repeated immersion and reduction could be utilized successfully to increase the metal content in the BCP film. This could easily be visualized by a color change of the films from purple to dark blue for gold or to a more intensive yellow-brown color in the case of silver.

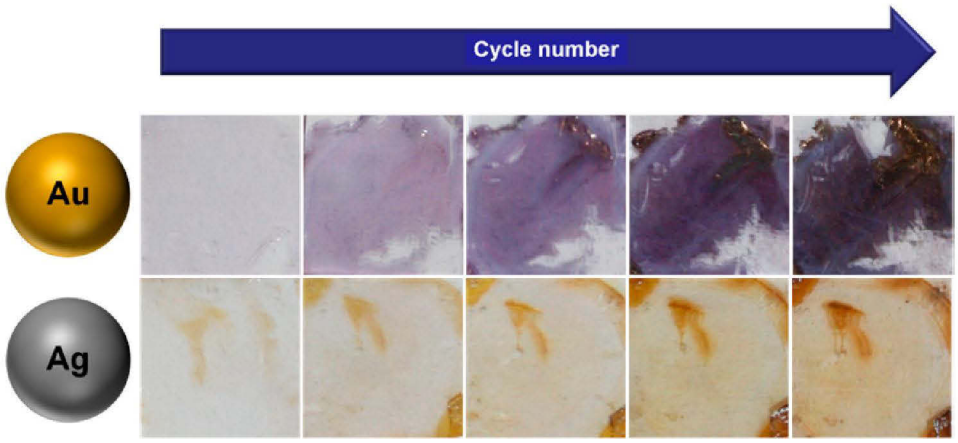

Figure 5.3: Photographs (~ 1×1 cm) of PS-*b*-P2VP films with increasing metal content after different numbers of complexation-reduction cycles.

After the first reduction TEM investigations revealed the presence of spherical particles with a diameter of 14.3 ± 2.5 nm diameter in the case of gold (**Figure 5.4**). The following cycle led to an increase of the particle size (18.1 ± 4.9 nm) but fusion into nonspherical particles started to occur. With increasing cycle number elongated rod-like structures from dozens to hundreds of nanometers length were produced and spherical particles became the minority.

UV-Vis spectra of the Au-BCP films were characterized by an increased intensity of the surface plasmon resonance with increasing filling factor (**Figure 5.5**). A redshift of the plasmon peak occurred towards 550 nm in comparison to gold particles in solution.

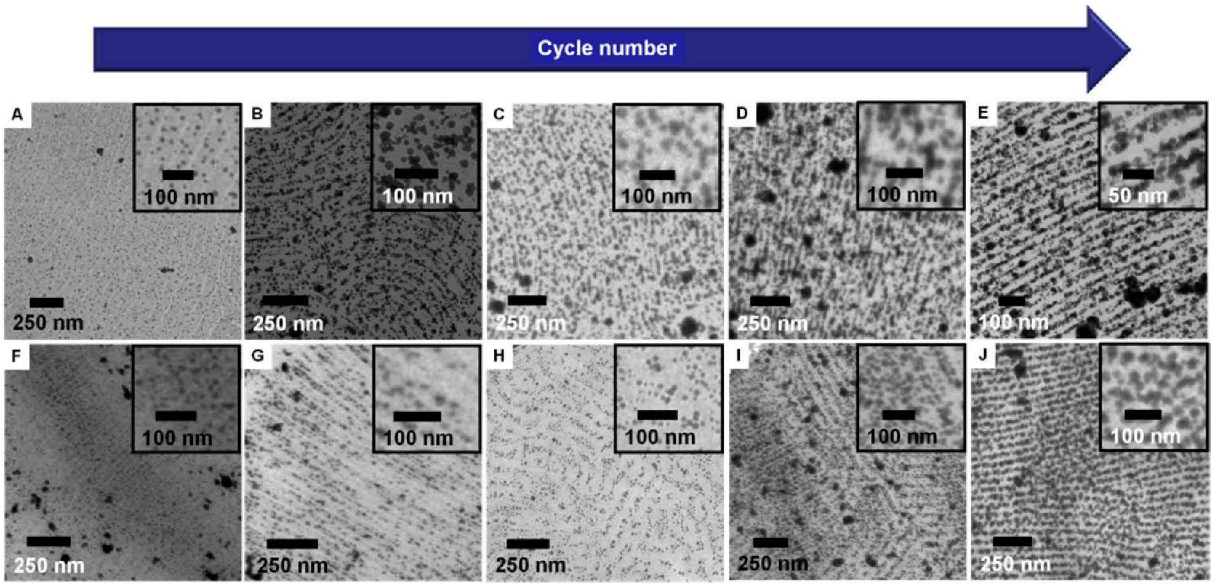

Figure 5.4: TEM images of PS-*b*-P2VP films with increasing metal content. Top – gold. Bottom – silver.

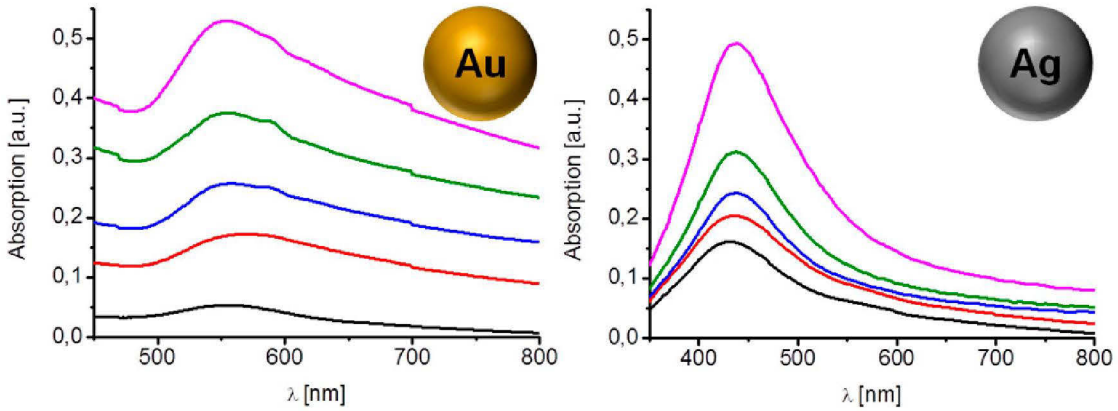

Figure 5.5: UV-Vis spectra of PS-*b*-P2VP films with increasing metal content. Black – cycle 1, red – cycle 2, blue – cycle 3, green – cycle 4, violet – cycle 5.

This effect could be attributed to the presence of the polymer on the particle surface or non-spherical particles produced during the reduction. With increasing cycle number an additional shift to higher wavelengths took place and a shoulder arose due to the decreased interparticle distance. Through the elongation of the particles additionally a strong broad absorption in the near IR region was produced since non-spherical structures, in particular nanorods, feature a second plasmon peak at higher wavelengths.[51]

In contrast to gold, films prepared with silver showed mostly the presence of spherical particles (12.5 ± 2.5 nm, 14 ± 3.3 nm, 16.2 ± 3.8 nm, 18.7 ± 4.4 nm, 22 ± 4.8 nm, respectively) with increasing cycle number. Similarly to gold, at first a general redshift of the

LSPR occured in comparison to the solution and an increased intensity was observed with higher silver content. However, the absorption in the near IR region was rather low compared to gold due to the absence of rod-like structures. These differences most likely represent silver's susceptibility against oxidation which leads to a deterioration of the nanoparticles and, hence, also to a lower metal content in the films. Additionally, the complexation mechanism in the strongly confined solid P2VP phase might differ from the one in solution.

To summarize, a versatile approach to synthesize plasmonic block copolymer composites could be developed. The utilized strategy involved repeated immersion-reduction cycles to tune the metal content. Solvent annealing was performed to prepare PS-*b*-P2VP films with an ordered lamellar phase separation. Afterwards, metal ions were complexed in the P2VP phase of the copolymer. Through reduction nanoparticles are formed and the pyridine units are released allowing a new complexation step. In this way, block copolymer films with tunable optical properties could successfully be prepared as demonstrated by UV-Vis spectroscopy and TEM. Additionally, the morphology could be tuned from a spherical shape to rod-like structures in the case of gold.

6. Summary

Fueled by a wide range of possibilities to tune their interactions with light, a strong increase of interest could be witnessed in the field of plasmonic nanoparticle research in the recent years. The adjustable size, geometry and spatial arrangement to each other enables to control the optical response of such nanostructures at will. This translates into a plethora of potential applications for medicinal therapy, analytics, catalysis, energy conversion and even for devices with completely artificial optical properties. In order to obtain the building blocks for these materials, strategies to synthesize well-defined particles and their assemblies are required.

This thesis addressed the synthesis and characterization of plasmonic nanoparticle structures. Linear and tetrahedral linkers based on oligo(phenylene-ethynylenes) (OPE)s bearing thio endgroups were synthesized by Sonogashira cross-coupling reactions. Based on strong sulfur-metal interactions the self-assembly could be introduced through bonding of nanoparticles to the ends of the molecules. Variable amounts of the linear linker were added to citrate stabilized gold nanoparticles. The successful formation of assemblies was evident *via* a bathochromic shift and broadening of the surface plasmon resonance with increasing linker concentration. Separation of single particles from assemblies could be achieved by density gradient centrifugation. Analysis of the obtained fractions revealed an increase in the mean diameter towards the bottom and a color change from initially red to violet for the bottom fraction. Transmission electron microscopy investigations of the last fraction revealed the presence of mostly dimers. Through surface-enhanced Raman spectroscopy (SERS) a linear binding mode of the linker could be proven. For the direct investigation of a single dimer a scanning technique based on spatial modulation of the sample in combination with a lock-in detection of the transmitted signal was developed. An excellent agreement of the obtained extinction values with the numerically predicted ones could be revealed.

To create stable functional self-assembled monolayers (SAMs) a convenient approach to synthesize these kinds of ligands could be developed. By esterification of pentaerythritol tribromide with carboxylic acids, followed by conversion with potassium thioacetate tripodal ligands bearing azide, alkyne, furane and maleimide groups could be obtained in good yields. Maleimide functionalized particles were reacted with a corresponding P2VP-*b*-PEO block copolymer containing a single furan unit. UV-Vis spectroscopy indicated the presence of a shell and, in contrast to the initial particles, polymer functionalization led to the stabilization

of the particles in water. TEM investigations finally confirmed the shell formation utilizing staining procedures.

The synthesis of large anisotropic clusters consisting of hundreds of individual particles could be demonstrated by the reaction of branched PEI and $HAuCl_4$ in DMF. In this case the simultaneous formation of nanoparticles and the assembly occurred. The underlying mechanism was elucidated by a systematic variation of the reaction parameters. 25 kDA bPEI was required to obtain stable solutions; lower molar masses led to complete or partial aggregation. Primary amino groups were identified as a crucial parameter since the cluster formation could equally be achieved with PAAm but not with linear PEI. Evolution of hydrochloric acid during the synthesis led to insolubilization of the polymer as shown by a control reaction with NH_4Cl. Formation of a crosslinked network could be attributed to the complexation of the gold ions with the polymer chains and partial oxidation of the backbone. A kinetic investigation was conducted by measuring TEM and UV-Vis spectra at different reaction times. A stepwise reduction of Au^{3+} to Au^{+} and finally to Au^{0} through the amine groups could be observed. Concomitantly, small polymer structures grow into larger spheres. The variation of the reactant concentration enabled a tunable synthesis of either single particles or clusters from dozens to hundreds of nanometers in size. The amount of metal as well as the size of the embedded colloids could be increased by employing pre-synthesized particles which can be encapsulated during the synthesis.

To gather more control over the filling factor a seeded growth approach was developed. By application of a growth solution on seed clusters the synthesis of either Au-PEI clusters or Au-Ag-core-shell clusters with adjustable filling factors could be demonstrated. TEM revealed increasing particle diameters with decreasing seed concentrations. As a consequence, the interparticle distance decreases and additional coupling between the particles occured as evidenced by UV-Vis spectroscopy. For the gold clusters a bathochromic shift and broadening of the LSPR took place, whereas for silver initially a hypsochromic shift followed by a broadening was observed. A detailed view of the internal cluster structure could be obtained by cutting slices with a focused ion beam (FIB). Dark field microscopy was carried out to investigate the scattering spectra of single clusters. Thereby, the trend obtained by UV-Vis spectroscopy could be confirmed. Simulations of the structures based on the Mie theory revealed a good agreement with the experimental results. Additionally, the contribution of the magnetic dipole moment to the spectra could be observed.

For the synthesis of ordered plasmonic nanoparticle assemblies on large areas, block copolymer lithography could successfully be utilized. AFM measurements were conducted to investigate the phase separation after solvent annealing. By annealing of PS-*b*-P2VP films in methylene chloride vapor the desired lamellar phase separation could be obtained. Complexation and reduction of gold or silver ions resulted in the formation of metallic nanoparticles only in one phase. In order to increase the metal content a cyclic approach was introduced. With increasing cycle number the size of the nanoparticles increased with a concomitant decrease of the interparticle distance as demonstrated by TEM. UV-Vis showed an increased LSPR intensity and a small bathochromic shift with higher filling factor due to plasmon coupling. In case of gold, additionally a strong absorption was observed in the near IR region which could be attributed to the formation of rod-like structures from fusion of single particles.

In conclusion, the present thesis deals with the synthesis and characterization of plasmonic nanoparticles and their assemblies. Rigid-rod linkers could be utilized for the formation of small clusters like nanoparticle dimers. The synthesis of tripodal thioacetates for the preparation of functional SAMs on gold surfaces was performed. Au-PEI and Au-Ag core-shell clusters with tunable optical properties were prepared which could serve as promising building blocks for metamaterials. Block copolymer lithography in combination with a cyclic complexation-reduction approach could be utilized to create ordered plasmonic nanostructures on micrometer surface areas..

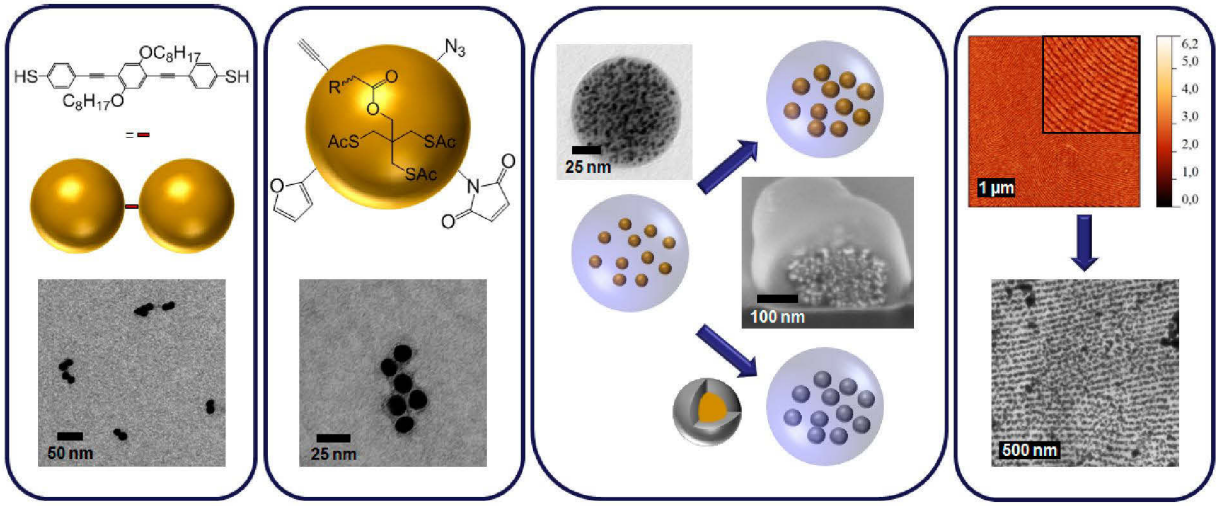

Figure 6.1: Overview of different strategies for the preparation of plasmonic nanostructures investigated in this thesis: Gold-dimers assembled *via* a rigid rod linker, surface functionalization of gold nanoparticles, synthesis of gold as well as gold-silver core-shell nanoparticle clusters and preparation of ordered block copolymer-gold/silver nanostructures.

Future work should be devoted to the formation of 3D structures and the synthesis of nanoshells or particles based on other materials like silicon and metal oxides/nitrides. Additionally, chiral and patchy particles as well as plasmonic molecules could be used to develop structures with attractive optical properties

7. Zusammenfassung

Die Forschung an plasmonischen Nanopartikeln erlebte ein rasante Entwicklung in den vergangenen Jahren aufgrund einer Vielzahl von Möglichkeiten, ihre Wechselwirkung mit Licht zu beeinflussen. Die veränderbare Größe, Form und Anordnung der Partikel zueinander ermöglichen eine nahezu beliebige Einstellung der optischen Eigenschaften. Dadurch ergibt sich eine Fülle an potentiellen Anwendungen in der Medizin, Analytik, Katalyse und Energieumwandlung. Ebenso lassen sich Materialien mit Eigenschaften, wie sie in der Natur nicht existieren, herstellen. Um die Bausteine für solche Anwendungen zu erhalten, bedarf es gezielter Strategien Nanopartikel und deren Anordnungen in definierter Qualität zu synthetisieren.

Im Rahmen dieser Dissertation wurden plasmonische Nanostrukturen synthetisiert und charakterisiert. Basierend auf Oligo(*p*-phenylenethynylenen) wurden starre lineare und tetraederförmige Linker mit Schwefelendgruppen mittels der Sonogashira-Kreuzkupplung hergestellt. Aufgrund der starken Schwefel-Metall Wechselwirkung wird eine Bindung des Partikels an den Enden der Moleküle ermöglicht, wodurch eine Selbstassemblierung der Kolloide stattfindet. Variable Mengen des linearen Linkermoleküls wurden zu einer Lösung Citrat-stabilisierter Goldnanopartikel gegeben. Die Bildung von Clustern zeigte sich anhand der Rotverschiebung und einer Verbreiterung der Oberflächenplasmonenresonanz mit steigender Linkerkonzentration. Durch die Zentrifugation in einem Dichtegradienten konnte eine Trennung einzelner Partikel und von angeordneten Strukturen erreicht werden. Eine Analyse einzelner Fraktionen ergab einen Anstieg des Durchmessers in Richtung Boden sowie eine Farbänderung von anfänglich rot zu violett für die unterste Fraktion. Transmissionselektronenmikroskop (TEM)-Untersuchungen dieser Fraktion zeigten vorrangig Nanopartikeldimere während mittels oberflächenverstärkter Raman-Spektroskopie (SERS) ein linearer Bindungsmodus des Linkers an die Partikel festgestellt werden konnte. Für die direkte Untersuchung eines einzelnen Dimers wurde eine Scan-Methode basierend auf der räumlichen Modulation der Probe in Kombination mit einem Lock-in-Verstärker entwickelt. Dabei zeigte sich eine ausgezeichnete Übereinstimmung der dabei erhaltenen Extinktionswerte mit den berechneten Werten.

Für die Anwendung hinsichtlich stabiler funktioneller selbstassemblierter Monolagen (SAMs) konnte ein praktischer Ansatz für die Synthese der benötigten Liganden entwickelt werden.

Veresterung von Pentaerythritoltribromid mit Carbonsäuren und anschließendes Umsetzen mit Kaliumthioacetat ergab die azid-, alkin-, furan- und maleimidfunktionalisierten tripodalen Liganden in guten Ausbeuten. Maleimidfunktionalisierte Goldpartikel wurden mit einem P2VP-*b*-PEO-Blockcopolymer, welches eine einzelne Furaneinheit trug, umgesetzt. UV-Vis Spektroskopie wies auf die Anwesenheit einer Hülle hin, da die ursprünglichen Partikel, im Gegensatz zu den polymerfunktionalisierten Partikeln, in Wasser nicht stabil waren. Mittels TEM-Untersuchungen konnte die Ausbildung einer Hülle bestätigt werden.

Die Synthese großer anisotroper Cluster, welche aus hunderten Einzelpartikeln bestehen, konnte durch die Umsetzung von verzweigtem Polyethylenimin (bPEI) mit Tetrachloridogoldsäure in DMF ermöglicht werden. In diesem Fall erfolgte eine simultane Bildung der Metallpartikel und die Ausbildung der sphärischen Anordnung. Anhand der Variation der Reaktionsparameter konnte der Entstehungsmechanismus aufgeklärt werden. bPEI mit einer Molmasse (M_n) von 25.000 g/mol wird zur Herstellung stabiler Lösungen benötigt, da kürzere Polymere zu partieller oder vollständiger Aggregation führten. Die primären Amingruppen sind ein Schlüsselfaktor der Clusterbildung, da lineares Polyallylamin, im Gegensatz zu linearem PEI, ebenfalls zur Entstehung einer Hülle führte. Die Kontrollreaktion von bPEI mit NH_4Cl zeigte, dass die Entwicklung von HCl während der Synthese verantwortlich für das Entstehen einer Dispersion ist. Komplexierung der Goldionen sowie die Oxidation des Polymerrückgrates führt zu einem unlöslichen Netzwerk. Durch TEM-Messungen und UV-Vis Spektroskopie-Untersuchungen zu unterschiedlichen Zeiten während der Reaktion konnte die Reaktionskinetik ermittelt werden. Es erfolgte eine stufenweise Reduktion durch die Aminogruppen von Au^{3+} zu Au^{+} und schließlich zu Au^{0}. Gleichzeitig bilden sich große Polymerpartikel aus kleineren Strukturen. Anhand der Variation der Gesamtkonzentration der Reaktanden konnten entweder einzelne Partikel oder Cluster mit einstellbarer Größe (zwischen einigen Dutzend und mehreren hundert Nanometern) hergestellt werden. Der Metallanteil und die Größe der Goldpartikel konnte durch Einkapselung von vorgelegten Partikeln während der Synthese erhöht werden.

Um eine bessere Kontrolle über den Füllfaktor zu erlangen, wurde ein "seeded growth" Ansatz verwendet. Durch Mischen einer Wachstumslösung mit Keimclustern konnte die Synthese von Au-PEI Clustern oder Au-Ag Core-Shell Clustern mit maßgeschneiderten Füllfaktoren erreicht werden. TEM-Aufnahmen zeigten größere Partikeldurchmesser mit sinkender Seedkonzentration. Dadurch sank der Partikelabstand und zusätzliche Kopplungen traten zwischen den Partikeln auf. Mittels UV-Vis Spektroskopie konnte im Falle der Au-PEI

Cluster eine bathochrome Verschiebung und Verbreiterung der Oberflächenplasmonenresonanz beobachtet werden, während die Au-Ag Core-Shell Cluster zuerst eine Verschiebung zu niedrigeren Wellenlängen zeigten. Durch Schneiden mit einem fokussierten Ionenstrahl konnte eine detaillierte Ansicht der inneren Clusterstruktur gewonnen werden. Über Dunkelfeldmikroskopie wurden die Streuspektren einzelner Cluster erhalten, welche den selben Trend wie die in Lösung ermittelten UV-Vis-Spektren aufwiesen. Anhand von Simulationen basierend auf der Mie-Theorie zeigte sich eine gute Übereinstimmung mit den experimentellen Ergebnissen. Damit konnte zusätzlich der Beitrag des magnetischen Dipolmoments zu den Spektren ermittelt werden.

Für die Herstellung geordneter plasmonischer Strukturen auf ausgedehnten Flächen konnte erfolgreich die Blockcopolymerlithographie verwendet werden. Mit Hilfe von Rasterkraftmikroskopie (AFM)-Messungen wurde die Phasenseparation beim Sintern mit verschiedenen Lösungsmitteldämpfen untersucht. Dichlormethan ergab dabei die gewünschte lamellare Phasenseparation eines PS-*b*-P2VP-Films. Die Komplexierung und anschließende Reduktion von Gold- oder Silberionen führte zur Bildung metallischer Nanopartikel in nur einer der Phasen. Um den Metallanteil zu erhöhen, wurde ein zyklischer Ansatz eingeführt. Mit steigender Anzahl der Zyklen erhöhte sich die Größe der Nanopartikel mit gleichzeitig sinkendem Partikelabstand, was mittels TEM-Untersuchungen gezeigt werden konnte. Die UV-Vis-Spektren wiesen höhere Intensität sowie eine geringe Rotverschiebung aufgrund zusätzlicher Kopplungen mit erhöhtem Füllfaktor auf. Bei Gold zeigte sich durch Bildung stäbchenförmiger Strukturen zusätzlich eine starke Absorption im nahen IR Bereich.

Zusammenfassend beschäftigte sich diese Arbeit mit der Synthese und Charakterisierung plasmonischer Nanopartikel und deren Anordungen. Starre Linkermoleküle konnten für die Bildung kleiner Cluster, z.B. Nanopartikeldimere, genutzt werden. Ebenso konnten tripodale Thioacetate für die Herstellung funktioneller SAMs auf Gold synthetisiert werden. Es wurden Au-PEI sowie Au-Ag Core-Shell-Cluster mit abstimmbaren optischen Eigenschaften hergestellt, welche als vielversprechende Bausteine für Metamaterialien dienen könnten. Die Kombination von Blockcopolymerlithographie mit einem Komplexierungs-Reduktions-Ansatz konnte für die Herstellung geordneter plasmonischer Strukturen auf einer Mikrometerflächenskala erreicht werden. Zukünftig sollte die Herstellung von 3D Strukturen und Nanoshells sowie die Synthese von Partikeln basierend auf Silizium oder Metalloxiden/nitriden ins Auge gefasst werden. Ebenso könnten chirale und gefleckte Partikel

oder plasmonische Moleküle für die Entwicklung von Materialien mit interessanten optischen Eigenschaften verwendet werden.

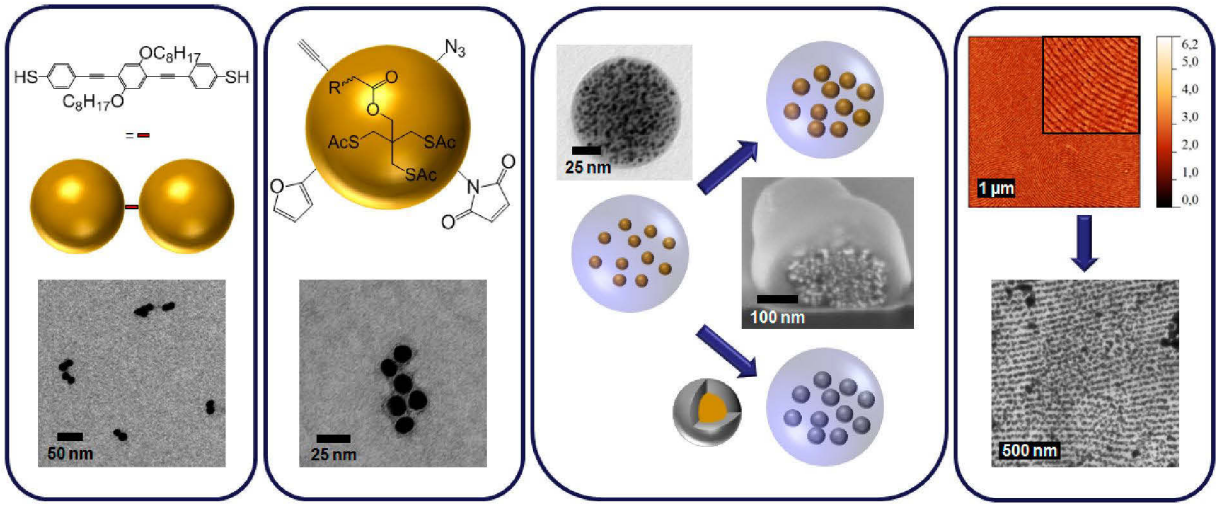

Figure 7.1: Übersicht der unterschiedlichen Strategien für die Herstellung plasmonischer Nanostrukturen welche im Rahmen der Arbeit untersucht wurden: Herstellung von Gold-Dimeren mittels eines starren Linkers, Oberflächenfunktionalisierung von Goldnanopartikeln, Synthese von Gold- sowie Gold-Silber Kern-Schale-Nanopartikeln und Herstellung geordneter Blockcopolymer-Gold/Silber Nanostrukturen.

8 References

[1] L. B. Hunt, *Gold Bull.* **1976**, *9*, 134-139.
[2] J. Lafait, S. Berthier, C. Andraud, V. Reillon, J. Boulenguez, *C. R. Phys.* **2009**, *10*, 649-659.
[3] I. Freestone, N. Meeks, M. Sax, C. Higgitt, *Gold Bull.* **2007**, *40*, 270-277.
[4] A. Moores, F. Goettmann, *New J. Chem.* **2006**, *30*, 1121-1132.
[5] N. J. Halas, S. Lal, W. S. Chang, S. Link, P. Nordlander, *Chem. Rev.* **2011**, *111*, 3913-3961.
[6] D. K. Lim, K. S. Jeon, H. M. Kim, J. M. Nam, Y. D. Suh, *Nat. Mater.* **2010**, *9*, 60-67.
[7] J. N. Anker, W. P. Hall, O. Lyandres, N. C. Shah, J. Zhao, R. P. Van Duyne, *Nat. Mater.* **2008**, *7*, 442-453.
[8] Y. Xia, W. Li, C. M. Cobley, J. Chen, X. Xia, Q. Zhang, M. Yang, E. C. Cho, P. K. Brown, *Acc. Chem. Res.* **2011**, *44*, 914-924.
[9] E. C. Dreaden, M. A. El-Sayed, *Acc. Chem. Res.* **2012**, *45*, 1854-1865.
[10] Y. Wang, K. C. Black, H. Luehmann, W. Li, Y. Zhang, X. Cai, D. Wan, S. Y. Liu, M. Li, P. Kim, Z. Y. Li, L. V. Wang, Y. Liu, Y. Xia, *ACS Nano* **2013**, *7*, 2068-2077.
[11] H. A. Atwater, A. Polman, *Nat. Mater.* **2010**, *9*, 205-213.
[12] E. A. Parlak, T. Aslı Tumay, N. Tore, Ş. Sarıoğlan, P. Kavak, F. Türksoy, *Sol. Energy Mater. Sol. Cells* **2013**, *110*, 58-62.
[13] T. Mallat, A. Baiker, *Annu. Rev. Chem. Biomol. Eng.* **2012**, *3*, 11-28.
[14] K. Yao, Y. Liu, in *ArXiv e-prints, Vol. 1312*, **2013**, pp. 4614-4671.
[15] P. Y. Chen, J. Soric, A. Alu, *Adv. Mater.* **2012**, *24*, 281-304.
[16] Y. Liu, X. Zhang, *Chem. Soc. Rev.* **2011**, *40*, 2494-2507.
[17] J. C. M. Garnett, *Philos. T. R. Soc. Lond.* **1904**, *203*, 385-420.
[18] L. Lorenz, in *Œuvres scientifiques de L. Lorenz, revues et annotées par H. Valentiner*, Tome Premier, Libraire Lehmann & Stage, Kopenhagen, **1898**, pp. 403-529.
[19] G. Mie, *Ann. Phys.* **1908**, *330*, 377-445.
[20] R. Ritchie, *Phys. Rev.* **1957**, *106*, 874-881.
[21] K. A. Willets, R. P. Van Duyne, *Annu. Rev. Phys. Chem.* **2007**, *58*, 267-297.
[22] J. Griffin, A. K. Singh, D. Senapati, E. Lee, K. Gaylor, J. Jones-Boone, P. C. Ray, *Small* **2009**, *5*, 839-845.
[23] A. B. Evlyukhin, S. M. Novikov, U. Zywietz, R. L. Eriksen, C. Reinhardt, S. I. Bozhevolnyi, B. N. Chichkov, *Nano Lett.* **2012**, *12*, 3749-3755.
[24] A. Boltasseva, H. A. Atwater, *Science* **2011**, *331*, 290-291.
[25] G. V. Naik, J. Kim, A. Boltasseva, *Opt. Mater. Express* **2011**, *1*, 1090-1099.
[26] S. A. Maier, *Plasmonics: Fundamentals and Applications*, Springer, **2007**.
[27] S. Biswas, D. Nepal, K. Park, R. A. Vaia, *J. Phys. Chem. Lett.* **2012**, *3*, 2568-2574.
[28] S. Underwood, P. Mulvaney, *Langmuir* **1994**, *10*, 3427-3430.
[29] L. M. Liz-Marzán, M. Giersig, P. Mulvaney, *Langmuir* **1996**, *12*, 4329-4335.
[30] T. Ung, L. M. Liz-Marzán, P. Mulvaney, *J. Phys. Chem. B* **2001**, *105*, 3441-3452.
[31] E. Prodan, C. Radloff, N. J. Halas, P. Nordlander, *Science* **2003**, *302*, 419-422.
[32] M. Chandra, A. M. Dowgiallo, K. L. Knappenberger, Jr., *J. Am. Chem. Soc.* **2012**, *134*, 4477-4480.
[33] S. Mühlig, C. Rockstuhl, V. Yannopapas, T. Bürgi, N. Shalkevich, F. Lederer, *Opt. Express* **2011**, *19*, 9607-9016.
[34] S. Mühlig, A. Cunningham, S. Scheeler, C. Pacholski, T. Burgi, C. Rockstuhl, F. Lederer, *ACS Nano* **2011**, *5*, 6586-6592.
[35] A. Cunningham, S. Mühlig, C. Rockstuhl, T. Bürgi, *J. Phys. Chem. C* **2012**, *116*, 17746-17752.

[36] I. Pastoriza-Santos, L. M. Liz-Marzán, *Adv. Funct. Mater.* **2009**, *19*, 679-688.
[37] F. Fiévet, R. Brayner, in *Nanomaterials: A Danger or a Promise?* (Eds.: R. Brayner, F. Fiévet, T. Coradin), Springer London, **2013**, pp. 1-25.
[38] J. Turkevich, P. C. Stevenson, J. Hillier, *Discuss. Faraday. Soc.* **1951**, *11*, 55-75.
[39] G. Frens, *Nature* **1973**, *241*, 20-22.
[40] D. K. Smith, B. A. Korgel, *Langmuir* **2008**, *24*, 644-649.
[41] A. Kedia, P. S. Kumar, *J. Phys. Chem. C* **2012**, *116*, 23721-23728.
[42] P. C. Angelomé, H. Heidari Mezerji, B. Goris, I. Pastoriza-Santos, J. Pérez-Juste, S. Bals, L. M. Liz-Marzán, *Chem. Mater.* **2012**, *24*, 1393-1399.
[43] J. Kimling, M. Maier, B. Okenve, V. Kotaidis, H. Ballot, A. Plech, *J. Phys. Chem. B* **2006**, *110*, 15700-15707.
[44] W. A. Saidi, H. Feng, K. A. Fichthorn, *J. Phys. Chem. C* **2013**, *117*, 1163-1171.
[45] W. A. Al-Saidi, H. Feng, K. A. Fichthorn, *Nano Lett.* **2012**, *12*, 997-1001.
[46] M. McEachran, D. Keogh, B. Pietrobon, N. Cathcart, I. Gourevich, N. Coombs, V. Kitaev, *J. Am. Chem. Soc.* **2011**, *133*, 8066-8069.
[47] X. Xia, J. Zeng, L. K. Oetjen, Q. Li, Y. Xia, *J. Am. Chem. Soc.* **2012**, *134*, 1793-1801.
[48] M. R. Langille, M. L. Personick, J. Zhang, C. A. Mirkin, *J. Am. Chem. Soc.* **2012**, *134*, 14542-14554.
[49] M. Eguchi, D. Mitsui, H. L. Wu, R. Sato, T. Teranishi, *Langmuir* **2012**, *28*, 9021-9026.
[50] H. L. Wu, C. H. Kuo, M. H. Huang, *Langmuir* **2010**, *26*, 12307-12313.
[51] L. Vigderman, B. P. Khanal, E. R. Zubarev, *Adv. Mater.* **2012**, *24*, 4811-4841.
[52] M. R. Langille, M. L. Personick, J. Zhang, C. A. Mirkin, *J. Am. Chem. Soc.* **2012**, *134*, 14542-14554.
[53] S. Koeppl, F. P. V. Koch, W. Caseri, R. Spolenak, *J. Mater. Chem.* **2012**, *22*, 14594-14601.
[54] Z. Wang, L. Tang, L. H. Tan, J. Li, Y. Lu, *Angew. Chem. Int. Ed.* **2012**, *51*, 9078-9082.
[55] J. Zhang, M. R. Langille, C. A. Mirkin, *Nano Lett.* **2011**, *11*, 2495-2498.
[56] N. G. Bastus, J. Comenge, V. Puntes, *Langmuir* **2011**, *27*, 11098-11105.
[57] C. Ziegler, A. Eychmüller, *J. Phys. Chem. C* **2011**, *115*, 4502-4506.
[58] X. Liu, H. Xu, H. Xia, D. Wang, *Langmuir* **2012**, *28*, 13720-13726.
[59] K. C. Ng, W. Cheng, *Nanotechnology* **2012**, *23*, 105602-105611.
[60] C. Damm, D. Segets, G. Yang, B. F. Vieweg, E. Spiecker, W. Peukert, *Small* **2011**, *7*, 147-156.
[61] M. Min, C. Kim, Y. I. Yang, J. Yi, H. Lee, *Chem. Commun.* **2011**, *47*, 8079-8081.
[62] M. R. Jones, K. D. Osberg, R. J. Macfarlane, M. R. Langille, C. A. Mirkin, *Chem. Rev.* **2011**, *111*, 3736-3827.
[63] C. R. Bridges, P. M. DiCarmine, A. Fokina, D. Huesmann, D. S. Seferos, *J. Mater. Chem. A* **2013**, *1*, 1127-1133.
[64] M. Lahav, T. Sehayek, A. Vaskevich, I. Rubinstein, *Angew. Chem. Int. Ed.* **2003**, *42*, 5575-5579.
[65] S. Vignolini, N. A. Yufa, P. S. Cunha, S. Guldin, I. Rushkin, M. Stefik, K. Hur, U. Wiesner, J. J. Baumberg, U. Steiner, *Adv. Mater.* **2012**, *24*, 23-27.
[66] C. Shankar, A. T. Dao, P. Singh, K. Higashimine, D. M. Mott, S. Maenosono, *Nanotechnology* **2012**, *23*, 245704-245713.
[67] T. C. Preston, R. Signorell, *ACS Nano* **2009**, *3*, 3696-3706.
[68] M. McEachran, D. Keogh, B. Pietrobon, N. Cathcart, I. Gourevich, N. Coombs, V. Kitaev, *J. Am. Chem. Soc.* **2011**, *133*, 8066-8069.
[69] D. H. Tsai, L. F. Pease, R. A. Zangmeister, M. J. Tarlov, M. R. Zachariah, *Langmuir* **2009**, *25*, 140-146.

[70] D. H. Tsai, T. J. Cho, F. W. DelRio, J. Taurozzi, M. R. Zachariah, V. A. Hackley, *J. Am. Chem. Soc.* **2011**, *133*, 8884-8887.
[71] A. Hofmann, P. Schmiel, B. Stein, C. Graf, *Langmuir* **2011**, *27*, 15165-15175.
[72] Q. Huo, J. G. Worden, *J. Nanopart. Res.* **2006**, *9*, 1013-1025.
[73] F. Sander, U. Fluch, J. P. Hermes, M. Mayor, *Small* **2014**, *10*, 349-359.
[74] J. P. Hermes, F. Sander, U. Fluch, T. Peterle, D. Thompson, R. Urbani, T. Pfohl, M. Mayor, *J. Am. Chem. Soc.* **2012**, *134*, 14674-14677.
[75] S. J. Tan, M. J. Campolongo, D. Luo, W. Cheng, *Nat. Nanotechnol.* **2011**, *6*, 268-276.
[76] I. Lubitz, A. Kotlyar, *Bioconjugate Chem.* **2011**, *22*, 2043-2047.
[77] D. K. Lim, K. S. Jeon, J. H. Hwang, H. Kim, S. Kwon, Y. D. Suh, J. M. Nam, *Nat. Nanotechnol.* **2011**, *6*, 452-460.
[78] B. Ding, Z. Deng, H. Yan, S. Cabrini, R. N. Zuckermann, J. Bokor, *J. Am. Chem. Soc.* **2010**, *132*, 3248-3249.
[79] A. Kuzyk, R. Schreiber, Z. Fan, G. Pardatscher, E. M. Roller, A. Hogele, F. C. Simmel, A. O. Govorov, T. Liedl, *Nature* **2012**, *483*, 311-314.
[80] Y. Yan, J. I. Chen, D. S. Ginger, *Nano. Lett.* **2012**, *12*, 2530-2536.
[81] T. Wu, Q. Zhang, J. Hu, G. Zhang, S. Liu, *J. Mater. Chem.* **2012**, *22*, 5155-5163.
[82] L. N. Kim, E.-G. Kim, J. Kim, S.-E. Choi, W. Park, S. Kwon, *Bull. Korean Chem. Soc.* **2012**, *33*, 3735-3739.
[83] A. Cunningham, S. Mühlig, C. Rockstuhl, T. Bürgi, *J. Phys. Chem. C.* **2011**, *115*, 8955-8960.
[84] A. Yoshida, K. Imazu, X. Li, K. Okamoto, K. Tamada, *Langmuir* **2012**, *28*, 17153-17158.
[85] S. Mehdizadeh Taheri, S. Fischer, S. Förster, *Polymers* **2011**, *3*, 662-673.
[86] V. V. Terekhin, O. V. Dement'eva, V. M. Rudoy, *Russ. Chem. Rev.* **2011**, *80*, 453-472.
[87] S. Mössmer, J. P. Spatz, M. Möller, T. Aberle, J. Schmidt, W. Burchard, *Macromolecules* **2000**, *33*, 4791-4798.
[88] A. Horechyy, B. Nandan, N. E. Zafeiropoulos, P. Formanek, U. Oertel, N. C. Bigall, A. Eychmüller, M. Stamm, *Adv. Funct. Mater.* **2013**, *23*, 483-490.
[89] Z. Liu, H. Huang, T. He, *Small* **2013**, *9*, 505-510.
[90] B. Yan, S. V. Boriskina, B. M. Reinhard, *J. Phys. Chem. C* **2011**, *115*, 4578-4583.
[91] F. Holzner, C. Kuemin, P. Paul, J. L. Hedrick, H. Wolf, N. D. Spencer, U. Duerig, A. W. Knoll, *Nano Lett.* **2011**, *11*, 3957-3962.
[92] M. Xie, L. Ding, Z. You, D. Gao, G. Yang, H. Han, *J. Mater. Chem.* **2012**, *22*, 14108-14118.
[93] S. G. Jang, A. Khan, C. J. Hawker, E. J. Kramer, *Macromolecules* **2012**, *45*, 1553-1561.
[94] N. Pazos-Pérez, W. Ni, A. Schweikart, R. A. Alvarez-Puebla, A. Fery, L. M. Liz-Marzán, *Chem. Sci.* **2010**, *1*, 174-178.
[95] S. Gwo, M. H. Lin, C. L. He, H. Y. Chen, T. Teranishi, *Langmuir* **2012**, *28*, 8902-8908.
[96] J. Yang, T. Ichii, K. Murase, H. Sugimura, *Langmuir* **2012**, *28*, 7579-7584.
[97] R. Abargues, S. Albert, J. L. Valdés, K. Abderrafi, J. P. Martínez-Pastor, *J. Mater. Chem.* **2012**, *22*, 22204-22211.
[98] X. Liu, H. Liu, W. Zhou, H. Zheng, X. Yin, Y. Li, Y. Guo, M. Zhu, C. Ouyang, D. Zhu, A. Xia, *Langmuir* **2010**, *26*, 3179-3185.
[99] J. P. Novak, D. L. Feldheim, *J. Am. Chem. Soc.* **2000**, *122*, 3979-3980.
[100] J. M. Wessels, H. G. Nothofer, W. E. Ford, F. von Wrochem, F. Scholz, T. Vossmeyer, A. Schroedter, H. Weller, A. Yasuda, *J. Am. Chem. Soc.* **2004**, *126*, 3349-3356.

[101] M. Orbach, M. Lahav, P. Milko, S. G. Wolf, M. E. van der Boom, *Angew. Chem. Int. Ed.* **2012**, *51*, 7142-7145.
[102] P. Ahonen, T. Laaksonen, A. Nykanen, J. Ruokolainen, K. Kontturi, *J. Phys. Chem. B.* **2006**, *110*, 12954-12958.
[103] M. P. Stemmler, Y. Fogel, K. Mullen, M. Kreiter, *Langmuir* **2009**, *25*, 11917-11922.
[104] H. Yan, S. I. Lim, L.-C. Zhang, S.-C. Gao, D. Mott, Y. Le, R. Loukrakpam, D.-L. An, C.-J. Zhong, *J. Mater. Chem.* **2011**, *21*, 1890-1901.
[105] R. Kaminker, M. Lahav, L. Motiei, M. Vartanian, R. Popovitz-Biro, M. A. Iron, M. E. van der Boom, *Angew. Chem.* **2010**, *122*, 1240-1243.
[106] A. Singh, D. H. Dahanayaka, A. Biswas, L. A. Bumm, R. L. Halterman, *Langmuir* **2010**, *26*, 13221-13226.
[107] N. Pazos-Perez, C. S. Wagner, J. M. Romo-Herrera, L. M. Liz-Marzán, F. J. García de Abajo, A. Wittemann, A. Fery, R. A. Alvarez-Puebla, *Angew. Chem. Int. Ed.* **2012**, *51*, 12688-12693.
[108] D. Lin-Vien, N. D. Colthup, W. G. Fateley, J. G. Grasselli, *The Handbook of Infrared and Raman Characteristic Frequencies of Organic Molecules*, Elsevier, **1991**.
[109] X. Gao, J. P. Davies, M. J. Weaver, *J. Phys. Chem.* **1990**, *94*, 6858-6864.
[110] E. C. Le Ru, S. A. Meyer, C. Artur, P. G. Etchegoin, J. Grand, P. Lang, F. Maurel, *Chem. Commun.* **2011**, *47*, 3903-3905.
[111] A. L. Kanibolotsky, I. F. Perepichka, P. J. Skabara, *Chem. Soc. Rev.* **2010**, *39*, 2695-2728.
[112] L. Fenenko, G. Shao, A. Orita, M. Yahiro, J. Otera, S. Svechnikov, C. Adachi, *Chem. Commun.* **2007**, 2278-2280.
[113] D. J. Lavrich, S. M. Wetterer, S. L. Bernasek, G. Scoles, *J. Phys. Chem. B.* **1998**, *102*, 3456-3465.
[114] T. Weidner, N. Ballav, U. Siemeling, D. Troegel, T. Walter, R. Tacke, D. G. Castner, M. Zharnikov, *J. Phys. Chem. C.* **2009**, *113*, 19609-19617.
[115] P. Chinwangso, A. C. Jamison, T. R. Lee, *Acc. Chem. Res.* **2011**, *44*, 511-519.
[116] S. Perumal, A. Hofmann, N. Scholz, E. Ruhl, C. Graf, *Langmuir* **2011**, *27*, 4456-4464.
[117] N. Garg, A. Mohanty, N. Lazarus, L. Schultz, T. R. Rozzi, S. Santhanam, L. Weiss, J. L. Snyder, G. K. Fedder, R. Jin, *Nanotechnology* **2010**, *21*, 405501-405508.
[118] J. A. Camerano, M. A. Casado, M. A. Ciriano, F. J. Lahoz, L. A. Oro, *Organometallics* **2005**, *24*, 5147-5156.
[119] T. Weidner, N. Ballav, U. Siemeling, D. Troegel, T. Walter, R. Tacke, D. G. Castner, M. Zharnikov, *J. Phys. Chem. C* **2009**, *113*, 19609-19617.
[120] T. Weidner, A. Kramer, C. Bruhn, M. Zharnikov, A. Shaporenko, U. Siemeling, F. Trager, *Dalton Trans.* **2006**, 2767-2777.
[121] K. H. Lau, C. Huang, N. Yakovlev, Z. K. Chen, S. J. O'Shea, *Langmuir* **2006**, *22*, 2968-2971.
[122] J. Kumar, K. G. Thomas, *J. Phys. Chem. C.* **2011**, *2*, 610-615.
[123] S. Y. Lee, L. Hung, G. S. Lang, J. E. Cornett, I. D. Mayergoyz, O. Rabin, *ACS Nano* **2010**, *4*, 5763-5772.
[124] C. Sonnichsen, B. M. Reinhard, J. Liphardt, A. P. Alivisatos, *Nat. Biotechnol.* **2005**, *23*, 741-745.
[125] S. Mühlig, A. Cunningham, S. Scheeler, C. Pacholski, T. Bürgi, C. Rockstuhl, F. Lederer, *ACS Nano* **2011**, *5*, 6586-6592.
[126] S. Mühlig, C. Rockstuhl, V. Yannopapas, T. Bürgi, N. Shalkevich, F. Lederer, *Opt. Express* **2011**, *19*, 9607-9616.
[127] J. Dintinger, S. Mühlig, C. Rockstuhl, T. Scharf, *Opt. Mater. Express* **2012**, *2*, 269-278.
[128] D. I. Gittins, A. S. Susha, B. Schoeler, F. Caruso, *Adv. Mater.* **2002**, *14*, 508-512.

[129] K. Y. van Berkel, C. J. Hawker, *J. Polym. Sci., Part A: Polym. Chem.* **2010**, *48*, 1594-1606.
[130] M. Xiao, C. Zhao, H. Chen, B. Yang, J. Wang, *Adv. Funct. Mater.* **2012**, *22*, 4526-4532.
[131] F. Richard Keene, *Coordin. Chem. Rev.* **1999**, *187*, 121-149.
[132] Y. Nagel, W. Beck, *Z. Anorg. Chem.* **1985**, *529*, 57-60.
[133] J. Rodriguez-Fernandez, J. Perez-Juste, F. J. Garcia de Abajo, L. M. Liz-Marzán, *Langmuir* **2006**, *22*, 7007-7010.
[134] N.-H. Shen, T. Koschny, M. Kafesaki, C. Soukoulis, *Phys. Rev. B* **2012**, *85*, 075120-075124.
[135] X. Dong, X. Ji, H. Wu, L. Zhao, J. Li, W. Yang, *J. Phys. Chem. C* **2009**, *113*, 6573-6576.
[136] H. Li, H. Xia, D. Wang, X. Tao, *Langmuir* **2013**, *29*, 5074-5079.
[137] C. Jing, Z. Gu, Y. L. Ying, D. W. Li, L. Zhang, Y. T. Long, *Anal. Chem.* **2012**, *84*, 4284-4291.
[138] J. R. Navarro, M. H. Werts, *The Analyst* **2013**, *138*, 583-592.
[139] S. Mühlig, C. Rockstuhl, J. Pniewski, C. R. Simovski, S. A. Tretyakov, F. Lederer, *Phys. Rev. B* **2010**, *81*, 075317-075324.
[140] Y.-l. Xu, *Appl. Opt.* **1997**, *36*, 9496-9508.
[141] S. Sun, K. Y. Yang, C. M. Wang, T. K. Juan, W. T. Chen, C. Y. Liao, Q. He, S. Xiao, W. T. Kung, G. Y. Guo, L. Zhou, D. P. Tsai, *Nano Lett.* **2012**, *12*, 6223-6229.
[142] L. Johnson, D. A. Walsh, *J. Mater. Chem.* **2011**, *21*, 7555-7559.
[143] F. S. Bates, G. H. Fredrickson, *Phys. Today* **1999**, *52*, 32-38.
[144] M. W. Matsen, F. S. Bates, *Macromolecules* **1996**, *29*, 1091-1098.
[145] E. Bhoje Gowd, B. Nandan, M. K. Vyas, N. C. Bigall, A. Eychmuller, H. Schlorb, M. Stamm, *Nanotechnology* **2009**, *20*, 415302-415311.
[146] A. del Campo, E. Arzt, *Chem. Rev.* **2008**, *108*, 911-945.
[147] Y. Wang, U. Gosele, M. Steinhart, *Nano Lett.* **2008**, *8*, 3548-3553.

List of abbreviations

AA	Ascorbic acid
AFM	Atomic force microscopy
BCP	Block copolymer
CTAB	Cetyltrimethylammonium bromide
DBU	Diazabicycloundecene
DCC	Dicyclohexylcarbodiimide
DLS	Dynamic light scattering
DMAP	4-Dimethylaminopyridine
DMF	*N,N*-Dimethylformamide
FIB	Focused ion beam
ITO	Indium tin oxide
LSPR	Localized surface plasmon resonance
OPE	Oligo(phenylene ethynylene)
PAA	Poly(acrylic acid)
PAAm	Poly(allyl amine)
PDI	Polydispersity index
PEI	Poly(ethylene imine)
PEO	Poly(ethylene oxide)
PS	Polystyrene
PVP	Poly(vinyl pyrrolidone)
P2VP	Poly(2-vinyl pyridine)
SAM	Self-assembled monolayer
SEM	Scanning electron microscopy
SERS	Surface enhanced Raman spectroscopy
TEA	Triethylamine
TEM	Transmission electron microscopy
THF	Tetrahydrofuran

Curriculum vitae

27.06.1986	Born in Saalfeld/Saale
1996-2004	Erasmus-Reinhold Gymnasium in Saalfeld/Saale
26.6.2004	Abitur
08/2004-04/2005	Civilian service at the Grünflächenamt in Saalfeld/Saale
10/2005-11/2010	Study of chemistry at the Friedrich Schiller University Jena
11/2009-11/2010	Diploma thesis in the group of Prof. Dr. U. S. Schubert at the Friedrich Schiller University Jena
	Title: "Conjugated Low Band Gap Donor-Acceptor-Polymer Library: Synthesis and Characterization of a Copolymer Series"
22/10/2010	Diploma
Since 12/2010	PhD student at the Friedrich Schiller University Jena in the group of Prof. Dr. U. S. Schubert

Jena, den

_____

Florian Kretschmer

Publication list

Peer-reviewed publications:

1.

A. Teichler, J. Perelaer, **F. Kretschmer**, M. D. Hager, U. S. Schubert

"Systematic Investigation of a Novel Low-Bandgap Terpolymer Library via Inkjet Printing: Influence of Ink Properties and Processing Conditions"

Macromol. Chem. Phys. **2013**, *214*, 664-672.

2.

A. Teichler, S. Hölzer, J. Nowotny, **F. Kretschmer**, C. Bader, J. Perelaer, M. D. Hager, S. Hoeppener, U. S. Schubert

"Combinatorial Screening of Inkjet Printed Ternary Blends for Organic Photovoltaics: Absorption Behavior and Morphology"

ACS Comb. Sci. **2013**, *15*, 410-418.

3.

F. Kretschmer, U. Mansfeld, S. Hoeppener, M. D. Hager, U. S. Schubert

"Tunable Synthesis of Poly(ethylene imine)-gold Nanoparticle Clusters"

Chem. Commun. **2014**, *50*, 88-90.

4.

F. Kretschmer, A. Wild, M. Hager, U. S. Schubert

"Synthesis of a Rigid Tetrahedral Linker with Thioether End Groups"

Synthesis **2014**, *46*, 475-478.

5.

O. Synooka, **F. Kretschmer**, M. D. Hager, M. Himmerlich, S. Krischok, D. Gehrig, F. Laquai, U. S. Schubert, G. Gobsch, H. Hoppe

"Modification of the Active Layer/PEDOT:PSS Interface by Solvent Additives Resulting in Improvement of the Performance of Organic Solar Cells"

ACS Appl. Mater. Interf. **2014**, *6*, 11068-11081.

6.

F. Kretschmer, S. Mühlig, S. Hoeppener, A. Winter, M. D. Hager, C. Rockstuhl, T. Pertsch, U. S. Schubert

"Survey of Plasmonic Nanoparticles: From Synthesis to Application"

Part. Part. Syst. Char. **2014**, *31*, 721-744.

7.

T. Rudolph, M. J. Barthel, **F. Kretschmer**, U. Mansfeld, S. Hoeppener, M. D. Hager, U. S. Schubert, F. H. Schacher

"Poly(2-vinyl pyridine)-*block*-Poly(ethylene oxide) Featuring a Furan Group at the Block Junction - Synthesis and Functionalization"

Macromol. Rapid Commun. **2014**, *35*, 916-921.

8.

F. Kretschmer, M. Fruhnert, R. Geiss, U. Mansfeld, C. Höppener, S. Hoeppener, C. Rockstuhl, T. Pertsch, U. S. Schubert

"Plasmonic Nanoparticle Clusters with Tunable Plasmonic Resonances in the Visible Spectral Region"

J. Mater. Chem. C **2014**, *2*, 6415-6422.

9.

F. Kretschmer, M. D. Hager, U. S. Schubert

"Synthesis of Functional Tripodal Thioacetates"

Synthesis DOI: 10.1055/s-0034-1378497.

Submitted publications

1.

F. Kretschmer, S. Stumpf, U. Mansfeld, F. H. Schacher, S. Hoeppener, U. S. Schubert

"Tunable PS-*b*-P2VP Plasmonic Nanostructures *via* a Cyclic Complexation-reduction Approach"

J. Mater. Chem. C, submitted

Manuscripts in preparation

1.

M. Fruhnert, **F. Kretschmer**, R. Geiss, I. Perevyazko, D. Cialla, Michael Steinert, Norik Janunts, Dmitry Sivun, S. Hoeppener, M. D. Hager, U. S. Schubert, T. Pertsch, C. Rockstuhl
"Synthesis, Separation and Hypermethod Characterization of Gold Nanoparticle Dimers Connected by a Rigid Rod Linker"

2.

C. von der Ehe, **F. Kretschmer**, C. Weber, S. Crotty, S. Stumpf, S. Hoeppener, M. Gottschaldt, U. S. Schubert
"RAFT Copolymerization of Thioglycosidic Glycomonomers with NiPAm and Subsequent Immobilization onto Gold Nanoparticles"

3.

T. Jähnert, **F. Kretschmer**, T. Janoschka, A. Wild, M. Hager, U. S. Schubert
"Novel Disulfide- and Dithiolane-polymers and their Application in All-organic Batteries"

Acknowledgements/Danksagung

Finally, I would like to express my gratitude to all the people who contributed to this work and who helped creating this thesis.

At first, I want to thank Prof. Dr. Ulrich S. Schubert who gave me the opportunity to work on this topic and the BMBF for financial support (PhoNa project, No. 03IS2101A).

Second, I would like to thank my daily supervisors Dr. Martin Hager and Dr. habil. Stephanie Höppener for helpful comments and advices as well as for the reading and correction of my thesis and manuscripts. I am also grateful to Stephanie for an awful number of TEM measurements, introduction to the AFM and social activities.

My gratitude goes to Steffi Stumpf for the TEM and SEM measurements as well as the lithography, help with the AFM and the supply of sweets. I would like to thank Dr. Ulrich Mansfeld for lots of TEM measurements and helpful discussions. Furthermore, I would like to thank Dr. Stephan Mühlig and Martin Fruhnert for the simulations and discussions. I am also grateful to Reinhard Geiss for lots of discussions, the FIB milling, preparation of patterned substrates and optical measurements. I would like to thank Dr. Christiane Höppener for the dark field microscopy, Raman measurements and discussions. My gratitude goes also to Dr. Dana Cialla for the SERS measurements. Many thanks to He Liu for a small introduction to chinese (food) culture and help with the AFM. I am also grateful to Prof. Felix Schacher for valuable discussions on block copolymers.

I would like to thank Dr. Esra Altuntas and Nicole Fritz for the ESI measurements, Renzo Paulus for the help with hard- and software related problems, Dr. Andreas Winter for correction of the review, Beate Lentvogt and Sandra Köhn for lots of elemental analyses, Sarah Crotty for the MALDI measurements, Igor Perevyazko for the ultracentrifugation and his patience. My gratitude goes also to the administrative team (Uwe Köhn, Silvia Pfeifer, Sylvia Braunsdorf, Simone Burchardt, Tanja Wagner) for help and keeping everything running.

Special gratitude goes to the former team of Lab 115 for a nice lab atmosphere, food supply and refreshments in summer ☺. Rene Burges for "Friday" (*et al.*), den Swag aufdrehen, lots of fun and keeping the lab running. Thomas Jähnert for lots of fun and his vivid fantasy. Andreas

Wild for lots of discussions and suggestions on synthesis and for a nice lab entertainment, Junge ☺. Tobias Rudolph and Tobias Janoschka for being themselves. I am also grateful to the "team" (*i.e.* Almut) of Lab 128/ZAF and the office E003/ZAF (Almut, Martin, He) for a nice working atmosphere.

Last but not least I would like to thank my family for their support and the "Jena group" (Rainer, Christian, Silvio, Lutz, Tobi) for the pleasant time.

Declaration of authorship / Selbstständigkeitserklärung

Ich erkläre, dass ich die vorliegende Arbeit selbständig und unter Verwendung der angegebenen Hilfsmittel, persönlichen Mitteilungen und Quellen angefertigt habe.

I certify that the work presented here is, to the best of my knowledge and belief, original and the result of my own investigations, except as acknowledged, and has not been submitted, either in part or whole, for a degree at this or any other university.

Jena, den

_____

Florian Kretschmer

Publications P1-P8

Publication P1

Survey of Plasmonic Nanoparticles: From Synthesis to Application

F. Kretschmer, S. Mühlig, S. Hoeppener, A. Winter, M. D. Hager, C. Rockstuhl, T. Pertsch, U. S. Schubert

Part. Part. Syst. Char. **2014**, *31*, 721-744.

Particle & Particle Systems Characterization
www.particle-journal.com

Survey of Plasmonic Nanoparticles: From Synthesis to Application

*Florian Kretschmer, Stefan Mühlig, Stephanie Hoeppener, Andreas Winter, Martin D. Hager, Carsten Rockstuhl, Thomas Pertsch, and Ulrich S. Schubert**

The unique properties of plasmonic nanostructures have fuelled research based on the tremendous amount of potential applications. Their tailor-made assemblies in combination with the tunable size and morphology of the initial building blocks allow for the creation of materials with a desired optical response. In this respect, it is crucial to synthesize nanoparticles with a defined shape that are at the core of such developments. Moreover, the interaction of individual nanoparticles with an incident electromagnetic field cannot only be influenced by their structure, but in fact, also by their spatial arrangement to each other. To harvest such opportunities, a profound theoretical understanding of these interactions is required as well as concise strategies to create such ordered assemblies. A quantitative evaluation of their optical properties can only be conducted when discrete structures of high uniformity can be achieved. As a consequence, separation steps have to be applied in order to obtain materials of high purity and uniformity. This also allows for an easier structural characterization of the nanoparticles and their assembled superstructures. In this progress report, an overview about the current development in this field of research is provided.

1. Introduction

When in the fourth century Roman glass makers crafted the famous Lycurgus cup, they were certainly unaware that finely dispersed metal nanoparticles were the origin of its intriguing optical features.[1] When irradiated from the outside, the cup appears green from the reflected light, whereas if irradiated from the inside, a ruby red color from the transmitted light arises. Over the following centuries, gold and silver in their colloidal form were used for fabricating stained glass or porcelain.[2,3] However, Michael Faraday, who undertook initial systematic investigations on their preparation in solution more than 150 years ago, was the first scientist to realize that it must be very tiny gold particles that are formed during the synthesis.[4] In the beginning of the twentieth century, James C. Maxwell[5] and Gustav Mie[6] among others provided the theoretical background to describe the optical properties of small particles. In particular for small metallic nanoparticles, they were shown to be dominated by surface plasmon polaritons, i.e., an excitation where the electromagnetic field is coupled resonantly to the charge density oscillations in the metals. Research during the 1950s showed that these surface plasmon polaritons can exist at the extended interface between a metal and a dielectric. They eventually correspond to guided modes at the interface that obey a characteristic dispersion relation. These propagating surface plasmon polaritons were experimentally demonstrated by Ritchie.[7] In contrast, in small metallic nanoparticles localized surface plasmon polaritons can be excited at discrete frequencies. These resonance frequencies depend for sufficiently small particles only on the permittivities of the sphere material and the ambiance. Assuming idealistically but justified that the permittivity of metals is described by a Drude-type material dispersion, the resonances of the localized plasmon polaritons occur at frequencies only slightly smaller than the plasma frequency of the metals. This plasma frequency, therefore, can be easily used to estimate the spectral range for which a nanoparticle from a given material can sustain such plasmonic resonances. Unfortunately, only few metals exhibit this surface plasmon resonance in the visible region of light. Even less of them, most notably gold and silver, are chemically stable enough to be used in practice, and hence, these two metals receive the most attention. In the past few years, the field has exploded owing to a tremendous diversification of the field. The foundations for this extraordinary interest lie in the size-, shape-, and distance-dependent optical properties of these nanoparticles, which allow light to be forged in unprecedented ways.[8] A multitude of novel particle structures in combination with a

F. Kretschmer, Dr. S. Hoeppener, Dr. A. Winter, Dr. M. D. Hager, Prof. U. S. Schubert
Laboratory of Organic and Macromolecular Chemistry (IOMC)
Friedrich-Schiller-Universität Jena
Humboldtstr. 10, 07743 Jena, Germany
E-mail: ulrich.schubert@uni-jena.de

F. Kretschmer, Dr. S. Hoeppener, Dr. A. Winter, Dr. M. D. Hager, Prof. U. S. Schubert
Jena Center for Soft Matter (JCSM)
Friedrich-Schiller-Universität Jena
Philosophenweg 7, 07743 Jena, Germany

Dr. S. Mühlig, Prof. C. Rockstuhl
Institute of Condensed Matter Theory and Solid State Optics
Abbe Center of Photonics, Friedrich-Schiller-Universität Jena
Max-Wien-Platz 1, 07743 Jena, Germany

Prof. T. Pertsch
Institute of Applied Physics
Abbe Center of Photonics
Friedrich-Schiller-Universität Jena
Max-Wien-Platz 1, 07743 Jena, Germany

DOI: 10.1002/ppsc.201300309

plethora of assembly methods makes the number of potential superstructures almost unlimited. This enormous development would have hardly been possible without simultaneous advances in separation and characterization techniques. In addition, improvements on the theoretical understanding of the interactions of plasmonic particles with light enable interesting structures to be simulated. Taken together, this culminates in potential applications penetrating a broad range of research fields. Medical applications, such as photothermal therapy[9] or drug delivery,[10] sensing,[11] diagnostics, energy conversion,[12] and (chiral) metamaterials,[13–16] are just a few examples where plasmonic nanoparticles could be utilized.

Owing to the tremendous development in this field, it is hardly possible to provide a complete overview. Therefore, this progress report aims on an introduction of general strategies to synthesize plasmonic nanostructures. In section 2, we introduce the important techniques to synthesize such particles with well-defined shape and size. In section 3, we elaborate on the underlying theoretical principles responsible for the optical properties of plasmonic nanoparticles. The possibilities to assemble these particles into superstructures via bottom-up and top-up approaches are explored in section 4. Section 5 summarizes strategies to separate and purify plasmonic nanoparticles or their assemblies, and section 6 discusses emerging technologies for their characterization. Finally, in section 7, we conclude and give a short prospect on potential future developments in this field of research.

2. Strategies for the Synthesis of Plasmonic Nanoparticles

The synthesis of defined nanoparticles in high purity as well as uniform size is crucial for understanding the relationship between their structure and their physical as well as physiological properties. Already in the early stages of nanoparticle synthesis, the importance of the choice of solvents,[17] or even the brand of chemical,[18] used was noted as even trace amounts of certain components can alter the shape of the particles significantly. But it was not until recently that the exact nature of the underlying principles is being elucidated. In this section, we highlight novel advances in the synthesis of nanoparticles and profound research for factors governing their morphology with special focus on wet chemistry approaches. Differently sized and shaped particles can in general be synthesized by four different ways: a) one-pot-one-step synthesis, b) seeded growth, c) reshaping/etching, and d) templated synthesis (**Figures 1** and **2**). It should be noted that up to now, the exact formation mechanism has not been elucidated for every particle shape, and also mixed mechanisms could apply.

2.1. One-Pot-One-Step Synthesis of Plasmonic Nanoparticles

The most straightforward approach for the synthesis of plasmonic nanoparticles is the direct one-pot-one-step synthesis. Depending on the reaction conditions (e.g., temperature, solvent, additives), certain morphologies can be obtained. In the following section, some approaches will be highlighted that

Florian Kretschmer studied chemistry at the Friedrich-Schiller-Universität Jena, Germany, where he received his M.Sc. in 2010 for work on conjugated organic polymers. Since 2010, he has been a Ph.D. student in Prof. Ulrich S. Schubert's group at the Friedrich-Schiller-Universität Jena, where he has been working on the synthesis and self-assembly of plasmonic nanoparticles.

Stefan Mühlig studied physics in Dresden and Jena in Germany and received his Diploma degree in physics from the Friedrich-Schiller-Universität Jena, Germany, in 2009. Currently, he is working toward his Ph.D. degree in the Institute of Condensed Matter Theory and Solid State Optics, Friedrich-Schiller-Universität Jena. In 2012, he was on leave with the Optics and Photonics Technology Laboratory, Ecole Polytechnique Fédérale de Lausanne (EPFL), Neuchatel, Switzerland. His work focuses on self-assembled bottom-up metamaterials and their potential applications in the visible regime.

Ulrich S. Schubert studied chemistry at the Universities of Frankfurt and Bayreuth (Germany) and the Virginia Commonwealth University, Richmond (USA). He carried out his Ph.D. under the supervision of Prof. C. D. Eisenbach (Bayreuth) and Prof. G. R. Newkome (Florida). After postdoctoral training with Prof. J.-M. Lehn at the Université Strasbourg (France), he moved to the Munich University of Technology (Germany) to obtain his habilitation in 1999 (with Prof. O. Nuyken). From 1999 to 2000, he held a temporary position as a professor at the Center for NanoScience (CeNS) at the LMU Munich (Germany). From 2000 to 2007, he was a full professor at the Eindhoven University of Technology, the Netherlands. Since 2007, he has been a full professor at the Friedrich-Schiller-Universität Jena, Germany.

DOI: 10.1002/ppsc.201300309

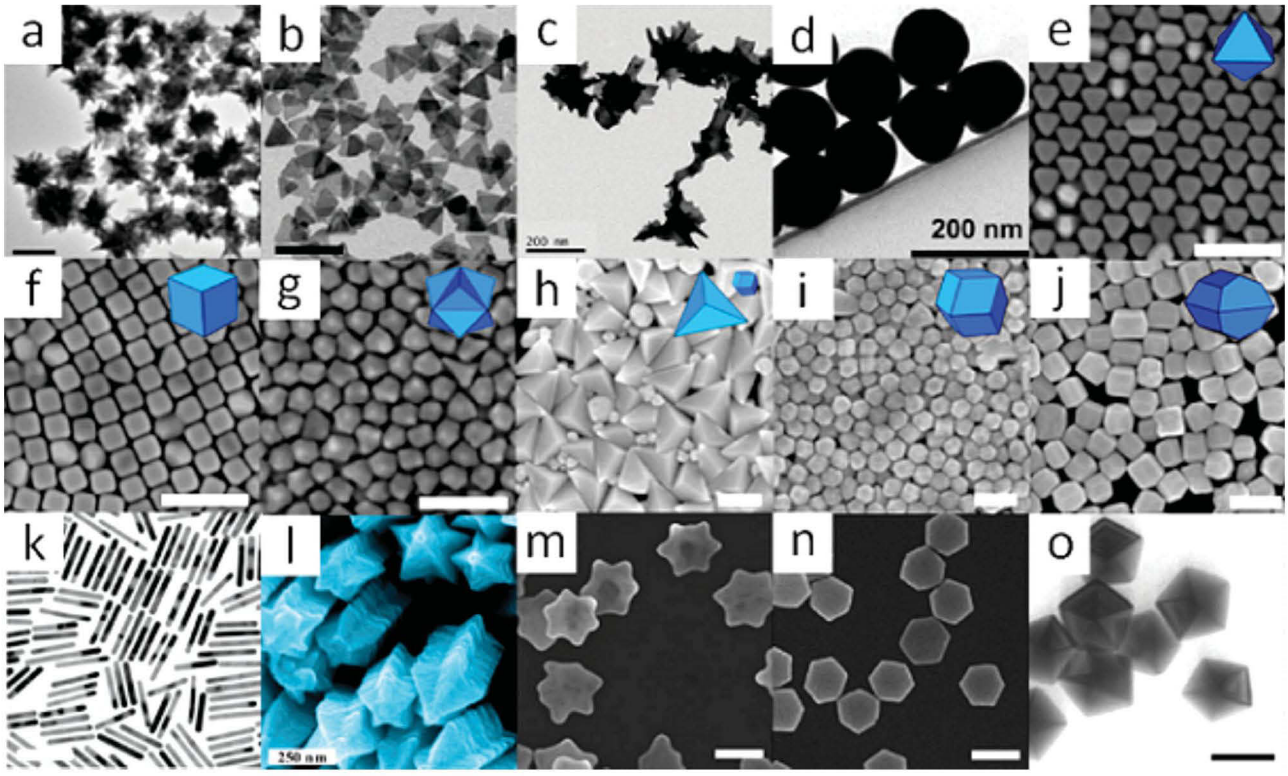

Figure 1. Representative images of selected gold and silver nanoparticles synthesized via the one-pot-one-step synthesis or the seeded growth approach. a) Gold nanostars,[25] b) silver nanoprisms,[28] c) twisted single crystalline gold particles,[26] d) spherical nanoparticles,[29] e) gold nanooctahedra,[30] f) gold nanocubes,[30] g) gold nanotrisoctahedra,[30] h) gold nanobipyramids,[30] i) gold rhombic dodecahedra,[30] j) gold-truncated ditetragonal nanoprisms,[30] k) gold nanorods,[31] l) starfruit-shaped gold nanorods,[32] m) six-pointed gold nanostars,[33] n) hexagonal gold nanoplates,[33] and o) silver decahedra.[34] Scale bars: a, b, k = 100 nm; c–j, m–o = 200 nm; l = 250 nm; o = 50 nm. Images a, c, e–l reproduced with permission.[25,26,30,32] Copyright 2012, ACS. Images b, d, o reproduced with permission.[28,29,34] Copyright 2011, ACS. Images m, n reproduced with permission.[33]

were used to synthesize particles with specific shapes, e.g., stars, rods, plates, and prisms.

Polyvinylpyrrolidone (PVP) is a commonly used reducing and capping agent for nanoparticles. Owing to its interaction with metal ions and surfaces as well as the preferable attachment to distinct crystal facets of certain metals (e.g., silver),[19–24] PVP can potentially modify the nucleation, growth, and final shape of nanoparticles.

Inspired by these earlier reports, Kedia and Kumar[25] elucidated the effect of the solvent on the synthesis of gold nanoparticles, where the authors could tune the particle shape from spherical to star-shaped just by changing the solvent. PVP possesses polar carbonyl oxygen and nitrogen atoms as well as an unpolar backbone. These are capable of forming hydrogen bonds and hydrophobic interactions for which the nature and strength could be determined by NMR spectroscopy, X-ray photoelectron spectroscopy, and Fourier transform infrared spectroscopy studies. It could clearly be shown that not only the polymer but, in fact, also the interactions between PVP, solvent, and metal ions are responsible for forming a specific structure.

While the synthesis of gold or silver nanoparticles is usually carried out at room or elevated temperature, Angelomé et al.[26] went in the opposite direction and investigated the effect of cooling on the shape of the particles. Using cetyltrimethylammonium chloride (CTAC) as the structure-directing agent and conducting the reaction below to 10 °C, they obtained gold particles with a tunable surface plasmon resonance from 600 to 1400 nm. These optical characteristics arise from a completely anisotropic shape of the particles; however, by using 3D tomography and high-angle annular dark-field scanning transmission electron microscopy (HAADF-STEM) of the particles, the authors could show that, despite some small deviations in the crystalline orientation, the particles are defect free and single crystalline. The origin of this structure is found in the modification of the reaction kinetics by the low temperature and micellization of the CTA–$AuCl_4$ complex. Moreover, the etching power of the chloride ions is important. The reaction could not be conducted with CTACs larger analog CTAB (i.e., bromide instead of chloride). It will be interesting to see how lower temperatures will affect the particle shapes in the case of other nanoparticles syntheses.

In the synthesis of silver particles, a long-held believe is that citrate and PVP are the crucial reagents for obtaining nanoprisms.[27] Fresh insights into these processes were obtained by Zhang et al.,[28] who could show that, surprisingly, citrate can be replaced by a variety of other di- or tricarboxylic acids and PVP can be even omitted completely. Instead, they identified hydrogen peroxide (H_2O_2) as irreplaceable because it enables the formation of planar-twinned defects which are a requirement for the formation of nanoprisms. By subtle adaption of the reaction conditions, the size and the optical properties of the nanoprisms could be tuned. The important fact in the

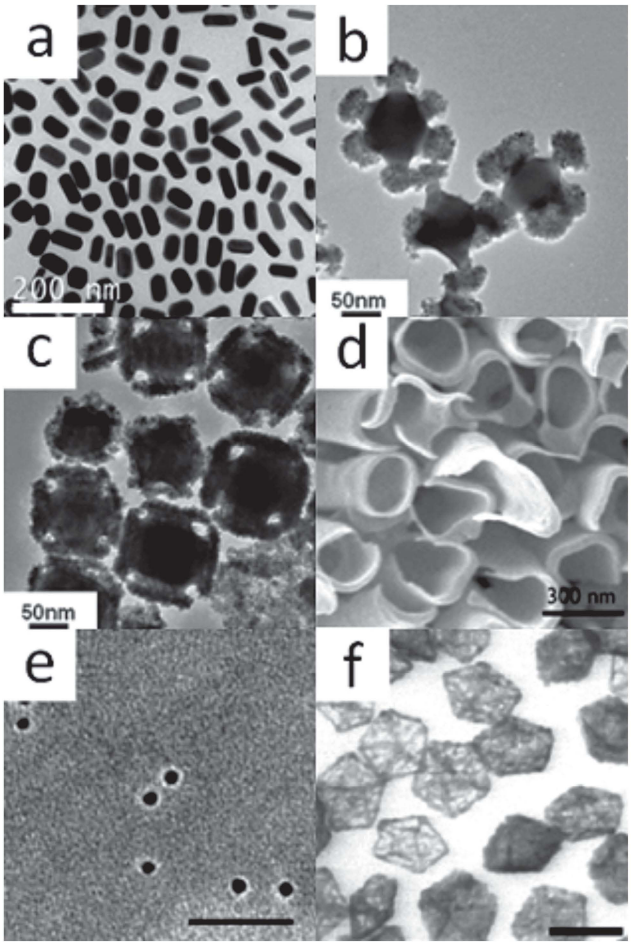

Figure 2. Representative images of selected gold nanoparticles synthesized via the reshaping/etching or the templated approach. a) Low aspect ratio gold nanorods,[57] b) gold/platinum nanohexapods,[59] c) etched gold/platinum nanocubes,[59] d) gold nanotubes,[60] e) gold-ferritine core–shell nanoparticles,[61] and f) gold nanoframes.[34] Scale bars: a = 100 nm; b, c, e, f = 50 nm; d = 300 nm. Image a reproduced with permission.[57] Copyright 2012, IOP Publishing. Images c and d reproduced with permission.[59,60] Copyright 2011, RSC. Image e reproduced with permission.[61] Image f reproduced with permission.[34] Copyright 2011, ACS.

choice of the carboxylic acid is the distance between two carboxylate groups that should be separated by two or three carbon atoms to attach to the Ag {111} facet.

Otherwise the formation of prisms is significantly lowered or, e.g., in the case of acetate, is not possible at all. In addition, the authors found $NaBH_4$ acting not only as the reducing agent but also as a capping agent, which alters the nucleation kinetics and influences thereby the thickness and aspect ratio of the particles.

2.2. Synthesis of Plasmonic Nanoparticles via Seeded Growth

Seeded growth of nanoparticles involves at least two reaction steps. In the first step, usually small nanoparticle nuclei are formed via a metal salt and a strong reducing agent, and in the next step, these preformed seeds are added to a growth solution or vice versa. Depending on the desired structure, further steps with different growth solutions can be applied to obtain highly sophisticated nanoparticle architectures.

For plasmonic applications, an important factor is not only the particle shape but also the particle size. While usually starting with nanoparticles less than 10 nm in diameter, one can easily synthesize particles up to several hundred nanometers in size from these seeds.

The famous Turkevich/Frens method,[35,36] utilizing a sodium citrate and a $HAuCl_4$ solution, yields spherical gold nanoparticles only for rather small diameters. It is also possible to synthesize particles up to 150 nm diameter in this way; however, these particles are usually misshaped, elongated in one direction, and feature a low uniformity in size. Several possibilities, e.g., seeded growth via hydroxylamine,[37] or CTAB and ascorbic acid,[38] are available to synthesize larger particles starting from citrate-stabilized particles. However, these methods usually suffer from high dilutions required to minimize the formation of nonspherical structures due to agglomeration, multiple growth steps, and long reaction times. In addition, some capping agents are hard to remove and cytotoxic, which limits the later utilization of these particles in life science applications.[39] Taking into account these issues, Bastús et al.[29] developed a growth method based on citrate. At first, nanoparticles were synthesized via the Turkevich method at 100 °C, subsequently, by sequential addition of sodium citrate and $HAuCl_4$, the authors could tune the particle size up to 200 nm after running 14 addition cycles. A crucial point was the adjustment of the pH value and the lowering of the growth temperature to 90 °C to prevent the formation of new particles and to ensure the spherical shape. Instead of the stepwise approach, Ziegler and Eychmüller[40] conducted the reaction in a similar way, however, via continuously adding $HAuCl_4$ and a mixture of sodium citrate and ascorbic acid to preformed seeds at room temperature. At this stage, only "blackberry-like" particles are present as small particle clusters are formed on the surface of the seeds. Spherical particles up to 300 nm could then be obtained via heating the solution, which leads to ripening and smoothing of the surface. Hydrogen peroxide is usually applied as etchant in the synthesis of nonspherical silver particles, but it is worth noticing that in the case of gold, another mechanism can be applied whereby the oxidizing agent turns into a reducing agent. Liu et al.[41] took advantage of this fact and were able to synthesize spherical nanoparticles up to 230 nm in size from particles made by the Turkevich method in only 1 min. Astonishingly, without seeds the combination of H_2O_2 and $HAuCl_4$ leads only to irregularly shaped nanoparticles with a broad size distribution.

The attractiveness of the seeded growth approach lies in the possibility to form a menagerie of nanoparticle structures starting from one specific kind of seed just by adjusting the reaction conditions. Halide and silver ions are known to play an important role in the formation of multifaceted structures, however, contradictory theories exist in explaining their structure-directing properties.

In a groundbreaking study, Langille et al.[30] shed light on the factors governing the structure of polyhedral gold particles synthesized via the seeded growth method. By changing the concentration of the halide and silver ions as well as the reducing

DOI: 10.1002/ppsc.201300309

agent, the authors were able to synthesize 10 different nanoparticle morphologies. Several parameters direct the growth of the particles. The larger the halide ion, the slower the nanoparticles will grow due to a higher affinity of larger halide ions to the gold surface as well as a lower solubility and a lower reduction potential of the $[AuHal_2]^-$ complex, which yields thermodynamically favored particles with lower energy facets. Particles with a high amount of surface facets can be synthesized with the aid of silver ions. Via underpotential deposition, a monolayer of silver can be formed on the facets preventing the attachment of gold atoms and, hence, shielding the facet against growth. Increasing the amount of silver ions therefore leads to structures with more surface facets as more of them can be stabilized. Addition of a large amount of bromide or iodide ions to growth solutions with silver undermines the protecting effect of the protecting layer yielding less-defined particles, especially in the case of iodide. In contrast, a low amount of these halide ions leads to higher index particles. A more detailed investigation on the effect of the reducing agent was conducted by Eguchi et al.[42] and Wu et al.[43] Kinetically preferred particles with high-energy surface facets are formed by a faster reduction of gold ions resulting from an increase of the ascorbic acid concentration. By subtle changing the amount of reducing agent, they were able to synthesize six types of polyhedral gold nanoparticles from small seeds.

Gold nanorods are particularly interesting for applications in photothermal therapy or drug delivery.[44] Despite continuous research in recent years, fine-tuning the aspect ratio (AR) and the monodispersity of nanorods without shape impurities still remains challenging. Ye et al.[31] introduced aromatic additives for which interactions between CTAB micelles and the developing gold nanorods allow narrowing of the size distribution. By contrast, Wen et al.[45] used copper ions to tailor the reactivity of the initial gold seeds. Etching of preformed particles leads to more reactive seeds with a smaller polydispersity. By growing these seeds, nanorods with a low size distribution can be obtained.

Koeppl et al.[46] harnessed an innovative yet rarely applied approach to reproducibly synthesize nanorods with exceptionally high AR. Utilizing isotope effects, the authors were able to double the length of nanorods just by changing the solvent from H_2O to D_2O yielding rods with an AR up to 19. The reduction rate of Au(III) ions is alleviated by exchange of the hydrogen atoms in the hydroxyl groups of ascorbic acid by deuterons, which presumably leads to a more selective growing of the thermodynamically favored nanoparticle ends on the long axis.

Though the growth of rods is usually performed with different chemicals, an extraordinary approach is to use light as the directing agent. Through plasmonic excitation of silver seeds with wavelengths from 600 to 750 nm, Zhang et al.[47] could tailor the AR of silver nanorods. The process proceeds via reduction of silver ions in the presence of citrate, which, however, acts only as a reducing agent when the solution is irradiated with a defined wavelength. Formation of high aspect ratio rods was facilitated by longer wavelengths as the reduction takes place preferably at the end of the rods.

The synthesis of star-like particles is of special interest for applications like surface-enhanced Raman scattering (SERS) as the spiky structure significantly enhances the electromagnetic field. However, these structures are often limited to two dimensions with several branches starting from one spherical metal particle center.[48] Notable exceptions are gold[49] and silver[50] dendritic nanostructures as well as gold multipods.[51,52] Recently, Vigderman and Zubarev[32] for the first time utilized nanorods as base material. Starting from pentagonally twinned gold nanorods, the authors managed to grow preferably the long side of the rods by assistance of silver ions leading to branched starfruit like structures up to a mesoscopic size.

For plasmonic applications, silver is theoretically the material of choice owing to its superior optical properties compared with gold;[53] however, the practical implementation is seriously limited by the susceptibility of silver against oxidation. Shankar et al.[54] synthesized Au/Ag core–shell structures from gold nanoparticle seeds. They could show that the stability of the silver layer is significantly enhanced compared with pure silver particles due to an electron transfer from the gold core to the silver shell making this approach an interesting starting point for the stabilization of other silver nanostructures.

DNA has witnessed a tremendous interest in the field of nanoscience, e.g., by means of DNA origami for the preparation of nanoarchitectures or DNA interactions for the assembly of plasmonic nanostructures.[55] However, recently, it has also been found to be an interesting tool also for the synthesis of nanoparticles. Utilizing different kinds of DNA, Wang et al.[33] were able to identify the "genetic code" that controls the morphology of gold particles. At first, the seeded growth of nanoparticles was conducted; with one-base oligonucleotides of adenine, thymine, cytosine, and guanine being used as structure-directing agents, raspberry, star-like, platelet, and hexagonal platelet structures were obtained, respectively. Without addition of DNA only undefined structures could be synthesized. In a second approach, two-base oligonucleotides were applied with different ratios between the bases. It could be shown that different competitive and synergistic interplays between two bases or dominating effects of one base direct the morphology of the nanoparticles.

Small gaps between plasmonic nanoparticles are particularly interesting for the possibility to detect substances down to the single-molecule level via SERS. Generally, such structures are formed through self-assembly of nanoparticles, but Lim et al.[56] could show that by seeded growth of gold particles similar structures can be obtained. Modification of these nanoparticles with thiopegylated DNA, which functions as a protecting shell of the particle, gave a core–shell structure after applying a growth solution. The results of this approach are remarkable: on the one hand, a defined gap of 1 nm between the inner core and the shell is formed; on the other hand, small nanobridges are present, which interconnect these moieties. Interestingly, these bridges lead to a significant field enhancement compared with a normal fully separated core–shell structure presumably due to symmetry breaking.

2.3. Synthesis of Plasmonic Nanoparticles via Reshaping/Etching

While reshaping of particles is already indirectly used during many synthetic procedures, postsynthetical ageing and transformation

of nanoparticles is often an undesired process as it limits the lifetime and usability of a specific particle type. However, the mechanisms for these processes need to be understood in order to improve their stability. In addition, it is also possible to intentionally make use of them in order to obtain new nanostructures. Ng and Cheng[57] sought to simplify the tunable synthesis of gold nanorods. Instead of starting with nanoparticle seeds and adjusting the reaction parameters to obtain rods with different lengths, the authors synthesized a rod solution with a defined aspect ratio and then applied reshaping steps at temperatures between 50 and 100 °C. By this means, particles with lower aspect ratio and finally sphere-like structures were obtained. The origin of the shape transformation lies in the desorption of stabilizing ligands at higher temperatures from the side of the rods with a concomitant growth of the sides via residual gold ions in solution or mediated by surface melting.

A different mechanism was proposed for silver nanorods by Damm et al.[58] In this case, reshaping occurs due to the presence of dissolved oxygen, which etches or even can break up the rods. Dissolved silver ions can then be re-reduced at different positions of the same or another rod, leading to nanobuns. In addition, also secondary nucleation can take place whereupon spherical particles are obtained.

In a combination of a top-down and a bottom-up approach, Min et al.[59] synthesized gold–platinum nanoparticles with sophisticated morphologies. In the first step, platinum was deposited at different positions of gold nanospheres, cubes, and octahedras synthesized via the polyol process. Subsequently, cyanide solution was added that preferably etches the gold surface resulting in, e.g., gold nanohexapods or empty platinum shells depending on the initial structure.

2.4. Template-Assisted Synthesis of Plasmonic Nanoparticles

Templated synthesis is a powerful method as it opens up the possibility to obtain unprecedented structures since the morphology is not necessarily governed by the reactivity of certain crystal facets but mostly by the shape of the template. In general, metal, metal oxide, or polymeric materials are applied as scaffolds that direct the growth of the nanoparticle in one or more directions.[62] Bridges et al.[60] used an electrochemical synthesis of gold nanotubes using anodized aluminum oxide as the template. In contrast to similar approaches,[63] they were able to vary the thickness and shape of the tubes with the aid of different polymers. At first, several thiophene monomers were electropolymerized inside the template yielding a polymer-filled tube. Addition of the gold-plating solution leads to a collapse of the polythiophene derivative due to its hydrophobicity. The final structure depends on the polymer structure. Finally, gold tubes are synthesized by electrolytic deposition and set free by etching the polymer and the template.

While deposition of gold on silver particles or vice versa usually yields core–shell structures, skillful adjustment of the reaction conditions facilitates the deposition only on certain facets. Pentagonally twinned silver nanoparticles exhibit {111} facets, which are more stabilized by citrate than other facets. McEachran et al.[34] made use of this fact and deposited gold on the edges between {111} facets. Etching the silver core with hydrogen peroxide retains the gold scaffold, which corresponds to the external structure. In this way, fascinating gold nanostructures hold together by ultrathin nanowires could be obtained.

It is worth remarking that also biological templates can be utilized for the synthesis of nanoparticles, whereas their attractiveness lies in their low size polydipersity. The protein ferritine is responsible for the iron storage in plant and animal tissue and can in its apo form be visualized as an empty nanocage. While normally containing iron oxide hydroxide, it was shown by Fan et al.[64] that it is also possible to fill the 7 nm in size interior of horse-spleen apoferritine with gold ions. To specifically synthesize nanoparticles, only on the inside a desalting step was applied, which removes the gold ions on the outside. Reduction finally leads to highly monodisperse gold nanoparticles.

The interest in chiral plasmonic nanostructures has gained momentum recently due to their outstanding optical activity as well as their potential for generating negative index materials.[15,16] However, up to now, strategies to synthesize such structures mostly rely on top-down approaches. The bottom-up synthesis relies mostly on nanoclusters, which do not sustain a surface plasmon resonance. Block copolymers (BCPs) can serve not only as a tool to assemble nanoparticles but, in fact, can also be utilized as a versatile template to direct the synthesis of plasmonic nanoparticles. Hsueh et al.[65] employed a polystyrene-*b*-poly(L-lactide) (PS-PLLA) BCP, which forms a gyroid microphase-separated structure. Hydrolysis of the PLLA domain leads to the formation of nanochannels. Subsequently, the scaffold was immersed in a gold salt solution followed by addition of hydrazine leading to small gold particles attached to the walls of the channels. In the next step, a growth solution was applied. Depending on the growth time, twisted gold structures or a completely penetrating gold network could be synthesized. While this structure is not chiral, in a similar approach, Vignolini et al.[66] utilized a poly-(isoprene-*b*-styrene-*b*-ethylene oxide) triblock copolymer. The polymer was spin-coated onto a conductive substrate followed by removal of the isoprene block. Electrodeposition of gold into the pores lead to a large gyroid gold network. In this case, however, the chirality of the underlying BCP scaffold was transferred into the final gold structure evidenced by the optical activity of the sample. Such a large network can hardly be referred to as a particle but lowering the deposition time or combination with the seeded growth approach could pave the way for a versatile chiral plasmonic nanoparticle synthesis method.

It is obvious that an almost unlimited number of nanoparticle structures can be synthesized. Further complexity and optical properties can be introduced via the ordered assembly of these particles. This requires not only the understanding of the interactions between electromagnetic fields with single particles but also with their assembled superstructures.

3. Design Considerations of Self-Assembled Plasmonic Nanostructures

The previous section provides an overview about the possible geometries of single nanoparticles that can be obtained by

Part. Part. Syst. Charact. 2014,
DOI: 10.1002/ppsc.201300309

different synthetic procedures. The next step to enlarge the resulting properties of such materials is an ordering of these nanoparticles by chemical self-assembly processes to so-called nanoparticle superstructures. Here, the focus is on the discussion of how photonic materials formed by these nanoparticle superstructures can be used to obtain functional devices with a desired optical response in the near- as well as in the far-field. Since this field is much too large for a comprehensive discussion, we narrow the focus of this section to photonic materials for which the typical spatial dimensions are comparable to, or eventually smaller than the wavelengths of interest. Typical dimensions can refer here to a lattice constant or to the spatial extend of an isolated superstructure. These sub-wavelength dimensions entail a convenient theoretical description of the complicated self-assembled bulk materials based on effective medium theories,[67–70] as discussed below. Furthermore, only photonic materials are considered that can be used for applications in the visible or near IR regime of the spectrum.

The question of a desired optical response for self-assembled photonic materials with sub-wavelength dimensions is typically linked to the requirement that the material shall allow for a resonant interaction with light. Without any resonant response associated to either the isolated superstructure or its spatial arrangement in a lattice, the optical response of the self-assembled material would be merely explainable by considering the spatial average of the intrinsic material properties of its constituents. Therefore, one has to ensure that the fabricated samples sustain resonances in the visible or IR light region. Since we are only interested in sub-wavelength structures, the resonance properties that can be induced only by the lattice formation are limited. Therefore, resonances of the nanoparticles themselves are the key ingredient to achieve desired optical responses. Usually, the localized surface plasmon polariton resonances (LSPRs) of metal nanoparticles are exploited. There, the free negative charges of metal nanoparticles can be driven into resonance by an impinging electromagnetic field at a resonance frequency. For a sub-wavelength metallic sphere in the quasi-static limit, an analytical expression for the resonance frequency of the LSPRs is obtained according to the book of Bohren and Huffman:[71]

$$\mathrm{Re}\left[\varepsilon_{\mathrm{sph}}(\omega)\right]+2\varepsilon_{\mathrm{emb}}=0, \tag{1}$$

where $\varepsilon_{\mathrm{sph}}(\omega)$ and $\varepsilon_{\mathrm{emb}}$ are the permittivities of the metallic sphere and the surrounding, respectively. In a vacuum, the LSPRs of metallic nanoparticles are excited if the real part of the metal permittivity is equal to −2. Taking material parameters from Johnson and Christy,[72] this is achieved for silver at around 350 nm and for gold at around 500 nm. Of course, there are much more plasmonic materials available for the visible and IR, but gold and silver are the two most commonly used ones due to their relatively low imaginary part of the permittivity at the LSPRs and their preferential chemical properties as discussed in the previous section.[53,73,74] The imaginary part accounts for the absorption in the metal and is therefore a crucial parameter that dictates the resonance strength.

From the equation above, it is obvious that the resonance position of metal nanoparticles can be tuned by changing the permittivity of the surrounding. Further tunability can be induced by employing nonspherical nanoparticles. A large variety of different geometries can be synthetized, as shown in the last section. For nonspherical nanoparticles, the resonance wavelengths will depend essentially on the axis ratio. Eventually, comparable to the expression above for a sphere, an analytical expression can be given for an ellipsoidal particle characterized by three semiaxes a_i in the quasi-static approximation. It reads as[75]

$$3\varepsilon_{\mathrm{emb}}+3L_i\left[\mathrm{Re}\left[\varepsilon_{\mathrm{sph}}(\omega)\right]-\varepsilon_{\mathrm{emb}}\right]=0 \tag{2}$$

where L_i is a geometrical factor given by

$$L_i=\frac{a_1a_2a_3}{2}\int_0^{\infty}\frac{\mathrm{d}q}{\left(a_i^2+q\right)\sqrt{\left(q+a_1\right)^2\left(q+a_2\right)^2\left(q+a_3\right)^2}} \tag{3}$$

With this basic expression, many of the properties of nonspherical metallic particles can be easily expressed, e.g., the appreciation that multiple resonances are supported by nanoparticles when their semiaxes are different and, moreover, the resonances are red (blue)-shifted for the axes larger (smaller) with respect to the radius of a sphere having the same volume as the ellipsoid. This understanding can then be easily extrapolated to slightly more complicated geometries that deviate from a perfect ellipsoidal shape. For example, Van der Zande et al.[76] showed among others that nanorods may sustain two LSPRs.[77] For one resonance, the free electrons are oscillating along the long axis and for the other resonance, they are oscillating along the short axis. The long-axis resonance appears at longer and the short-axis resonance at shorter wavelengths. The optical response of such nanorods therefore sustains an additional feature: it depends on the polarization of the incident field, meaning it is anisotropic; i.e., uniaxial anisotropic to be precise. In terms of optical properties, nonspherical nanoparticles[78–87] and core–shell particles attracted equally considerable interest. The later one being able to tune the resonance wavelength across extended spectral domains as demonstrated by Prodan et al.[88,89]

Apart from tuning the resonance position by the shape or the environment, coupling between adjacent nanoparticles in a superstructure allows for a huge degree of tuning. If the metallic nanoparticles have truly sub-wavelength dimensions, their scattered field can be treated as purely electrical dipolar. Therefore, the coupling between two nanoparticles can be described in terms of electric dipole coupling. A very prominent scheme, introduced by Nordlander et al.,[88,91] that takes this dipole coupling between two nanoparticles into account is called plasmon hybridization[90] and was adapted from molecular physics. It reveals four possible eigenmodes if two nanoparticles are coupled to each other. Two of them are termed bright, as they can couple to the far-field, and two of them are dark eigenmodes. The bright eigenmodes are characterized by an in-phase oscillation of the electric dipoles of the nanoparticles, whereas the dark eigenmodes are characterized by an out-of-phase oscillation. In particular, the latter kind of eigenmodes provides the possibility to encounter completely new optical responses. These dark eigenmodes are no longer dominated by electric dipole radiation to the far-field. In particular, magnetic dipoles can be excited in two

strongly coupled nanoparticles.[91–93] These magnetic dipoles play a pivotal role in the field of self-assembled metamaterials. They allow not just the tuning of the effective permittivity of the fabricated material but they may feature also a dispersive effective permeability,[68] sometimes termed artificial magnetism. Completely new phenomena become accessible by controlling the permeability of a self-assembled metamaterial in the visible and IR region since all natural occurring materials show no response to the magnetic field in this spectral domain. The list of postulated applications ranges from cloaking devices,[14,94–97] perfect lenses,[98–100] to the huge field of transformation optics,[101,102] where the light propagation through a metamaterial can be controlled at will. Apart from these dark eigenmodes, the bright eigenmode of two coupled nanoparticles offers equally extraordinary optical properties. One bright eigenmode is excited, if both electrical dipoles of the nanoparticles are oscillating in phase to each other along the connection line of the nanoparticles. The resonance wavelength of this eigenmode is extremely sensitive to the environment and to the precise separation of the particles. Zhang et al.[103] demonstrated that the environmental sensitivity can be used to probe even single molecules.[104] This has an extreme impact for the fabrication of sensing devices. The distance dependency is used to construct so-called plasmonic rulers, as suggested by Sönnichsen et al.[105–107] These are devices that are proposed to measure the extension of molecules with sub-nanometer precision and possibly also to dynamically track modifications of their arrangements.

Apart from the coupling of just two nanoparticles, also larger assemblies have attracted a lot of interest. Most of these larger clusters are made of nanospheres as the basic-building block. Fano-type resonances have been demonstrated for a large class of different geometries, e.g., in quadrumer,[108] heptamer,[109] or heteropentamer[110] clusters. Fano-type resonances result in an asymmetric line shape of the extinction cross section, which is a very uncommon optical response.[111] It can be explained by the coupling between one-bright and one-dark eigenmode at a specific wavelength region. Zhang et al.[112] showed that this concept can be further used to achieve plasmon-induced transparency. Apart from Fano-type resonances, also magnetic resonances can be excited in clusters of nanoparticles. Prominent examples are trimer,[113,114] quadrumer,[110] and tetramer[115] clusters as well as 2D rings of nanospheres.[116,117] Since these clusters represent 2D planar structures, one purpose is to extend them into the third dimension. This was demonstrated in the case of magnetic resonances for supramolecular clusters[118–120] with a spherical shape and for so-called core–shell clusters (Figure 2).[121] The supramolecular clusters consist of an amorphous arrangement of metal nanoparticles that forms a superstructure with a nearly spherical shape. The magnetic response of these clusters can be explained as follows. A bulk material made of randomly arranged metallic nanoparticles exhibits an effective permittivity with Lorentzian line shape centered at the resonance wavelength of the LSPR sustained in the cluster. At longer wavelengths (compared with the LSPR), the real part of the effective permittivity is much larger than unity. Forming a sphere out of such a material allows the excitation of resonances that are associated to high permittivity spheres, i.e., Mie resonances. The lowest order resonance is the aspired magnetic dipole resonance. The second example, the previously mentioned core–shell clusters, consists of a dielectric core that is covered by a large number of tiny metal nanoparticles forming the shell. The electric dipoles of every nanoparticle at the shell can be excited in such a way, that they are all oscillating around the core at one specific wavelength. This oscillation forms an effective current that is associated with a magnetic dipole moment,[121–123] as discussed by Simovski et al. The magnetic dipole moment of such core–shell clusters is much stronger compared with the supramolecular cluster (**Figure 3**), as the amount of metal is drastically reduced for this design.

Additionally, besides to control effective materials properties such as the permittivity or permeability that is possible, while relying on nanoparticle configurations that either sustain a strong electric or magnetic dipolar response, other more primary optical properties can be subject of concern as well. For example, whereas the materials properties just mentioned ask for highly symmetric nanoparticle configurations to achieve an isotropic response, introducing deliberately a break in symmetry may offer equally unprecedented opportunities to observe new phenomena for the propagation of light. The phenomenon that attracted potentially the most interest is linked to chiral assemblies of metallic nanoparticles.[124] This opens a route toward devices that can control the polarization state of light in a more drastic manner when compared with natural materials.[125,126] It also constitutes a viable route toward negative index materials[127–130] (see section 6 on applications).

Chirality in first instance is a geometrical property. It suggests that the mirror image of a structure is not super-imposable with the original structure by a proper rotation. Structures with such geometrical properties can be found in many situations not only on the molecular level but also on macroscopic scales. In the context of this status report, the specific structures of concern are of course chiral nanoparticle assemblies.[15,16] The optically observable property of a chiral material is circular dichroism. It corresponds to a differential intensity transmission of right- and left-handed circular polarized light. Circular dichroism is, in general, accompanied by a difference in the phase advance for right- and left-handed circular polarized light due to causality, i.e., the real and imaginary part of the wavenumber for both fields inside the material differs.[131] Although many molecules are intrinsically chiral, the magnitude of the circular dichroism is weak and effects are only encountered to a notable extent while propagating light across macroscopic distances. Therefore, enhancing chirality is of utmost importance. The intrinsic circular dichroism of molecules can be enhanced, e.g., if they are combined with achiral metallic nanoparticles.[132,133] Then, in the spectral domain where the LSPR is supported, the effective chirality will show a strong dispersion.

Nonetheless, a chiral arrangement of metallic nanoparticles itself can also significantly enhance the circular dichroism. It, moreover, mitigates the requirement of having intrinsically chiral molecules available. Pioneering works have been done with top-down fabricated nanostructures[134,135] but also structures amenable for a bottom-up fabrication were suggested. These bottom-up structures either consist of complicated chiral geometries for an isolated object,[136] e.g., a referential example might be a Möbius strip,[137] but especially nanoparticles arranged along helical trajectories[138] or chiral arrangements of

Part. Part. Syst. Charact. 2014,
DOI: 10.1002/ppsc.201300309

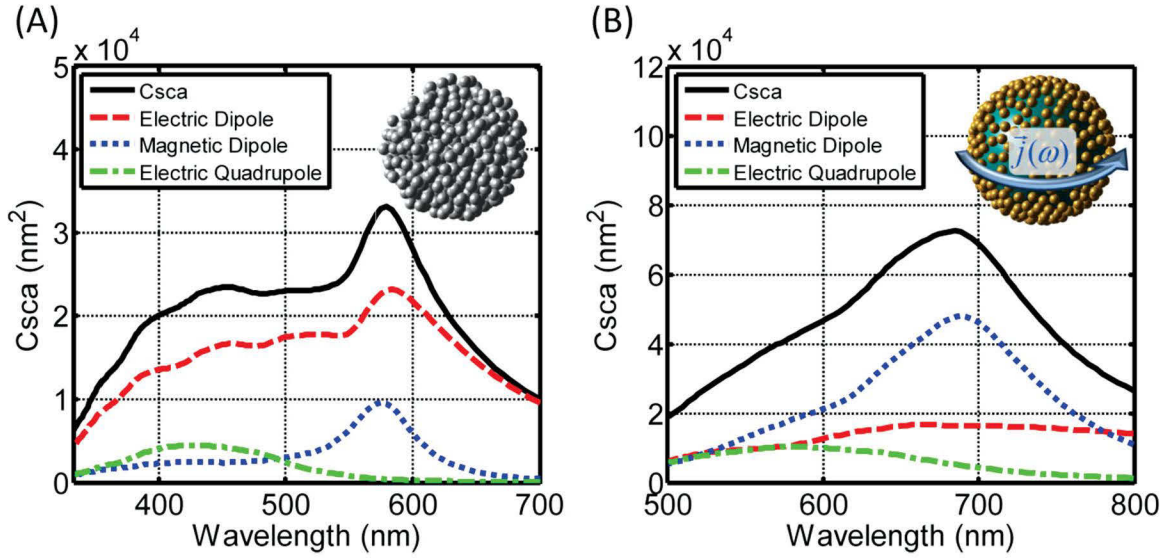

Figure 3. Simulation of the contributing multipole moments to the scattering cross section (Csca) for two examples of self-assembled superstructures (the insets present a sketch of the geometry) offering a magnetic dipole response in the visible spectral range. The shown multipole moments are presented such that their sum yields the entire scattering cross section. A) Randomly arranged silver nanospheres (6 nm radii) form a supramolecular cluster with a spherical outer shape (radius of 75 nm). The supramolecular cluster is embedded in a dielectric with a permittivity of 2.6. The magnetic dipole resonance (blue-dotted curve) can be seen at around 580 nm. Reprinted with permission.[120] Copyright 2012, OSA. B) Core–shell cluster made of a silica core (radius of 130 nm) that is covered by gold nanospheres (radius of 10 nm) forming a shell. The core–shell cluster is dissolved in water. The magnetic dipole resonance is observed at around 700 nm. The blue arrow around the sketch of the core–shell cluster indicates the effective current that is induced in the shell at the magnetic resonance. Reprinted with permission.[121] Copyright 2011, ACS.

only a few but different nanoparticles (either in terms of material or size composition)[139–141] attracted interest.

One aspect that has been swept under the rug up to now is linked to local optical properties of photonic materials. All previously mentioned examples are based on far-field properties that can be probed, e.g., by extinction or scattering measurements. But of course, self-assembled photonic materials offer appealing near-field properties as well. This is attributed to the fact that distances can be controlled by self-assembly in the nanometer or even in the sub-nanometer range. This allows the observation of extremely coupled nanoparticles. Mühlschlegel et al.[142] demonstrated that the above-mentioned bright eigenmode of two coupled nanoparticles can be applied for producing huge local-field enhancements. This is exploited in a widely used spectroscopy technique, known as SERS.[143] In a first-order approximation, the SERS cross section scales with the forth power of the local electromagnetic field. Therefore, high local-field enhancements are appropriate to enhance the SERS efficiency. Two strongly coupled gold nanospheres and nanoshells have been proven to extremely enhance the SERS efficiency.[144] Apart from these rather simple geometries, also complex clusters of nanoparticles of different size[145] or materials[146] can offer significant local-field enhancements. Recently, it has been demonstrated by Ye et al.[147] that Fano-type resonances in complex superstructures can enhance the SERS efficiency.[147] Apart from achieving a large local electromagnetic field by coupling of nanoparticles, also the shape of the single particle can be used, e.g., nanoflowers[148] or nanocubes[149] can enhance the SERS efficiency.

Another proposed application of local-field effects has recently attracted a lot of interest. If one considers the interaction of light with molecules, one usually assumes that the electromagnetic field does not vary across the size of the molecule; in other words, the gradient of the field can be neglected. Although this assumption is entirely applicable, while considering the free-space interaction of light with molecules, it ceases to be justified for highly localized near-fields close to nanoparticle superstructures. It has been proven by Filter et al.[150] among others that these near-fields possess huge gradients of the electromagnetic fields at lengths scales of a typical molecule.[151] Therefore, the interaction between these near-fields and the molecules allows for the excitation of free-space forbidden transitions in the molecule. Although, the experimental prove of this concept is still missing, it can be anticipated that this feature would enable a complete new perspective for spectroscopic and sensing applications.

This section has presented a compact overview of the possible optical response features and resulting applications of self-assembled photonic materials, based on the far- as well as on the near-field properties. Although we have witnessed already tremendous progress, there remain numerous challenges to be solved in this growing field. The first one is linked to the filling fraction of the metallic nanoparticles. A desired optical response can be only achieved if the filling fraction is high enough, even if resonances, such as LSPRs, are exploited. A higher filling fraction will sharpen all resonance features and also the dispersion of effective material parameters such as permittivity and permeability would be increased. However, it constitutes a challenging task to arrange nanoparticles sufficiently dense by self-assembly techniques into superstructures. The problem is that the conductive coupling between the individual nanoparticles must be avoided since otherwise all resonance

features fade away. Apart from the filling fraction, another problem is linked to the intrinsic absorption of the nanoparticles. Since metallic nanoparticles serve as the building blocks for self-assembled superstructures and, thus, the resulting photonic material, they suffer from absorption in the metal due to the non-negligible imaginary part of the metal permittivity. One possible solution might be the incorporation of gain into these materials.[152] This might be possible by using fluorescent dyes, semiconductor quantum dots or rare earth metals.[153,154] The incorporation of these materials asks also for an appropriate and challenging way to describe their optical response, e.g., based on two- or four-level systems. Though a few possible examples have been demonstrated, most noticeably the demonstration of a spaser,[155–158] a lot of work still remains to be done to understand these gain assisted systems.

Next to the challenges to theoretically predict the properties of complex architectures of superstructures also their experimental realization requires delicate self-assembly strategies. In the following paragraph, experimental approaches to fabricate multiparticle superstructures are highlighted.

4. Self-Assembly Strategies for Plasmonic Nanoparticles

To a large extent, the potential of plasmonic nanoparticles is not only determined by the metal, the particle size or shape itself but it also relies on their ordered assembly. The formation of nanoparticle superstructures gives rise to further electromagnetic interactions between them and external fields, thereby opening the possibility to even create (meta)materials with properties not existent in nature.

Three general approaches exist to form plasmonic superstructures. Top-down approaches involve the modification of a large preformed structure where, e.g., a noble metal is evaporated onto a substrate or, alternatively, certain parts of a large metal layer are etched away. An advantage of this method is the large area, which can be patterned; however, it suffers from long fabrication times. In contrast, bottom-up approaches utilize either metal salts or already formed nanoparticles in combination with different assembly methods to create particle aggregates. This allows the fast and easy formation of superstructures in high amounts, but ultimately it is crucial to assemble these superstructures again to form a device. The top-up approach lies in-between by first forming a large patterned substrate where, subsequently, nanoparticles are deposited.

In this section, we intend to illuminate the recent progress for the last two approaches and the different methodologies used within to assemble plasmonic nanostructures. For an overview of possible structures, see **Figures 4** and **5**.

4.1. Bottom-up Assembly of Plasmonic Nanoparticles

A multitude of chemical reactions, like click,[159] Diels–Alder,[160] esterification[161] or complex-forming reactions,[162] can be utilized to form nanoparticle assemblies. This is motivated by the possibility to create discrete assemblies, e.g., gold–silver heterodimers. However, these reactions are usually performed in solution with particles possessing thousands or more reactive

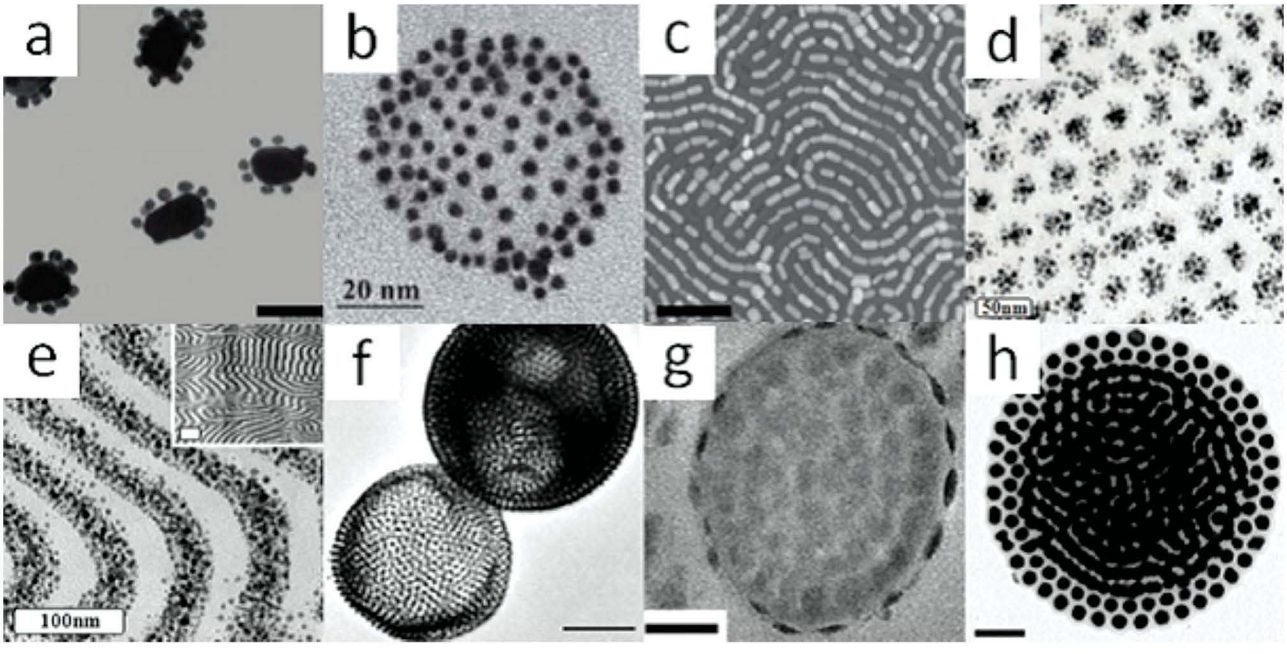

Figure 4. Representative images of selected gold nanoparticle assemblies prepared via different bottom-up approaches. a) Gold nanoflowers,[168] b) polymer/gold core–shell satellite structure,[175] c) assembly of gold nanorods in a lamellar BCP phase,[177] d) assembly of gold nanoparticles in a hexagonal BCP phase,[178] e) assembly of gold nanoparticles in a lamellar BCP phase,[178] f) assembly of gold nanoparticles in BCP vesicles,[179] g) gold cluster patches in a BCP,[180] and h) gold particle clusters assembled via hydrophobic interactions.[181] Scale bars: a, e, g = 100 nm; b = 20 nm; c, f, h = 200 nm; d = 50 nm. Image a reproduced with permission.[168] Copyright 2011, ACS. Image b reproduced with permission.[175] Copyright 2012, RCS. Image c reproduced with permisssion.[177] Copyright 2013, RSC. Images d–h reproduced with permission.[178,181] Copyright 2012, ACS.

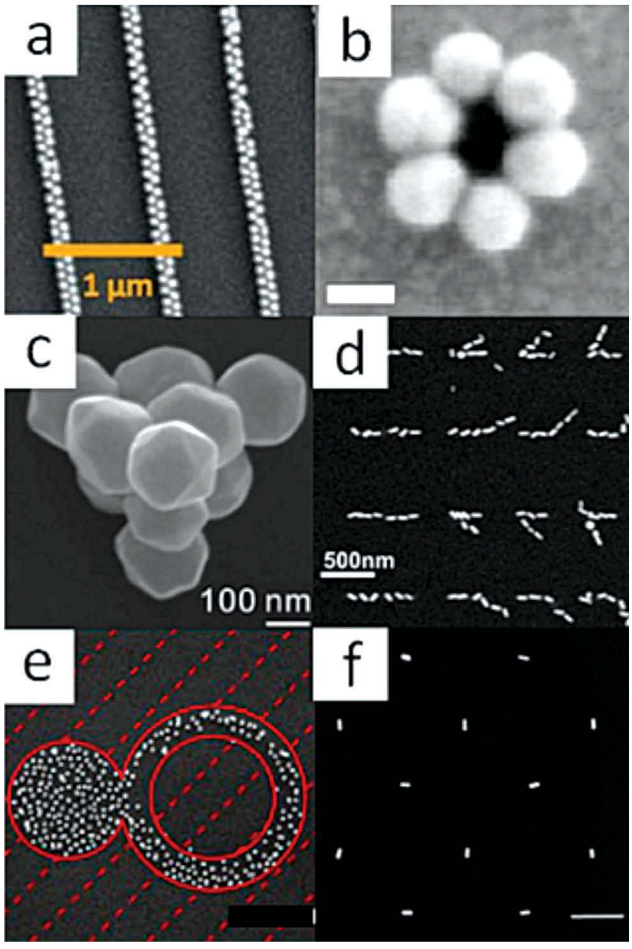

Figure 5. Representative images of selected gold nanoparticle assemblies prepared via different top-up approaches. a) Lines of gold nanoparticles assembled via wrinkle drying,[193] b) gold particle hexamer assembled via a templated approach,[194] c) gold particle pyramid assembled via a nanomanipulator,[195] d) gold nanorods assembled via capillary forces,[196] e) gold nanoparticles assembled via differences in the surface hydrophilicity,[198] and f) oriented assembly of gold nanorods.[199] Scale bars: a = 1 µm; b = 50 nm; c = 100 nm; d–f = 500 nm. Image a reproduced with permission.[193] Copyright 2010, RSC. Images b and e reproduced with permission.[194,196] Copyright 2011, ACS. Images c and e reproduced with permission.[195,198] Copyright 2012, ACS. Image f reproduced with permission.[199]

moieties. Hence, reactions between complementary (e.g., azide and alkyne functionalized) particles or of one particle type with a reactive bifunctional linker are merely statistical processes. Although some tuning is certainly possible, these reactions usually lead to dimers, trimers or higher oligomers with a rather undefined structure. In addition, also single particles are still present and, therefore, enrichment/separation steps have to be applied in order to obtain a pure sample of a defined assembly.

One possibility to mitigate these problems is the desymmetrization of the particles. In this respect, the most straightforward approach is the immobilization of the particles on a surface, thereby rendering one side inaccessible to reactants. Commonly monothiols are then utilized to functionalize the non-shielded side of the particles.[163] However, mixing particles with complementary thiols will result only in particles with a mixed thiol layer, owing to the steady equilibrium of the thiols between the gold surface and the solution. Hofmann et al.[164] addressed these issues by attaching gold nanoparticles to a glass slide and subsequent functionalization of the side facing away from the glass with tripodal ligands. The chelating effect leads to an excellent stabilization of the thiol layer and inhibits the subsequent exchange with monothiol ligands. After detachment of the particles from the glass slide, the assembly was performed by addition of a rigid α,ω-dithiol to the particles. After removal of the excess dithiol, another batch of particles with a free side was added, resulting in the connection between the particles. In a second approach, the particles were selectively functionalized with amine or carboxylic groups, and the complementary particles were then reacted with each other. By this means, samples containing the nanoparticle dimers could be synthesized; however, "only" up to 57% of the dimer could be achieved.

A subtle strategy is to modify nanoparticles in a way that they contain only one single reactive moiety. Early reports required the tedious purification from non- and higher functionalized particles.[165] Hermes et al.[166] were able to discretely functionalize gold nanoparticles in just one step. A solution of $HAuCl_4$ was reduced in the presence of dendrimers bearing multiple thioether groups and one alkyne group. The obtained nanoparticles were 1–2 nm in diameter and contained only one or two terminal triple bonds, depending on the size of the used dendrimer. Glaser coupling of the particles resulted either in the formation of polymeric assemblies (in case of two groups per particle), or, in the case when one single alkyne moiety is present, mostly dimers are formed. For plasmonic applications, these particles are rather small. However, if extended to higher generation dendrimers or even polymers, large particles could easily be functionalized with a defined number of moieties resulting in fascinating base materials for discrete assemblies.

Reactions between biomacromolecules, such as oligonucleotides, have a long history for the assembly of nanoparticles, immunogold labeling being a famous example.[167] DNA is commonly used as a connecting unit between particles, yielding a broad range of extraordinary structures. A limiting factor for successful applications is the rather long length of the strands, as a requirement for effective electromagnetic interactions between the particles is a small interparticle distance. Lubitz and Kotlyar[168] addressed this fact by synthesizing parallel stranded G-quadruplexes with defined length between 1.6 and 6.4 nm. At first, gold nanoparticles were incubated with an excess of the DNA. Citrate-stabilized particles were subsequently added. They attached to the other end of the DNA and, finally, flowerlike assemblies could be obtained. As evidenced by UV–vis spectroscopy, the longitudinal plasmon resonance could be tuned by the length of the DNA strands.

DNA origami is a versatile tool, which enables the creation of sophisticated nanostructures. In combination with plasmonic nanoparticles, assemblies with precise control over the exact position and orientation of the particles can be achieved. Ding et al.[169] utilized a triangular DNA assembly in order to create a chain of gold nanoparticles. Certain domains on the DNA scaffold are able to react with complementary DNA. The authors now functionalized gold nanoparticles of different sizes with different DNA strands. Depending on the respective

functionalization, particles of a certain size could only attach to a specific domain on the triangular structure. Since the reactive moieties were positioned only on one side, a chain of particles with a gradient in size could be synthesized. In a similar way, Pal et al.[170] were able to assemble anisotropic nanoparticles. Gold nanorods were functionalized with thiolated DNA and reacted with a triangular DNA scaffold. By subtle tuning of the reactive positions on the organic superstructure, the authors could control the orientation of two nanorods to each other from a linear chain, toward angular or side-to-side structures. Moreover, also heterodimers consisting of single particles and nanorods could be synthesized.

Kuzyk and co-workers explored the application of DNA origami as basis for chiral plasmonic nanostructures. Left- and right-handed helical DNA assemblies with a 56-nm helical pitch were synthesized. By subtle tuning of the reaction conditions, almost each strand could be covered with exactly nine 10-nm gold particles, thereby creating a strong CD signal. The intensity could be further increased by use of 16 nm particles, which decreases the interparticle distance and, therefore, enhances the plasmonic interactions between the particles. This also allowed tuning the position of the CD signal to higher wavelengths. Lower wavelength signals could be achieved via growth of a pure silver or a gold–silver alloy shell around the gold particles.

Instead of chemical reactions between gold nanoparticles, they can be assembled directly by exploiting their high affinity toward functional groups, especially thiols or to a lesser extend amines. Rigid or flexible bi-, tri-, or tetrafunctional linkers[171,172] are commonly applied; however, open questions still remain on the exact nature of the assembly process. These linkers are usually small compared with the particles making the attachment of several ends of one linker to one particle likely. Additionally, a defined end-to-end distance of the functional groups in the utilized molecule does not necessarily result in particle assemblies with the same distance as highlighted by Stemmler et al.[173] Owing to these facts, different kinds of architectures are hence obtained from the same type of molecules. A worthwhile approach is to construct molecules in a way that particles are forced into a defined distance. Lee and Scherman[174] employed cucurbit[5]uril to assemble gold nanoparticles. The molecule can be visualized as a nanosized 3D cage with each five carbonyl groups at the top and bottom of the cage. The so-obtained superstructures exhibit a defined interparticle distance. The rather low affinity of the oxygen to the gold surface makes these assemblies still somewhat fragile. However, sulfur analogs of this and similar compounds (like polysilsesquioxanes) could be promising tools to obtain stable structures.

The high affinity of gold toward thiols was also utilized by Xie et al.[175] for the synthesis of spherical clusters. At first, a highly branched amphiphilic polymer bearing acrylate groups was synthesized. Subsequent cross-linking with oligothiols by means of the thiol-ene reaction leads to the formation of polymer nanoparticles, which feature a functionalized surface with free thiol groups. Covalent bonding of gold nanoparticles to these moieties led to a coverage of the surface depending on the employed thiol, e.g., a tetrathiol yields a higher degree of coverage than a dithiol. Additionally, it is remarkable that the structure of the whole cluster could be tuned from spherical to wormlike by changing the overall concentration.

When working in aqueous solution, nanoparticles are mostly stabilized by electrostatic repulsion arising from surface bound molecules with the same charge. Especially variations in pH value or salt concentration modify these interactions and can, therefore, be utilized to assemble particles. Additionally, charged templates can be employed to synthesize defined structures.

Wang et al.[176] utilized pyrenecarbaldehyde nanorods as template, which are formed via π–π stacking of the aromatic molecules. The surface was positively charged through Schiff-base formation between polyallylamine and the free aldehyde groups with subsequent reduction of the imine. Addition of citrate-stabilized nanoparticles leads to the decoration of the rods. Also particles with positive charge could be assembled on the rods, due to the affinity of amine groups toward gold surfaces.

Synthesis of particle clusters via electrostatic interactions was achieved by Mühlig et al.[121] Using silica particles as a template, the surface was functionalized with an aminosilane rendering it positively charged. Negatively charged nanoparticles were then used to decorate the silica particles. UV–vis spectroscopy showed a redshift and broadening of the plasmon resonance compared with single gold particles. In accordance with simulations, the clusters revealed a magnetic dipole moment in the visible region (Figure 2).

The monodispersity and the ability to form superlattices in combination with charges located on their surfaces make proteins an excellent scaffold for nanostructures. Kostiainen et al.[182] took advantage of this fact by using cowpea chlorotic mottle viruses and ferritin as template. The authors could tune the charge of certain patches on the surface of the proteins by adapting the pH value. Self-assembly of positively charged gold nanoparticles only took place, when the pH value was above the isoelectric point as this renders the proteins to be negatively charged. In addition, the ionic strength had to be controlled to adjust the attraction between the two building blocks. In this way, superlattices with highly ordered nanoparticle structures could be obtained. Beyond that, the assembly is astonishing as it attains an AB_8^{fcc} structure, which was hitherto only known from large polymer nanoparticles.

Electrostatic interactions between polyelectrolytes can be used to coat nanoparticles with polymer shells. The layer-by-layer (LBL) approach in most cases applies spin-coating of alternating polycation and polyanion layers. Interactions of the polymers with charged nanoparticles can then guide the formation of plasmonic structures. The usefulness of this method lies in the possibility to easily cover large surface areas with nanoparticles.

Cunningham et al.[183] described the realization, characterization, and simulation of a large array of gold nanoparticles with a tunable distance. In the first step, a glass slide was coated with gold nanoparticles. Subsequently, alternating layers of oppositely charged polyelectrolytes were coated on top of the particles. Afterward, a second layer of gold particles was deposited onto the polymer. The optical properties of the superstructure could be tailored depending on the number of polyelectrolyte layers, which determine the distance between the particles. The resulting effects are particularly intriguing, when the same approach is applied to a structure where one of the layers consists of silver particles as the symmetry breaking leads to the formation of dark and bright eigenmodes.[121,184]

Part. Part. Syst. Charact. 2014,
DOI: 10.1002/ppsc.201300309

An innovative approach was introduced by Yoshida et al.,[185] which relies on the mechanical assembly of nanoparticle layers by utilizing Langmuir–Blodgett films. Oleylamine-capped gold particles were self-assembled at the air–water interface. The particle layer was compressed until it became one sheet, which, subsequently, was transferred to a silicon substrate. By repeating this process, multiple layers could be deposited on top of each other. It was found that an increase in the number of layers redshifted the absorption to the near infrared (NIR) due to electromagnetic coupling between the particles.

Not only chemical reactions can be used to assemble nanoparticles but it is also possible to utilize external stimuli such as light, temperature, and magnetic fields to trigger the formation of superstructures. Yan et al.[186] introduced photoswitchable DNA that can be employed to assemble (or disassemble) gold nanoparticles depending on the wavelength of the irradiated light. Azobenzene moieties within the DNA molecules were used as photosensitive units. Blue light leads to a *trans–cis* isomerization that initiates melting and, hence, hybridization of complementary DNA strands yielding nanoparticle assemblies. Disassembly is achieved by irradiation of UV light, which induces the reverse process.

Wu et al.[187] synthesized core–shell nanoparticle clusters with a thermoresponsive shell. Starting from silica nanoparticles, a shell of poly(*N*-isopropylacrylamide) (PNIPAM) was grown from the surface. PNIPAM is well-known for its lower critical solution temperature that leads to a collapse of the polymer strand in solution if heated above a certain temperature. The surface of the shell was then functionalized with 1,2-dithiolane moieties on which gold nanoparticles were attached. The so-obtained clusters showed a tunable surface plasmon resonance as "breathing" induced by cooling or heating lead to a temperature-dependent distance between the particles.

Composite particles from iron oxide and gold allow the implementation of a unique self-assembly method based on magnetic fields. Kim et al.[188] demonstrated the synthesis of Fe_3O_4–SiO_2–Au core–shell–shell particles. In the first step, the magnetic core is prepared whereupon a silica shell is grown. Gold nanoparticles are deposited on the silica layer, which are then grown to form a gold shell. Upon application of an external magnetic field, the particles assemble along the field lines to form 1D nanochains. The orientation of the chains changes with the orientation of the field and, remarkably, even upright standing assemblies can be obtained.

Sánchez-Iglesias et al.[181] succeeded in the reversible formation of gold nanoparticle clusters by hydrophobic interactions. Gold particles were functionalized with polystyrene thiol in tetrahydrofuran. Addition of a non-solvent leads to the formation of completely flat spherical clusters, the assembly process could be stopped by addition of a poly(styrene)-*block*-poly(acrylic acid) (PS-*b*-PAA) BCP. This also causes a rearrangement to a 3D spherical structure and stabilization in water due to the polar PAA block. Tailor-made optical properties could be obtained by tuning the PS-thiol length, which influences the interparticle distance as well as the filling factor and the cluster diameter.

BCPs are a versatile tool for the fabrication of nanomaterials as they offer a multitude of possibilities to guide the assembly of nanoparticles.[189,190] Their flexibility allows the creation of fascinating plasmonic structures. In solution, they are able to form micelles or vesicles, while in the solid state phase, separation of the blocks can generate hexagonal, lamellar, or gyroid nanostructures on large surface areas. In most cases, BCP films are spin-coated and, afterward, annealed thermally or by solvent vapor to obtain the desired phase separation.

Incorporation of plasmonic nanoparticles into the phases can be accomplished by three ways: 1) The nanostructure is formed and already synthesized nanoparticles are incorporated preferably in one phase by capillary forces or electrostatic interactions, 2) nanoparticles and the BCP are mixed with subsequent spin-coating and annealing or 3) metal salts are mixed with the BCP and particles are synthesized within the polymer film.

Synthesis within the BCP film has the disadvantage that only spherical particles can be obtained. Both other approaches allow also the incorporation of other particle structures. Liu et al.[177] prepared poly(styrene)-*block*-poly(methylmethacrylate) (PS-*b*-PMMA) BCP films with a lamellar orientation. Afterwards, the PMMA phase was oxidized, thereby, creating deep valleys between the PS phases. Gold nanorods were deposited by capillary forces. Depending on the block lengths of the utilized BCPs, the assembly could be tuned from a side-by-side fashion to linear nanowire-like structures.

Premixing of BCPs with nanoparticles and successful phase separation is often difficult to accomplish due to macroscopic separation. Functionalization of the particle surface with one of the blocks attenuates this problem; however, it is still entropically disfavored and, hence, only applicable for low particle fractions. Jang et al.[178] sought to tackle this problem by stabilizing the superstructure through hydrogen bonds. Gold nanoparticles functionalized with a poly(styrene)-*block*-polyvinylphenol) BCP were mixed with a poly(styrene)-*block*-poly(2-vinylpyridine) BCP. The authors could show that hydrogen bonding between the phenol and pyridine units makes volume fractions of nanoparticles larger than 50% possible. Interestingly, the form of the superstructure was not only influenced by annealing but also by the amount of particles resulting in a hexagonal structure for low loads and a cylindrical structure for high loads.

Amphiphiles possess a hydrophilic and hydrophobic end, which enable them to form vesicles or micelles in solution. If colloids are attached to one of their ends, self-assembly can guide the formation of plasmonic superstructures. He et al.[179] introduced gold nanoparticles tethered with a poly(ethylene oxide)-*block*–poly(styrene) amphiphilic BCP, which assemble into spherical- or tubular-like clusters depending on the nanoparticle size or the BCP molar mass. Electromagnetic interactions between the particles could be tailored by decreasing the PS block length, which results in smaller interparticle distances.

BCP particles with distinct gold nanoparticle patches could be synthesized by Kim et al.[180] A poly(styrene)-*block*-poly(4-vinylpyridine) BCP particle can be envisioned as an arrangement of P4VP spheres separated by polystyrene. Addition of $HAuCl_4$ leads to a loading of the P4VP moieties. However, only units on the outer surface of the particles are loaded as the gold precursor cannot penetrate the PS layer. For small polymer particles, reduction of the incorporated gold ions led to patches of gold particles on the surface, whereas for particles larger than 800 nm, fingerprint-like gold structures were obtained.

Up to this point, the creation of plasmonic structures relied on preformed nanoparticles, which form assemblies under

different kinds of stimuli or already formed superstructures in which particles were synthesized. A much less investigated field is the concomitant synthesis and arrangement of particles.

The formation of hollow spherical nanoparticle clusters was achieved by Song et al.[191] utilizing a specifically designed gold-binding peptide. In the presence of a reducing agent, gold ions are reduced to 8 nm nanoparticles, subsequently, the peptide takes over, binds to the gold surface, and attracts more nanoparticles. In the first stage, nanoparticle islands are formed that create clusters less than 100 nm in size over the course of the reaction.

Liang et al.[192] were able to synthesize gold particle cluster by means of an amino-substituted calix[6]biscrown. Protonation of the amino groups by $HAuCl_4$ and the solvent mixture drives the formation of vesicles. At the same time, the incorporated gold ions are reduced to nanoparticles. Interestingly, this approach is applicable for a variety of metal precursors and, e.g., also silver or platinum particle clusters could be synthesized.

4.2. "Top-up" Assembly of Plasmonic Nanoparticles

"Top-up" methods involve different approaches to create nanoparticle assemblies by mechanical manipulation of already synthesized particles or by combining these particles with other preformed superstructures. While a common drawback is the longer fabrication of the superstructures, the top-up approach allows the fabrication of unprecedented plasmonic structures that are neither available by top-down nor bottom-up technologies. A tremendous advantage is also the possibility to create nanostructures on a large area, which is a requirement for real-world applications.

Efforts by Pazos-Pérez et al.[193] resulted in highly uniform nanoparticle arrays by drying a gold colloid solution in small grooves of a polymer stamp. At first, a polydimethylsiloxane sheet is stretched and the top layer is oxidized to SiO_2. Upon relaxing the substrate to its original size, it forms wrinkles. A gold particle solution was then dropped on a glass slide and the stamp placed onto the glass. Drying of the solution and removal of the stamp yielded highly ordered lines of nanoparticles whose line width and interline distance could be controlled by the type of stamp fabricated.

Optical properties of nanoparticle assemblies are highly dependent on their number and their arrangement to each other. While clusters of dozens or hundreds of nanoparticles are relatively easy to synthesize, it is much more complicated to assemble a distinct number of particles with a precise geometry.

Yan et al.[194] succeeded in the formation and optical investigation of clusters with a defined number of particles. A PMMA-covered indium tin oxide (ITO) substrate was patterned by electron beam lithography to yield spherical cavities whose diameters were controlled by the size of the electron beam. The patterns were functionalized with a thiol, which allowed binding of gold nanoparticles. Depending on the size, only one to seven particles could enter the cavities and, additionally, they were forced to attain a distinct geometry. It is worth mentioning here that it was also possible to control the angle between particles, e.g., a trimer could be tuned from a linear chain, to intermediate structures and finally a triangular form.

Gwo et al.[195] manipulated single particles into ordered arrays. Utilizing different kinds of nanoparticle shapes in combination with a nanomanipulator allowed the precise arrangement of, e.g., nanoprisms from tip-to-tip toward a side-by-side fashion. Plasmonic nanoantenna arrays with different lengths were obtained by placing nanocubes of different number and different interparticle distance next to each other. Fascinatingly, this technology also allows the formation of 3D structures like nanopyramids. However, fabrication times are very long.

Scanning probe lithography (SPL) was employed by Holzner et al.[196] to "write" nanostructures into a poly(phthalaldehyde) film. Heating the tip to 350 °C and scanning of the film lead to the removal of the polymer at the probed sites. A solution of gold nanorods was then dropped on the substrate and by capillary forces, the particles entered the inscribed grooves. The geometrical arrangement was controlled by the formed superstructure, while the orientation of the rods to each other is highly dependent on the width of the grooves.

Yang et al.[197] used SPL to locally oxidize the self-assembled monolayer (SAM) of an alkylsilane on an ITO substrate. The probed sites are devoid of alkyl chains and were subsequently functionalized with amino groups. The substrate was immersed in a solution of citrate-stabilized gold nanoparticles and the electrostatic interactions with the positively charged amino groups caused a selective deposition of particles. By this means, long parallel lines of nanoparticles were obtained. When the particles were functionalized afterward with dodecanethiol and immersed again in the solution, further particles arranged around the initial ones thus creating broader lines.

Charged particle beams are another method to pattern surfaces in a way that electrostatic interactions guide the deposition of particles. However, Kolibal et al.[198] revised the view that the particle beam leads to subsurface charging. Instead, the authors propose a mechanism, which is based on the alteration of the surface chemistry. SAM-functionalized silicon substrates were irradiated with ion or electron beams and gold nanoparticles could be attached either to the irradiated or the non-irradiated sites. The origin of this feature is independent of the beam charge as both beams cause an oxidation of the exposed sites for low exposure doses. In contrast, high exposure doses cause a deposition of hydrophobic fluorine compounds from destruction of the SAM, thus preventing nanoparticle absorption.

A fascinating approach was explored by Kuemin et al.[199] Brownian motion of nanorods in solution leads to all kinds of orientations. However, if a solution is placed on a substrate and heated slightly, the convective force drives the rods to the air–water–substrate interface thereby locally increasing the rod concentration. Upon further heating parallel rows of nanorods are formed at the boundary of the drop. The solution was then moved across a template with nanoscale holes leading to the ordered deposition of rods in the cavities due to capillary forces. The orientation of the rods depends on the movement of the droplet, changing it from left to right to up and down changes equally the angle of the rods by 90°. In this manner also substrates with a defined mixed orientation of the rods could be obtained.

This section has given a brief overview about a multitude of synthetic strategies to create plasmonic nanoparticle superstructures. In many cases, the size and morphology of the

DOI: 10.1002/ppsc.201300309

individual nanoparticles have to be tuned in order to obtain a desired optical response of the final assembly. This requires both high-purity samples of the initial single particles as well as the obtained superstructure. In addition, the increased complexity of the assemblies requires sophisticated characterization methods.

5. Separation and Characterization of Plasmonic Nanoparticles

Despite continuous efforts to synthesize nanoparticles or their assemblies with defined size, shape, or structure, many procedures still remain challenging in a way that polydisperse samples, concomitantly present particle shapes or differently assembled nanostructures, can be obtained. However, for optical analysis and practical applications, it is highly desirable to obtain pure materials. Direct analysis of such heterogeneous samples via UV–vis spectroscopy or transmission electron microscopy (TEM) can certainly indicate that a desired structure is present, but it is hard to exactly quantify their occurrence and their optical properties. Therefore, it is crucial to include separation steps in order to purify particles and assemblies. Once separation has been accomplished a more profound structural and optical characterization can be performed.

In this section, we shortly introduce the separation technologies commonly utilized for plasmonic nanoparticles and assemblies as well as analytical methods for their characterization beyond standard UV–vis spectroscopy or TEM imaging.

5.1. Separation Techniques for Plasmonic Particles

Density gradient centrifugation is a powerful technique that employs a vial with a continuously changing density of the liquid phase within. Application of a centrifugal field leads to separation of particles in different layers. This method is particularly attractive as it allows preparative separation of particles as well as analytical determination of particle shapes and size distributions.

Pazos-Perez et al.[200] synthesized clusters from two to seven gold particles by emulsification of the particles in the presence of a BCP and toluene (**Figure 6**). The particles arranged around the solvent droplets and assembled into defined geometries upon slow evaporation of the solvent. Separation of the clusters was achieved by centrifugation in a glycerol/water gradient. For clusters of five to seven particles, only a mixed fraction could be obtained due to their similar density; however, distinct bands formed for the smaller clusters, which could be successfully isolated.

Steinigeweg et al.[201] explored the separation of gold nanoparticles from 20 to 250 nm in diameter. While aqueous CsCl gradients led to severe aggregation, a water/glycerol gradient was used to separate mixtures of nanoparticles. An important feature found was the size difference between the particles. The authors could show that for small particles (≪50 nm), separation is possible for a size difference of 10 nm between the particles, whereas for large particles, the size difference needs to be larger than 50 nm in order to obtain an efficient separation.

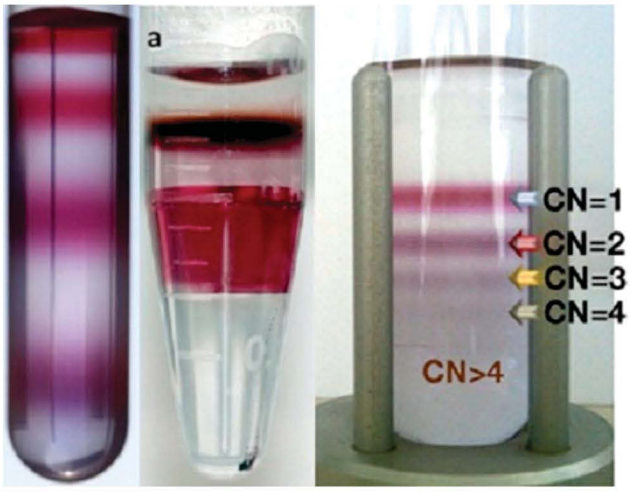

Figure 6. Separation of spherical gold nanoparticles according to their size via centrifugation in a density gradient (left). Image reproduced with permission.[201] Separation of gold nanorods from spheres via centrifugation in a multiphase aqueous system (middle). Image reproduced with permission.[202] Copyright 2012, ACS. Separation of gold nanoparticle clusters according to their cluster number via centrifugation in a density gradient (right). Image reproduced with permission.[200]

Akbulut et al.[202] recently introduced a new centrifugation approach based on aqueous multiphase systems. Instead of a solution of one compound with a gradient concentration, the system relies on stacked solutions of different components. This setup is remarkable as, in comparison to density gradient centrifugation, the phases are thermodynamically stable and do not mix upon standing, therefore such gradients are long-term storable. If mixed manually, they separate again after centrifugation and the distinct phase separation makes the sample collection more feasible. In this way, the authors could easily separate nanospheres from rods and larger particles in a three-phase system were each of the fractions separated in one of the phases.

Selective precipitation utilizes the addition of salts or surfactants to nanoparticle solutions to induce flocculation of distinct species depending on their shape or size. Up to now, this methodology has been only applied to particles but its attractiveness lies in fact that it enables separation of particles on a preparative scale.

Guo et al.[203] targeted the seeded growth of nanoparticles in order to obtain rods or prisms, however, in each case a large proportion of the samples still contained sphere-like particles (**Figure 7**). Electrostatic repulsion between the particles keeps them well dispersed but upon addition of NaCl, the screening is reduced with concomitant precipitation of the particles. By subtle adjustment of the salt concentration, it was possible to separate rods and prisms in high purity. A striking fact is that the isotropic particles remain in the supernatant solution. The authors proposed a mechanism based on interfacial interactions. Isotropic particles exhibit a high curvature, which minimizes the contact area to other particles. In contrast, rods offer a long side and prisms a large facet, which increases interactions between these structures.

The influence of the surfactant concentration on the shape separation of plasmonic nanoparticles was first already noted

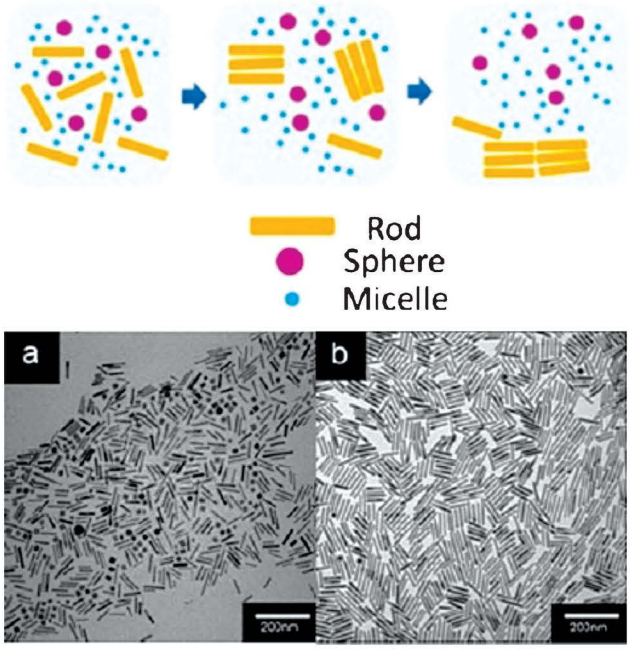

Figure 7. Mechanism for the separation of nanoparticles via depletion-induced precipitation (top). TEM images of a mixture of nanorods and spheres (bottom left) and the separated rods (bottom right). Images reproduced with permission.[205] Copyright 2012, ACS.

by Jana.[204] Park et al.[205] sought to clarify this role and proposed a mechanism based on depletion-induced separation.[206] Imagine a solution containing two colloids, e.g., gold particles and micelles, the micelles being in excess and the separation distance between the colloids is smaller than the micelle size. In such a system, an attractive force is induced between the gold particles by a local concentration gradient induced by exclusion of the micelles between the particles. Each particle shape and size features its own critical micelle concentration, which keeps one type in solution, whereas another type precipitates. The authors could demonstrate this principle by separating a mixture of cubes and rods. The precipitated rods could be easily redispersed by addition of water, which decreases the micelle concentration.

Asymmetric flow field-flow fractionation (AF4) is based on the particle separation in a cross flow. In a channel, a horizontal flow of particles in a liquid medium is distracted by a second flow arising from small holes in the bottom of the channel. During the passage, small particles remain in the middle of the flow, whereas larger particles are directed downward and, hence, move more slowly through the channel. By this means, small nanoparticles are collected first. The method allows both separation of particles and analysis of particle sizes, if calibrated. However, it is limited mostly to analytical separations as the high dilution during the flow limits preparative applications.

Tsai et al.[207] synthesized gold nanoparticle clusters by salt-induced electrostatic assembly. Utilizing AF4, the superstructures could be successfully separated into distinct assemblies of two to five particles. The separation was furthermore proven by scanning electron microscopy and UV–vis spectroscopy, which showed additional plasmon modes resulting from the assemblies.

Dynamic light scattering (DLS) is intrinsically biased toward larger particles, Calzolai et al.[208] demonstrated the analysis of a 1:1:1 mixture of 5, 15, and 45 nm particles by separation via AF4. While normal DLS measurement would show only particles of 45 nm diameter with a relative high size distribution, the AF4 analysis clearly showed the presence of distinct subfractions and their respective quantity.

Electrophoresis involves the separation of molecules or particles according to their charge, size, and shape under an external electrical field. This method is mostly applied for the separation of particles functionalized with biomacromolecules like DNA. In order to synthesize assemblies, it is a prerequisite to separate functionalized particles from unfunctionalized ones.

Wen et al.[209] prepared DNA-functionalized nanoparticles but in order to separate them, elongation of the DNA was necessary to achieve a high resolution. After separation, the extension was cleaved off, followed by hybridization and particle dimers as well as tetramers with different shapes and particle sizes could be obtained. The crude mixture was again purified by electrophoresis as single particles showed a significantly different migration behavior than assemblies.

Zhou and co-workers[210] synthesized a mixture of spherical gold nanoparticles and nanoplates with a large size polydispersity. By first applying density gradient centrifugation, they were only able to narrow down the size distribution; however, the fractions still contained a mixture of particle types. Therefore, agarose gel electrophoresis was utilized to separate the fractions obtained via centrifugation. In this way, it was possible to separate spherical particles from plates. The process could easily be monitored by the naked eye due to the large differences in absorbance of the particles.

Size exclusion chromatography (SEC) relies on the flow of macromolecules or particles in solution through a column packed with a stationary phase of porous beads. Small particles continuously enter and exit the pores, while larger particles can only enter the larger pores and, hence, flow faster through the column and elute first. By this method, it is possible to separate different particle sizes, shapes, and assemblies. When calibrated with samples of known composition, it can also be used as a fast method of quality control.

SEC was used by Liu[211] to investigate size variations in microwave-synthesized gold nanoparticles. The method was validated by measuring five times samples of gold nanoparticles with 12, 21, 40, and 60 nm diameter. The elution volume shifted to higher values with decreasing particle size and the standard deviations were well below 0.3% indicating a high reproducibility. The calibration could then be used to monitor the effect of different temperatures and additives on the nanoparticle size.

5.2. Characterization Tools for Plasmonic Nanoparticle Analysis

TEM is generally not a method to quantitatively evaluate the bulk composition of a nanoparticle sample. However, statistical evaluation of a larger number of particles or clusters can provide very good estimations of the size distribution and the

abundance of certain shapes. Hence, TEM is probably the method that provides the most information about a sample. Small changes in reaction conditions can have a large impact on the particle shape or size. However, sample preparation is time consuming, drying effects can additionally lead to artifacts, and eventually the method is rather expensive compared with other techniques. While it is easy to synthesize a large number of different samples, fast and reliable methods are urgently required for high-throughput analysis of plasmonic nanoparticles.

Light scattering measurements are commonly applied for spherical particles. The principle can, however, also be used to characterize anisotropic colloids as shown by Antoniou et al.[212] The authors applied polarized and depolarized dynamic (DLS) and static light scattering (SLS) for the analysis of silver nanoprisms. Determination of the radius of gyration by SLS fit well with the one obtained by TEM measurements. Particle anisotropy was determined via polarized DLS as in contrast to spherical particles a second contribution arises from different orientations. However, it was not possible to determine the exact shape and also the polydispersity of the sample made a quantitative analysis difficult.

An innovative method to counteract these limitations was introduced by Reddy et al.[213] Particle movement was controlled by a flow field and time-dependent optical measurements were conducted. A tumbling motion can be observed for anisotropic particles. By determining the orientation distribution function, the aspect ratio can be calculated. The oscillatory function is dampened when different sizes or shapes are present and, as a consequence, can be used as an indicator for the polydispersity. The aspect ratios could be determined for different samples of gold nanorods and dodecahedrons and the so-obtained values correlated well with those obtained via TEM. Flow dichroism is especially attractive for plasmonic particles as a strong absorption and scattering is a requirement for successful measurements.

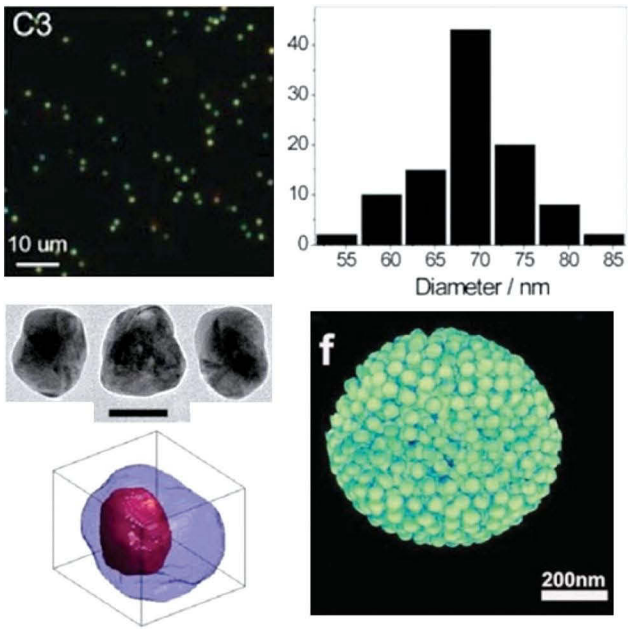

Figure 8. Dark-field microscopy image and derived size distribution of gold nanoparticles (top). Image reproduced with permission. [214] 2012, ACS. Reconstruction of a core–shell gold–silver nanoparticle via electron tomography (bottom left, scale bar = 50 nm). Image reproduced with permission.[215] Copyright 2012, ACS. Reconstruction of a cluster of gold nanoparticles via incoherent bright-field STEM (bottom right). Image reproduced with permission.[216]

The principle of dark-field microscopy involves the capturing of scattered light from a sample. In contrast to the bright-field mode, the light used to illuminate the sample is irradiated in a way that it does not reach the collecting objective directly. Hence, the background of the image is black, whereas the light scattered from the particle is collected and gives bright colors.

The color, i.e., the scattered light of plasmonic nanoparticles in a dark-field image, depends on their size and shape. Jing et al.[214] were able to utilize this technique to determine the size of spherical particles without electron microscopy (**Figure 8**). The color of the particles could be converted into the red, green, and blue values, which reflect both a certain wavelength and intensity of light. In this way, the picture of a particle can be converted into a scattering spectrum. By applying the Mie theory, it was now possible to calculate the particle size from the spectra. Additionally, also changes of the surrounding medium could be determined. The method was employed to particles of 52, 59, and 70 nm in size and showed good correlations with sizes as extracted from TEM images by an error of less than 5 nm. Moreover, by virtue of measuring times of less than 600 ms, it can also be applied to real-time measurements in, e.g., biological tissues.

In a similar way, this technology can also be applied to ascertain the orientation of plasmonic particles as shown by Biswas et al.[217] Nanorods exhibit both a longitudinal and transversal surface plasmon resonance. Therefore, the scattering of the particles depends on the polarization of the irradiated light. The angle-dependent color change could then be used to determine the orientation of the rods with a resolution of 2.3°.

A major limitation of standard TEM imaging regarding particle analysis is the 2D projection of a 3D material, which can lead to a significant information loss. This is especially critical for core–shell particles or clusters as the highly electron scattering plasmonic metal prevents to elucidate the internal structure or spatial arrangement of the particles. Electron tomography is an excellent method to counteract these issues. Additionally, it can provide detailed insights into the crystal structure of metal particles with unprecedented resolutions.

The correlation between the internal structure and the plasmonic response of core–shell gold–silver particles was investigated by Chuntonov et al.[215] Electron tomography was performed by conducting a tilt series from +70° to –70° in steps of 3°. Subsequently, an iterative alignment algorithm was applied that uses translational displacements of each image of the series to reconstruct a trial tomogram. The contrast can be used as a figure-of-merit and through maximizing this number the alignment of the single pictures can be optimized to calculate the final tomogram. Electron tomography revealed a variation of up to 20% in one batch for the volume fractions of gold as well as silver and deviations compared with normal TEM reached 100% for small cores. Additionally, sometimes large deviations from a spherical structure were found. Single-particle dark-field spectroscopy of particles with different core–shell sizes was conducted to obtain the plasmon spectra, which showed a

good correlation with the simulated ones. However, the authors could demonstrate that the optical response depends merely on the size of the core and the shell than on their shape or position to each other.

Goris et al.[218] shed light on the nature of gold nanorods that are not a definite particle type itself but can contain different crystal structures depending on the growth conditions. HAADF-STEM was utilized to obtain high resolution images of rods grown in the presence of CTAB or a gemini surfactant, which already revealed a different structure. To reconstruct the 3D structure of the rods, just four images were required taken along different zone axes of the rods. In this way, the index of the different facets could be clearly assessed. The already reported {100}, {110} plane structure for rods grown in the presence of CTAB was confirmed, whereas for rods with the gemini surfactant, a {520} structure was determined.

Standard HAADF-STEM measurements are sufficient to determine the structure of nanoparticle clusters for rather small sizes, however, artifacts occur, which increase with increasing cluster size or atomic number. The cupping artifact arises from higher multiple and back scattering for large assemblies resulting in an underestimation of the intensity in the center of the cluster. Incoherent bright-field STEM was utilized by Altantzis et al.,[216] which depends on the thickness of the sample. While this gave better results, the method still suffers from the same artifact. However, by additionally applying the total variation minimization algorithm, the authors could successfully reconstruct the 3D structure of a 670-nm-sized cluster consisting of 40-nm gold nanoparticles.

This section introduced strategies to separate and characterize plasmonic nanoparticles as well as their assemblies. Further advances in this field can contribute not only to the characterization of the final structure but also to the understanding of the underlying mechanisms, which are responsible for their formation. Rapid techniques could, e.g., allow for the visualization of how asymmetry is introduced during the development of small seeds to larger particles or overall increase the throughput for screening different reaction parameters.

6. Potential Applications of Plasmonic Nanoparticles

The unique properties of plasmonic nanoparticles pave the way for a myriad of potential optical, analytical, and medical applications. In many cases, it is only the combination of their optical properties and the "nano" feature, which enables a certain functionality. While applications of gold or silver particles, e.g., for SERS measurements are well known, other fields have begun to receive increasing attention in recent years. Additionally, up to now, many applications with great potential still exist only in theory and simulations. However, some of the base materials or methods are already known and have just to be employed or combined for the proof-of-concept. In this section, we discuss already realized as well as potential applications of plasmonic particles and their assemblies.

The pivotal point in SERS measurements is electromagnetic field enhancements generated close to metal surfaces, which provide large signal intensities. To achieve resolutions down to the single-molecule level, even larger enhancements are required. This can be accomplished by hot spots formed in metal clusters since the field intensity is maximized in the gap between the particles.

Cho et al.[219] were able to fabricate highly reproducible SERS substrates from a PS-*b*-P4VP BCP. Silver nitrate was complexated in the polymer micelles, which subsequently were spin-casted on a silicon substrate and silver nanoparticles were formed by UV irradiation. In this way, an ordered array of nanoparticles was formed. The distance between the particles was influenced by adjusting the PS block length whereby reducing the length created more narrow arrays. By means of the shortest block enhancement factors of up to 10^8 could be achieved on a large area. A critical gap distance of 10 nm was identified for silver nanoparticles, which increased up to 20 nm for clusters.

DNA-based self-assembly was utilized by Zheng et al.[220] to create SERS substrates (**Figure 9**). In the first step, DNA-conjugated gold nanoparticles were absorbed on an amino-functionalized glass slide. Subsequently, complementary particles were added, thereby creating gold satellite structures with defined interparticle distance. Benzene thiol was employed as the reporter molecule and the highest signal intensity was achieved with irradiation at 782 nm, which enabled a detection limit down to 1×10^{-9} M.

Photothermal therapy is a method that utilizes thermal energy created by irradiation of light to induce the death of cancer cells. NIR light is required to reach deep tissues as it is not absorbed by water or tissue, a phenomenon known as the NIR window. NIR dyes can be generally used as absorbers. However, they suffer from low cross sections and photobleaching. Gold nanoparticles do not feature these disadvantages. In contrast, they are highly stable and their surface plasmon resonance can be tuned to fit well with the NIR window. Furthermore, resulting from their small size, they are enriched in cancer cells due to the enhanced permeability and retention effect. They can additionally be loaded with drugs or functionalized with biomolecules to increase cancer cell targeting.

Wang et al.[221] investigated the potential of gold nanohexapods, nanorods and nanocages for photothermal therapy (**Figure 10**). Each of the structures was synthesized in a way that the LSPR was approximately at 800 nm. At first, samples were irradiated with a NIR laser in aqueous solution, which resulted in temperatures between 45 and 50 °C. A control solution with only water stayed almost constant at room temperature when irradiated in the same way. Cell viability was excellent for all structures except gold nanorods at high concentrations independent on the stabilizing ligand (polyethylene glycol or CTAB). Biodistribution in mice over 7 d revealed an enrichment of the particles in liver, spleen, and tumor tissue. Intravenous injection of the solutions followed by irradiation showed a strong temperature increase at the tumor site and a reduction of tumor metabolism by 80%–90% could be achieved.

Gold–silica core–shell nanoparticles were utilized by Day et al.[222] for the treatment of glioma. The particles were conjugated with the vascular endothelial growth factor (VEGF) for enhanced tumor targeting. In comparison to the same particles coated with PEG, the number of VEGF particles was doubled in

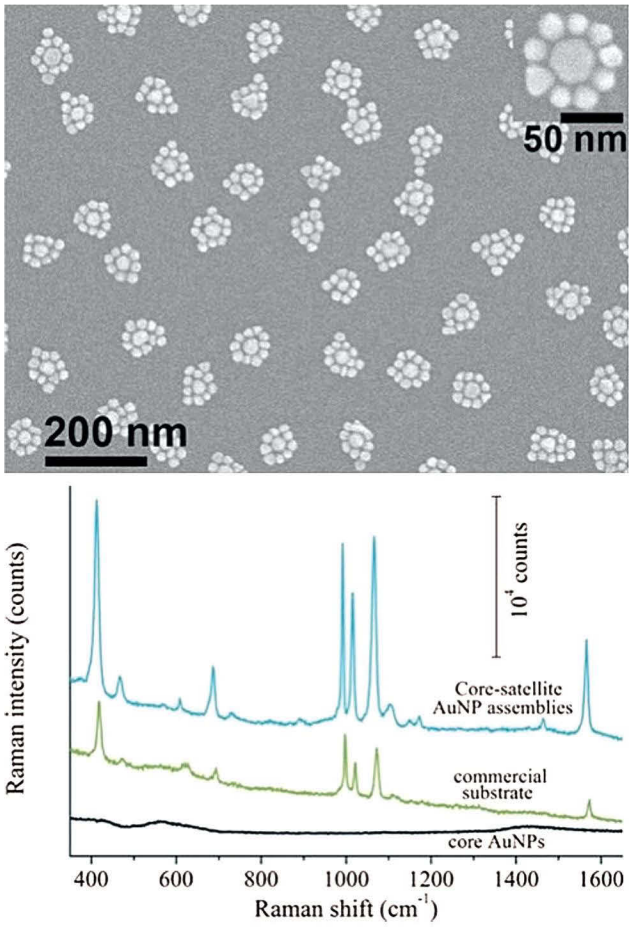

Figure 9. TEM image of satellite structures assembled via DNA (top). Comparison of the Raman intensity of single gold nanoparticles, a commercial substrate, and the satellite structures. Images reproduced with permission.[220]

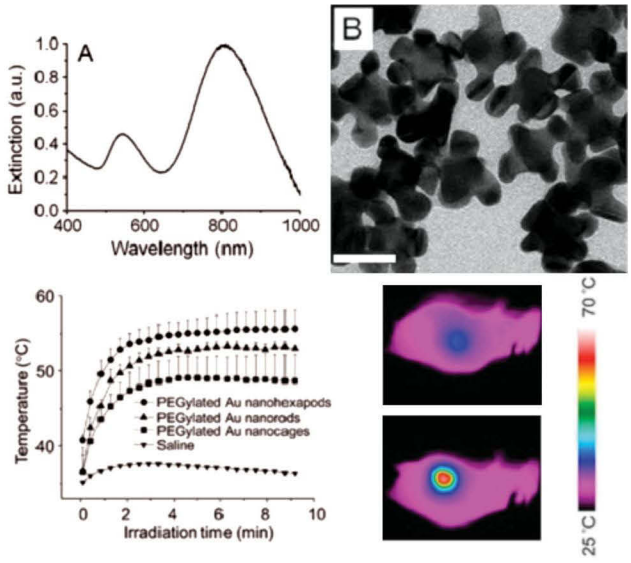

Figure 10. UV–vis spectra and corresponding TEM image of gold nanohexapods (top, scale bar = 50 nm). Thermography of tumor-bearing mice after irradiation with an NIR laser at different times (bottom left). Thermal images of mice treated with saline solution or gold nanohexapods irradiated with a NIR laser (bottom right). Images reproduced with permission.[221] Copyright 2013, ACS.

vivo in tumor tissue. The authors could demonstrate that upon NIR laser irradiation, the tumor vasculature was destroyed in the presence of the particles, whereas pure saline solution showed no effect. Additionally, in both cases the brain function of the mice stayed intact. How well advanced this field is can also be reflected by the fact that first human trials are currently in progress for the treatment of head and neck cancer with the same particle type.[223]

Solar power is probably one of the key energy technologies for the twenty-first century. Ongoing research leads to increasing efficiencies of solar cells and new materials like organic compounds for light harvesting were introduced in recent years. Crucial points are not only absorption and charge generation behavior but also the price and abundance of the utilized raw materials such as indium. Plasmonic nanoparticles can overcome some of these issues, e.g., a monolayer of these particles on top of a solar cell can increase the absorption by coupling light into the cell and trapping of light by backscattering into the active layer. If embedded in the active layer itself, the particles can increase locally the charge generation by their high absorption cross section.[12,224]

Plasmonic particle-enhanced thin film silicon solar cells were created by Chen et al.[225] The authors tailored the silver particles to increase the scattering and to minimize at the same time their absorption. The final shape can be ideally visualized as a large particle onto which small half spheres of other particles are attached. The particles were deposited on a dielectric layer on top of the silicon substrate. A surface coverage from 5% to 20% was utilized; however, the best values were obtained at a coverage of 10% and for a nanoparticle size of 200 nm. A significant increase of the short-circuit current and the external quantum efficiency could be determined, resulting in an overall relative increase of the power conversion efficiency of 23%.

Parlak et al.[226] demonstrated the versatility of plasmonic enhancement by incorporation of silver nanoparticles into the active layer of an organic solar cell. Hexadecylamine-capped particles were mixed with a poly(2,7-carbazole-*alt*-dithienylbenzothiadiazole)/phenyl-C_{61}-butyric acid methylester solution solution and bulk heterojunction devices were fabricated with a 0.4% and 0.7% mass fraction of silver. With increasing mass fraction of silver, the short-circuit currents, open-circuit voltages, and power conversion efficiencies increased. Overall, an efficiency of 1.72 % could be achieved, which was almost threefold the value of the cells without nanoparticles.

The potential of plasmonic particles to function as superabsorbers was investigated by Yannopapas and Psarobas.[227] A square and hexagonal arrangement of gold nanochains was chosen to simulate the effect of the chain length on the absorption properties. Averaged over all incident angles and polarization modes, a particle radius of 3.3 nm and a layer number of 256 resulted in an absorption of 79% in the visible regime. While this gray body yet only exists in theory, similar structures have been realized by gold particles coated with mesogens.[228] The critical points in this development to be accomplished are an increased particle size and higher layer thicknesses.

Cloaking is certainly the most fascinating property of metamaterials enabling techniques like stealth devices. This has already been realized for the microwave[229] and NIR[230] region but invisibility to the human eyes via plasmonic cloaking could not be realized up to know. The biggest hurdle is the minimization of the devices as with decreasing wavelength, the size of the subunits (meta-atoms) has to be decreased as well, reaching down to the nanometer scale for cloaking in the visible region. Plasmonic nanoparticles could be an excellent base material for their final realization.

A cloak based on a spherical shell composed of gold nanoparticles surrounding a large dielectric sphere was proposed by Mühlig et al.[97] The envisioned material relies on scattering cancellation where destructive interference of the scattering signal from the core material with the signal from the shell enables the cloaking properties. The shell can be visualized in this case as an effective medium and the cloaking effect was investigated for a core size of 70 nm and a filling factor of 34% of the 10 nm gold particles. It could be demonstrated that a scattering signal reduction of up to 70% can be accomplished by this setup.

Monti et al.[231] explored the cloaking potential of silica–silver core–shell particles. A column-shaped periodical array of the particles surrounding a dielectric cylinder was used as effective medium and a scattering reduction of 6 dB at approximately 400 nm was achieved. Moreover, while such simulated perfect arrays are hard to accomplish via self-assembly, the authors could also show that perturbations of the superstructure have negligible effects as long as it remains a homogenous medium.

Chiral metamaterials are an additional approach to create materials with a negative refractive index by means of their large optical activity.[128] The materials investigated by Droulias and Yannopapas[232] consists of twisted gold nanoparticle chains. Each meta-atom is composed of 11 chains of 10 nm gold particles, which form a 2D lattice. A large circular dichroism from 650 to 1000 nm could be demonstrated and, counter intuitively, as the underlying mechanism not the chiral meta-atom structure but the lattice parameter was disclosed. The realization of such materials can eventually be accomplished with the help of liquid crystals. Furthermore, Hur et al.[233] could show that triblock copolymers enable chiral plasmonic structures, the pivotal role being the gyroid morphology, which forms upon self-assembly.

The destructive interference between a narrow and a broad resonance creates a phenomenon known as the Fano resonance. Due to large effects of the local environment or perturbations of the structure on the resonance, many potential sensing applications could be designed. Spherical plasmonic particles itself exhibit this feature owing to the dipole and quadrupole resonance, however, with only small intensities. In order to mitigate this, many approaches rely on split-ring resonators or other structures created by top-down approaches like electron-beam lithography. A bottom-up approach was introduced by Fan et al.[109] through the self-assembly of SiO_2–Au core–shell particles. Modification of the particles with a thiolated polymer was conducted to achieve a defined distance upon cluster formation, the latter being performed by drying of small droplets of the particle solution. Several structures, like dimers and trimers, were investigated but only symmetric flower-shaped heptamers showed the Fano resonance. This was evidenced by a strong dip in the scattering and extinction spectra at about 1450 nm and also confirmed by simulations.

Peña-Rodríguez et al.[234] were interested in a simplification of the method, as self-assembly always involves an additional reaction step and yields mixtures of clusters. The authors explored the potential of multilayered SiO_2–Au particles and could show that it is also possible to create Fano resonances with these structures. The most important feature was the thickness of the outer gold layer, which allows tuning of the resonance from 600 to 950 nm.

The equivalent of the laser in the field of plasmonics is the spaser (surface plasmon amplified stimulated emission of radiation), where surface plasmons instead of photons are emitted.[235] This tool creates local optical fields on the nanoscale, however, not necessarily with the emission of light, thus enabling extraordinary resolutions. Up to now, a pitfall for spaser realization is the loss from absorption.

This was overcome by synthesizing Au–SiO_2 core–shell particles with a dye-doped shell to introduce gain into the system.[157] Pumping at 488 nm showed a stimulated emission at 531 nm and the emission kinetics revealed a second peak as expected for a spaser. The most intriguing feature is certainly the light emission, rendering these particles the first laser working at visible frequencies on the nanoscale.

To further increase the spasing efficiency, a structure was proposed based on a silver semi-shell surrounding a silica particle with an optical gain material included.[236] It could be shown that the symmetry breaking leads to unidirectional emission with a power flow, which is one order of magnitude larger than for a full-shell system. Similar structures based on gold and without gain materials were recently realized.[237]

In this section, we have given an overview about the tremendous amount of potential applications facilitated by the field of plasmonic nanoparticles. It is already obvious that their tunable physical as well as physiological properties will have a significant impact on a broad range of research areas. It will be interesting to see in which way the current theoretical applications will be realized in the lab and how they are eventually transferred into real-world devices.

7. Conclusion and Outlook

In this review, we have introduced the basic principles to synthesize plasmonic nanoparticles and techniques to assemble them into well-defined superstructures. Moreover, strategies to obtain materials with a desired optical response were explored. We have presented a brief overview on analytical methods used for separation and characterization of nanoparticles. Finally, we have discussed a number of applications where plasmonic particles could already be utilized, e.g., as analytical devices or for medical therapy. Additionally, a vast number of theoretical applications yet remain to be realized albeit the base materials or assembly strategies already exist. In this respect, the collaboration of scientists is of vigorous importance as research on plasmonic nanoparticles has become a melting pot for physics, chemistry, and biology.

Part. Part. Syst. Charact. 2014,
DOI: 10.1002/ppsc.201300309

The exploding number of synthesizable particle structures makes a tremendous amount of superstructures possible. For the time being, it is obvious that most assembly methods utilize spherical gold particles and, to a smaller extent, nanorods. Other structures or assemblies of silver nanoparticles are scarce. In the case of silver, practical applications are mostly hampered by the degradation of the metal under ambient conditions. However, first strategies are being implemented to overcome this issue. The questions remains: is there something beyond these metals? In fact, an almost unexplored field exists with silicon[238] or metal oxides/nitrides[239,240] as novel base materials for plasmonic structures. This will result in new challenges to structure such particles but also offers more potential combinations and eventually lower cost devices.

In terms of assemblies, an interesting feature still in its infancy is the introduction of asymmetry. Janus or patchy particles are one possibility to implement such structures.[241,242] If the strategy to functionalize particles with a defined number of reactive groups can be extended to other complementary moieties, larger particles or different particle structures, another technique would become at hand. Such large "plasmonic molecules" in combination with protecting group chemistry could facilitate the creation fabrication of complex superstructures as equally their small counterparts do for organic chemistry. In particular, for metamaterial applications, a demanding task is the synthesis of 3D/bulk structures. Novel methods have to be developed as the fabrication of hundreds of layers with techniques such as LBL is a challenging endeavor.

The structural analysis of nanoparticles or their assemblies is still a bottleneck for the development of new structures. Heterogeneous samples cannot be characterized without TEM imaging and, in particular, 3D or quantitative analysis is a time-consuming task. Hence, there is a strong demand for high-throughput methods, which fit into this gap.

Fuelled by the tremendous development in this field, one can witness a growing number of potential applications some of which already hit the point where they can be transferred from the lab into real live. It is certainly unknown what novel properties and applications will be discovered, but it is doubtless that the field of plasmonic nanoparticles has an exciting future.

Acknowledgements

Financial support by the Federal Ministry of Education and Research (Spitzencluster PHONA) and from the State of Thuringia within the ProExcellence project MeMa is acknowledged.

Received: September 10, 2013
Revised: November 10, 2013
Published online:

[1] I. Freestone, N. Meeks, M. Sax, C. Higgitt, *Gold Bull.* **2007**, *40*, 270.
[2] L. B. Hunt, *Gold Bull.* **1976**, *9*, 134.
[3] J. Lafait, S. Berthier, C. Andraud, V. Reillon, J. Boulenguez, *C. R. Phys.* **2009**, *10*, 649.
[4] M. Faraday, *Phil. Trans. R. Soc. Lond.* **1857**, *147*, 145.
[5] J. C. M. Garnett, *Phil. Trans. R. Soc. Lond.* **1904**, *203*, 385.
[6] G. Mie, *Ann. Phys.* **1908**, *330*, 377.
[7] R. Ritchie, *Phys. Rev.* **1957**, *106*, 874.
[8] N. J. Halas, S. Lal, W. S. Chang, S. Link, P. Nordlander, *Chem. Rev.* **2011**, *111*, 3913.
[9] X. Huang, P. K. Jain, I. H. El-Sayed, M. A. El-Sayed, *Laser. Med. Sci.* **2008**, *23*, 217.
[10] T. L. Doane, C. Burda, *Chem. Soc. Rev.* **2012**, *41*, 2885.
[11] Y. Jin, *Adv. Mater.* **2012**, *24*, 5153.
[12] H. A. Atwater, A. Polman, *Nat. Mater.* **2010**, *9*, 205.
[13] Y. Liu, X. Zhang, *Chem. Soc. Rev.* **2011**, *40*, 2494.
[14] P. Y. Chen, J. Soric, A. Alu, *Adv. Mater.* **2012**, *24*, 281.
[15] A. Ben-Moshe, B. M. Maoz, A. O. Govorov, G. Markovich, *Chem. Soc. Rev.* **2013**, *42*, 7028.
[16] A. Guerrero-Martínez, J. L. Alonso-Gómez, B. Auguié, M. M. Cid, L. M. Liz-Marzán, *Nano Today* **2011**, *6*, 381.
[17] R. He, X. Qian, J. Yin, Z. Zhu, *J. Mater. Chem.* **2002**, *12*, 3783.
[18] D. K. Smith, B. A. Korgel, *Langmuir* **2008**, *24*, 644.
[19] I. Pastoriza-Santos, L. M. Liz-Marzán, *Adv. Funct. Mater.* **2009**, *19*, 679.
[20] M. Behera, S. Ram, *Int. Nano Lett.* **2013**, *3*, 17.
[21] Y. Borodko, S. E. Habas, M. Koebel, P. Yang, H. Frei, G. A. Somorjai, *J. Phys. Chem. B* **2006**, *110*, 23052.
[22] W. A. Al-Saidi, H. Feng, K. A. Fichthorn, *Nano Lett.* **2012**, *12*, 997.
[23] X. Xia, J. Zeng, L. K. Oetjen, Q. Li, Y. Xia, *J. Am. Chem. Soc.* **2012**, *134*, 1793.
[24] W. A. Saidi, H. Feng, K. A. Fichthorn, *J. Phys. Chem. C* **2013**, *117*, 1163.
[25] A. Kedia, P. S. Kumar, *J. Phys. Chem. C* **2012**, *116*, 23721.
[26] P. C. Angelomé, H. Heidari Mezerji, B. Goris, I. Pastoriza-Santos, J. Pérez-Juste, S. Bals, L. M. Liz-Marzán, *Chem. Mater.* **2012**, *24*, 1393.
[27] G. S. Métraux, C. A. Mirkin, *Adv. Mater.* **2005**, *17*, 412.
[28] Q. Zhang, N. Li, J. Goebl, Z. Lu, Y. Yin, *J. Am. Chem. Soc.* **2011**, *133*, 18931.
[29] N. G. Bastus, J. Comenge, V. Puntes, *Langmuir* **2011**, *27*, 11098.
[30] M. R. Langille, M. L. Personick, J. Zhang, C. A. Mirkin, *J. Am. Chem. Soc.* **2012**, *134*, 14542.
[31] X. Ye, L. Jin, H. Caglayan, J. Chen, G. Xing, C. Zheng, V. Doan-Nguyen, Y. Kang, N. Engheta, C. R. Kagan, C. B. Murray, *ACS Nano* **2012**, *6*, 2804.
[32] L. Vigderman, E. R. Zubarev, *Langmuir* **2012**, *28*, 9034.
[33] Z. Wang, L. Tang, L. H. Tan, J. Li, Y. Lu, *Angew. Chem Int. Ed.* **2012**, *51*, 9078.
[34] M. McEachran, D. Keogh, B. Pietrobon, N. Cathcart, I. Gourevich, N. Coombs, V. Kitaev, *J. Am. Chem. Soc.* **2011**, *133*, 8066.
[35] J. Turkevich, P. C. Stevenson, J. Hillier, *Discuss. Faraday Soc.* **1951**, *11*, 55.
[36] G. Frens, *Nature* **1973**, *241*, 20.
[37] K. R. Brown, D. G. Walter, M. J. Natan, *Chem. Mater.* **2000**, *12*, 306.
[38] N. R. Jana, L. Gearheart, C. J. Murphy, *Chem. Mater.* **2001**, *13*, 2313.
[39] A. M. Alkilany, C. J. Murphy, *J. Nanopart. Res.* **2010**, *12*, 2313.
[40] C. Ziegler, A. Eychmüller, *J. Phys. Chem. C* **2011**, *115*, 4502.
[41] X. Liu, H. Xu, H. Xia, D. Wang, *Langmuir* **2012**, *28*, 13720.
[42] M. Eguchi, D. Mitsui, H. L. Wu, R. Sato, T. Teranishi, *Langmuir* **2012**, *28*, 9021.
[43] H. L. Wu, C. H. Kuo, M. H. Huang, *Langmuir* **2010**, *26*, 12307.
[44] A. M. Alkilany, L. B. Thompson, S. P. Boulos, P. N. Sisco, C. J. Murphy, *Adv. Drug Delivery Rev.* **2012**, *64*, 190.
[45] T. Wen, Z. Hu, W. Liu, H. Zhang, S. Hou, X. Hu, X. Wu, *Langmuir* **2012**, *28*, 17517.
[46] S. Koeppl, F. P. V. Koch, W. Caseri, R. Spolenak, *J. Mater. Chem.* **2012**, *22*, 14594.
[47] J. Zhang, M. R. Langille, C. A. Mirkin, *Nano Lett.* **2011**, *11*, 2495.
[48] A. Guerrero-Martínez, S. Barbosa, I. Pastoriza-Santos, L. M. Liz-Marzán, *Curr. Opin. Colloid Interface Sci.* **2011**, *16*, 118.

[49] J. Fang, X. Ma, H. Cai, X. Song, B. Ding, *Nanotechnology* **2006**, *17*, 5841.
[50] X. Wen, Y. T. Xie, M. W. Mak, K. Y. Cheung, X. Y. Li, R. Renneberg, S. Yang, *Langmuir* **2006**, *22*, 4836.
[51] S. Chen, Z. L. Wang, J. Ballato, S. H. Foulger, D. L. Carroll, *J. Am. Chem. Soc.* **2003**, *125*, 16186.
[52] Z. Li, W. Li, P. H. Camargo, Y. Xia, *Angew. Chem Int. Ed.* **2008**, *47*, 9653.
[53] P. Tassin, T. Koschny, M. Kafesaki, C. M. Soukoulis, *Nat. Photonics* **2012**, *6*, 259.
[54] C. Shankar, A. T. Dao, P. Singh, K. Higashimine, D. M. Mott, S. Maenosono, *Nanotechnology* **2012**, *23*, 245704.
[55] S. J. Tan, M. J. Campolongo, D. Luo, W. Cheng, *Nat. Nanotechnol.* **2011**, *6*, 268.
[56] D. K. Lim, K. S. Jeon, J. H. Hwang, H. Kim, S. Kwon, Y. D. Suh, J. M. Nam, *Nat. Nanotechnol.* **2011**, *6*, 452.
[57] K. C. Ng, W. Cheng, *Nanotechnology* **2012**, *23*, 105602.
[58] C. Damm, D. Segets, G. Yang, B. F. Vieweg, E. Spiecker, W. Peukert, *Small* **2011**, *7*, 147.
[59] M. Min, C. Kim, Y. I. Yang, J. Yi, H. Lee, *Chem. Commun.* **2011**, *47*, 8079.
[60] C. R. Bridges, P. M. DiCarmine, A. Fokina, D. Huesmann, D. S. Seferos, *J. Mater. Chem. A* **2013**, *1*, 1127.
[61] R. Fan, S. W. Chew, V. V. Cheong, B. P. Orner, *Small* **2010**, *6*, 1483.
[62] M. R. Jones, K. D. Osberg, R. J. Macfarlane, M. R. Langille, C. A. Mirkin, *Chem. Rev.* **2011**, *111*, 3736.
[63] M. Lahav, T. Sehayek, A. Vaskevich, I. Rubinstein, *Angew. Chem Int. Ed.* **2003**, *42*, 5575.
[64] R. Fan, S. W. Chew, V. V. Cheong, B. P. Orner, *Small* **2010**, *6*, 1483.
[65] H. Y. Hsueh, H. Y. Chen, Y. C. Hung, Y. C. Ling, S. Gwo, R. M. Ho, *Adv. Mater.* **2013**, *25*, 1780.
[66] S. Vignolini, N. A. Yufa, P. S. Cunha, S. Guldin, I. Rushkin, M. Stefik, K. Hur, U. Wiesner, J. J. Baumberg, U. Steiner, *Adv. Mater.* **2012**, *24*, 23.
[67] S. Mühlig, C. Rockstuhl, in *Amorphous Nanophotonics* (Eds: C. Rockstuhl, T. Scharf), Springer, Heidelberg **2013**, p. 89.
[68] C. Rockstuhl, C. Menzel, S. Mühlig, J. Petschulat, C. Helgert, C. Etrich, A. Chipouline, T. Pertsch, F. Lederer, *Phys. Rev. B* **2011**, *83*, 245119.
[69] M. Albooyeh, D. Morits, S. A. Tretyakov, *Phys. Rev. B* **2012**, *85*, 205110.
[70] C. Helgert, C. Rockstuhl, C. Etrich, C. Menzel, E. B. Kley, A. Tünnermann, F. Lederer, T. Pertsch, *Phys. Rev. B* **2009**, *79*, 233107.
[71] C. F. Bohren, D. R. Huffmann, *Absorption and Scattering of Light by Small Particles*, Wiley-VCH, Weinheim, Germany **2004**.
[72] P. B. Johnson, R. W. Christy, *Phys. Rev. B* **1972**, *6*, 4370.
[73] A. Boltasseva, H. A. Atwater, *Science* **2011**, *331*, 290.
[74] G. V. Naik, J. Kim, A. Boltasseva, *Opt. Mater. Express* **2011**, *1*, 1090.
[75] S. A. Maier, *Plasmonics: Fundamentals and Applications*, Springer, Berlin, Germany **2007**.
[76] B. M. I. van der Zande, L. Pagès, R. A. M. Hikmet, A. van Blaaderen, *J. Phys. Chem. B* **1999**, *103*, 5761.
[77] O. L. Muskens, G. Bachelier, N. D. Fatti, F. Vallée, A. Brioude, X. Jiang, M.-P. Pileni, *J. Phys. Chem. C* **2008**, *112*, 8917.
[78] J. Perezjuste, I. Pastorizasantos, L. Liz-Marzán, P. Mulvaney, *Coord. Chem. Rev.* **2005**, *249*, 1870.
[79] B. V. Enustun, J. Turkevich, *J. Am. Chem. Soc.* **1963**, *85*, 3317.
[80] J. Kimling, M. Maier, B. Okenve, V. Kotaidis, H. Ballot, A. Plech, *J. Phys. Chem. B* **2006**, *110*, 15700.
[81] P. C. Lee, D. Meisel, *J. Phys. Chem.* **1982**, *86*, 3391.
[82] F. Hao, C. L. Nehl, J. H. Hafner, P. Nordlander, *Nano Lett.* **2007**, *7*, 729.
[83] C.-J. Huang, Y.-H. Wang, P.-H. Chiu, M.-C. Shih, T.-H. Meen, *Mater. Lett.* **2006**, *60*, 1896.
[84] X. Lu, M. Rycenga, S. E. Skrabalak, B. Wiley, Y. Xia, *Annu. Rev. Phys. Chem.* **2009**, *60*, 167.
[85] H. Wang, D. W. Brandl, F. Le, P. Nordlander, N. J. Halas, *Nano Lett.* **2006**, *6*, 827.
[86] S. Duraiswamy, S. A. Khan, *Nano Lett.* **2010**, *10*, 3757.
[87] T. C. Preston, R. Signorell, *ACS Nano* **2009**, *3*, 3696.
[88] E. Prodan, C. Radloff, N. J. Halas, P. Nordlander, *Science* **2003**, *302*, 419.
[89] T.-H. Park, P. Nordlander, *Chem. Phys. Lett.* **2009**, *472*, 228.
[90] S. Riikonen, I. Romero, F. García de Abajo, *Phys. Rev. B* **2005**, *71*, 235104.
[91] P. Nordlander, C. Oubre, E. Prodan, K. Li, M. I. Stockman, *Nano Lett.* **2004**, *4*, 899.
[92] S. Mühlig, C. Menzel, C. Rockstuhl, F. Lederer, *Metamaterials* **2011**, *5*, 64.
[93] P. Grahn, A. Shevchenko, M. Kaivola, *Phys. Rev. B* **2012**, *86*, 035419.
[94] W. Cai, U. K. Chettiar, A. V. Kildishev, V. M. Shalaev, *Nat. Photonics* **2007**, *1*, 224.
[95] J. B. Pendry, D. Schurig, D. R. Smith, *Science* **2006**, *312*, 1780.
[96] U. Leonhardt, *Science* **2006**, *312*, 1777.
[97] S. Mühlig, M. Farhat, C. Rockstuhl, F. Lederer, *Phys. Rev. B* **2011**, *83*, 195116.
[98] J. B. Pendry, *Phys. Rev. Lett.* **2000**, *85*, 3966.
[99] T. Paul, C. Menzel, C. Rockstuhl, F. Lederer, *Adv. Mater.* **2010**, *22*, 2354.
[100] P. Alitalo, S. Maslovski, S. Tretyakov, *J. Appl. Phys.* **2006**, *99*, 064912.
[101] M. Wegener, S. Linden, *Physics Today* **2010**, *63*, 32.
[102] M. Kadic, S. Guenneau, S. Enoch, P. A. Huidobro, L. Martín-Moreno, F. J. García-Vidal, J. Renger, R. Quidant, *Nanophotonics* **2012**, *1*, 51.
[103] W. Zhang, L. Huang, C. Santschi, O. J. Martin, *Nano Lett.* **2010**, *10*, 1006.
[104] N. Liu, M. L. Tang, M. Hentschel, H. Giessen, A. P. Alivisatos, *Nat. Mater.* **2011**, *10*, 631.
[105] C. Sonnichsen, B. M. Reinhard, J. Liphardt, A. P. Alivisatos, *Nat. Biotechnol.* **2005**, *23*, 741.
[106] J. N. Anker, W. P. Hall, O. Lyandres, N. C. Shah, J. Zhao, R. P. Van Duyne, *Nat. Mater.* **2008**, *7*, 442.
[107] N. Liu, M. Hentschel, T. Weiss, A. P. Alivisatos, H. Giessen, *Science* **2011**, *332*, 1407.
[108] W. Zhang, A. Govorov, G. Bryant, *Phys. Rev. Lett.* **2006**, *97*, 146804.
[109] J. A. Fan, C. Wu, K. Bao, J. Bao, R. Bardhan, N. J. Halas, V. N. Manoharan, P. Nordlander, G. Shvets, F. Capasso, *Science* **2010**, *328*, 1135.
[110] J. A. Fan, Y. He, K. Bao, C. Wu, J. Bao, N. B. Schade, V. N. Manoharan, G. Shvets, P. Nordlander, D. R. Liu, F. Capasso, *Nano Lett.* **2011**, *11*, 4859.
[111] B. Lukyanchuk, N. I. Zheludev, S. A. Maier, N. J. Halas, P. Nordlander, H. Giessen, C. T. Chong, *Nat. Mater.* **2010**, *9*, 707.
[112] S. Zhang, D. A. Genov, Y. Wang, M. Liu, X. Zhang, *Phys. Rev. Lett.* **2008**, *101*, 047401.
[113] L. Chuntonov, G. Haran, *Nano Lett.* **2011**, *11*, 2440.
[114] R. Watanabe-Tamaki, A. Ishikawa, T. Tanaka, T. Zako, M. Maeda, *J. Phys. Chem. C* **2012**, *116*, 15028.
[115] Y. A. Urzhumov, G. Shvets, J. A. Fan, F. Capasso, D. Brandl, P. Nordlander, *Opt. Express* **2007**, *15*, 14129.
[116] A. Alu, A. Salandrino, N. Engheta, *Opt. Express* **2006**, *14*, 1557.
[117] A. Alu, N. Engheta, *Opt. Express* **2009**, *17*, 5723.
[118] N. Shalkevich, A. Shalkevich, L. Si-Ahmed, T. Burgi, *Phys. Chem. Chem. Phys.* **2009**, *11*, 10175.
[119] S. Mühlig, C. Rockstuhl, V. Yannopapas, T. Bürgi, N. Shalkevich, F. Lederer, *Opt. Express* **2011**, *19*, 9607.

Part. Part. Syst. Charact. **2014**,
DOI: 10.1002/ppsc.201300309

[120] J. Dintinger, S. Mühlig, C. Rockstuhl, T. Scharf, *Opt. Mater. Express* **2012**, *2*, 269.
[121] S. Mühlig, A. Cunningham, S. Scheeler, C. Pacholski, T. Burgi, C. Rockstuhl, F. Lederer, *ACS Nano* **2011**, *5*, 6586.
[122] C. R. Simovski, S. A. Tretyakov, *Phys. Rev. B* **2009**, *79*, 045111.
[123] A. Vallecchi, M. Albani, F. Capolino, *Opt. Express* **2011**, *19*, 2754.
[124] A. H. Sihvola, A. J. Viitanen, I. V. Lindell, S. A. Tretyakov, *Electromagnetic Waves in Chiral and Bi-Isotropic Media*, Artech House, Boston, US **1994**.
[125] M. Hentschel, M. Schäferling, T. Weiss, N. Liu, H. Giessen, *Nano Lett.* **2012**, *12*, 2542.
[126] C. Helgert, E. Pshenay-Severin, M. Falkner, C. Menzel, C. Rockstuhl, E. B. Kley, A. Tunnermann, F. Lederer, T. Pertsch, *Nano Lett.* **2011**, *11*, 4400.
[127] C. M. Soukoulis, M. Wegener, *Nat. Photonics* **2011**, *5*, 523.
[128] J. B. Pendry, *Science* **2004**, *306*, 1353.
[129] S. Zhang, Y.-S. Park, J. Li, X. Lu, W. Zhang, X. Zhang, *Phys. Rev. Lett.* **2009**, *102*, 023901.
[130] E. Plum, J. Zhou, J. Dong, V. Fedotov, T. Koschny, C. Soukoulis, N. Zheludev, *Phys. Rev. B* **2009**, *79*, 035407.
[131] M. Decker, M. W. Klein, M. Wegener, S. Linden, *Opt. Lett.* **2007**, *32*, 856.
[132] C. Gautier, T. Bürgi, *Chem. Phys. Chem.* **2009**, *10*, 483.
[133] H. Behar-Levy, O. Neumann, R. Naaman, D. Avnir, *Adv. Mater.* **2007**, *19*, 1207.
[134] M. Hentschel, T. Weiss, S. Bagheri, H. Giessen, *Nano Lett.* **2013**, *13*, 4428.
[135] B. Frank, X. Yin, M. Schaferling, J. Zhao, S. M. Hein, P. V. Braun, H. Giessen, *ACS Nano* **2013**, *7*, 6321.
[136] A. G. Mark, J. G. Gibbs, T. C. Lee, P. Fischer, *Nat. Mater.* **2013**, *12*, 802.
[137] C. Rockstuhl, C. Menzel, T. Paul, F. Lederer, *Phys. Rev. B* **2009**, *79*, 035321.
[138] Z. Fan, A. O. Govorov, *J. Phys. Chem. C* **2011**, *115*, 13254.
[139] Z. Fan, A. O. Govorov, *Nano Lett.* **2010**, *10*, 2580.
[140] A. J. Mastroianni, S. A. Claridge, A. P. Alivisatos, *J. Am. Chem. Soc.* **2009**, *131*, 8455.
[141] Z. Fan, H. Zhang, A. O. Govorov, *J. Phys. Chem. C* **2013**, *117*, 14770.
[142] P. Mühlschlegel, H. J. Eisler, O. J. Martin, B. Hecht, D. W. Pohl, *Science* **2005**, *308*, 1607.
[143] K. Hering, D. Cialla, K. Ackermann, T. Dorfer, R. Moller, H. Schneidewind, R. Mattheis, W. Fritzsche, P. Rosch, J. Popp, *Anal. Bioanal. Chem.* **2008**, *390*, 113.
[144] C. E. Talley, J. B. Jackson, C. Oubre, N. K. Grady, C. W. Hollars, S. M. Lane, T. R. Huser, P. Nordlander, N. J. Halas, *Nano Lett.* **2005**, *5*, 1569.
[145] A. Gopinath, S. V. Boriskina, W. R. Premasiri, L. Ziegler, B. M. Reinhard, L. Dal Negro, *Nano Lett.* **2009**, *9*, 3922.
[146] V. Joseph, M. Gensler, S. Seifert, U. Gernert, J. P. Rabe, J. Kneipp, *J. Phys. Chem. C* **2012**, *116*, 6859.
[147] J. Ye, F. Wen, H. Sobhani, J. B. Lassiter, P. Van Dorpe, P. Nordlander, N. J. Halas, *Nano Lett.* **2012**, *12*, 1660.
[148] J. Xie, Q. Zhang, J. Y. Lee, D. I. Wang, *ACS Nano* **2008**, *2*, 2473.
[149] S. Y. Lee, L. Hung, G. S. Lang, J. E. Cornett, I. D. Mayergoyz, O. Rabin, *ACS Nano* **2010**, *4*, 5763.
[150] R. Filter, S. Mühlig, T. Eichelkraut, C. Rockstuhl, F. Lederer, *Phys. Rev. B* **2012**, *86*, 035404.
[151] A. M. Kern, O. J. F. Martin, *Phys. Rev. A* **2012**, *85*, 022501.
[152] S. Campione, M. Albani, F. Capolino, *Opt. Mater. Express* **2011**, *1*, 1077.
[153] A. De Luca, M. P. Grzelczak, I. Pastoriza-Santos, L. M. Liz-Marzan, M. La Deda, M. Striccoli, G. Strangi, *ACS Nano* **2011**, *5*, 5823.
[154] M. A. Noginov, G. Zhu, M. Bahoura, J. Adegoke, C. E. Small, B. A. Ritzo, V. P. Drachev, V. M. Shalaev, *Opt. Lett.* **2006**, *31*, 3022.
[155] D. Bergman, M. Stockman, *Phys. Rev. Lett.* **2003**, *90*, 027402.
[156] N. I. Zheludev, S. L. Prosvirnin, N. Papasimakis, V. A. Fedotov, *Nat. Photonics* **2008**, *2*, 351.
[157] M. A. Noginov, G. Zhu, A. M. Belgrave, R. Bakker, V. M. Shalaev, E. E. Narimanov, S. Stout, E. Herz, T. Suteewong, U. Wiesner, *Nature* **2009**, *460*, 1110.
[158] R. F. Oulton, V. J. Sorger, T. Zentgraf, R. M. Ma, C. Gladden, L. Dai, G. Bartal, X. Zhang, *Nature* **2009**, *461*, 629.
[159] N. Li, W. H. Binder, *J. Mater. Chem.* **2011**, *21*, 16717.
[160] X. Liu, H. Liu, W. Zhou, H. Zheng, X. Yin, Y. Li, Y. Guo, M. Zhu, C. Ouyang, D. Zhu, A. Xia, *Langmuir* **2010**, *26*, 3179.
[161] R. Abargues, S. Albert, J. L. Valdés, K. Abderrafi, J. P. Martínez-Pastor, *J. Mater. Chem.* **2012**, *22*, 22204.
[162] C. A. Otter, P. J. Patty, M. A. Williams, M. R. Waterland, S. G. Telfer, *Nanoscale* **2011**, *3*, 941.
[163] R. Sardar, T. B. Heap, J. S. Shumaker-Parry, *J. Am. Chem. Soc.* **2007**, *129*, 5356.
[164] A. Hofmann, P. Schmiel, B. Stein, C. Graf, *Langmuir* **2011**, *27*, 15165.
[165] Q. Huo, J. G. Worden, *J. Nanopart. Res.* **2006**, *9*, 1013.
[166] J. P. Hermes, F. Sander, U. Fluch, T. Peterle, D. Thompson, R. Urbani, T. Pfohl, M. Mayor, *J. Am. Chem. Soc.* **2012**, *134*, 14674.
[167] W. Page Faulk, G. Malcolm Taylor, *Immunochemistry* **1971**, *8*, 1081.
[168] I. Lubitz, A. Kotlyar, *Bioconjugate Chem.* **2011**, *22*, 2043.
[169] B. Ding, Z. Deng, H. Yan, S. Cabrini, R. N. Zuckermann, J. Bokor, *J. Am. Chem. Soc.* **2010**, *132*, 3248.
[170] S. Pal, Z. Deng, H. Wang, S. Zou, Y. Liu, H. Yan, *J. Am. Chem. Soc.* **2011**, *133*, 17606.
[171] R. Kaminker, M. Lahav, L. Motiei, M. Vartanian, R. Popovitz-Biro, M. A. Iron, M. E. van der Boom, *Angew. Chem.* **2010**, *122*, 1240.
[172] I. Hussain, M. Brust, J. Barauskas, A. I. Cooper, *Langmuir* **2009**, *25*, 1934.
[173] M. P. Stemmler, Y. Fogel, K. Müllen, M. Kreiter, *Langmuir* **2009**, *25*, 11917.
[174] T. C. Lee, O. A. Scherman, *Chemistry* **2012**, *18*, 1628.
[175] M. Xie, L. Ding, Z. You, D. Gao, G. Yang, H. Han, *J. Mater. Chem.* **2012**, *22*, 14108.
[176] Z. Wang, A. G. Skirtach, Y. Xie, M. Liu, H. Möhwald, C. Gao, *Chem. Mater.* **2011**, *23*, 4741.
[177] Z. Liu, H. Huang, T. He, *Small* **2013**, *9*, 505.
[178] S. G. Jang, A. Khan, C. J. Hawker, E. J. Kramer, *Macromolecules* **2012**, *45*, 1553.
[179] J. He, Y. Liu, T. Babu, Z. Wei, Z. Nie, *J. Am. Chem. Soc.* **2012**, *134*, 11342.
[180] M. P. Kim, D. J. Kang, D. W. Jung, A. G. Kannan, K. H. Kim, K. H. Ku, S. G. Jang, W. S. Chae, G. R. Yi, B. J. Kim, *ACS Nano* **2012**, *6*, 2750.
[181] A. Sanchez-Iglesias, M. Grzelczak, T. Altantzis, B. Goris, J. Perez-Juste, S. Bals, G. Van Tendeloo, S. H. Donaldson Jr., B. F. Chmelka, J. N. Israelachvili, L. M. Liz-Marzan, *ACS Nano* **2012**, *6*, 11059.
[182] M. A. Kostiainen, P. Hiekkataipale, A. Laiho, V. Lemieux, J. Seitsonen, J. Ruokolainen, P. Ceci, *Nat. Nanotechnol.* **2013**, *8*, 52.
[183] A. Cunningham, S. Mühlig, C. Rockstuhl, T. Bürgi, *J. Phys. Chem. C* **2011**, *115*, 8955.
[184] A. Cunningham, S. Mühlig, C. Rockstuhl, T. Bürgi, *J. Phys. Chem. C* **2012**, *116*, 17746.
[185] A. Yoshida, K. Imazu, X. Li, K. Okamoto, K. Tamada, *Langmuir* **2012**, *28*, 17153.
[186] Y. Yan, J. I. Chen, D. S. Ginger, *Nano Lett.* **2012**, *12*, 2530.
[187] T. Wu, Q. Zhang, J. Hu, G. Zhang, S. Liu, *J. Mater. Chem.* **2012**, *22*, 5155.
[188] L. N. Kim, E.-G. Kim, J. Kim, S.-E. Choi, W. Park, S. Kwon, *Bull. Korean Chem. Soc.* **2012**, *33*, 3735.

[189] S. Mehdizadeh Taheri, S. Fischer, S. Förster, *Polymers* **2011**, *3*, 662.
[190] V. V. Terekhin, O. V. Dementeva, V. M. Rudoy, *Russ. Chem. Rev.* **2011**, *80*, 453.
[191] C. Song, G. Zhao, P. Zhang, N. L. Rosi, *J. Am. Chem. Soc.* **2010**, *132*, 14033.
[192] Q. Liang, C. Li, G. Chen, M. Jiang, *J. Colloid Interface Sci.* **2012**, *383*, 82.
[193] N. Pazos-Pérez, W. Ni, A. Schweikart, R. A. Alvarez-Puebla, A. Fery, L. M. Liz-Marzán, *Chem. Sci.* **2010**, *1*, 174.
[194] B. Yan, S. V. Boriskina, B. M. Reinhard, *J. Phys. Chem. C* **2011**, *115*, 4578.
[195] S. Gwo, M. H. Lin, C. L. He, H. Y. Chen, T. Teranishi, *Langmuir* **2012**, *28*, 8902.
[196] F. Holzner, C. Kuemin, P. Paul, J. L. Hedrick, H. Wolf, N. D. Spencer, U. Duerig, A. W. Knoll, *Nano Lett.* **2011**, *11*, 3957.
[197] J. Yang, T. Ichii, K. Murase, H. Sugimura, *Langmuir* **2012**, *28*, 7579.
[198] M. Kolibal, M. Konecny, F. Ligmajer, D. Skoda, T. Vystavel, J. Zlamal, P. Varga, T. Sikola, *ACS Nano* **2012**, *6*, 10098.
[199] C. Kuemin, L. Nowack, L. Bozano, N. D. Spencer, H. Wolf, *Adv. Funct. Mater.* **2012**, *22*, 702.
[200] N. Pazos-Perez, C. S. Wagner, J. M. Romo-Herrera, L. M. Liz-Marzan, F. J. Garcia de Abajo, A. Wittemann, A. Fery, R. A. Alvarez-Puebla, *Angew. Chem Int. Ed.* **2012**, *51*, 12688.
[201] D. Steinigeweg, M. Schutz, M. Salehi, S. Schlücker, *Small* **2011**, *7*, 2443.
[202] O. Akbulut, C. R. Mace, R. V. Martinez, A. A. Kumar, Z. Nie, M. R. Patton, G. M. Whitesides, *Nano Lett.* **2012**, *12*, 4060.
[203] Z. Guo, X. Fan, L. Xu, X. Lu, C. Gu, Z. Bian, N. Gu, J. Zhang, D. Yang, *Chem. Commun.* **2011**, *47*, 4180.
[204] N. R. Jana, *Chem. Commun.* **2003**, 1950.
[205] K. Park, H. Koerner, R. A. Vaia, *Nano Lett.* **2010**, *10*, 1433.
[206] R. Tuinier, J. Rieger, C. G. de Kruif, *Adv. Colloid Interface Sci.* **2003**, *103*, 1.
[207] D. H. Tsai, T. J. Cho, F. W. DelRio, J. Taurozzi, M. R. Zachariah, V. A. Hackley, *J. Am. Chem. Soc.* **2011**, *133*, 8884.
[208] L. Calzolai, D. Gilliland, C. P. Garcia, F. Rossi, *J. Chromatogr. A* **2011**, *1218*, 4234.
[209] Y. Wen, C. K. McLaughlin, P. K. Lo, H. Yang, H. F. Sleiman, *Bioconjugate Chem.* **2010**, *21*, 1413.
[210] W. Wu, J. Huang, L. Wu, D. Sun, L. Lin, Y. Zhou, H. Wang, Q. Li, *Sep. Purif. Technol.* **2013**, *106*, 117.
[211] F.-K. Liu, *ISRN Chromatography* **2012**, *2012*, 1.
[212] E. Antoniou, P. Voudouris, A. Larsen, B. Loppinet, D. Vlassopoulos, I. Pastoriza-Santos, L. M. Liz-Marzán, *J. Phys. Chem. C* **2012**, *116*, 3888.
[213] N. K. Reddy, J. Perez-Juste, I. Pastoriza-Santos, P. R. Lang, J. K. Dhont, L. M. Liz-Marzan, J. Vermant, *ACS Nano* **2011**, *5*, 4935.
[214] C. Jing, Z. Gu, Y. L. Ying, D. W. Li, L. Zhang, Y. T. Long, *Anal. Chem.* **2012**, *84*, 4284.
[215] L. Chuntonov, M. Bar-Sadan, L. Houben, G. Haran, *Nano Lett.* **2012**, *12*, 145.
[216] T. Altantzis, B. Goris, A. Sánchez-Iglesias, M. Grzelczak, L. M. Liz-Marzán, S. Bals, *Part. Part. Syst. Char.* **2013**, *30*, 84.
[217] S. Biswas, D. Nepal, K. Park, R. A. Vaia, *J. Phys. Chem. Lett.* **2012**, *3*, 2568.
[218] B. Goris, S. Bals, W. Van den Broek, E. Carbo-Argibay, S. Gomez-Grana, L. M. Liz-Marzan, G. Van Tendeloo, *Nat. Mater.* **2012**, *11*, 930.
[219] W. J. Cho, Y. Kim, J. K. Kim, *ACS Nano* **2012**, *6*, 249.
[220] Y. Zheng, T. Thai, P. Reineck, L. Qiu, Y. Guo, U. Bach, *Adv. Funct. Mater.* **2013**, *23*, 1519.
[221] Y. Wang, K. C. Black, H. Luehmann, W. Li, Y. Zhang, X. Cai, D. Wan, S. Y. Liu, M. Li, P. Kim, Z. Y. Li, L. V. Wang, Y. Liu, Y. Xia, *ACS Nano* **2013**, *7*, 2068.
[222] E. S. Day, L. Zhang, P. A. Thompson, J. A. Zawaski, C. C. Kaffes, M. W. Gaber, S. M. Blaney, J. L. West, *Nanomedicine* **2012**, *7*, 1133.
[223] Pilot study of AuroLase therapy, http://clinicaltrials.gov/ct2/show/NCT00848042 (accessed December 2013).
[224] M. Gu, Z. Ouyang, B. Jia, N. Stokes, X. Chen, N. Fahim, X. Li, M. J. Ventura, Z. Shi, *Nanophotonics* **2012**, *1*, 235.
[225] X. Chen, B. Jia, J. K. Saha, B. Cai, N. Stokes, Q. Qiao, Y. Wang, Z. Shi, M. Gu, *Nano Lett.* **2012**, *12*, 2187.
[226] E. A. Parlak, T. Aslı Tumay, N. Tore, Ş. Sarıoğlan, P. Kavak, F. Türksoy, *Sol. Energy Mater. Sol. Cells* **2013**, *110*, 58.
[227] V. Yannopapas, I. E. Psarobas, *J. Phys. Chem. C* **2012**, *116*, 15599.
[228] X. Zeng, F. Liu, A. G. Fowler, G. Ungar, L. Cseh, G. H. Mehl, J. E. Macdonald, *Adv. Mater.* **2009**, *21*, 1746.
[229] D. Schurig, J. J. Mock, B. J. Justice, S. A. Cummer, J. B. Pendry, A. F. Starr, D. R. Smith, *Science* **2006**, *314*, 977.
[230] L. H. Gabrielli, J. Cardenas, C. B. Poitras, M. Lipson, *Nat. Photonics* **2009**, *3*, 461.
[231] A. Monti, F. Bilotti, A. Toscano, *Opt. Lett.* **2011**, *36*, 4479.
[232] S. Droulias, V. Yannopapas, *J. Phys. Chem. C* **2013**, *117*, 1130.
[233] K. Hur, R. G. Hennig, F. A. Escobedo, U. Wiesner, *Nano Lett.* **2012**, *12*, 3218.
[234] O. Pena-Rodriguez, A. Rivera, M. Campoy-Quiles, U. Pal, *Nanoscale* **2013**, *5*, 209.
[235] M. I. Stockman, *Nat. Photonics* **2008**, *2*, 327.
[236] X. Meng, U. Guler, A. V. Kildishev, K. Fujita, K. Tanaka, V. M. Shalaev, *Sci. Rep.* **2013**, *3*, 1241.
[237] D. Rodríguez-Fernández, J. Pérez-Juste, I. Pastoriza-Santos, L. M. Liz-Marzán, *ChemistryOpen* **2012**, *1*, 90.
[238] A. B. Evlyukhin, S. M. Novikov, U. Zywietz, R. L. Eriksen, C. Reinhardt, S. I. Bozhevolnyi, B. N. Chichkov, *Nano Lett.* **2012**, *12*, 3749.
[239] A. Boltasseva, H. A. Atwater, *Science* **2011**, *331*, 290.
[240] G. V. Naik, J. Kim, A. Boltasseva, *Opt. Mater. Express* **2011**, *1*, 1090.
[241] M. Lattuada, T. A. Hatton, *Nano Today* **2011**, *6*, 286.
[242] J. Du, R. K. O'Reilly, *Chem. Soc. Rev.* **2011**, *40*, 2402.

Publication P2

Synthesis, Separation, and Hypermethod Characterization of Gold Nanoparticle Dimers Connected by a Rigid Rod Linker

M. Fruhnert, F. Kretschmer, R. Geiss, I. Perevyazko, D. Cialla-May, Michael Steinert, Norik Janunts, Dmitry Sivun, S. Hoeppener, M. D. Hager, U. S. Schubert, T. Pertsch, C. Rockstuhl

In preparation

Synthesis, separation, and hypermethod characterization of gold nanoparticle dimers connected by a rigid rod linker

Martin Fruhnert[*,†], *Florian Kretschmer*[¶,‡], *Reinhard Geiss*[§], *Igor Perevyazko*[¶,‡] *Dana Cialla-May*[#,$], *Michael Steinert*[§], *Norik Janunts*[§], *Dmitry Sivun*[§] *Stephanie Hoeppener*,[¶,‡] *Martin D. Hager*,[¶,‡] *Thomas Pertsch*[§], *Ulrich S. Schubert*[¶,‡] *and Carsten Rockstuhl*[‖,⊥]

† Institute of Condensed Matter Theory and Solid State Optics, Abbe Center of Photonics, Friedrich Schiller University Jena, D-07743 Jena, Germany

¶ Laboratory of Organic and Macromolecular Chemistry, Friedrich Schiller University Jena, D-07743 Jena, Germany

Friedrich Schiller University Jena, Institute of Physical Chemistry, Helmholtzweg 4, 07743 Jena, Germany

$ Leibniz Institute of Photonic Technology, Albert-Einstein-Straße 9, 07745 Jena, Germany

§ Institute of Applied Physics, Abbe Center of Photonics, Friedrich Schiller University Jena, D-07743 Jena, Germany

‡ Jena Center for Soft Matter, Friedrich Schiller University Jena, D-07743 Jena, Germany

‖Institute of Theoretical Solid State Physics, Karlsruhe Institute of Technology, D-76131 Karlsruhe, Germany

⊥Institute of Nanotechnology, Karlsruhe Institute of Technology, D-76021 Karlsruhe, Germany

Email: martin.fruhnert@uni-jena.de

KEYWORDS: Nanoparticles, Plasmonics, Self-Assembly, Bottom-Up, Dimers, Surface Enhanced Raman Scattering, Extinction Measurement, Hybridization

ABSTRACT

Bonding individual metallic nanoparticles at small separation distances to let them form dimers and making them available in large quantities is a key requirement for various applications that exploit the tremendous enhancement of electromagnetic fields in plasmonic junctions. Although progress has been witnessed in the past concerning the fabrication of dimers mediated by rigid molecular linkers still the exact bonding mechanism remains elusive. Here, we describe the fabrication of the necessary rigid linker molecule and demonstrate its feasibility to achieve dimers made from closely spaced metallic nanoparticles in large quantities. Although the topography of the dimers proofs the success of the fabrication method, we use what we call here a hypermethod characterization approach to study the optical properties of dimers from various perspectives. Measuring the surface enhanced Raman scattering signal of the linker molecule allows tracing directly the optical environment it perceives. By reaching a strong field enhancement in the gap of the dimers we are able to investigate optical and geometrical properties of the linker. Moreover, upon isolation of the dimers, we use single particle extinction spectroscopy to study the optical response of a fabricated dimer directly. Full wave numerical simulations corroborate the experimental results and provide insights into quantities inaccessible in experiments. The ability to fabricate and to characterize rigidly linked nanoparticles will pave the way towards various plasmonic applications such as sensors, photocatalysis, and plexcitonics.

INTRODUCTION

The field of plasmonics has gone through a rapid development in recent years. The understanding and the manipulation of the electromagnetic response of metal nanoparticles (NPs) made considerable progress in the past. The development was motivated by a vast variety of promising applications in key impact areas such as sensing[1-3], medicine[4,5], nanochemistry[6,7], or nanobiology[8,9]. When a NP made from a noble metal is illuminated with electromagnetic radiation at an appropriate frequency, i.e. in the visible range of the spectrum, the conduction electrons perform a collective oscillation that can be driven into resonance. Such excitation is known as the localized surface plasmon polariton resonance (LSP). Bringing two or more NPs in close vicinity causes LSPs to couple[10], thereby forming bonding and anti-bonding states with unique properties. Most notably, the coupling allows for eigenmodes that are characterized by a strong field enhancement in a confined area in the junction of the NPs. This is easy to understand by regarding the junction in lowest order approximation as a parallel plate capacitance. The electric field for a fixed potential in such capacitance scales inversely proportional to the distance. Small distances, therefore, tremendously enhance the field if only sufficiently small separations are in reach. Such huge fields are highly desirable for many applications, for which surface enhanced Raman spectroscopy (SERS) might be a referential example. The strong field confinements in such junctions allow chemical recognition of single molecules[11], which opens unprecedented opportunities in, e.g., catalysis or nanomedical applications.

A straightforward implementation of such junctions are NP dimers. Bottom-up methods are commonly utilized to form plasmonic NP dimers or multimers, e.g., *via* complementary DNA,[12] click chemistry,[13] Diels-Alder[14] and other chemical reactions as well as the

formation of metal complexes.[15] As gold shows a high affinity towards sulfur and to a smaller extend towards nitrogen it is also possible to utilize bis- and higher functionalized organic molecules in order to initialize the assembly process. These linker molecules comprise a multitude of different structures and functionalities like flexible dithiols or rigid molecules with a conjugated or metal complex backbone.[16-20] However, the exact bonding mode of these kinds of linkers remains an open question since contradictory results have been reported in literature. A shift of the plasmon band over time during the NP assembly by a polyphenylene dendrimer was noted which could indicate a transformation from assemblies of particles with the maximum possible distance to assemblies with distances shorter than the length of the linker.[21] Additionally, analysis of the plasmon band of particles linked via trigonal and quadratic planar rigid structures revealed that, due to a chelating effect, these linkers only bind to two instead of the expected three or four particles.[22,23] These findings are in contrast to earlier reports[24]. In most cases the NPs used are significantly larger than the linker molecules. Hence, for a linker molecule the surface of the spherical particle occurs more or less flat. Therefore, for low linker concentrations, the attachment of both ends of, e.g. a linear linker molecule to only one particle, is likely. In contrast, high linker concentrations facilitate a perpendicular orientation with only one end of the linker attached to the surface of the NP.

Moreover, once being fabricated, it remains challenging to measure the optical properties of an isolated NP or dimer, or even just finding its exact position on a substrate without destroying the sample. But the characterization of NPs at the level of a single constituent is of utmost importance, particularly, if bottom-up techniques were used for the fabrication. These self-assembly techniques often lead to complexly shaped NPs where the fabricated ensemble is formed from many NPs composed of a large variety of different geometries[6,25,26]. The strongly dispersive nature causes the optical response to be featureless and all details from the

individual structures are hidden in the ensemble average when measurements are conducted in solution. However, most studies that aim for single particle spectroscopy only work reliable for rather large particles for which the scattering response remains notable. Since the scattering cross section scales with the sixth power of the radius, particles with a size of a few tens of nanometers can conveniently be analyzed by means of dark-field microscopy[27]. It can be also extended with spectroscopic equipment to analyze optical details[28] and not just accessing their location on a substrate. However, the technique has its limits when small NPs are at the focus of interest. Then, absorption dominates and particles are usually seen only in extinction. An alternative route to glimpse onto individual particles would be scanning near-field optical microscopy (SNOM). There, a tip is scanned across the surface of a sample and the field in close vicinity to the NPs can be measured. The method provides a high spatial optical and topographic resolution that is determined roughly by the size of the tip apex. Common to these tip-based scanning schemes are the complex interactions between tip and sample making it difficult to extract optical properties of single gold NPs having sizes comparable or smaller than the tip apex size[29-31]. Therefore, for all these challenges a modern characterization approach can no longer rely on a single source of information. Quite on the contrary, only the combination of different techniques allows unraveling details of a particular structure that is expected from fabrication. And each of these techniques should concentrate on measuring properties at the level of a single constituent to understand what has been actually achieved.

To provide satisfying answers to all these questions, we present in this work a self-assembly process to synthesize gold nanosphere dimers with a rigid linker molecule especially designed for this purpose. The advantage of such molecule is its high stability and its precise length allowing for an excellent adjustment of interparticle distances. Depending on the concentration of the linker molecule, the nanospheres assemble in varying cluster sizes, which can be separated

via density gradient centrifugation. After that, we combine two characterization methods to detect and to characterize the optical properties of the fabricated dimers from various perspectives. They focus on different aspects and shall highlight features of either the linker molecule or the NP dimer.

The first approach concerns the detection of the linker molecule that bonds the metallic NPs to form a dimer by means of SERS. The signal of the linker between the metal surfaces is shown to be strongly enhanced. The detailed analysis of the measured spectra not only provides a highly precise SERS signal, but it also allows identifying the structural orientation of the linker molecule and its relative position to the dimer.

In a second approach we use a far-field detection technique of the extinction signal from a single dimer. With this approach we put emphasis on probing the optical response from the dimer itself. Our method relies on a spatial modulation of the sample located in the focus spot of a laser beam and subsequent lock-in detection of the transmitted optical intensity to extract the small signal induced by the NP from the huge background of the diffraction limited far-field spot. Single particles with diameters down to 5 nm can be detected with this method[32]. The characterization of gold dimers by spatial modulation microscopy so far has only been reported for dimers made from much larger metallic NPs, i.e. they consist of two 100 nm diameter disks or cubical metallic NPs[33,34] .

Comparing those measurement techniques with full wave simulations of the optical response from the dimers provides insights into quantities otherwise unobservable in experiments.

The paper is structured as follows. In the second section we detail the synthesis of the NP aggregates and describe the separation of assemblies from single particles using centrifugation. Structural characterization with a transmission electron microscope (TEM) provides

topographical information on the pertinent samples. We concentrate afterwards on describing SERS measurements made from the dimers and detail how the features from the spectra allow understanding the structural composition of the entire dimer. Afterwards we outline the far-field extinction measurements from dimers that were suitably isolated on a substrate.

SYNTHESIS OF NANO-SPHERE AGGREGATES

The synthesis of the linker molecule **3** was carried out via a Pd catalyzed Sonogashira reaction between thioacetate **1** and the diethynyl compound **2** (See Fig. 1 and supporting information for experimental details). Owing to the rigid conjugated backbone a defined end-to-end distance of ~ 2 nm is achieved. While self-assembled monolayers (SAMs) on gold surfaces are commonly formed via thiols or disulfides due to their higher affinity in comparison to, e.g., thioethers[35-38], introduction of a protecting group for the thiol was necessary in order to perform the cross coupling reaction. Additionally, acetylation also shows to be useful to ensure the long-term stability of the compound.

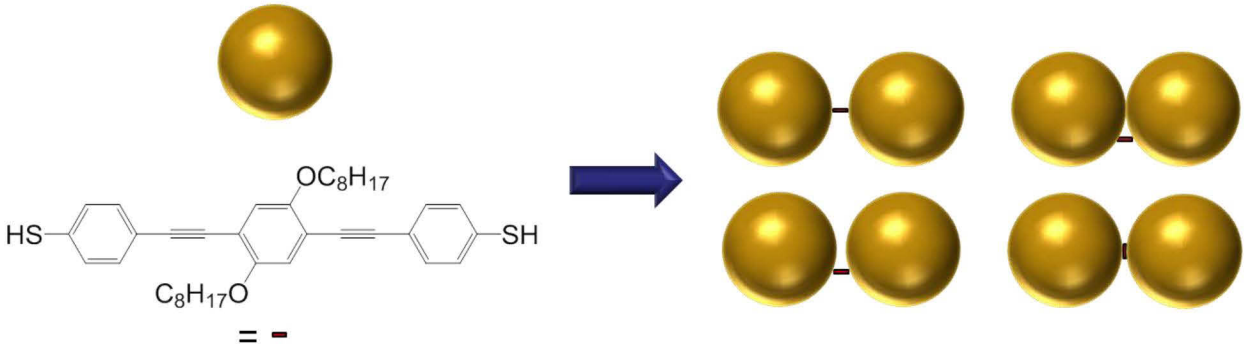

Figure 1: Schematic representation of different possible assembly modes of gold nanoparticles (d = 15 nm) with the deprotected linker molecule **3** (S-S = 2 nm).

Citrate stabilized gold NPs were prepared via the Turkevich method[39]. TEM imaging of a sample showed mainly spherical particles with a mean diameter of around 13 nm (Fig. 2). The presence of aggregated particles can be attributed to drying effects. For the assembly of the particles, generally, a solution of diazabicycloundecene (DBU)was added to a solution of the linker molecule to cleave off the acetyl group and generate the free thiol.[40] The mixture was subsequently added to the gold NPs. Increasing concentrations of the linker molecule were used to tune the assembly of the particles, a process being followed by UV-vis spectroscopy (Fig. 3). At low linker concentrations only a small bathochromic shift of the plasmon peak at 520 nm is

obtained probably due to the different refractive index of the solution and the presence of only a few dimers. Increasing concentrations led to a larger red shift and a significant broadening of the plasmon resonance due to the larger contribution of the underlying longitudinal plasmon resonance from NP assemblies. Depending on the amount of linker added, the solution changed its color from red at the lowest concentration to a dark violet at the highest concentration, verifying the assembly of the NPs.

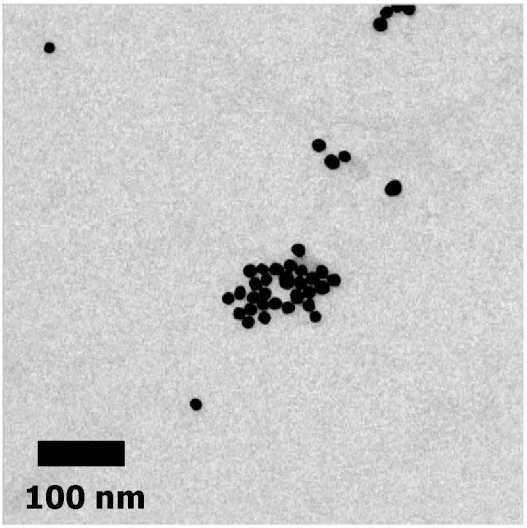

Figure 2. TEM image of single gold NPs prepared by the Turkevich method.

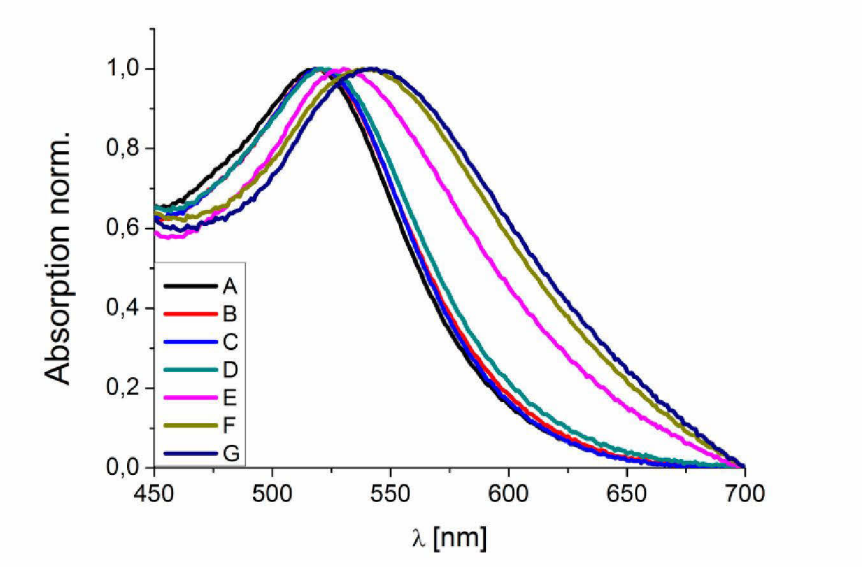

Figure 3. UV-vis spectra of single gold NPs, gold NPs with only DBU and gold NPs with different amounts of the linker solution. A - Au NP solution, B - Au NP control solution with only DBU (100 µg/mL), C-G - Au NP solutions with increasing amounts of 3 and DBU (20, 40, 60, 80, 100 µg/mL) respectively.

However, while after addition of the linker solution most of the reaction was finished after a few minutes, over the course of several hours and days a further darkening of the solutions occurred indicating some further aggregation. In order to shorten the assembly process and to obtain a defined end point, it was found that addition of poly(acrylic acid) (PAA) stabilized the solutions and stopped further linking and aggregation, respectively, of the particles.

Increasing the ionic strength of solutions containing gold NPs by means of acids, bases or salts leads to destabilization with concomitant aggregation.[41] Since DBU acts as a base in aqueous solutions a blank test with gold NPs and only the DBU solution was conducted to exclude that the formation of assembled particles is merely due to the presence of the base. It turned out that even the amount of DBU used to deprotect the highest concentrated linker solution leads only to a small red shift of the plasmon resonance (red curve Fig. 3). In comparison the same amount of DBU with the linker leads to a strong broadening (blue curve Fig. 3) indicating that the assembly process can clearly be attributed to the presence of the dithiol linker.

The generation of linked particles can be increased by even larger amounts of the linker; however, it has to be taken into account that the formation of assemblies is only a statistical process due to the possible attachment of more than one molecule to the surface. While at low concentrations of the linker only small aggregates consisting of dimers, trimers etc. will form, increasing concentrations lead to linking of these aggregates resulting at some point in the complete precipitation of the particles.

The hydrodynamic behavior of the NPs depends both, on their size and on their shape. It is clear that frictional coefficient will be larger for dimers than for single particles, due to an increased average cross section. On the other hand, dimers will have twice the molar mass of the monomer and this will overcompensate the increased frictional coefficients, resulting in higher sedimentation coefficients of dimers. . It can therefore be expected that the clusters could be separated by density gradient centrifugation[42-44] (see Supporting Information). In Fig. 4 the results of such a centrifugation are presented. The process leads to the formation of several areas corresponding obviously to the population of single NPs (I^{st}, II^{nd} and III^{rd} region) and their assemblies (IV^{th} region) which are clearly separated. Sedimentation velocity analysis (Fig. 4B) showed reasonable shifting of the average sedimentation coefficients to the higher values for the later fractions. Moreover the color of the fractions changes from the dark red for the I^{st} fraction to the violet for the IV^{th} fraction. Based on the estimated values of sedimentation coefficient and frictional ratio the size of the particles in the fractions was calculated (Fig. 4B). TEM images of the coated fractions (Fig. 5) show that the I^{st} fraction indeed consists almost exclusively of small monomers, while the fraction IV is made up of dimers and a small number of higher order assemblies. This fraction is used for the further analysis.

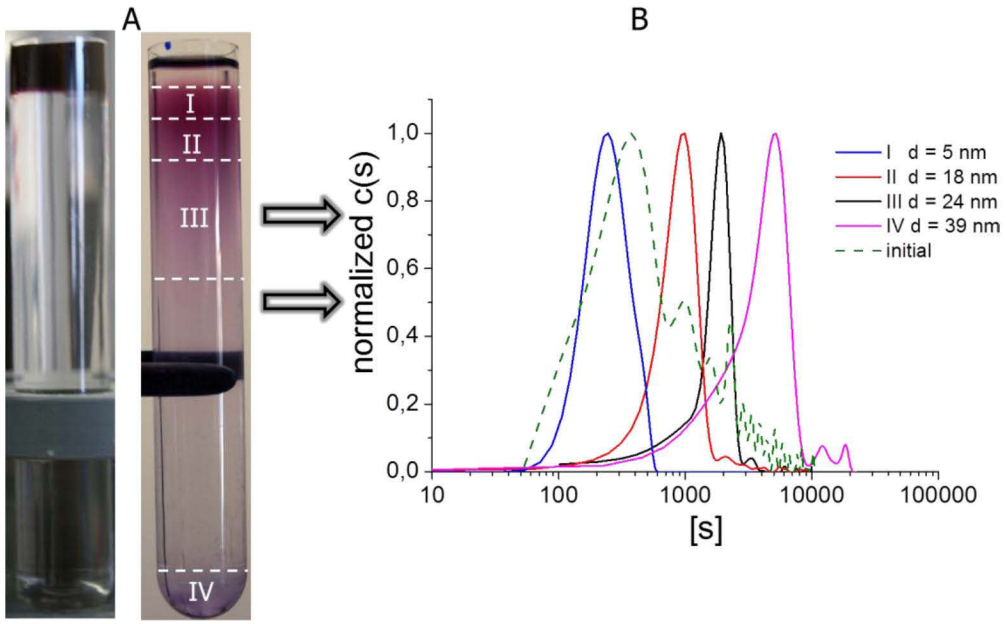

Figure 4. Density gradient centrifugation of gold nanoparticles. (A) Images of a centrifuge vial with the sample applied, before and after centrifugation. (B) Corresponding distributions of intrinsic sedimentation coefficients for different diameters d of the fractions collected.

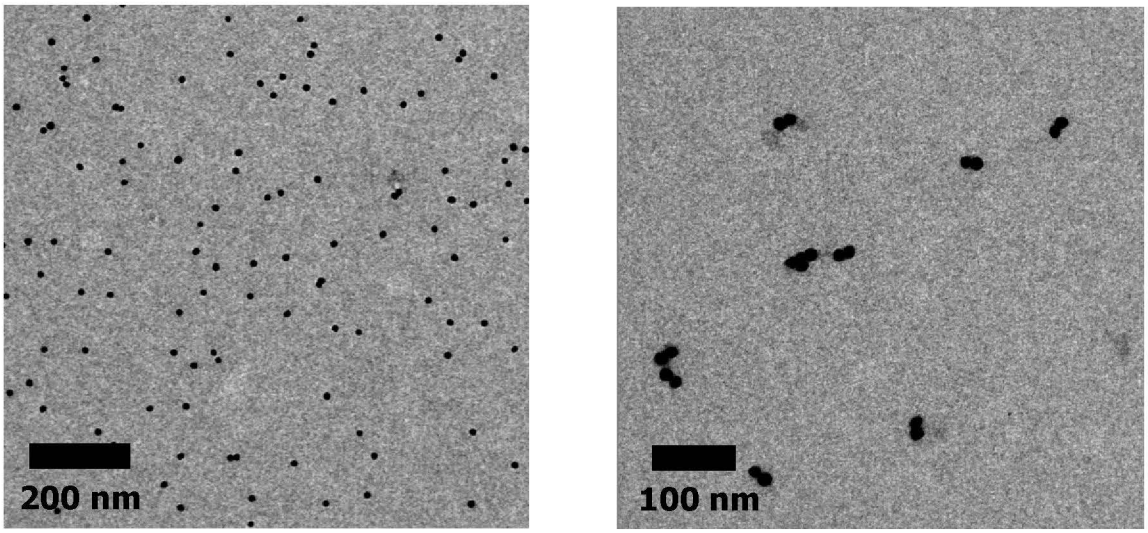

Figure 5. TEM images of the fractionated particles, top fraction I (left), bottom fraction IV (right).

SERS MEASUREMENTS

The synthesized structures are expected to provide a strong field enhancement that is interesting for a large number of potential applications. As such, SERS can be used to demonstrate the sensitivity of these measurements when utilizing NP dimers. These experiments allow furthermore to obtain deeper insight into the binding mechanism of the linker molecule.

Prior to the SERS-based investigation, reference Raman spectra of the linker were recorded since it is expected that the SERS spectrum of the gold NP clusters are dominated by contributions of molecules in close vicinity to the metal surface. In Fig. 6A a representative Raman spectrum of bulk material of the molecule is depicted. Despite the fluorescence background a specific Raman signature is detectable. The Raman mode at 2200 cm^{-1} is attributed to a C≡C stretching vibration. Both, the vibrations at 1581 cm^{-1} and 1543 cm^{-1} are assigned as C=C stretching vibration within the benzyl rings. The weak Raman mode at 1332 cm^{-1} is affected by CH_3 deformation vibrations. Due to the overlap of the CH_2 twisting and rocking and ring vibrations, the Raman mode at 1243 cm^{-1} is broadened. The very weak contribution at 1177 cm^{-1} is caused by a C-C stretching vibration. Finally, the Raman mode located at 1078 cm^{-1} is attributed to a ring breathing vibration.[49]

For the SERS-based characterization of the dimers, fraction IV of the gold NP clusters was coated on a glass substrate to allow the investigation of individual aggregates. In Fig. 6B the distribution of the prominent Raman mode at 2200 cm^{-1}, which is attributed to the contribution of the linker molecule, is shown. Thus, the bright spots on the surface indicate the presence of isolated NP clusters. Related SERS spectra (depicted without any pre-processing) are illustrated in Fig. 6C. The recorded SERS spectra a, b and c represent the characteristic signature of gold NP clusters, spectrum d shows that no significant background signal is recorded under the applied measuring conditions. The SERS spectra a, b and c are dominated by the contribution of

the linker molecule, which becomes clear when comparing the spectral position of the detected Raman modes with the reference Raman spectrum in Fig. 6A. Furthermore, the SERS spectra show a significant lower fluorescence background in relation to the Raman spectrum due to quenching processes, when molecules interact with the metallic surfaces of the NPs. Besides the demonstration that the linker molecule can be clearly detected due to the enhancement in the NP environment, further information about the binding characteristics of the linker molecules can be obtained from the data. Based on the surface selection rules the orientation of molecules towards the metal surface can be estimated by analyzing the SERS spectra.[45,46] Only Raman modes perpendicular to the metallic surface are enhanced preferentially which consequently dominate the SERS spectrum. Since the Raman modes at 2200 cm^{-1} (C≡C stretching vibration), 1578 cm^{-1} (C=C stretching vibration within the benzyl rings) and 1071 cm^{-1} (ring breathing) are preferably enhanced under SERS conditions and due to the linear conformation of the linker molecule, it is concluded that the linker molecule is oriented in upright or slightly tilted geometry with respect to the metal surface.

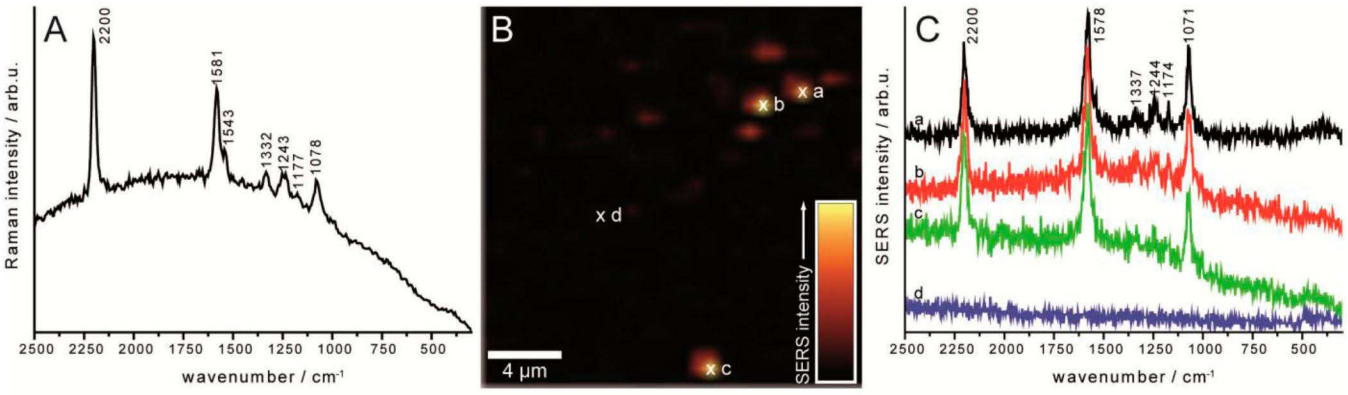

Figure 6. SERS-based characterization of gold nanoparticle cluster. (A) Reference Raman spectrum of the linker molecule. (B) SERS intensity map with bright spots indicating the

presence of nanoparticle clusters. (C) Related SERS spectra (a-c) and background signal of the substrate (d).

DETECTION OF SINGLE NANOCLUSTERS

In order to not only detect, but optically analyze small single NPs and NP dimers, a method based on a spatial modulation technique was employed[32] . The measurements are performed in a dual objective optical microscope setup (Fig. 7). The sample is illuminated from the bottom with a laser tightly focused by a 20x objective (Olympus LMPlan FLN, NA=0.4, WD=12 mm) to a diffraction-limited spot of about 1.5 µm in diameter. The forward scattered light is similarly collected with a 63x objective (Zeiss LD Plan-NEOFLUAR, 63x NA=0.75, WD=1.5 mm) from the top and detected by a photon multiplying tube (PMT).

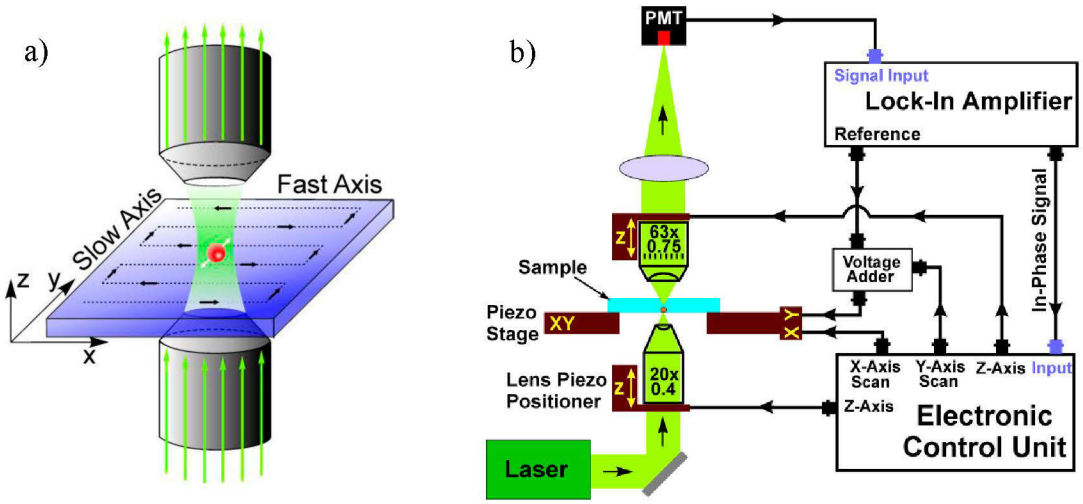

Figure 7: a) Illustration of the scanning regime. b) Schematic of the far-field detection setup consisting of a 2D scanning stage that modulates the position of the sample for lock-in detection while scanning. The modulation is added to the scanning by the voltage adder. The sample is illuminated by a laser from the bottom, while scattering light from the spatially modulated sample is collected from the top. Both objectives are hold by piezo positioners allowing precise alignment. The signal is detected with a PMT connected to the signal input of the lock-in amplifier. The in-phase signal from the lock-in amplifier is recorded.

The extinction coefficient of the tested dimers, illuminated by a laser beam with a wavelength near the surface plasmon resonance, is expected to be in the order of 10^{-4} in the given case. To distinguish such a small signal from the dominant background, spatial modulation of the sample position together with a lock-in detection scheme is implemented in the setup. The spatial modulation as well as the scanning is implemented by a single XY piezo stage, where the

modulation (with frequencies of several hundreds of Hz) is added to the slow scanning axis by a voltage adder, see schematic in Fig. 7 a. While scanning and oscillating the sample, the output of the PMT is measured with a lock-in amplifier at the frequency of the sample oscillations and the in-phase signal is recorded. The scanning speed is adjusted to allow for at least ten oscillations per scanning pixel. The electronic control unit performs the control of the piezo stage scanning, fine adjustments of the objective positioners, as well as detection of the signal.

The setup requires that the structure under investigation, i.e. the gold dimer NP, is isolated from adjacent particles within the radius of the diffraction-limited spot. However, the initial preparation technique of the samples relies on drying of a solution of NPs on a substrate, which typically results in an uncontrolled arrangement of particles. Hence a post-treatment of the samples is required to select the interesting particles for optical characterization.

At first, a diluted solution of the particles is dried on a fused silica substrate coated with a 10 nm layer of transparent conductive oxide. The resulting ensemble of particles distributed on the surface is inspected with a scanning electron microscope (SEM) and areas of clean and relatively isolated particles are identified. These areas are marked with alignment marks by means of focused ion-beam milling. Next, the entire area is imaged with high resolution by the scanning electron microscope, see Fig. 8. From the image, a single gold dimer is identified for optical testing. The coordinates of all particles in a 5 μm radius of the gold dimer are also extracted from the image. These coordinates are introduced in a lithography system which controls the focused ion-beam to etch away all unwanted particles leaving only the previously identified single NP on the substrate surface. To suppress unwanted scattering signals from the voids left after etching the particles, the ion beam was slightly defocused to a diameter of 200 nm, which results in smoother edges of the etched voids. It turned out that this is an important measure to reduce

disturbances of the actual measurement. A final high resolution SEM scan is performed to proof the absence of any gold NPs around the dimer NP which should be characterized. Eventually, the prepared sample was transferred to the optical far-field setup where the position of the dimer NP was identified based on the alignment marks.

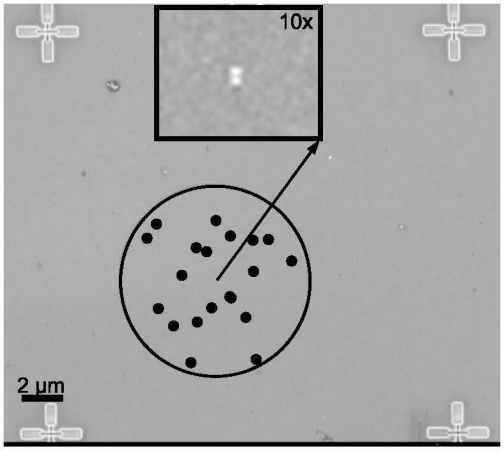

Figure 8: SEM image illustrating the sample preparation by removing particles adjacent to the central dimer with FIB milling at the black dots. Furthermore the alignment marks can be seen in the image. The inset shows the large magnification SEM image of the investigated dimer structure, which was isolated from all other plasmonic nanoparticles in the surrounding.

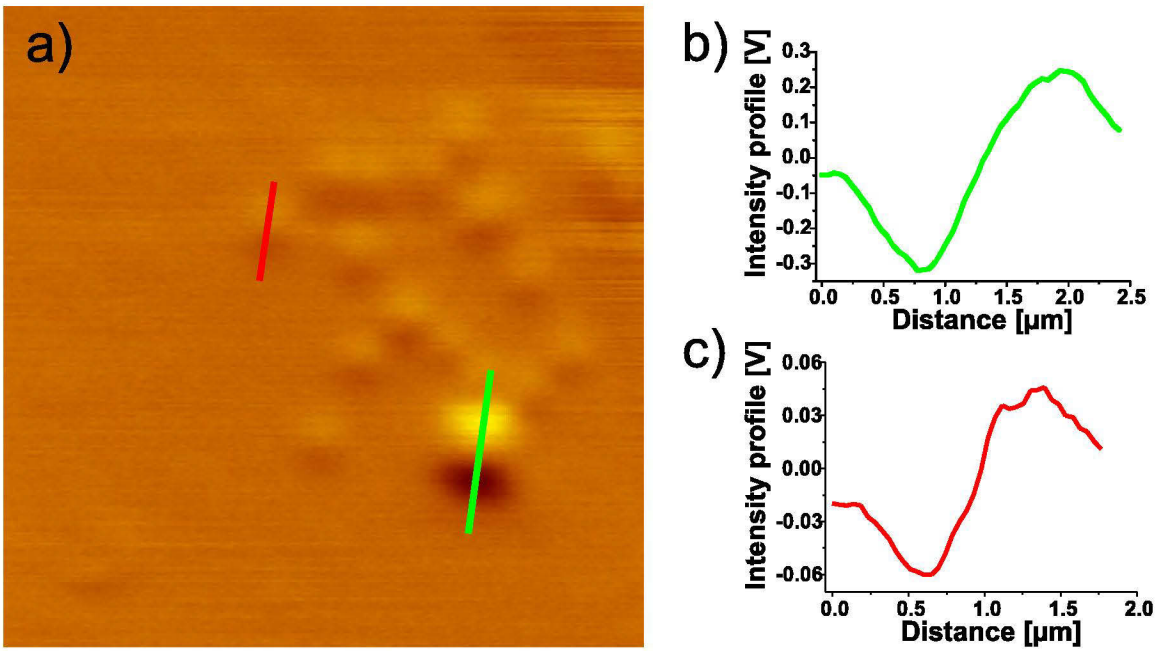

Figure 9: a) Recorded extinction image at a wavelength of 532 nm over an area of 12x12 µm². The strong double-lobe pattern at the position marked by the green line is the signature of the dimer nanoparticle, whereas the other features (one of them marked by red line) are signatures of the etched voids at the position of the removed nanoparticles. b) and c) Signal profiles along the lines indicated in the 2D plot. c) The extinction signal level of the dimer nanoparticle is five times higher than that of the voids.

The optical measurements of the dimer NP are performed at wavelengths of 532 nm and 561 nm and an illumination intensity of 0.2 µW. The sample oscillation amplitude was 0.97 µm at a frequency of 708.7 Hz. The results of the measurement, obtained with an illumination wavelength of 532nm, are presented in Fig. 9. The strong double-lobe pattern is the extinction signature of the dimer, resulting from the opposite phases of the signal derived from the lock-in amplifier. The spatial extension of this double-lobe in the image is determined rather by the diffraction limited focal spot size and not by the size of the dimer. In addition to the signal of the dimer, several similar patterns with less brightness can be seen in the image. They appear at the positions of the removed particles and are produced by the scattering of the etch voids formed during the particle removal. A comparison of the signal levels plotted in the inset of Fig. 9 shows

that the extinction ratio of the dimer is 5 times stronger than that of the voids. This demonstrates that the extinction of a dimer with elongation of about 25 nm can be unambiguously characterized.

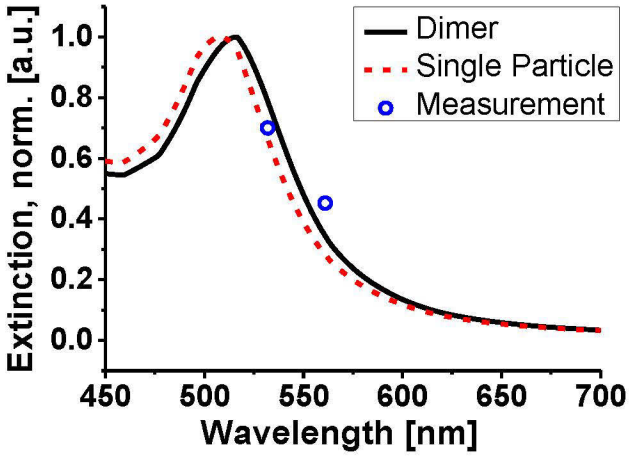

Figure 10: The plot shows normalized extinction cross sections calculated for a dimer composed from two spherical nanoparticles with radii of 7 nm and a distance of 2 nm (solid line), a single spherical particle with a radius of 7 nm (dashed line). The measured values (blue circles) at the wavelength of 532 nm and 561 nm are in good correspondence with the calculated ones.

From the respective extinction images that are recorded for wavelengths of 532 nm and 561 nm the absolute value of the extinction cross-sections was difficult to retrieve but a suitable normalisation allows for a comparison to simulations and allows especially to evaluate the relative strength of the extinction cross-sections at the two wavelengths. In Fig. 10 the measured extinction is compared to numerically calculated spectra.

Simulations are performed using a numerical method that solves Maxwell's equations self-consistently for a given illumination of an arbitrary constellation of spheres[47]. In this method the electromagnetic fields are expanded into eigenmodes, which are vector spherical harmonic functions. Enforcing the usual boundary condition at the interface of the spheres yields the

amplitudes of all eigenmodes from which the extinction cross-section can be calculated. Dimer structures consisting of spherical NPs with radii of 7 nm and a separation of 2 nm were considered, in full agreement with the known experimental details. The material parameter used for the simulation, i.e. the gold permittivity[48], includes a size dependent correction of the imaginary part. The permittivity of the surrounding medium is set to unity. The dimer is illuminated by a plane wave normal to the connection line of the NPs. The illumination is linearly polarized with an angle of 45° with respect to the connection line. In this way, both possible eigenmodes of the dimer can be excited under normal incidence. The only aspect that was not considered is the presence of the linker molecule in the junction and the dielectric substrate. Their influence can be assumed to be negligible.

The resulting normalized extinction spectra of the dimer and, for comparison, of a single spherical particle with a radius of 7 nm are shown in Fig. 10. Comparing the normalized spectra to the measured extinction cross-sections a very good agreement can be observed with respect to the relative strength of the measured extinction at the discrete wavelengths.

To provide finally insights into the fields directly in the junction, we calculated the electric field in the vicinity of the dimer with the same parameters. It turns out that the field at the presumed position of the linker molecule on the connection line of the spheres is highly localized and almost one order of magnitude stronger than the incident light ensuring strong fields for the SERS measurements (Fig. 11).

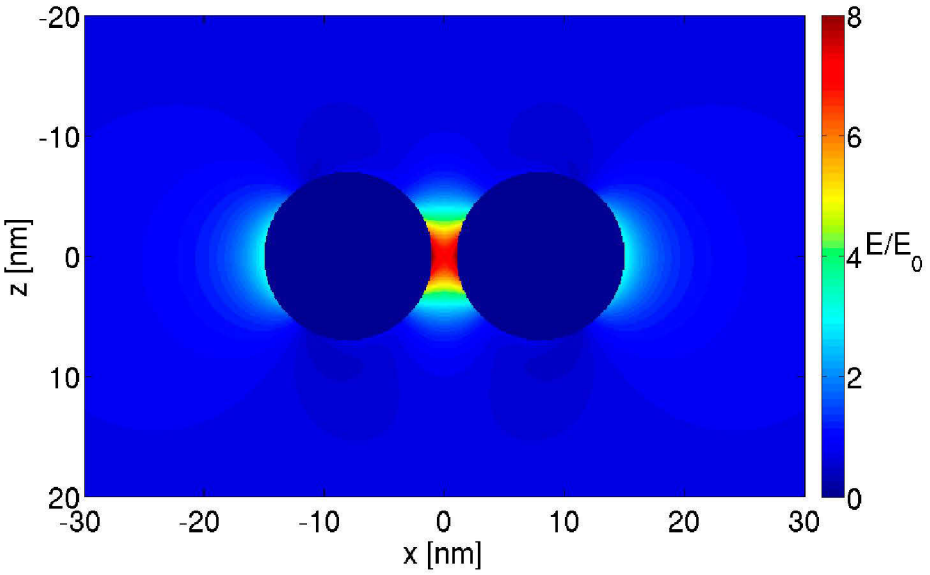

Figure 11: Absolute value of the electric field normalized with the amplitude of the incident field E_0.

It can be concluded that the optical detection method applied for these measurements proved to be very sensitive yielding results that show agreement with theoretical predictions.

CONCLUSION

We demonstrated the synthesis of gold NP clusters with a specially designed linker molecule. A solution of gold monomers mixed with an increasing amount of linker solution shows a significant red shift of the plasmon resonance, revealing that the linker indeed causes the NPs to assemble. By centrifugation of such a mixture we separated different NP fractions with distinct color shades and characteristic sedimentation coefficients and confirmed via TEM imaging that at least one fraction contains dimers.

With SERS technique we were able to measure the response from single dimers and could confirm the presence of the linker molecule in the junction of the dimer. It was confirmed that the linker molecule is in upright position on the surface by investigating the strength of the different Raman modes. Furthermore, we used a novel lock-in method to record an extinction signal of an isolated gold dimer at specific frequencies. This is possible by etching away nearby particles after the drying process. In principle, it is possible to measure complete extinction spectra of these dimers or other self-assembled NPs with the chosen method if the measurement is repeated for a large number of frequencies. This technique allows measuring the optical properties of single, isolated NPs as opposed to particles in a solution or on a lattice, making it easier to compare to numerical simulations and to characterize anisotropic NPs.

With the combination of measurement techniques it was demonstrated that we were able to fabricate and to characterize rigidly linked NPs. These findings elucidate moreover the binding mechanism and will pave the way towards various plasmonic applications such as sensors, photocatalysis, and plexcitonics. Especially the ability to form dimers where metallic NPs are separated by only a few nanometers, allows achieving huge fields and also huge gradients of the electric field on length scales comparable to the size of molecules. Then, potentially, even

electric dipole forbidden transitions can be excited in the molecules, which would open unprecedented spectroscopic opportunities and could open new paths to characterize and to understand the dynamics and chemical reactions at the level of singular molecules.

AUTHOR INFORMATION

Corresponding Author: martin.fruhnert@uni-jena.de

Author Contributions

MF and CR performed all simulation and have been providing the theoretical guidance. FK synthesized the molecule and performed UV-Vis spectroscopy. IP did the centrifugation, DC recorded SERS spectra and SH executed TEM measurements. RG and TP isolated the dimers and performed the extinction measurements. The manuscript was written through contributions of all authors. All authors have given approval to the final version of the manuscript. ‡These authors contributed equally.

ACKNOWLEDGMENT

This work was supported by the German Federal Ministry of Education and Research (PhoNa) and by the Thuringian State Government (MeMa).

REFERENCES

[1] D. R. Shankaran, K. V. Gobi, and N. Miura, Sensors Actuators B: Chem. **121**, 158 (2007).
[2] X. Wang, P. Wang, C. Chen, J. Chen, Y. Lu, H. Ming, and Q. Zhan, J. Appl. Phys. **107** (2010).
[3] Y. Chen and H. Ming, Photonic Sens **2**, 37 (2012).
[4] R. Perez-Pineiro, M. A. Correa-Duarte, V. Salgueirino, and R. A. Alvarez-Puebla, Nanoscale **4**, 113 (2012).
[5] L. Rodriguez-Lorenzo, Z. Krpetic, S. Barbosa, R. A. Alvarez-Puebla, L. M. Liz-Marzán, I. A. Prior, and M. Brust, Integr. Biol. **3**, 922 (2011).
[6] S. Mühlig, A. Cunningham, S. Scheeler, C. Pacholski, T. Bürgi, C. Rockstuhl, and F. Lederer, ACS Nano **5**, 6586 (2011).
[7] M. K. Hedayati, A. U. Zillohu, T. Strunskus, F. Faupel, and M. Elbahri, Appl. Phys. Lett. **104** (2014).
[8] T. Nagatsuka *et al.*, ACS Appl. Mater. Interfaces **5**, 4173 (2013).
[9] M. Wegener, in *Biophotonics: Spectroscopy, Imaging, Sensing, and Manipulation*, edited by B. D. Bartolo, and J. Collins (Springer Netherlands, 2011), pp. 19.

[10] P. K. Jain and M. A. El-Sayed, Chem. Phys. Lett. **487**, 153 (2010).
[11] R. Zhang *et al.*, Nature **498**, 82 (2013).
[12] D. Graham, D. G. Thompson, W. E. Smith, and K. Faulds, Nat. Nanotechnol. **3**, 548 (2008).
[13] M. Homberger, S. Schmid, J. Timper, and U. Simon, J. Cluster. Sci. **23**, 1049 (2012).
[14] X. Liu *et al.*, Langmuir **26**, 3179 (2010).
[15] Y. Chaikin, H. Leader, R. Popovitz-Biro, A. Vaskevich, and I. Rubinstein, Langmuir **27**, 1298 (2011).
[16] W. P. McConnell, J. P. Novak, L. C. Brousseau, R. R. Fuierer, R. C. Tenent, and D. L. Feldheim, J. Phys. Chem. B. **104**, 8925 (2000).
[17] T. Dadosh, Y. Gordin, R. Krahne, I. Khivrich, D. Mahalu, V. Frydman, J. Sperling, A. Yacoby, and I. Bar-Joseph, Nature **436**, 677 (2005).
[18] M. Orbach, M. Lahav, P. Milko, S. G. Wolf, and M. E. van der Boom, Angew. Chem. Int. Ed. **51**, 7142 (2012).
[19] J. W. Ying, D. R. Sobransingh, G. L. Xu, A. E. Kaifer, and T. Ren, Chem. Commun., 357 (2005).
[20] J. M. Wessels, H. G. Nothofer, W. E. Ford, F. von Wrochem, F. Scholz, T. Vossmeyer, A. Schroedter, H. Weller, and A. Yasuda, J. Am. Chem. Soc. **126**, 3349 (2004).
[21] M. P. Stemmler, Y. Fogel, K. Müllen, and M. Kreiter, Langmuir **25**, 11917 (2009).
[22] R. Kaminker, M. Lahav, L. Motiei, M. Vartanian, R. Popovitz-Biro, M. A. Iron, and M. E. van der Boom, Angew. Chem. Int. Ed. **49**, 1218 (2010).
[23] H. Yan, S. I. Lim, L.-C. Zhang, S.-C. Gao, D. Mott, Y. Le, R. Loukrakpam, D.-L. An, and C.-J. Zhong, J. Mater. Chem. **21**, 1890 (2011).
[24] J. P. Novak, C. Nickerson, S. Franzen, and D. L. Feldheim, Anal. Chem. **73**, 5758 (2001).
[25] A. Kuzyk, R. Schreiber, Z. Fan, G. Pardatscher, E.-M. Roller, A. Hogele, F. C. Simmel, A. O. Govorov, and T. Liedl, Nature **483**, 311 (2012).
[26] X. Zeng, F. Liu, A. G. Fowler, G. Ungar, L. Cseh, G. H. Mehl, and J. E. Macdonald, Adv. Mater. **21**, 1746 (2009).
[27] C. F. Bohren and D. R. Huffman, *Absorption and scattering of light by small particles* (John Wiley & Sons, 2008).
[28] C. Sonnichsen, B. M. Reinhard, J. Liphardt, and A. P. Alivisatos, Nat. Biotechnol. **23**, 741 (2005).
[29] W. Chen, A. Kimel, A. Kirilyuk, and T. Rasing, Phys. Status Solidi (b) **247**, 2047 (2010).
[30] D. Sadiq, J. Shirdel, J. S. Lee, E. Selishcheva, N. Park, and C. Lienau, Nano Lett. **11**, 1609 (2011).
[31] A. García-Etxarri, I. Romero, F. J. G. de Abajo, R. Hillenbrand, and J. Aizpurua, Phys. Rev. B **79**, 125439 (2009).
[32] A. Arbouet, D. Christofilos, N. Del Fatti, F. Vallée, J. Huntzinger, L. Arnaud, P. Billaud, and M. Broyer, Phys. Rev. Lett. **93**, 127401 (2004).
[33] P. Billaud *et al.*, J. Phys. Chem. C **112**, 978 (2008).
[34] D.-S. Kim, J. Heo, S.-H. Ahn, S. W. Han, W. S. Yun, and Z. H. Kim, Nano Lett. **9**, 3619 (2009).
[35] D. J. Lavrich, S. M. Wetterer, S. L. Bernasek, and G. Scoles, J. Phys. Chem. B. **102**, 3456 (1998).
[36] T. Weidner, N. Ballav, U. Siemeling, D. Troegel, T. Walter, R. Tacke, D. G. Castner, and M. Zharnikov, J. Phys. Chem. C. **113**, 19609 (2009).
[37] J. Noh, H. S. Kato, M. Kawai, and M. Hara, J. Phys. Chem. B. **106**, 13268 (2002).
[38] P. Chinwangso, A. C. Jamison, and T. R. Lee, Acc. Chem. Res. **44**, 511 (2011).

[39] J. Turkevich, P. C. Stevenson, and J. Hillier, Discuss. Faraday Soc. **11**, 55 (1951).
[40] A. Singh, D. H. Dahanayaka, A. Biswas, L. A. Bumm, and R. L. Halterman, Langmuir **26**, 13221 (2010).
[41] D. H. Tsai, L. F. Pease, R. A. Zangmeister, M. J. Tarlov, and M. R. Zachariah, Langmuir **25**, 140 (2009).
[42] M. K. Brakke, J. Am. Chem. Soc. **73**, 1847 (1951).
[43] G. Chen, Y. Wang, L. H. Tan, M. Yang, L. S. Tan, Y. Chen, and H. Chen, J. Am. Chem. Soc. **131**, 4218 (2009).
[44] O. Akbulut, C. R. Mace, R. V. Martinez, A. A. Kumar, Z. Nie, M. R. Patton, and G. M. Whitesides, Nano Lett. **12**, 4060 (2012).
[45] X. Gao, J. P. Davies, and M. J. Weaver, J. Phys. Chem. **94**, 6858 (1990).
[46] E. C. Le Ru, S. A. Meyer, C. Artur, P. G. Etchegoin, J. Grand, P. Lang, and F. Maurel, Chem. Commun. **47**, 3903 (2011).
[47] S. Mühlig, C. Rockstuhl, J. Pniewski, C. R. Simovski, S. A. Tretyakov, and F. Lederer, Phys. Rev. B **81**, 075317 (2010).
[48] P. B. Johnson and R. W. Christy, Phys. Rev. B **6**, 4370 (1972).

Supporting information for:

Synthesis, separation, and hypermethod characterization of gold nanoparticle dimers connected by a rigid rod linker

Martin Fruhnert[*,†], *Florian Kretschmer*[¶,‡], *Reinhard Geiss*[§], *Igor Perevyazko*[¶,‡] *Dana Cialla-May*[#,$], *Michael Steinert*[§], *Norik Janunts*[§], *Dmitry Sivun*[§] *Stephanie Hoeppener*,[¶,‡] *Martin D. Hager*,[¶,‡] *Thomas Pertsch*[§], *Ulrich S. Schubert*[¶,‡] *and Carsten Rockstuhl*[‖,⊥]

† Institute of Condensed Matter Theory and Solid State Optics, Abbe Center of Photonics, Friedrich Schiller University Jena, D-07743 Jena, Germany

¶ Laboratory of Organic and Macromolecular Chemistry, Friedrich Schiller University Jena, D-07743 Jena, Germany

Friedrich Schiller University Jena, Institute of Physical Chemistry, Helmholtzweg 4, 07743 Jena, Germany

$ Leibniz Institute of Photonic Technology, Albert-Einstein-Straße 9, 07745 Jena, Germany

§ Institute of Applied Physics, Abbe Center of Photonics, Friedrich Schiller University Jena, D-07743 Jena, Germany

‡ Jena Center for Soft Matter, Friedrich Schiller University Jena, D-07743 Jena, Germany

‖Institute of Theoretical Solid State Physics, Karlsruhe Institute of Technology, D-76131 Karlsruhe, Germany

⊥Institute of Nanotechnology, Karlsruhe Institute of Technology, D-76021 Karlsruhe, Germany

Email: martin.fruhnert@uni-jena.de

Instrumentation. ^{1}H and ^{13}C NMR spectra were recorded on a Bruker AC 250 (250 MHz) in deuterated chloroform. UV-Vis absorption spectra were recorded on a Thermo Scientific Unicam UV 500 spectrophotometer.

The Raman and SERS spectra were recorded applying a WITec Raman microscope (WITec GmbH, Ulm, Germany) equipped with a 300 lines/mm grating. As excitation source, the 633 nm line of a He–Ne laser was used. For recording the Raman reference spectra, a laser power of 5 mW incident on the sample and an integration time of 5 s were employed. In the case of the SERS measurements, the laser power incident on the sample was 0.6 mW to avoid burning effects and the integration time of the single spectra was 2 s. The Raman scattered light was detected by a CCD camera. A 100 x objective (NA 0.95) was used for focusing the laser light onto the samples and collecting the Raman signal. TEM measurements were performed on a Philips CM-120. 15 μL of the sample solution were blotted onto clean carbon coated TEM grids (Mesh 400, Quantifoil, Jena) and excess material was removed by a filter paper (Whatman No. 1); the samples were allowed to dry prior to the transfer to the microscope. Grid cleaning was performed by UV-ozone treatment for 40 s.

Materials and Preparation. All used chemicals and solvents were purchased from Biosolve, Sigma-Aldrich, Acros Organics, Apollo Scientific as well as Alfa Aesar and were used without further purification. Dry THF, was purchased from a Pure Solv MD-4-EN solvent purification system. Triethylamine was dried over KOH and distilled under nitrogen prior to usage. S-(4-iodophenyl) ethanethioate 1 and 1,4-diethynyl-2,5-bis(octyloxy)benzene 2 were prepared according to the literature.[1-2]

Synthesis of S,S'-(((2,5-bis(octyloxy)-1,4-phenylene)bis(ethyne-2,1-diyl))bis(4,1-phenylene)) diethanethioate 3

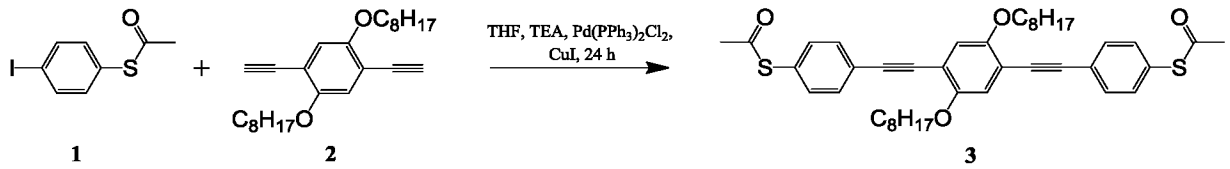

1 2 3

1 (441 mg, 1.60 mmol) and **2** (200 mg, 0.52 mmol) were dissolved in a mixture of 10 mL THF and 5 mL triethylamine. After purging the solution for 60 minutes with nitrogen, *bis*(triphenylphosphine)palladium(II) dichloride (18 mg, 26 µmol) and copper(I) iodide (5 mg, 26 µmol) were added. The solution was stirred for 2 d at room temperature. The solvent was evaporated and column chromatography (Silica 60) was performed (CH_2Cl_2: Hexanes 2:1) to obtain compound **3** as a yellow solid. Yield 251 mg (71% of theory)

^{1}H NMR (250 MHz, $CDCl_3$): δ = 7.92 (2 H, s, 3), 7.75 (2 H, s, 6), 6.99 (2 H, s, 1), 2.65 (4 H, t, α-CH_2, J = 7.5 Hz), 1.66 (4 H, m, α-CH_2, J = 6.6 Hz), 1.43-1.19 (12 H, m, 6 CH_2,), 0.86 (6 H, t, CH_3, J = 6.6 Hz) ppm.

^{13}C NMR (250 MHz, $CDCl_3$): δ = 152.6 (C7), 144.3 (C2), 139.0 (C4), 129.0 (C5), 126.0 (C6), 125.56 (C1), 121.5 (C3), 31.7, 30.7, 30.5, 29.1, 22.6, 14.1 ($CH_2(CH_2)_4CH_3$) ppm.

HR-MS (MALDI-TOF): m/z = 469.18 $[M+H]^+$.

EA: calculated for $C_{42}H_{50}O_4S_2$: C: 73.86%; H: 7.38%, S: 9.39%, O: 9.37% found: C: 74.12%; H: 7.41%, S: 9.35%.

Synthesis of gold nanoparticles

In a 250 mL round bottom flask 200 mL of a 1 mM $HAuCl_4$ solution was heated to 100 °C while stirring at 700 rpm. To the refluxing solution 1 mL of a 0.78 M sodium citrate solution was added at once. The color of the solution turned red after ~ 30 seconds. Heating was continued for 30 minutes, afterwards the solution was cooled down and stored in the dark at 4 °C.

Assembly protocol: Solutions of DBU and **3** were prepared in DMF (See table xy for exact concentrations) For the preparation always 100 µL of the linker solution and 10 µl of the respective DBU solution was mixed for 1 minute. 100 µL of this solution were then added to 1 mL of gold nanoparticles under stirring at 1000 rpm. After 1 minute of stirring 100 µL of an aqueous polyacrylic acid solution (10 mg/mL, M_n = 25.000 g/mol) was added and the solution was stirred again for 1 minute. UV-Vis measurements were conducted by diluting 100 µL of the nanoparticle solution with 900 µL water.

Solution	3 [mg/mL]	DBU [mg/mL]	Volume of solution 3 [µL]	Volume of the DBU solution [µL]
1	0,1	1	100	10
2	0,2	2	100	10
3	0,3	3	100	10
4	0,4	4	100	10
5	0,5	5	100	10
6	0,6	6	100	10
7	0,7	7	100	10

8	0,8	8	100	10
9	0,9	9	100	10
10	1	10	100	10
Control	-	10	100 pure DMF	10

Density gradient centrifugation

The linear density gradients were prepared in 14 mm diameter, 13.2 mL capacity ultracentrifuge tubes (ultra clear tubes, Beckman) using a gradient maker consisting of two chambers connected *via* a channel with a stopcock; final gradient volume was 11.7 mL. At first, 0.5 mL of 60% w/w sucrose solution was placed on the bottom of the tube before the main gradient solution was loaded. The main gradient was obtained by mixing 5.6 mL of 10% w/w and 5.6 mL of 40% w/w sucrose solution in a mixing chamber by the way that the lower density solution was loaded first into the centrifugal tube. The gradient prepared was then stored for an hour at room temperature. The initial particle solution (0.5 mL) was placed on the top of the gradient. The centrifugal tube was then placed in a swinging bucket rotor and centrifuged at 7,500 rpm for 75 minutes. After centrifugation, the fractions were collected by a pipette from the top of the vial, depending on the sample each 0.5 – 2 mL of the solution was collected. The fractions collected were then dialyzed against pure water, till the sucrose solution was completely removed from the solution. The dialyzed fractions were analyzed by analytical ultracentrifugation and scanning electron microscopy.

Analytical ultracentrifugation

Sedimentation velocity experiments were performed with a ProteomeLab XLI Protein Characterization System analytical ultracentrifuge (Beckman Coulter, Brea, CA), using

conventional double-sector Epon centerpieces of 12 mm optical path length and a four-hole rotor (AN-60Ti). Rotor speed was 1,000 to 40,000 rpm, depending on the sample. Cells were filled with 420 μL of sample solution at initial concentration and 440 μL of solvent. Before the run, the rotor was equilibrated for approximately 1 h at 20 °C in the centrifuge. Sedimentation profiles were obtained by absorbance and interference optics at the same temperature. For the analysis of the sedimentation velocity data ls-$g^*(s)$ as well as c(s).[3-4] Ls-$g^*(s)$ represents the least-square boundary analysis, which describes sedimentation of non-diffusing species. C(s) analysis based on the numerical resolution of the Lamm equation assuming the same frictional ratio values for each *s* value. As partial specific volume, $\nu = 0.052$ cm^3 g^{-1} was used.

[1] J. Wu, C. Chi, X. Wang, J. Li, X. Zhao, F. Wang, *Synth. Commun.* **2000**, *30*, 4293-4298.

[2] M. S. Khan, M. R. A. Al-Mandhary, M. K. Al-Suti, T. C. Corcoran, Y. Al-Mahrooqi, J. P. Attfield, N. Feeder, W. I. F. David, K. Shankland, R. H. Friend, A. Köhler, E. A. Marseglia, E. Tedesco, C. C. Tang, P. R. Raithby, J. C. Collings, K. P. Roscoe, A. S. Batsanov, L. M. Stimson, T. B. Marder, *New J. Chem.* **2003**, *27*, 140-149.

[3] P. Schuck, P. Rossmanith, *Biopolymers* **2000**, *54*, 328-341.

[4] P. Schuck, *Biophys. J.* **2000**, *78*, 1606-1619.

Publication P3

Synthesis of a Rigid Tetrahedral Linker with Thioether End Groups

F. Kretschmer, A. Wild, M. Hager, U. S. Schubert

Synthesis **2014**, *46*, 475-478.

Synthesis of a rigid tetrahedral linker with thioether end groups

Florian Kretschmer,[a,b] Andreas Wild,[a,b] Martin D. Hager,[a,b] Ulrich S. Schubert[a,b]*

[a] Laboratory of Organic and Macromolecular Chemistry (IOMC), Friedrich-Schiller-Universität Jena, Humboldtstr. 10, 07743 Jena, Germany

[b] Jena Center for Soft Matter (JCSM), Friedrich-Schiller-Universität Jena, Philosophenweg 7, 07743 Jena, Germany

Fax: 00493641948202

E-mail: ulrich.schubert@uni-jena.de

Received:

Abstract: The synthesis of a tetrahedral thio end-functionalized rigid oligo(*p*-phenylene ethynylene) (OPE) based on a convergent approach is reported.

Key words: Alkynes, Cross-coupling, Nanostructures.

There has been an increasing interest in the synthesis and self-assembly of noble metal nanoparticles in recent years. In particular gold and silver particles gathered attention as they feature a localized surface plasmon resonance in the visible region and due to their high environmental stability.[1] Their tunable size and structure allows to fabricate devices with tailor-made optical properties, which could be used in potential applications for energy conversion,[2] medicinal therapy,[3] sensors[4] and optical devices.[5] Moreover, their optical response is not only governed by their dimension or shape but, in fact, also by the spatial arrangement of the particles to each other. Hence, it is crucial to implement methods which enable the precise formation of ordered plasmonic nanoparticle assemblies. Top-down approaches involve the pattering of large preformed metal structures whereas the top-up strategy utilizes patterned surfaces which are subsequently functionalized with nanoparticles. The bottom-up approach relies on the assembly of nanoparticles, *e.g.* , *via* chemical reactions or electrostatic interactions. Click,[6] Diels-Alder[7] and oligonucleotide[8] reactions have successfully been used to create clusters with a precise number of particles. Moreover, mediated by polymers, clusters with dozens of particles can be synthesized.[9] Thiols and, to a smaller extend, amines show a strong affinity towards gold surfaces. Molecules with a defined geometry, *e.g.*, thio-endfunctionalized linear linkers therefore allow to create ordered nanoparticle structures. The electromagnetic interactions between the particles and, hence, the optical response is strongly dependent on the interparticle distance. As a result, a pivotal point is to utilize molecules with a defined distance between the functional moieties. While α,ω-alkane thiols have been employed to assemble gold nanoparticles the flexibility of the alkyl chain prevents a stable gap between the particles.[10] In order to evade this problem rigid linker molecules based on arylene vinylenes and arylene ethynylenes were introduced as a design principle.[11] However, up to now, there still remains uncertainty on the exact binding mode of such linkers. Yan and co-workers reported the synthesis of rigid quadratic and trigonal planar linkers but instead of binding three or four gold nanoparticles the chelating effect allowed only to bridge two particles.[12] In contrast, Novak *et al.* reported the successful formation of dimers and trimers with similar linkers.[13]

Here we report the synthesis of a tetrahedral molecule. By attaching **8** to a large gold nanoparticle surface the most probable structure is that three arms bind to the surface of the particle. The fourth arm stands out perpendicular to the surface able to bind another particle. If instead, compared to the linker size, small nanoparticles are employed each arm would be able to bind one particle resulting in a tetrahedral cluster.

Different strategies can be utilized to create these kinds of linkers.[14] In the divergent approach, starting from a tetraphenylmethane core in consecutive steps more and more phenyl ethynylene units could be coupled onto the core. However, side reactions or incomplete functionalization of all arms results in structures with similar properties (*e.g.*, R_f-value). Therefore, separation of these impurities from the desired product becomes a tedious task the longer the arm becomes. The second strategy involves the

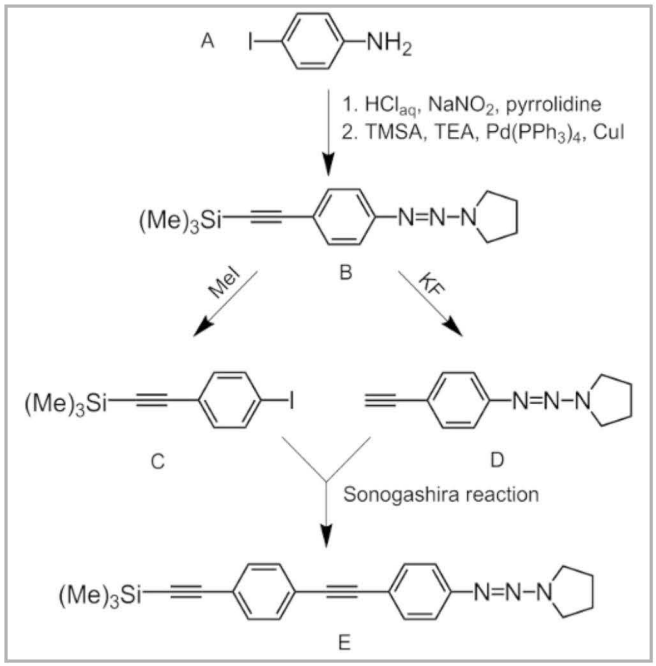

Scheme 1 Schematic representation of the synthesis of OPEs.[14]

convergent approach where first the arm is synthesized followed by the final attachment to the core. An acetylene functionalized core and an iodo functionalized arm could be coupled *via* a Sonogashira reaction. Star-star coupling of the core, however, leads to a complex mixture of byproducts. Hence, the more versatile approach is the utilization of an iodo substituted core and the respective arm. The creation of large rigid OPE structures can be accomplished in most cases by utilizing the bifunctional compound **C** which can be coupled onto an acetylene moiety *via* a Sonogashira reaction (**Scheme 1**).[15] Subsequent cleavage of the $SiMe_3$ protecting group followed by a reaction with **C** allows to increase the number of repeating units in consecutive steps. Another strategy involves the orthogonal deprotection of compound **B**, which can be converted either to compound **C** or to compound **D**.[16] **D** can be coupled with a corresponding iodo compound followed by conversion of the triazene moiety with, *e.g.*, MeI to yield the elongated iodo compound.

Para-iodoaniline (**A**) is a common starting material for both approaches; however, incorporation of side chains which improve the solubility is difficult to achieve. For an increasing number of repeating units the solubility of the OPEs decreases due to extensive π-stacking. Experiments conducted with linear linkers devoid of side-chains showed only poor solubility which hampers purification as well as potential applications.

Hydroquinone revealed to be a suitable starting material for linkers with increased solubility as it allows the introduction of long alkyl side chains *via* etherification of the hydroxyl groups. Moreover, halogenation with NBS and iodine followed by a Sonogashira reaction yields compound **1**, which is similar in its structure to **C**. The strength of the gold-sulfur interaction is to a large extend dependent on the nature of the thio moiety.[17] Thiol groups and disulfides bind most strongly; however, they interfere with the palladium catalyzed cross-coupling reaction. While thioacetates can be utilized as protecting groups for thiols we found that they are also cleaved off to a significant extend during the reaction hampering multiple consecutive synthetic steps with this moiety. Hence, while offering a less strong gold-sulfur interaction, thioethers were chosen due to their good chemical stability. Therefore, **1** was converted with *p*-ethynylthioanisole **2** in a Sonogashira reaction to yield **3** as a yellow solid. It should be noted that **1** can contain substantial amounts of the disubstituted trimethylsilylacetylene (TMSA) compound where additionally the bromine is substituted by TMSA. Both are difficult to separate *via* column chromatography, however, when converted with **2**

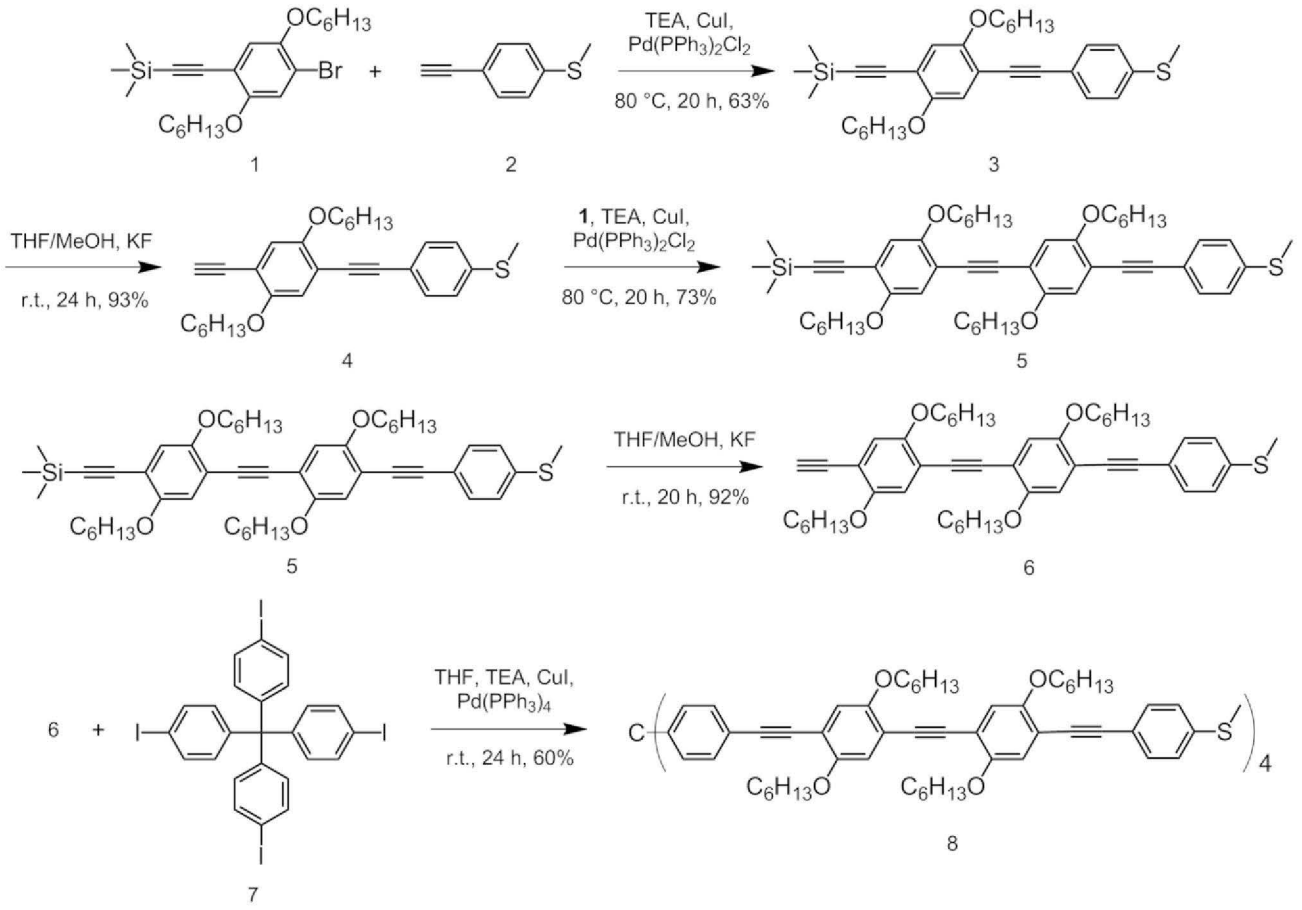

Scheme 2 Schematic representation of the synthesis of the tetrahedral linker.

only the bromo substituted compound reacts. Compound **3** can then easily be separated from the disubstituted compound by column chromatography. The conversion of the reaction and the attachment of the phenylene-ethynylene units can easily be followed by thin layer chromatography. Both the R_f-value and the fluorescence of the product change significantly as the length of the conjugated π system increases. In the following step cleavage of the trimethylsilyl group was achieved *via* conversion with potassium fluoride under an inert atmosphere to yield the acetylene **4**. Subsequently, a second Sonogashira reaction was applied in order to react **4** with compound **1** to yield **5** in 73% yield. Cleavage of the trimethylsilyl groups was accomplished in the same way as described before to yield the linker arm **6**. Through a Sonogashira reaction of the arm with tetrakis(4-iodophenylmethane) **7** finally the tetrahedral linker **8** could be synthesized. The compound shows good solubility in common organic solvents like chloroform, THF and DMF.

In conclusion, a novel rigid tetrahedral linker for the potential self-assembly of gold nanoparticles has been synthesized. The formation of plasmonic superstructures with this compound is currently under investigation.

Reagents and solvents were purchased from Carl Roth, Sigma-Aldrich, Fluka, Merck and VWR. All chemicals were used as received. THF was distilled over sodium/benzophenone under an argon atmosphere. Triethylamine was distilled over KOH under an argon atmosphere. ^{1}H and ^{13}C NMR spectra were recorded on a Bruker AC 300 at 298 K. Chemical shifts are reported in parts per million (ppm, δ scale) and were calibrated against residual protio-solvent. ESI-Q-TOF-MS measurements were performed with a micrOTOF (Bruker Daltonics) mass spectrometer. Elemental analyses were carried out on a Vario ELIII – Elementar Euro and an EA from HekaTech. Melting points were determined on a Stuart SMP3. IR spectra were measured on a Shimadzu IRAffinity-1 FTIR-spectrophotometer. Compounds **1**,[18] **2**[19] and **7**[20] were prepared as reported in the literature.

((2,5-Bis(hexyloxy)-4-((4-(methylthio)phenyl)-ethynyl)phenyl)ethynyl)trimethylsilane (3)

1 (3.06 g, 6.75 mmol), **2** (1 g, 6.75 mmol) and CuI (13 mg, 6.8 µmol) were dissolved in 50 mL TEA. The solution was purged with argon for 1 h and subsequently $Pd(PPh_3)_2Cl_2$ (48 mg, 6.8 µmol) was added. The solution was heated to 80 °C and stirred at this temperature for 20 h. Afterwards the solvent was removed under reduced pressure and the residue was dissolved in 100 mL $CHCl_3$. The organic phase was washed three times with water, dried over Na_2SO_4 and finally the solvent was removed under reduced pressure. The crude product was purified *via* column chromatography (SiO_2, methylene chloride:hexane, 1:1) to obtain compound **3** as a yellow solid. Yield 2.2 g (63% of theory).

Mp 67 °C

IR (FTIR): 2940, 2859, 2156, 1504, 1389, 1215, 1030, 891, 837, 810, 760, 637 cm^{-1}.

^{1}H NMR (300 MHz, CD_2Cl_2): δ = 7.46 (d, J = 8.2 Hz, 2 H), 7.25 (d, J = 8.2 Hz , 2 H), 7.00 (s, 1 H), 6.96 (s, 1 H), 4.02 (m, 4 H, 2 O-CH_2), 2.54 (s, 3 H, S-CH_3), 1.84 (m, 4 H, 2 CH_2), 1.58 (m, 4 H, 2 CH_2), 1.39 (m, 8 H, 4 CH_2), 0.94 (m, 6 H, 2 CH_3), 0.29 (s, 9 H, 3 Si-CH_3) ppm.

^{13}C NMR (75 MHz, CD_2Cl_2): δ = 155.4, 154.7, 141.09, 133.01, 127.01, 120.76, 118.43, 118.09, 115.49, 114.88, 102.47, 101.26, 95.82, 87.23, 70.88, 70.84, 32.91, 32.89, 30.62, 30.6, 27.02, 27.0, 23.95, 16.38, 15.14, 15.12, 0.91 ppm.

HRMS (ESI): *m/z* calculated for $[C_{32}H_{44}O_2SSi]^{Na+}$: 543.2723; found: 543.2712 [M + Na].

Anal. Calcd for $C_{32}H_{44}O_2SSi$: C, 73.79%; H, 8.51%; S, 6.16%; O: 6.14%, Si: 5.39%. Found: C, 74.00%; H, 8.46%; S, 6.16 %.

(4-((4-Ethynyl-2,5-bis(hexyloxy)phenyl)ethynyl)-phenyl)(methyl)sulfane (4)

1 (970 mg, 1.86 mmol) and potassium fluoride (540 mg, 9.29 mmol) were dissolved in 40 mL of a 1:1 mixture of MeOH and THF. After stirring at r.t. under an argon atmosphere for 24 h 100 mL toluene were added to the solution. The mixture was washed three times with water and afterwards dried with Na_2SO_4. The solvent was removed under reduced pressure and the crude product was purified *via* column chromatography (SiO_2, chloroform:hexane 1:1) to obtain **4** as a yellow solid. Yield 780 mg (93% of theory).

Mp 81°C

IR (FTIR): 3287, 2940, 2851, 2357, 1504, 1389, 1273, 1219, 1030, 864, 818, 733, 637 cm^{-1}.

^{1}H NMR (300 MHz, CD_2Cl_2): δ = 7.44 (d, J = 8.2 Hz, 2 H), 7.22 (d, J = 8.2 Hz, 2 H), 6.99 (s, 1 H), 6.98 (s, 1 H), 3.99 (m, 4 H, 2 O-CH_2), 3.38 (s, 1 H, CH), 2.50 (s, 3 H, S-CH_3), 1.80 (m, 4 H, 2 CH_2), 1.54 (m, 4 H, 2 CH_2), 1.36 (m, 8 H, 4 CH_2), 0.91 (m, 6 H, 2 CH_3) ppm.

^{13}C NMR (75 MHz, CD_2Cl_2): δ = 154.39, 153.59, 140.08, 131.94, 125.93, 119.62, 117.95, 116.88, 114.81, 112.59, 94.79, 86.02, 82.35, 80.19, 69.87, 69.81, 31.81, 31.76, 29.51, 29.38, 25.94, 25.81, 22.87, 22.82, 15.29, 14.03, 14.02 ppm.

HRMS (ESI): *m/z* calculated for $[C_{29}H_{36}O_2S]^{H+}$: 449.2509; found: 449.2488 [M + H].

Anal. Calcd for $C_{29}H_{36}O_2S$: C, 77.63%; H, 8.09%; S, 7.15%; O, 7.13%. Found: C, 77.66%; H, 8.30%; S, 6.95 %.

((4-((2,5-Bis(hexyloxy)-4-((4-(methylthio)phenyl)-ethynyl)phenyl)ethynyl)-2,5-bis(hexyloxy)phenyl)-ethynyl)trimethylsilane (5)

4 (1.2 g, 2.67 mmol) and **1** (1.21 g, 2.67 mmol) were dissolved in 50 mL TEA. The solution was purged with argon for 45 min. Subsequently, $Pd(PPh_3)_2Cl_2$ (18.9 mg 2.67 µmol) and CuI (5 mg, 2.67 µmol) were added, the solution was heated to 80 °C and stirred at this temperature overnight. 100 mL diethyl ether were added and the mixture was washed three times with 100 mL water. Afterwards, the organic phase was dried over Na_2SO_4 and the solvent was removed under reduced pressure. The crude product was purified *via* column chromatography (SiO_2, chloroform:hexane, 1:1) and afterwards recrystallized from EtOH to obtain **5** as a yellow solid. Yield 1.6 g (73% of theory).

Mp 70 °C

IR (FTIR): 2947, 2851, 2361, 2149, 1497, 1389, 1273, 1215, 1034, 841 cm^{-1}.

^1H NMR (300 MHz, CD_2Cl_2): δ = 7.48 (d, J = 8.0 Hz, 2 H), 7.26 (d, J = 8.2 Hz, 2 H), 7.05 (s, 1 H), 7.04 (s, 1 H), 7.00 (s, 1 H), 6.98 (s, 1 H), 4.04 (m, 8 H, 4 O-CH_2), 2.54 (s, 3 H, S-CH_3), 1.87 (m, 8 H, 4 CH_2), 1.56 (m, 8 H, 2 CH_2), 1.39 (m, 16 H, 8 CH_2), 0.94 (m, 12 H, 4 CH_3), 0.29 (s, 9 H, 3 Si-CH_3) ppm.

^{13}C NMR (75 MHz, CD_2Cl_2): δ = 154.68, 154.14, 154.07, 153.91, 140.37, 132.29, 126.31, 120.08, 117.81, 117.59, 117.54, 117.41, 114.91, 114.63, 114.48, 114.34, 101.76, 100.62, 95.2, 92.05, 91.87, 86.67, 70.26, 70.24, 70.17, 70.1, 32.2, 29.92. 29.86, 26.34, 26.29, 26.26, 26.24, 23.24, 15.66, 14.40, 0.19 ppm.

HRMS (ESI): *m/z* calculated for $[C_{52}H_{72}O_4SSi]^{H+}$: 821.4993; found: 821.4938 [M + H].

Anal. Calcd for $C_{52}H_{72}O_4SSi$: C, 76.05%; H, 8.84%; S, 3.9%; O, 7.79%; Si; 3.42%. Found: C, 76.35%; H, 8.86%; S, 4.29%.

(4-((4-((4-Ethynyl-2,5-bis(hexyloxy)phenyl)-ethynyl)-2,5-bis(hexyloxy)phenyl)ethynyl)-phenyl)(methyl)sulfane (6)

5 (830 mg, 1.01 mmol) and potassium fluoride (460 mg, 7.91 mmol) were dissolved in 40 mL of a 1:1 mixture of MeOH and THF. After stirring at r.t. under an argon atmosphere overnight 100 mL toluene were added to the solution. The mixture was washed three times with water and afterwards dried with Na_2SO_4. The solvent was removed under reduced pressure and the crude product was purified *via* column chromatography (SiO_2, dichloromethane:hexane 1:1) to obtain **6** as a yellow solid. Yield 700 mg (92% of theory).

Mp 82 °C

IR (FTIR): 3291, 2920, 2851, 2361, 1732, 1505, 1420, 1389, 1204, 1030, 860, 818, 617 cm^{-1}.

^1H NMR (300 MHz, CD_2Cl_2): δ = 7.45 (d, J = 8.0 Hz, 2 H), 7.23 (d, J = 8.2 Hz, 2 H), 7.05 - 6.95 (m, 4 x 1 H), 4.01 (m, 8 H, 4 O-CH_2), 3.39 (s, 1H, CH), 2.51 (s, 3 H, S-CH_3), 1.84 (m, 8 H, 4 CH_2), 1.52 (m, 8 H, 4 CH_2), 1.36 (m, 16 H, 8 CH_2), 0.90 (m, 12 H, 4 CH_3) ppm.

^{13}C NMR (75 MHz, CD_2Cl_2): δ = 155.11, 154.51, 154.46, 154.23, 140.74, 132.66, 126.68, 120.44, 118.81, 117.92, 117.84, 117.79, 115.68, 115.07, 114.78, 113.49, 95.58, 92.43, 92.06, 87.01, 83.15, 80.91, 70.68, 70.63, 70.56, 70.53, 32.55, 32.49. 30.29, 30.22, 30.21, 30.13, 26.70, 26.60, 26.55, 23.59, 23.54, 16.03, 14.76 ppm.

HRMS (ESI): *m/z* calculated for $[C_{49}H_{64}O_4S]^{H+}$: 749.4598; found: 749.4546 [M + H].

Anal. Calcd for $C_{49}H_{64}O_4S$: C, 78.56%; H, 8.61%; S, 4.28%; O, 8.54%. Found: C, 78.79%; H, 8.84%; S, 4.05%.

Tetrakis(4-((4-((2,5-bis(hexyloxy)-4-((4-(methyl-thio)phenyl)ethynyl)phenyl)ethynyl)-2,5-bis-(hexyloxy)phenyl)ethynyl)phenyl)methane (8)

6 (280 mg, 0.37 mmol), **7** (70 mg, 85.5 µmol), $Pd(PPh_3)_4$ (23 mg, 20 µmol) and CuI (3.8 mg, 20 µmol) were dissolved in 5 mL THF. The solution was purged 20 minutes with nitrogen and subsequently 5 mL TEA were added. The solution was stirred at r.t. for 24 h and afterwards heated to 80 °C for 3 h. Subsequently, the solvent was removed under reduced pressure and the crude product was purified *via* column chromatography (SiO_2, dichloromethane: hexane, 3:2) to obtain **8** as a dark yellow solid. Yield 170 mg (60% of theory).

Mp 90 °C

IR (FTIR): 2929, 2859, 2361, 1732, 1508, 1420, 1377, 1277, 1215, 1018, 860, 818 cm^{-1}.

^1H NMR (300 MHz, CD_2Cl_2): δ = 7.46 (m, 16 H), 7.22 (m, 16 H), 7.10 - 7.03 (m, 16 x 1 H), 4.05 (m, 32 H, 16 O-CH_2), 2.51 (s, 12 H, 4 S-CH_3), 1.86 (m, 32 H, 16 CH_2), 1.53 (m, 32 H, 16 CH_2), 1.36 (m, 64 H, 32 CH_2), 0.90 (m, 48 H, 16 CH_3) ppm.

^{13}C NMR (75 MHz, CD_2Cl_2): δ = 153.72, 153.57, 153.50, 146.06, 139.79, 131.72, 130.97, 125.73, 121.50, 119.51, 116.99, 116.95, 116.84, 114.16, 114.04, 113.94, 113.88, 94.62, 94.41, 91.52, 92.42, 86.43, 86.10, 69.70, 69.63, 69.60, 65.00, 31.63, 30.59. 29.34, 29.29, 25.75, 25.68, 22.66, 15.09, 13.83 ppm.

HRMS (ESI): *m/z* calculated for $[C_{221}H_{268}O_{16}S_4]^{H+}$: 3308.9174; found: 3309.2124 [M + H].

Anal. Calcd for $C_{221}H_{268}O_{16}S_4$: C, 80.22%; H, 8.16%; S, 3.88%; O, 7.74%. Found: C, 80.10%; H, 8.36%; S: 3.96%.

Acknowledgment

The authors thank the BMBF (Spitzencluster PhoNa project) for support.

References

(1) (a) Hartland, G. V. *Chem. Rev.* **2011**, *111*, 3858. (b) Halas, N. J.; Lal, S.; Chang, W. S.; Link, S.; Nordlander, P. *Chem. Rev.* **2011**, *111*, 3913.
(2) Linic, S.; Christopher, P.; Ingram, D. B. *Nat. Mater.* **2011**, *10*, 911.
(3) Dreaden, E. C.; El-Sayed, M. A. *Acc. Chem. Res.* **2012**, *45*, 1854.
(4) Vigderman, L.; Khanal, B. P.; Zubarev, E. R. *Adv. Mater.* **2012**, *24*, 4811.
(5) Zheludev, N. I.; Kivshar, Y. S. *Nat. Mater.* **2012**, *11*, 917.
(6) (a) Gandra, N.; Singamaneni, S. *Chem. Commun.* **2012**, *48*, 11540. (b) Voggu, R.; Suguna, P.; Chandrasekaran, S.; Rao, C. N. R. *Chem. Phys. Lett.* **2007**, *443*, 118.
(7) (a) Zhu, J.; Kell, A. J.; Workentin, M. S. *Org. Lett.* **2006**, *8*, 4993. (b) Liu, X.; Liu, H.; Zhou, W.; Zheng, H.; Yin, X.; Li, Y.; Guo, Y.; Zhu, M.; Ouyang, C.; Zhu, D.; Xia, A. *Langmuir* **2010**, *26*, 3179.
(8) (a) Xu, X.; Rosi, N. L.; Wang, Y.; Huo, F.; Mirkin, C. A. *J. Am. Chem. Soc.* **2006**, *128*, 9286. (b) Ohya, Y.; Miyoshi, N.; Hashizume, M.; Tamaki, T.; Uehara, T.; Shingubara, S.; Kuzuya, A. *Small* **2012**, *8*, 2335.
(9) (a) Sanchez-Iglesias, A.; Grzelczak, M.; Altantzis, T.; Goris, B.; Perez-Juste, J.; Bals, S.; Van Tendeloo, G.; Donaldson, S. H., Jr.; Chmelka, B. F.; Israelachvili, J. N.; Liz-Marzan, L. M. *ACS Nano* **2012**, *6*, 11059. (b) Kretschmer, F.; Mansfeld, U.; Hoeppener, S.; Hager, M. D.; Schubert, U. S. *Chem. Commun.* **2013**.
(10) (a) Ahonen, P.; Laaksonen, T.; Nykanen, A.; Ruokolainen, J.; Kontturi, K. *J. Phys. Chem. B.* **2006**, *110*, 12954. (b) Koole, R.; Luigjes, B.; Tachiya, M.; Pool, R.; Vlugt, T. J. H.; deMelloDonega, C.; Meijerink, A.; Vanmaekelbergh, D. *J. Phys. Chem. C.* **2007**, *111*, 11208.
(11) (a) Ying, J. W.; Sobransingh, D. R.; Xu, G. L.; Kaifer, A. E.; Ren, T. *Chem. Commun.* **2005**, 357. (b) Orbach, M.; Lahav, M.; Milko, P.; Wolf, S. G.; van der Boom, M. E. *Angew. Chem. Int. Ed.* **2012**, *51*, 7142.
(12) Yan, H.; Lim, S. I.; Zhang, L.-C.; Gao, S.-C.; Mott, D.; Le, Y.; Loukrakpam, R.; An, D.-L.; Zhong, C.-J. *J. Mater. Chem.* **2011**, *21*, 1890.
(13) (a) Brousseau III, L. C.; Novak, J. P.; Marinakos, S. M.; Feldheim, D. L. *Adv. Mater.* **1999**, *11*, 447. (b) Novak, J. P.; Feldheim, D. L. *J. Am. Chem. Soc.* **2000**, *122*, 3979.
(14) Kanibolotsky, A. L.; Perepichka, I. F.; Skabara, P. J. *Chem. Soc. Rev.* **2010**, *39*, 2695.
(15) Aujard, I.; Baltaze, J.-P.; Baudin, J.-B.; Cogné, E.; Ferrage, F.; Jullien, L.; Perez, É.; Prévost, V.; Qian, L. M.; Ruel, O. *J. Am. Chem. Soc.* **2001**, *123*, 8177.
(16) Zhang, J.; Moore, J. S.; Xu, Z.; Aguirre, R. A. *J. Am. Chem. Soc.* **1992**, *114*, 2273.
(17) (a) Lavrich, D. J.; Wetterer, S. M.; Bernasek, S. L.; Scoles, G. *J. Phys. Chem. B.* **1998**, *102*, 3456. (b) Häkkinen, H. *Nat. Chem.* **2012**, *4*, 443.
(18) Breul, A. M.; Schäfer, J.; Pavlov, G. M.; Teichler, A.; Höppener, S.; Weber, C.; Nowotny, J.; Blankenburg, L.; Popp, J.; Hager, M. D.; Dietzek, B.; Schubert, U. S. *J. Polym. Sci., Part A: Polym. Chem.* **2012**, *50*, 3192.
(19) Suga, H.; Koyama, E.; Tokuhisa, H.; Fujiwara, K.; Nagawa, Y.; Nakamura, T.; Nishioka, Y.; Kanesato, M.; Mizutani, W.; Ishida, T. *Surf. Sci.* **2007**, *601*, 68.
(20) Su, D.; Menger, F. M. *Tetrahedron Lett.* **1997**, *38*, 1485.

Rigid tetrahedral thio end-functionalized architecture

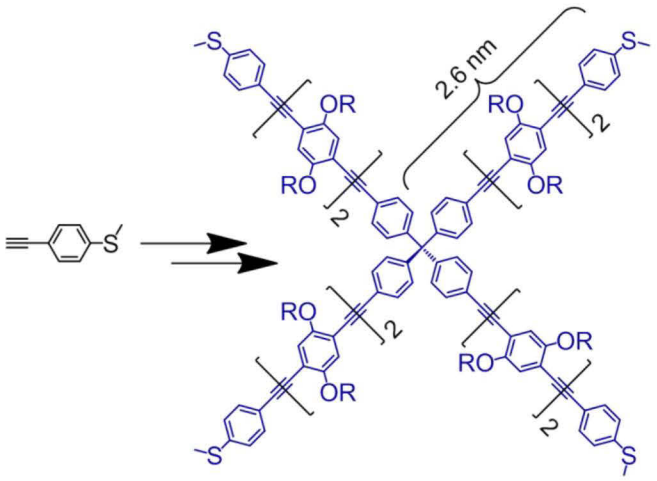

Supplementary information for:

Synthesis of a Rigid Tetrahedral Linker with Thioether End Groups

Florian Kretschmer,[a,b] Andreas Wild,[a,b] Martin D. Hager,[a,b] Ulrich S. Schubert[a,b]*

[a] Laboratory of Organic and Macromolecular Chemistry (IOMC), Friedrich-Schiller-Universität Jena, Humboldtstr. 10, 07743 Jena, Germany

[b] Jena Center for Soft Matter (JCSM), Friedrich-Schiller-Universität Jena, Philosophenweg 7, 07743 Jena, Germany

Fax: 00493641948202

E-mail: ulrich.schubert@uni-jena.de

Compound **3**:

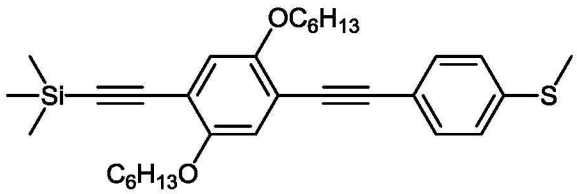

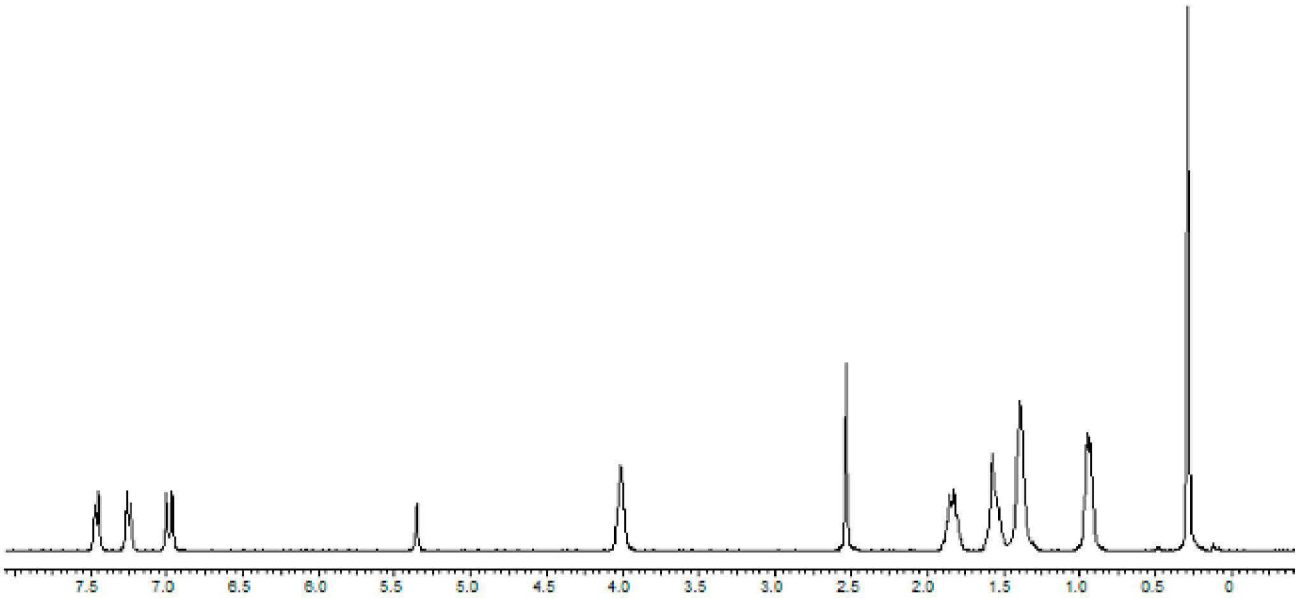

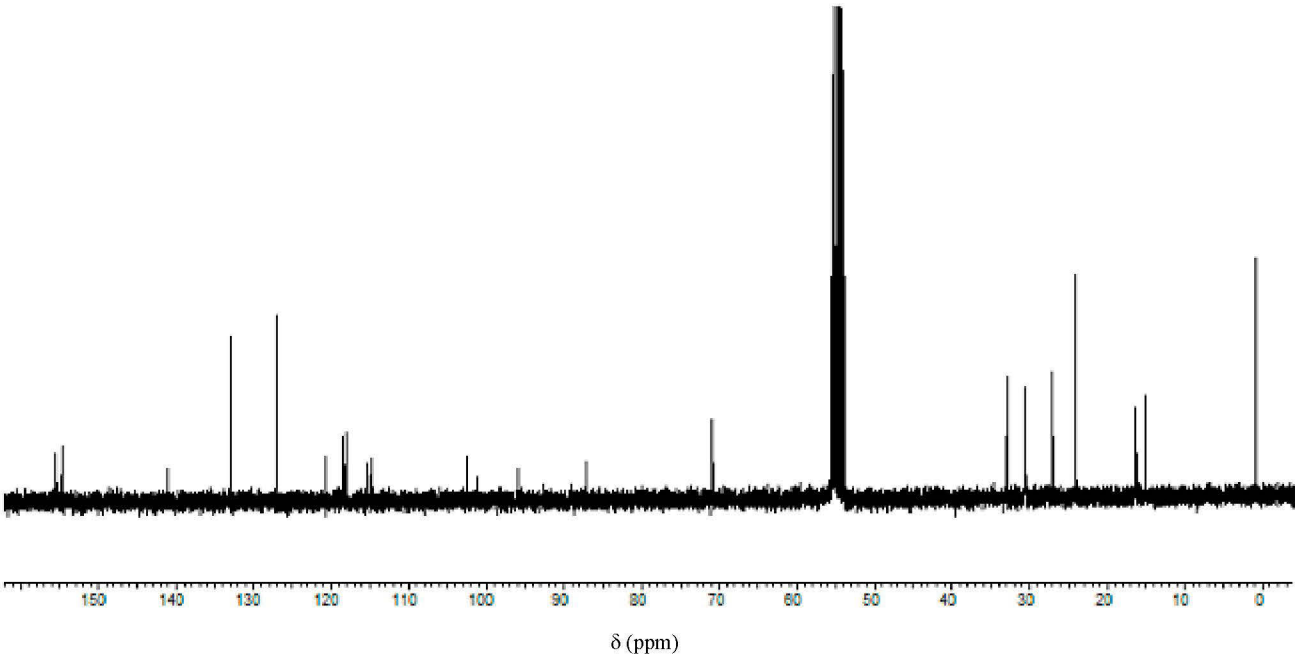
150
140
130
120
110
100
90
80
70
60
50
40
30
20
10
0
δ (ppm)

Compound **4**:

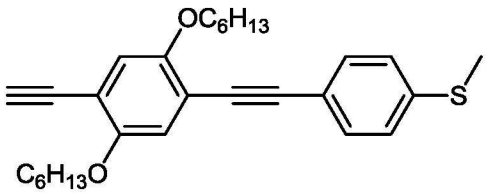
OC6H13
S
C6H13O

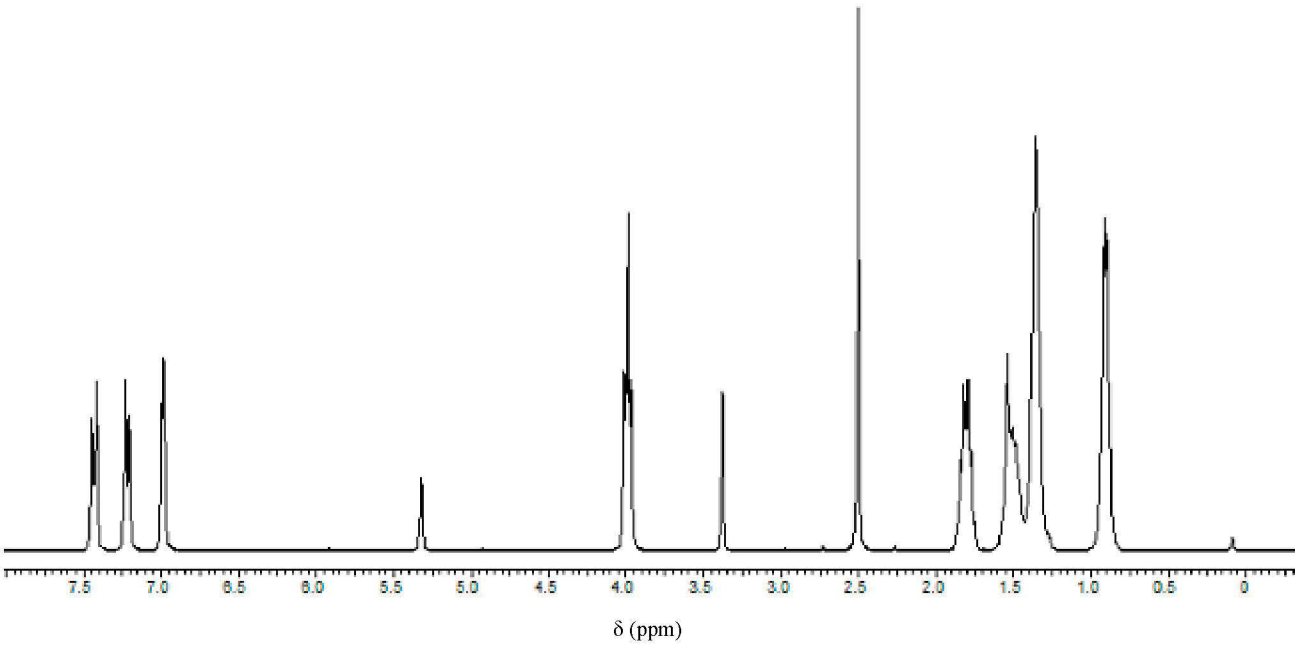
7.5
7.0
6.5
6.0
5.5
5.0
4.5
4.0
3.5
3.0
2.5
2.0
1.5
1.0
0.5
0
δ (ppm)

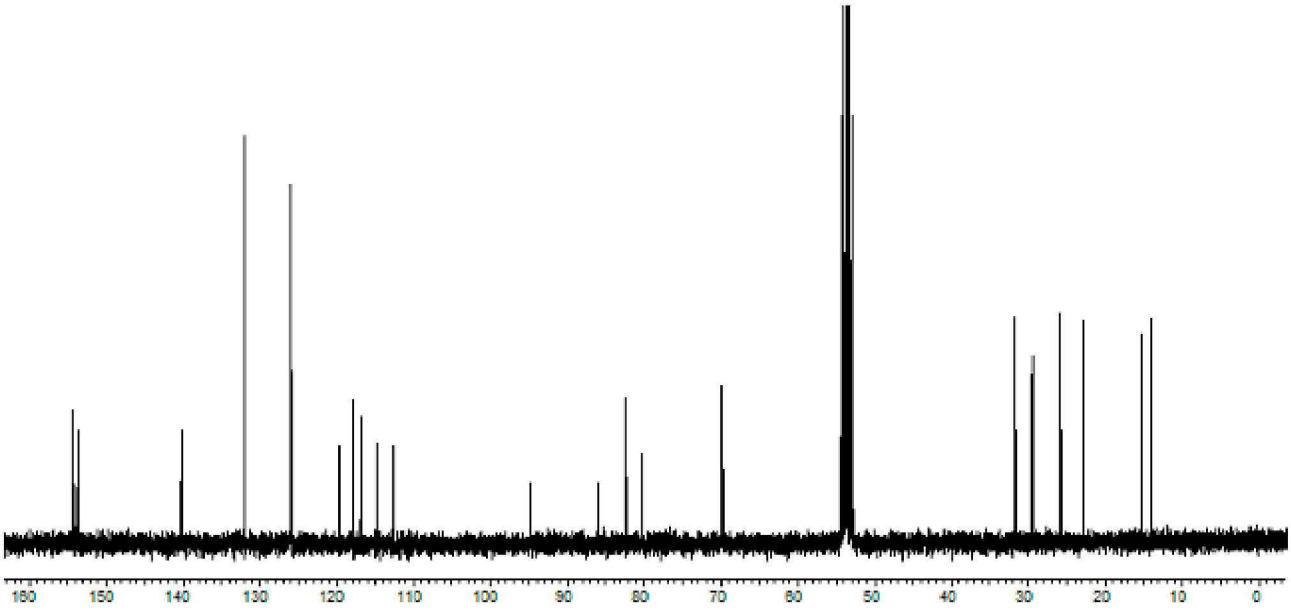
160
150
140
130
120
110
100
90
80
70
60
50
40
30
20
10
0
δ (ppm)

Compound **5**:

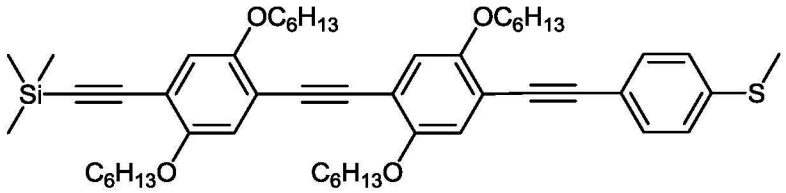
OC6H13
OC6H13
Si
S
C6H13O
C6H13O

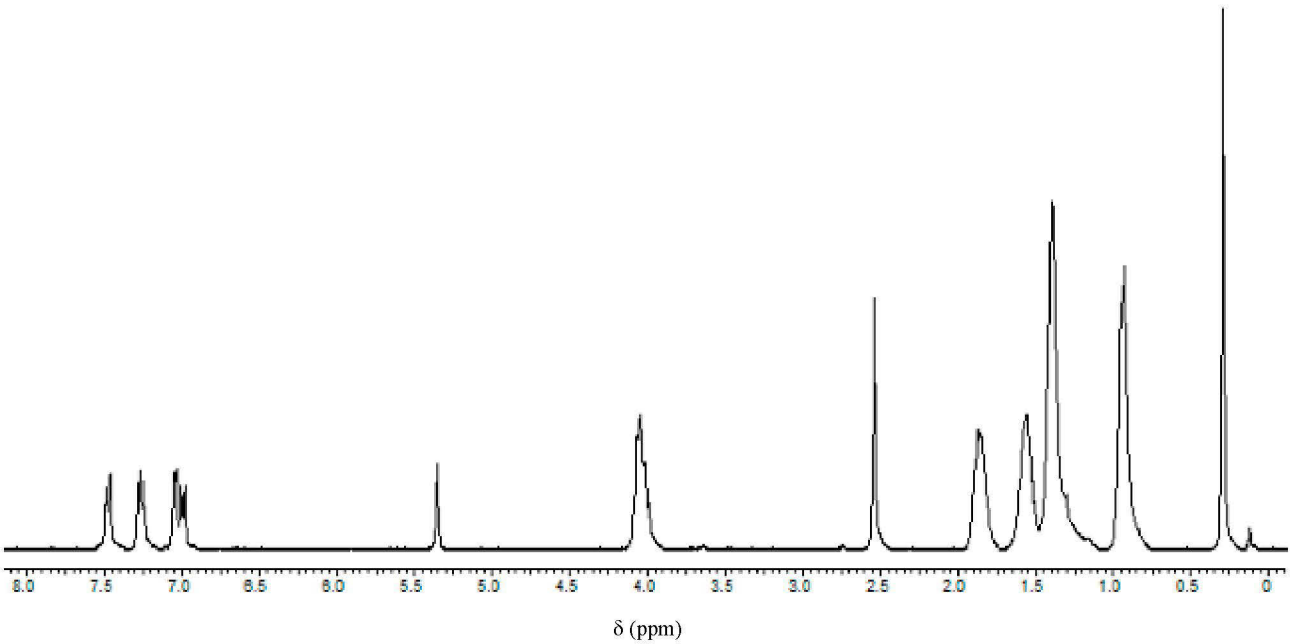
8.0
7.5
7.0
6.5
6.0
5.5
5.0
4.5
4.0
3.5
3.0
2.5
2.0
1.5
1.0
0.5
0
δ (ppm)

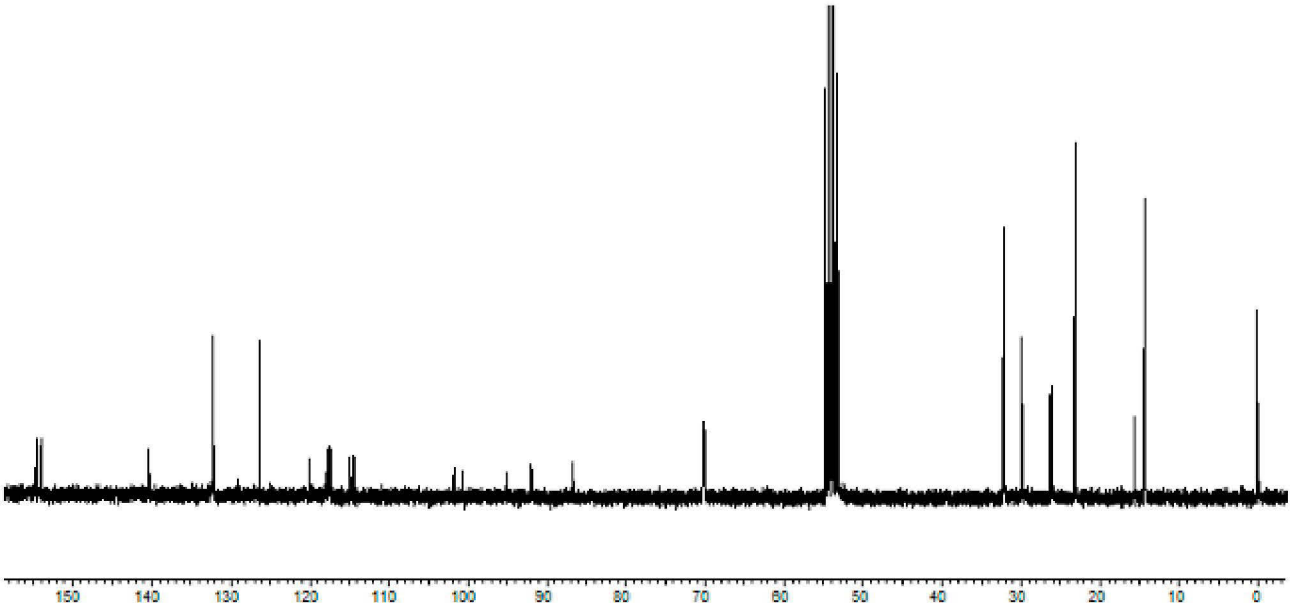
150
140
130
120
110
100
90
80
70
60
50
40
30
20
10
0
δ (ppm)

Compound **6**:

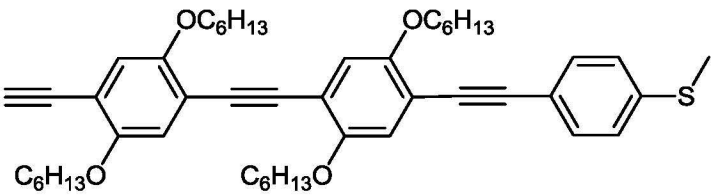
OC6H13
OC6H13
S
C6H13O
C6H13O

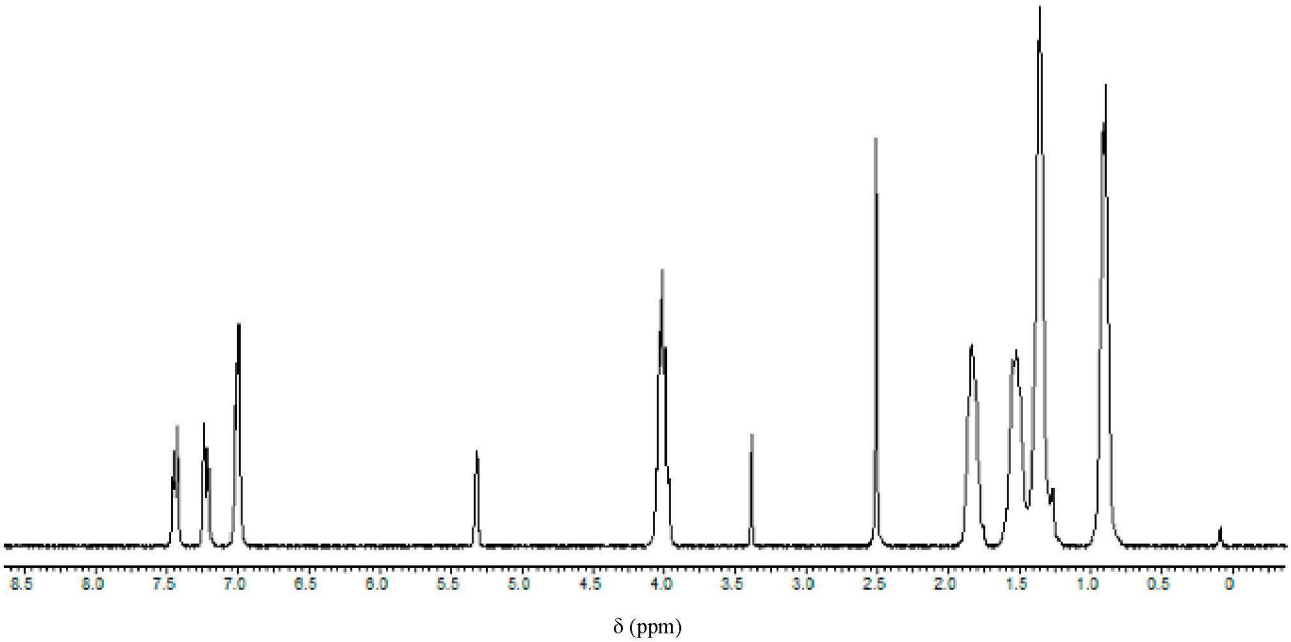
8.5
8.0
7.5
7.0
6.5
6.0
5.5
5.0
4.5
4.0
3.5
3.0
2.5
2.0
1.5
1.0
0.5
0
δ (ppm)

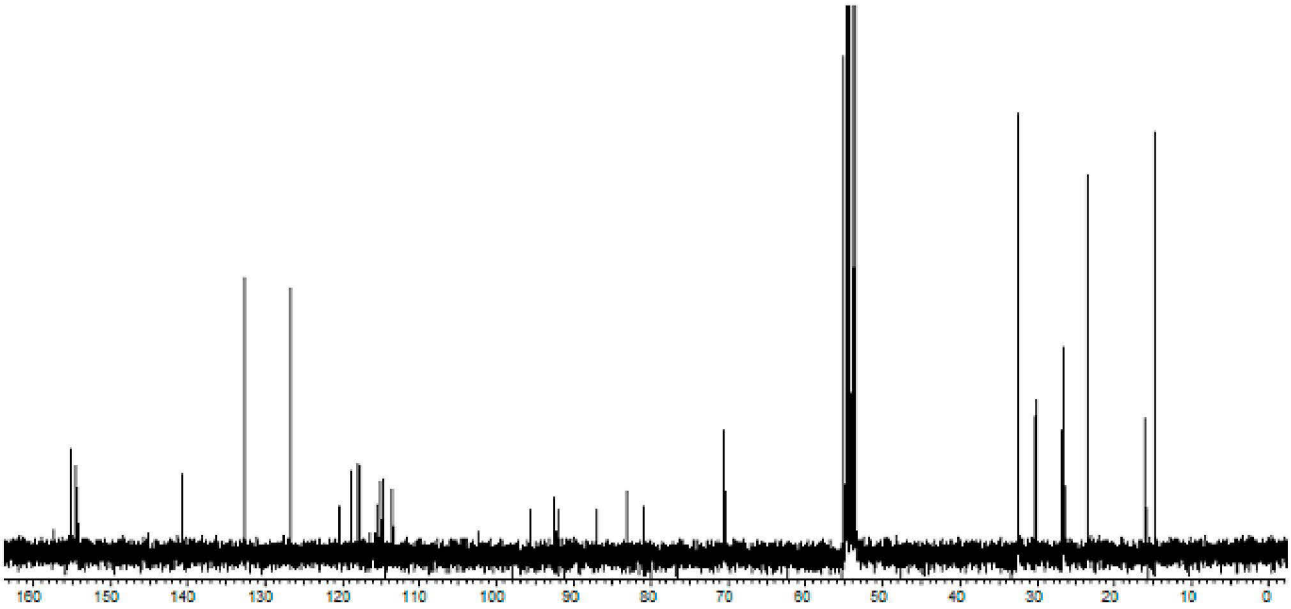
160
150
140
130
120
110
100
90
80
70
60
50
40
30
20
10
0
δ (ppm)

Compound **8**:

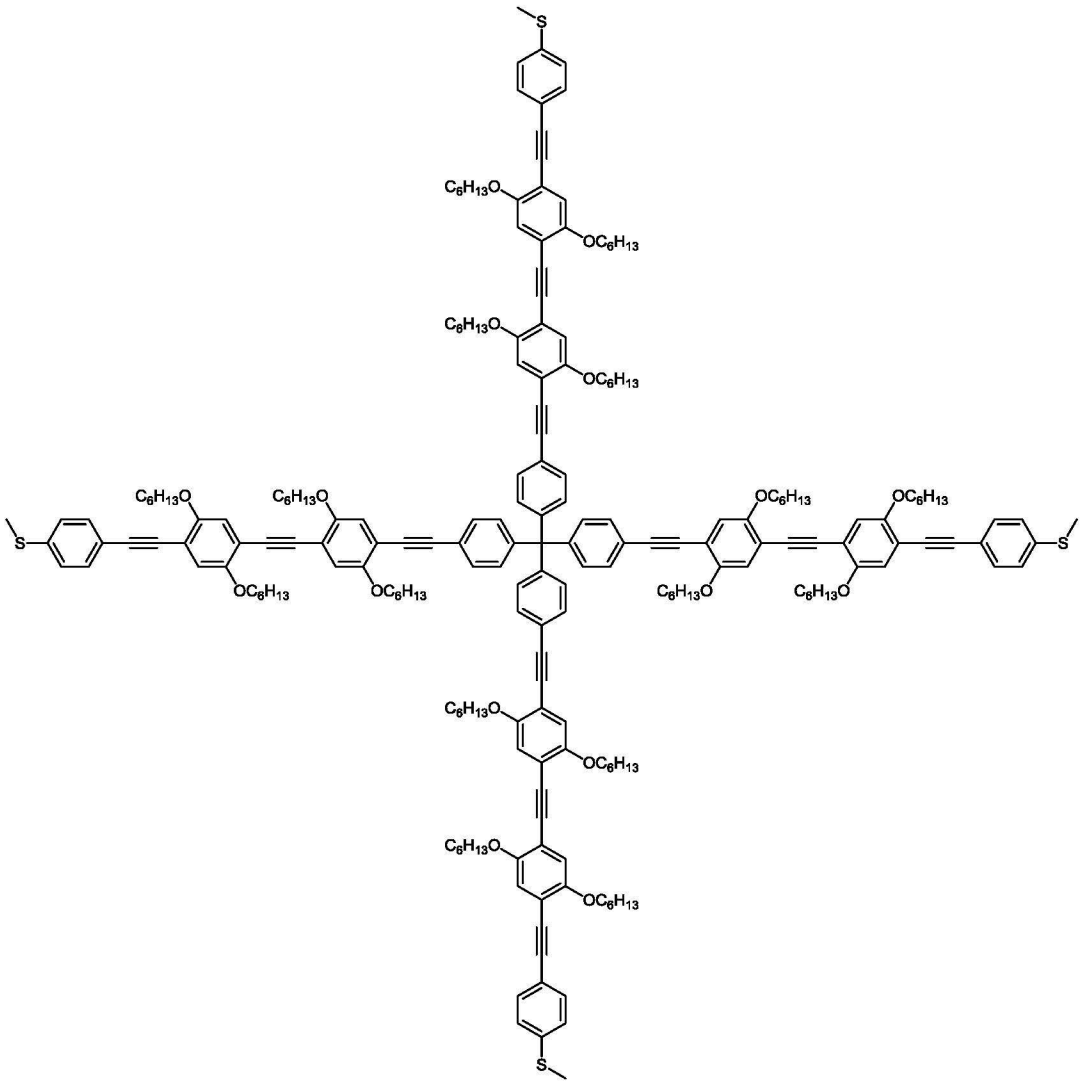
S
C6H13O
OC6H13
S

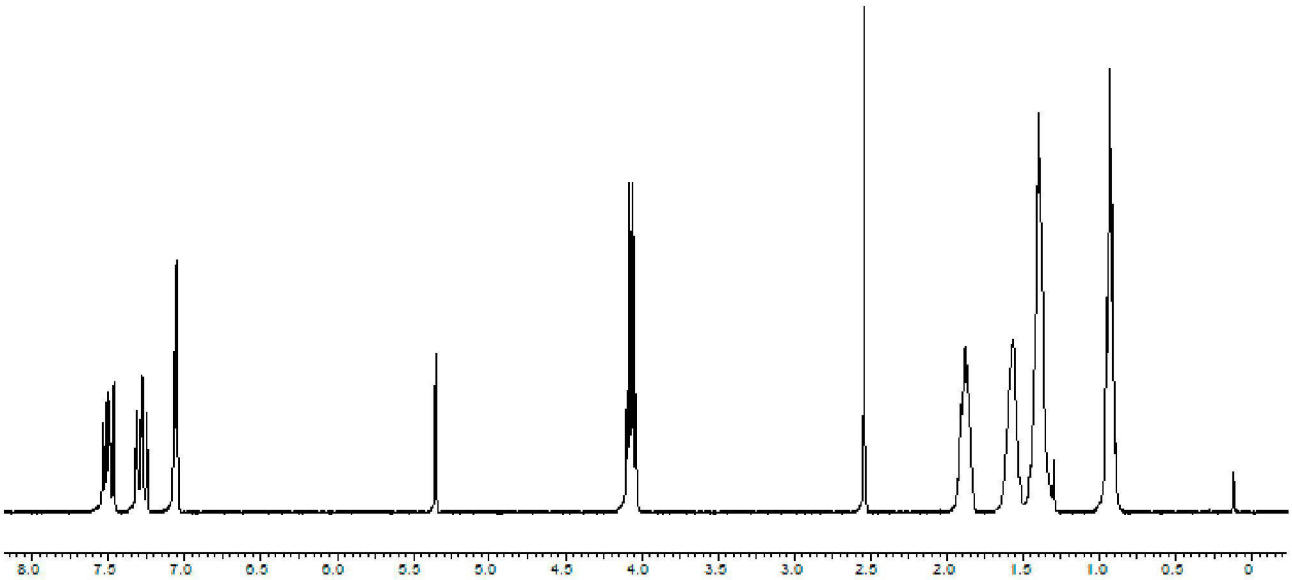
8.0
7.5
7.0
6.5
6.0
5.5
5.0
4.5
4.0
3.5
3.0
2.5
2.0
1.5
1.0
0.5
0

δ (ppm)

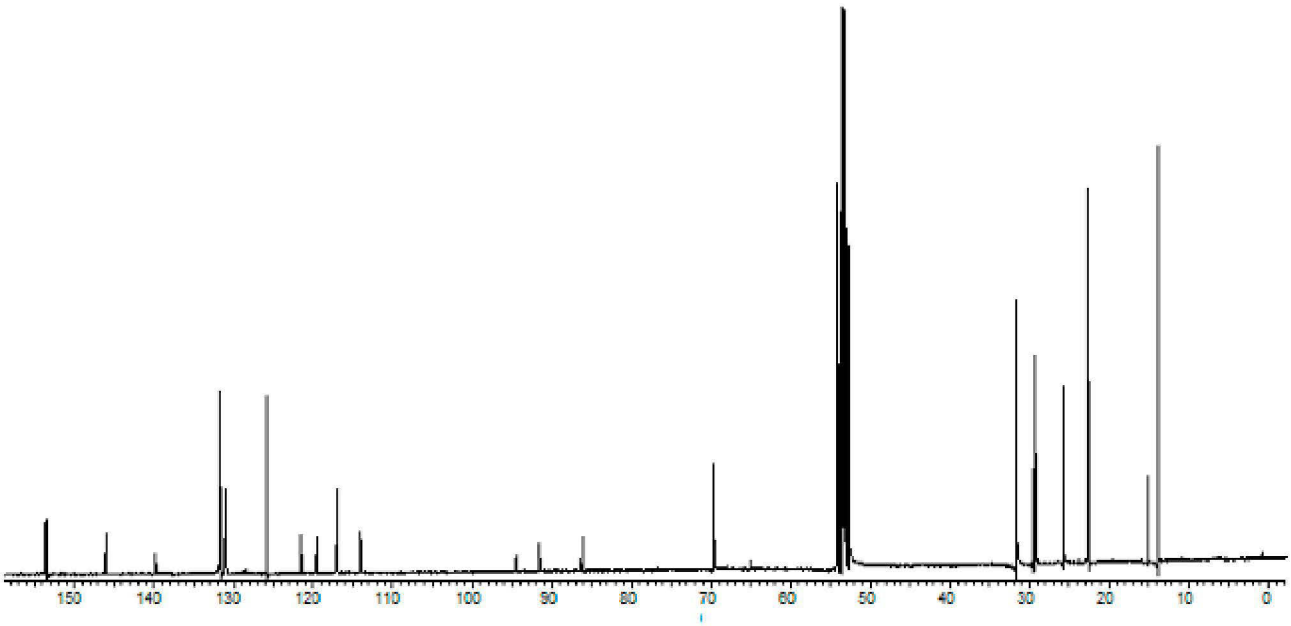
150
140
130
120
110
100
90
80
70
60
50
40
30
20
10
0

δ (ppm)

Publication P4

Synthesis of Functional Tripodal Thioacetates

F. Kretschmer, M. D. Hager, U. S. Schubert

Synthesis, DOI: 10.1055/s-0034-1378497.

Synthesis of Functional Tripodal Thioacetates

Florian Kretschmer,[a,b] Martin D. Hager,[a,b] Ulrich S. Schubert[a,b]*

[a] Laboratory of Organic and Macromolecular Chemistry (IOMC), Friedrich Schiller University Jena, Humboldtstr. 10, 07743 Jena, Germany

[b] Jena Center for Soft Matter (JCSM), Friedrich Schiller University Jena, Philosophenweg 7, 07743 Jena, Germany

Fax: +493641948202

E-mail: ulrich.schubert@uni-jena.de

Received:

Abstract: A versatile route for the synthesis of tripodal thioacetates is reported. Based on the esterification of commercial pentaerythritol tribromide, the method enables an easy introduction of different functional moieties, *e.g.*, into self-assembled monolayers.

Key words: Esterification, Nanostructures, Thiols.

The tremendous development in plasmonic nanoparticle synthesis[1] has fueled the interest in self-assembly[2] and surface functionalization[3] of these particles. Colloidal gold gathered special attention due to the high environmental stability and large affinity towards thiols which enables the efficient formation of self-assembled monolayers (SAMs). Moreover the unique optical features offer a plethora of potential applications in optics[4] and life science.[5]

SAMs on plasmonic nanoparticles or other materials provide a broad range of opportunities to tune the particle properties. For instance, changing the polarity enables stabilization in different solvents[6] whereas esterification,[7] click reactions[8] - and other reactions can direct the assembly of such particles into superstructures. The most commonly used compounds for the synthesis of SAMs on gold are monothiols. However, a major drawback of these monodentate ligands is their rapid exchange between the metal surface and the solution. Mixing two solutions of gold particles functionalized with different ligands will result in gold nanoparticles with a mixed monolayer.

In order to overcome these issues oligothiols can be used.[9] For such molecules the possibility arises to functionalize small particles with a discrete number of reactive moieties. This enables the assembly of gold particles into clusters with a defined particle number.[10] Also trivalent ligands have been used to shield one side of immobilized gold particles.[11] After redispersion the non-shielded side could be used to synthesize particle dimers *via* a rigid bithiol linker.

The stability of a self-assembled monolayer depends on a variety of parameters.[12] At first the affinity of gold towards sulfur groups is dependent on the type of the chemical moiety, *e.g.*, thioethers have a lower affinity towards gold surfaces than thiols.[13] In addition, bulky groups in the vicinity of the sulfur moiety lead to a lower stabilization of gold nanoparticles.[14]

Due to the chelating effect, multidentate ligands offer

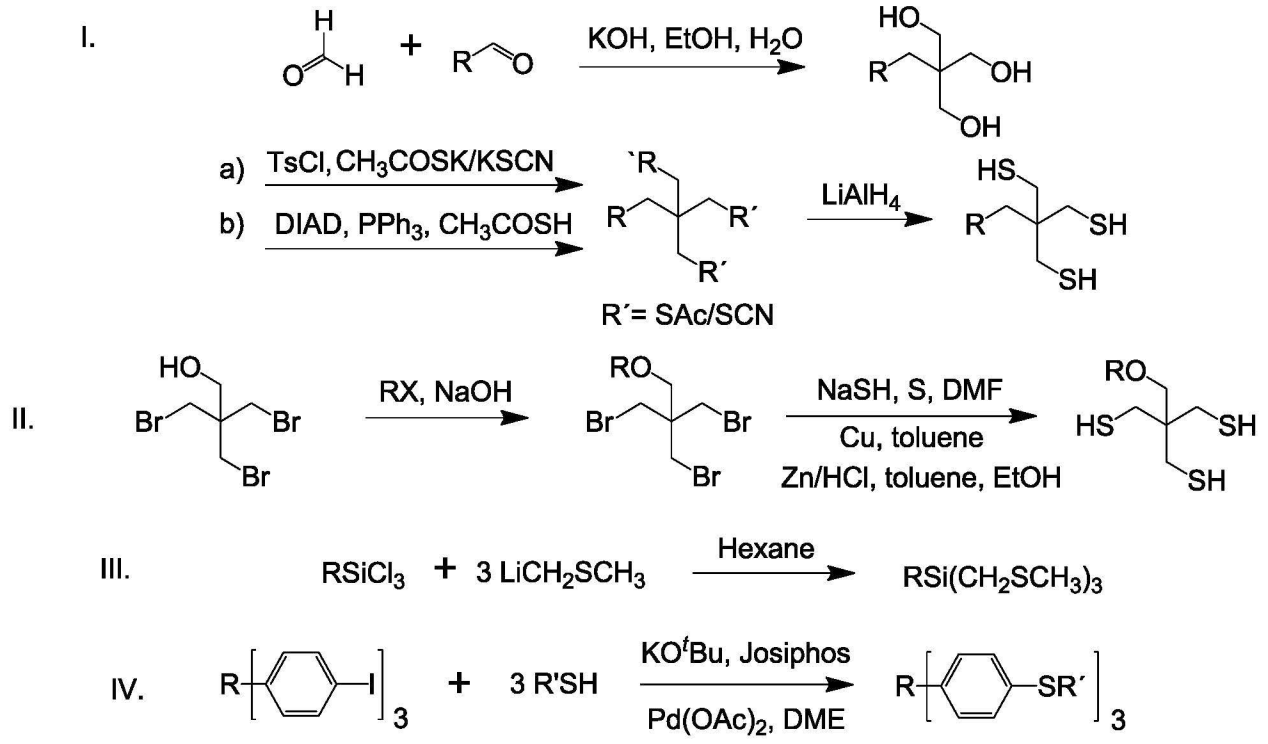

Scheme 1 Schematic representation of an overview on the synthesis of tripodal ligands for SAMs on gold.

a high kinetic stability of the SAM.[15] Also the chemical stability has to be taken into account, *e.g.*, dithiocarboxylates bind stronger to a gold surface in comparison to a monothiol, however, they also readily decompose under ambient conditions.[16]

Therefore, the most favorable configuration for a stable monolayer would involve a combination of all properties, *i.e.* a multidentate thiol ligand devoid of bulky groups.

Synthesis of higher dentate ligands often involves complex molecules like calixarenes,[17] cyclodextrines[18] or polymers.[19] However, there are numerous strategies available for the synthesis of tripodal ligands (Scheme 1). Strategy I employs aldol condensations in combination with a crossed Cannizzaro reaction to synthesize monosubstituted pentaerythritol derivatives.[20] In a similar approach also pentaerythritol can be utilized directly. Three hydroxyl groups are protected by triethylorthoacetate. In the next step the remaining OH group is functionalized through etherification, followed by deprotection.[21]

The monofunctional pentaerythritol derivatives can then be converted to tritosylates followed by conversion with thioacetates or thiocyanates (Ia). Alternatively, a Mitsunobu reaction can be used to synthesize the trithioacetate (Ib). Through reduction with $LiAlH_4$ the free thiols are generated.

Another strategy involves the etherification of pentaerythritol tribromide with an alkyl halide followed by conversion to the thiol (II).[22] However, drawbacks of this approach are side reactions arising from the tribromide which is an alkyl halide itself.

In addition, organosilanes[23] and cross-coupling reactions[24] have been used, in particular for the preparation of aromatic tripodal ligands (III+IV).

While thiols offer the highest affinity towards gold surfaces, a drawback is their susceptibility against oxygen which leads to disulfide formation or, in particular for compounds with multiple thiol groups, insoluble crosslinked networks can be formed.

A large variety of protecting groups is available for thiols, *e.g.*, thioethers,[25] or carbamates.[26] However, the most versatile protecting group for particle modification is the thioacetate, since it is readily cleaved in the presence of a gold surface.[27]

Here we report a versatile two step synthesis for the preparation of tripodal ligands based on commercially available pentaerythritol tribromide. The approach allows an easy creation of trithioacetates with different functionalities (Scheme 2).

The first step involves the Steglich esterification of pentaerythritol tribromide; the progress could be easily followed by GC-MS. A pivotal point was the utilization of a slight excess of the acids, otherwise traces of the tribromide were hard to remove *via* column chromatography due to similar R_f values. In this way esters bearing alkyne, azide and furan units could be synthesized in good yields (3a-c). Initial experiments for the synthesis of thioacetates with different solvents were performed. Tetrahydrofuran, acetonitrile, acetone and methanol in combination with potassium thioacetate lead mostly to low conversions at room temperature. When conducted at elevated temperatures the conversion increased; however, also side reactions (*e.g.*, ester/thioacetate) cleavage) became more prominent. Finally, DMF was identified to be the solvent of choice. After stirring at room temperature for two days GC-MS did not show any educts. A large excess of potassium thioacetate had to be used to ensure a full conversion of the bromide units. For purification, at first simple evaporation of the solvent was used, however, this lead to decomposition of the products. Therefore, the excess of potassium thioacetate and the formed bromide was removed *via* precipitation with diethyl ether. Copious washing with water was then applied to remove the DMF. Additionally, also yellow side products could be removed in this way. After column chromatography, the trithioacetates were obtained in good yields (4a-c). It should be noted that both the tribromide and thioacetate of the furan derivative are prone to decomposition and should be quickly used.

In conclusion, an efficient route towards novel tripodal ligands for the functionalization of gold nanoparticles has been reported.

Reagents and solvents were purchased from Carl Roth, Sigma-Aldrich, Fluka, Merck and VWR. All

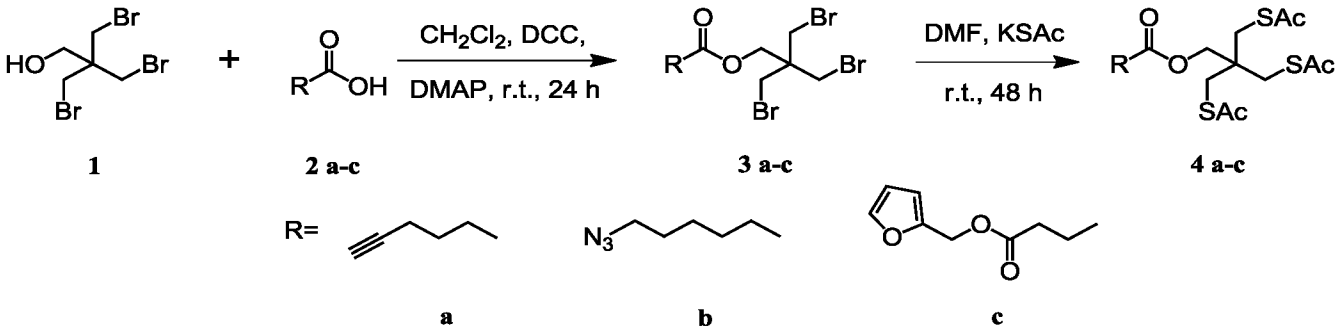

Scheme 2 Schematic representation of the tripodal thioacetate synthesis.

chemicals were used as received. Dry methylene chloride was obtained from a MB SPS-800 solvent purification system. ^{1}H and ^{13}C NMR spectra were recorded on a Bruker AC 300 at 298 K. Chemical shifts are reported in parts per million (ppm, δ scale) and were calibrated against residual protio-solvent. MALDI-TOF MS measurements were performed with a Bruker Ultraflex III MALDI TOF/TOF. GC-MS analysis was performed on a Shimadzu GC-2010 gas chromatograph coupled with a Shimadzu GCMS-QP2010S mass spectrometer. Elemental analyses were carried out on a Vario ELIII – Elementar Euro and an EA from HekaTech. IR spectra were measured on a Shimadzu IRAffinity-1 FTIR-spectrophotometer. Compounds 2b[28] and 2c[29] were prepared as reported in the literature.

3-Bromo-2,2-bis(bromomethyl)propyl-hex-5-ynoate

2a (1.50 g, 13.34 mmol), pentaerythritol tribromide (3.75 g, 11.5 mmol), DCC (2.49 g, 12.07 mmol) and DMAP (180 mg, 1.47 mmol) were dissolved in 75 mL methylene chloride and stirred at room temperature under nitrogen for 24 h. Afterwards the mixture was filtered and the clear solution was washed with 50 mL water. The organic phase was dried over sodium sulfate and the solvent was removed under reduced pressure. Subsequently, the crude product was purified *via* column chromatography (silica gel 60, methylene chloride) to obtain **3a**.

Yield 3.00 g (62%); colorless liquid.

IR (FTIR): 3294, 2967, 1740, 1427, 1242, 1146, 845, 633 cm^{-1}.

^{1}H NMR (300 MHz, $CDCl_3$): δ = 4.21 (s, 2 H, CH_2), 3.55 (s, 6 H, 3 CH_2), 2.52 (t, J = 7.4 Hz, 2 H, CH_2), 2.30 (m, 2 H, CH_2), 2.20 (t, J = 2.7 Hz, 1 H, CCH), 1.88 (q, J = 7.2 Hz, 2 H, CH_2) ppm.

^{13}C NMR (75 MHz, $CDCl_3$): δ = 172.01, 82.92, 69.42, 63.66, 42.72, 33.99, 32.60, 23.46, 17.77 ppm.

MS (EI): m/z 336 $[M\text{-}HBr]^{+}$.

Anal. Calcd for $C_{11}H_{15}Br_3O_2$: C, 31.54%; H, 3.61%; Br, 57.22; O: 7.64%. Found: C, 31.67%; H, 3.57%; Br, 57.02 %.

3-Bromo-2,2-bis(bromomethyl)propyl-6-azidohex-anoate

2b (1.45 g, 9.24 mmol), pentaerythritol tribromide (2.5 g, 7.7 mmol), DCC (2 g, 9.69 mmol) and DMAP (120 mg, 0.98 mmol) were dissolved in 50 mL methylene chloride and stirred at room temperature under nitrogen for 24 h. Afterwards the mixture was filtered and the clear solution was washed with 50 mL water. The organic phase was dried over sodium sulfate and the solvent was removed under reduced pressure. Subsequently the crude product was purified *via* column chromatography (silica gel 60, methylene chloride) to obtain **3b**.

Yield 2.6 g (73%); colorless liquid.

IR (FTIR): 2940, 2095, 1740, 1427, 1242, 1146, 849, 667, 610 cm^{-1}.

^{1}H NMR (300 MHz, $CDCl_3$): δ = 4.20 (s, 2 H, CH_2), 3.54 (s, 6 H, 3 CH_2), 3.29 (t, J = 6.7 Hz, 2 H, CH_2), 2.38 (m, 4 H, 2 CH_2), 1.45 (t, J = 7.1 Hz, 2 H, CH_2) ppm.

^{13}C NMR (75 MHz, CD_2Cl_2): δ = 171.88, 63.18, 50.75, 42.27, 33.54, 33.4, 28.09, 25.74, 23.99 ppm.

MS (EI): m/z 436 $[M\text{-}N_2]$.

Anal. Calcd for $C_{11}H_{18}Br_3N_3O_2$: C, 28.47%; H, 3.91%; N, 9.06%; O, 6.90%; Br, 51.66%. Found: C, 28.84%; H, 3.92%; N, 9.22%; Br: 51.83%.

3-Bromo-2,2-bis(bromomethyl)propyl (furan-2-ylmethyl) succinate

2c (2.4 g, 12.11 mmol), pentaerythritol tribromide (3.57 g, 11 mmol), DCC (3 g, 14.54 mmol) and DMAP (171 mg, 1.4 mmol) were dissolved in 50 mL methylene chloride and stirred at room temperature under nitrogen for 24 h. Afterwards the mixture was filtered and the clear solution was washed with 50 mL water. The organic phase was dried over sodium sulfate and the solvent was removed under reduced pressure. Subsequently the crude product was purified *via* column chromatography (silica gel 60, methylene chloride : hexane 1:1) to obtain **3c**.

Yield 4.3 g (70%); yellow oil.

IR (FTIR): 2970, 1740, 1427, 1346, 1227, 1150, 999, 918, 745 cm^{-1}.

^{1}H NMR (300 MHz, $CDCl_3$): δ = 7.44 (s, 1 H, CH), 6.42 (s, 1 H, CH), 6.38 (s, 1 H, CH_2), 5.11 (s, 2 H, CH_2), 4.25 (s, 2 H, CH_2), 3.55 (s, 6 H, 3 CH_2), 2.70 (s, 4 H, 2 CH_2) ppm.

^{13}C NMR (75 MHz, $CDCl_3$): δ = 171.23, 170.66, 148.70, 142.96, 110.44, 110.18, 63.49, 58.03, 42.38, 33.64, 28.57, 28.54 ppm.

MS (EI): m/z 505 $[M^{+}]$.

Anal. Calcd for $C_{14}H_{17}Br_3O_5$: C, 33.3%; H, 3.39%; Br, 47.47%; O, 15.84%. Found: C, 33.53%; H, 3.37%; Br, 47.15%.

3-(Acetylthio)-2,2-bis((acetylthio)methyl)propyl hex-5-ynoate

3a (1 g, 2.39 mmol) and potassium thioacetate (1.63 g, 14.7 mmol) were dissolved in 10 mL DMF and

stirred in a closed vial at room temperature for 48 h. Subsequently, 50 mL diethyl ether were added and the formed precipitate was filtered off. The organic solution was washed five times with 50 mL water followed by drying over sodium sulfate. Afterwards the solvent was removed under reduced pressure. The crude product was purified *via* column chromatography (silica gel 60, methylene chloride) to obtain **4a**.

Yield 435 mg (45%); yellow oil.

IR (FTIR): 3291, 2970, 1736, 1694, 1354, 1130, 953, 621 cm^{-1}.

^1H NMR (300 MHz, $CDCl_3$): δ = 3.94 (s, 2 H, CH_2), 3.07 (s, 2 H, 3 CH_2), 2.51 (t, J = 7.4, 2 H, CH_2), 2.36 (s, 9 H, 3 CH_3), 2.29 (m, 2 H, CH_2), 1.99 (t, J = 2.7, 1 H, CCH), 1.87 (q, J = 7.2, 2 H, CH_2) ppm.

^{13}C NMR (75 MHz, $CDCl_3$): δ = 194.14, 172.48, 83.23, 69.23, 66.00, 42.14, 32.95, 32.78, 30.60, 23.46, 17.87 ppm.

MS (EI): *m/z* 361 $[M\text{-}CH_3CO]^+$.

Anal. Calcd for $C_{17}H_{24}O_5S_3$: C, 50.47%; H, 5.98%; S, 23.78%; O, 19.77%. Found: C, 50.39%; H, 5.97%; S, 23.93%.

3-(Acetylthio)-2,2-bis((acetylthio)methyl)propyl 6-azidohexanoate

3b (0.5 g, 1.08 mmol) and potassium thioacetate (738 mg, 6.46 mmol) were dissolved in 5 mL DMF and stirred in a closed vial at room temperature for 48 h. Subsequently, 50 mL diethyl ether were added and the formed precipitate was filtered off. The organic solution was washed five times with 50 mL water followed by drying over sodium sulfate. Afterwards the solvent was removed under reduced pressure. The crude product was purified *via* column chromatography (silica gel 60, methylene chloride) to obtain **4b**.

Yield 296 mg (61%); yellow oil.

IR (FTIR): 2936, 2353, 2095, 1740, 1694, 1354, 1227, 1130, 1099, 953, 621 cm^{-1}.

^1H NMR (300 MHz, $CDCl_3$): δ = 3.92 (s, 2 H, CH_2), 3.29 (t, J = 6.8 Hz, 2 H, CH_2), 3.06 (s, 6 H, 3 CH_2) 2.37 (m, 2 H, CH_2), 2.35 (s, 9 H, 3 CH_3) 1.65 (m, 4 H, 2 CH_2), 1.44 (m, 2 H, CH_2) ppm.

^{13}C NMR (75 MHz, $CDCl_3$): δ = 194.11, 172.82, 65.92, 51.25, 42.14, 33.92, 32.94, 30.60, 28.57, 26.24, 24.29 ppm.

MS (MALDI-TOF): *m/z* 450 $[M+H]^+$.

Anal. Calcd for $C_{17}H_{27}N_3O_5S_3$: C, 45.41%; H, 6.05%; N, 9.35%; S, 21.40%; O, 17.79%. Found: C, 45.20%; H, 5.93%; N, 9.48%; S, 21.72%.

3-(Acetylthio)-2,2-bis((acetylthio)methyl)propyl (furan-2-ylmethyl) succinate

3c (1 g, 1.98 mmol) and potassium thioacetate (1.36 g, 12.27 mmol) were dissolved in 10 mL DMF and stirred in a closed vial at room temperature for 48 h. Subsequently, 50 mL diethyl ether were added and the formed precipitate was filtered off. The organic solution was washed five times with 50 mL water followed by drying over sodium sulfate. Afterwards the solvent was removed under reduced pressure. The crude product was purified *via* column chromatography (silica gel 60, methylene chloride) to obtain **4c**.

Yield 389 mg (40%); dark yellow oil.

IR (FTIR): 2970, 1740, 1694, 1354, 1207, 1130, 957, 748, 621 cm^{-1}.

^1H NMR (300 MHz, $CDCl_3$): δ = 7.43 (s, 1 H, CH), 6.42 (d, 1 H, CH), 6.37 (m, 1 H, CH), 5.09 (s, 2 H, CH_2), 3.95 (s, 2 H, CH_2), 3.06 (s, 6 H, 3 CH_2) 2.69 (s, 4 H, 2 CH_2), 2.35 (s, 9 H, 3 CH_3) ppm.

^{13}C NMR (75 MHz, CD_2Cl_2): δ = 194.12, 171.78, 171.53, 149.27, 143.27, 110.71, 110.56, 66.19, 58.33, 42.19, 32.86, 30.56, 29.01, 28.90 ppm.

MS (EI): *m/z* 447 $[M\text{-}CH_3CO]^+$.

Anal. Calcd for $C_{20}H_{26}O_8S_3$: C, 48.96%; H, 5.34%; S, 19.61%; O, 26.09%. Found: C, 48.56%; H, 5.33%; S, 19.63%.

Acknowledgment

Financial support from the research initiative PhoNa (Photonic nanomaterials), which is supported by the German Federal Ministry of Education and Research in the program "Spitzenforschung und Innovation in den Neuen Ländern" (support code 03IS2101A), is acknowledged.

References

(1) Zhao, P.; Li, N.; Astruc, D. *Coord. Chem. Rev.* **2013**, *257*, 638.
(2) Gong, J.; Li, G.; Tang, Z. *Nano Today* **2012**, *7*, 564.
(3) Vericat, C.; Vela, M. E.; Benitez, G.; Carro, P.; Salvarezza, R. C. *Chem. Soc. Rev.* **2010**, *39*, 1805.
(4) Halas, N. J.; Lal, S.; Chang, W. S.; Link, S.; Nordlander, P. *Chem. Rev.* **2011**, *111*, 3913.
(5) (a) Xia, Y.; Li, W.; Cobley, C. M.; Chen, J.; Xia, X.; Zhang, Q.; Yang, M.; Cho, E. C.; Brown, P. K. *Acc. Chem. Res.* **2011**, *44*, 914. (b) Jin, Y. *Adv. Mater.* **2012**, *24*, 5153.
(6) Wojczykowski, K.; Meissner, D.; Jutzi, P.; Ennen, I.; Hutten, A.; Fricke, M.; Volkmer, D. *Chem. Commun.* **2006**, 3693.

(7) (a) Abargues, R.; Albert, S.; Valdés, J. L.; Abderrafi, K.; Martínez-Pastor, J. P. *J. Mater. Chem.* **2012**, *22*, 22204. (b) Franzmann, E.; Khalil, F.; Weidmann, C.; Schroder, M.; Rohnke, M.; Janek, J.; Smarsly, B. M.; Maison, W. *Chem. Eur. J.* **2011**, *17*, 8596.
(8) (a) Li, N.; Binder, W. H. *J. Mater. Chem.* **2011**, *21*, 16717. (b) Gandra, N.; Singamaneni, S. *Chem. Commun.* **2012**, *48*, 11540.
(9) Pornsuriyasak, P.; Ranade, S. C.; Li, A.; Parlato, M. C.; Sims, C. R.; Shulga, O. V.; Stine, K. J.; Demchenko, A. V. *Chem. Commun.* **2009**, 1834.
(10) (a) Sander, F.; Fluch, U.; Hermes, J. P.; Mayor, M. *Small* **2014**, *10*, 349. (b) Hermes, J. P.; Sander, F.; Fluch, U.; Peterle, T.; Thompson, D.; Urbani, R.; Pfohl, T.; Mayor, M. *J. Am. Chem. Soc.* **2012**, *134*, 14674.
(11) Hofmann, A.; Schmiel, P.; Stein, B.; Graf, C. *Langmuir* **2011**, *27*, 15165.
(12) Chinwangso, P.; Jamison, A. C.; Lee, T. R. *Acc. Chem. Res.* **2011**, *44*, 511.
(13) (a) Weidner, T.; Ballav, N.; Siemeling, U.; Troegel, D.; Walter, T.; Tacke, R.; Castner, D. G.; Zharnikov, M. *J. Phys. Chem. C* **2009**, *113*, 19609. (b) Lavrich, D. J.; Wetterer, S. M.; Bernasek, S. L.; Scoles, G. *J. Phys. Chem. B* **1998**, *102*, 3456.
(14) Zhang, S.; Leem, G.; Srisombat, L. O.; Lee, T. R. *J. Am. Chem. Soc.* **2008**, *130*, 113.
(15) (a) Perumal, S.; Hofmann, A.; Scholz, N.; Ruhl, E.; Graf, C. *Langmuir* **2011**, *27*, 4456. (b) Kitagawa, T.; Idomoto, Y.; Matsubara, H.; Hobara, D.; Kakiuchi, T.; Okazaki, T.; Komatsu, K. *J. Org. Chem.* **2006**, *71*, 1362.
(16) Lee, T.-C.; Hounihan, D. J.; Colorado, R.; Park, J.-S.; Lee, T. R. *J. Phys. Chem. B* **2004**, *108*, 2648.
(17) Wei, A. *Chem. Commun.* **2006**, 1581.
(18) Nelles, G.; Weisser, M.; Back, R.; Wohlfart, P.; Wenz, G.; Mittler-Neher, S. *J. Am. Chem. Soc.* **1996**, *118*, 5039.
(19) Kang, J. S.; Taton, T. A. *Langmuir* **2012**, *28*, 16751.
(20) Garg, N.; Mohanty, A.; Lazarus, N.; Schultz, L.; Rozzi, T. R.; Santhanam, S.; Weiss, L.; Snyder, J. L.; Fedder, G. K.; Jin, R. *Nanotechnology* **2010**, *21*, 405501.
(21) Camerano, J. A.; Casado, M. A.; Ciriano, M. A.; Lahoz, F. J.; Oro, L. A. *Organometallics* **2005**, *24*, 5147.
(22) Valiulin, R. A.; Kutateladze, A. G. *J. Org. Chem.* **2008**, *73*, 335.
(23) Weidner, T.; Kramer, A.; Bruhn, C.; Zharnikov, M.; Shaporenko, A.; Siemeling, U.; Trager, F. *Dalton Trans.* **2006**, 2767.
(24) (a) Weidner, T.; Zharnikov, M.; Hobetabach, J.; Castner, D. G.; Siemeling, U. *J. Phys. Chem. C* **2010**, *114*, 14975. (b) Li, Q.; Jin, C.; Petukhov, P. A.; Rukavishnikov, A. V.; Zaikova, T. O.; Phadke, A.; LaMunyon, D. H.; Lee, M. D.; Keana, J. F. *J. Org. Chem.* **2004**, *69*, 1010.
(25) Blaszczyk, A.; Elbing, M.; Mayor, M. *Org. Biomol. Chem.* **2004**, *2*, 2722.
(26) Le Neindre, M.; Magny, B.; Nicolaÿ, R. *Polym. Chem.* **2013**, *4*, 5577.
(27) Lau, K. H.; Huang, C.; Yakovlev, N.; Chen, Z. K.; O'Shea, S. J. *Langmuir* **2006**, *22*, 2968.
(28) Grandjean, C.; Boutonnier, A.; Guerreiro, C.; Fournier, J. M.; Mulard, L. A. *J. Org. Chem.* **2005**, *70*, 7123.
(29) Isomura, S.; Wirsching, P.; Janda, K. D. *J. Org. Chem.* **2001**, *66*, 4115.

Functional tripodal thioacetates

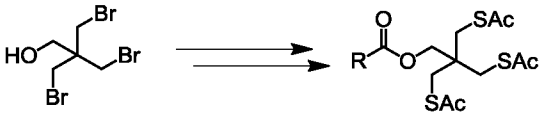

Supplementary information for:

Synthesis of Functional Tripodal Thioacetates

Florian Kretschmer,[a,b] Martin D. Hager,[a,b] Ulrich S. Schubert[a,b]*

[a] Laboratory of Organic and Macromolecular Chemistry (IOMC), Friedrich Schiller University Jena, Humboldtstr. 10, 07743 Jena, Germany

[b] Jena Center for Soft Matter (JCSM), Friedrich Schiller University Jena, Philosophenweg 7, 07743 Jena, Germany

Fax: 00493641948202

E-mail: ulrich.schubert@uni-jena.de

Compound **3a**:

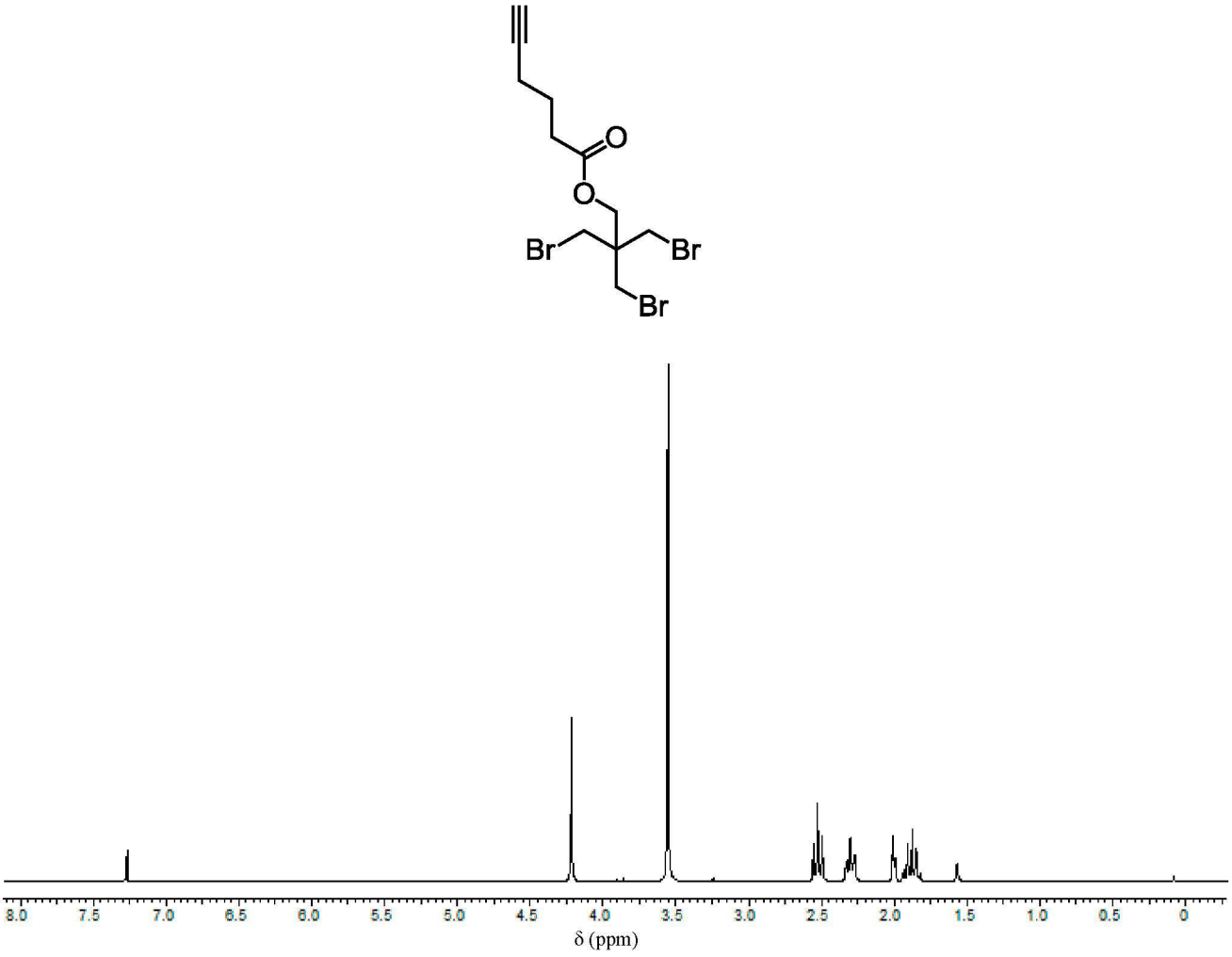

^{1}H NMR of **3a** in $CDCl_3$.

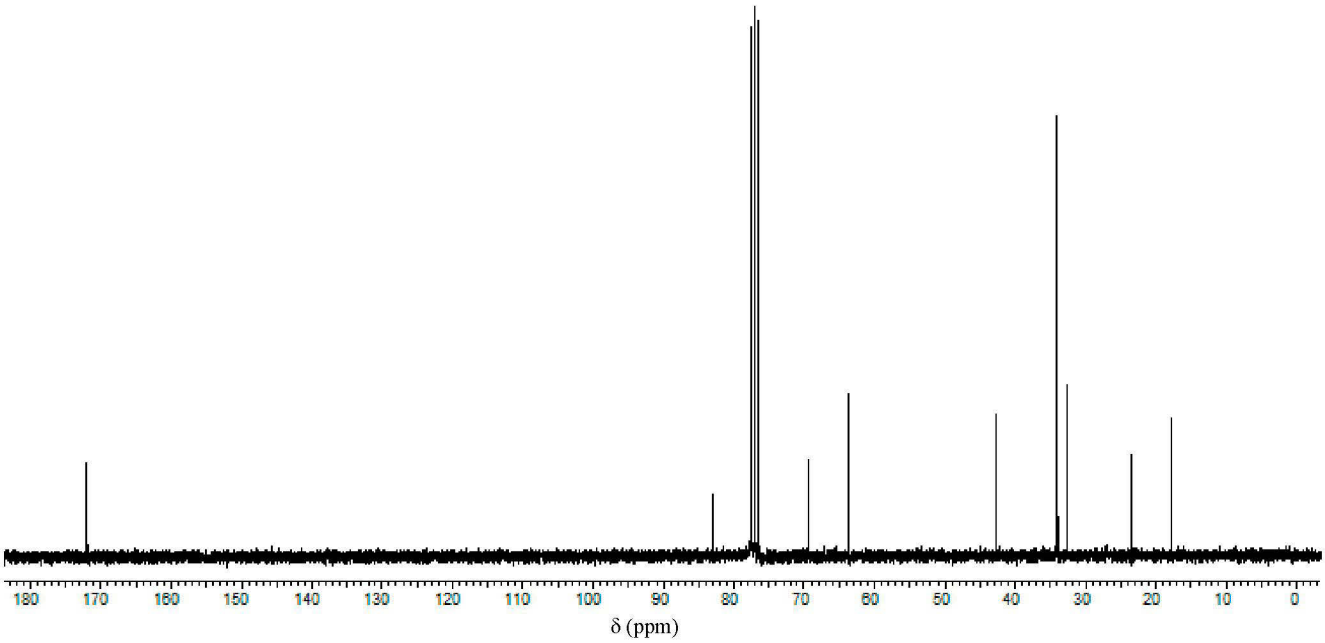

^{13}C NMR of **3a** in $CDCl_3$.

Compound **3b**:

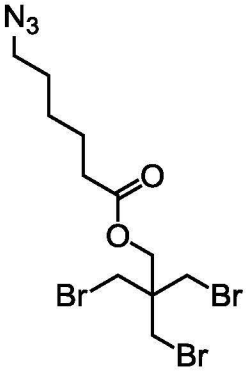

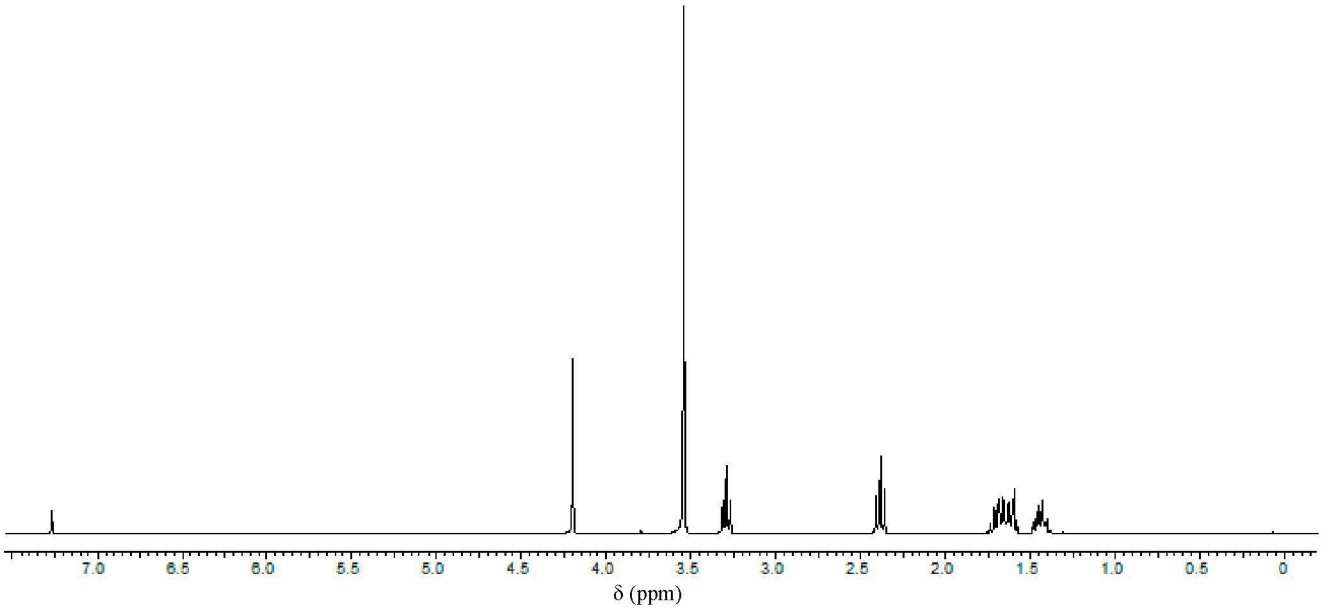

^{1}H NMR of **3b** in $CDCl_3$.

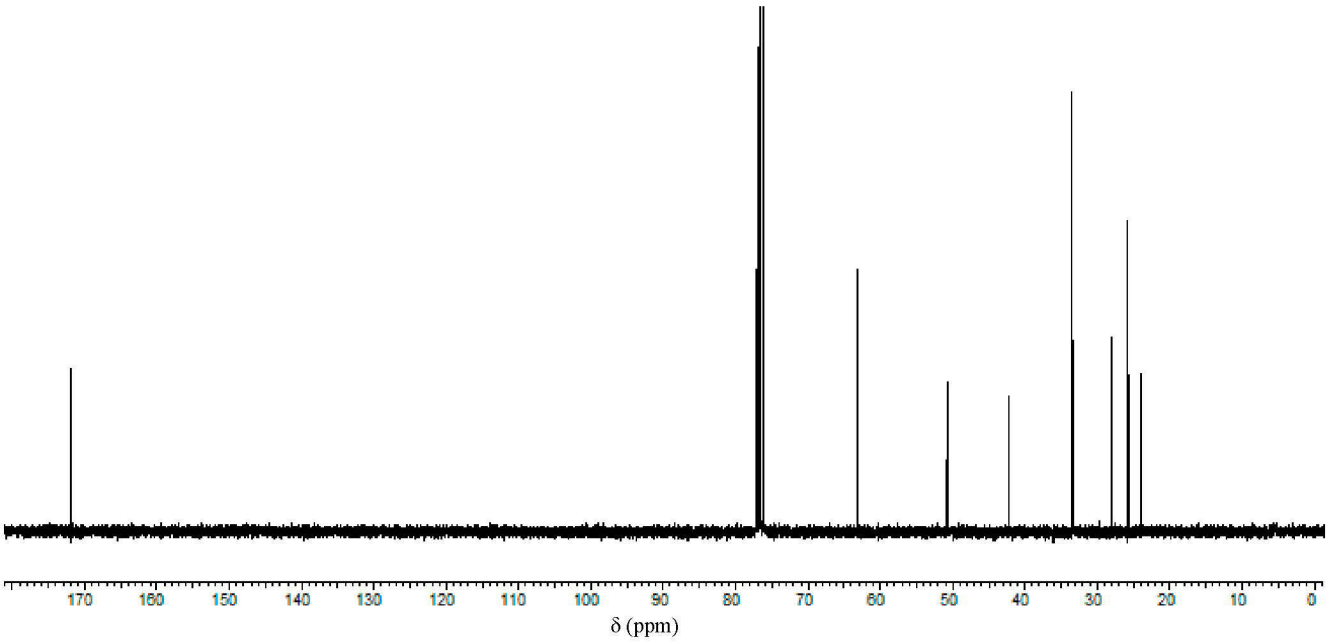

^{13}C NMR of **3b** in $CDCl_3$.

Compound **3c**:

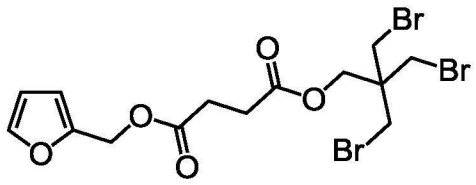

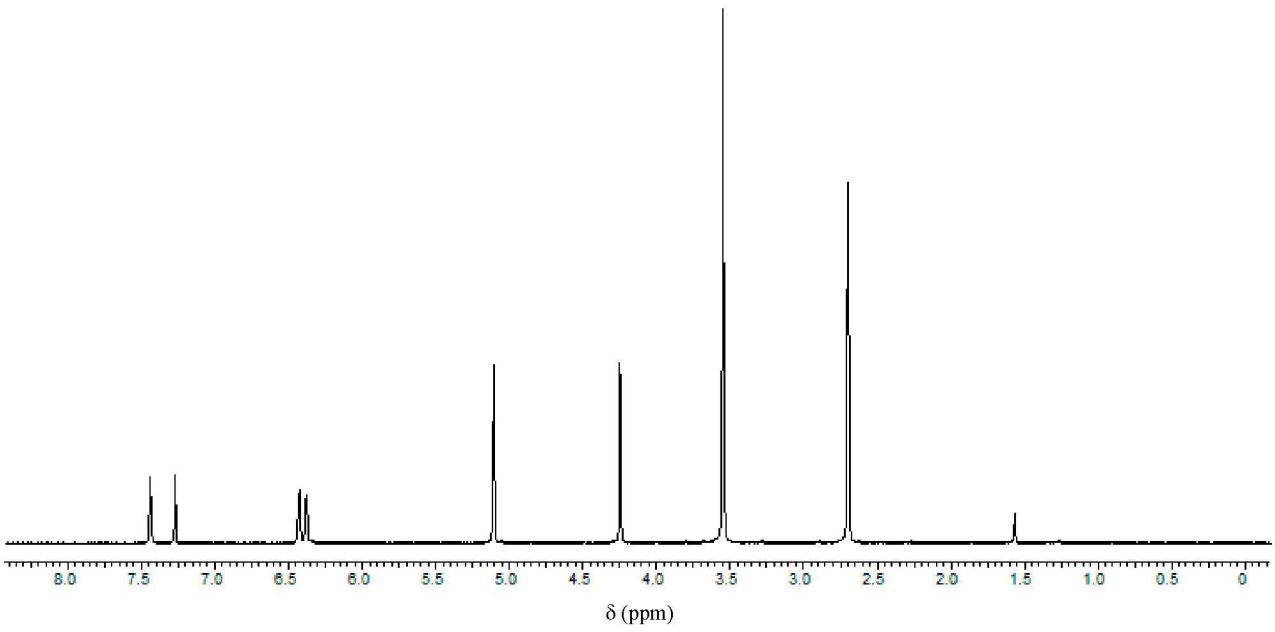

^{1}H NMR of **3c** in $CDCl_3$.

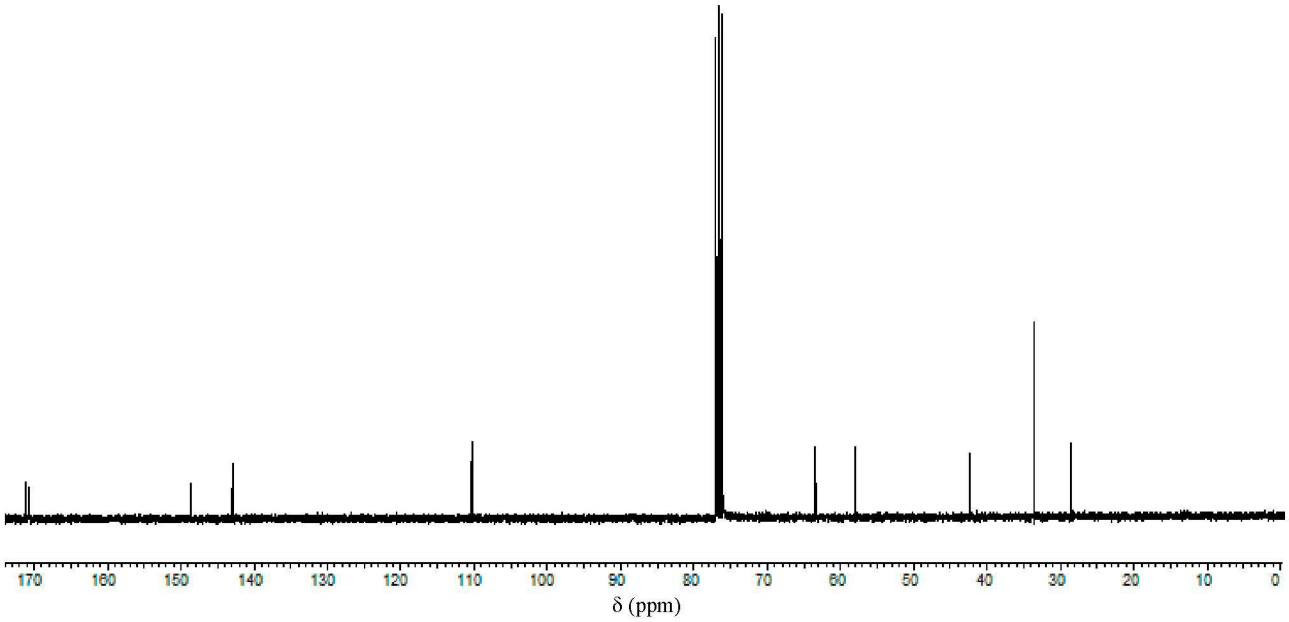

^{13}C NMR of **3c** in $CDCl_3$.

Compound **4a**:

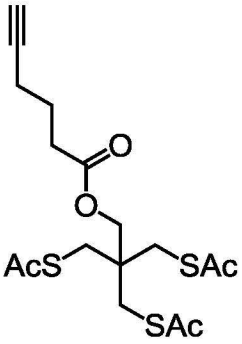

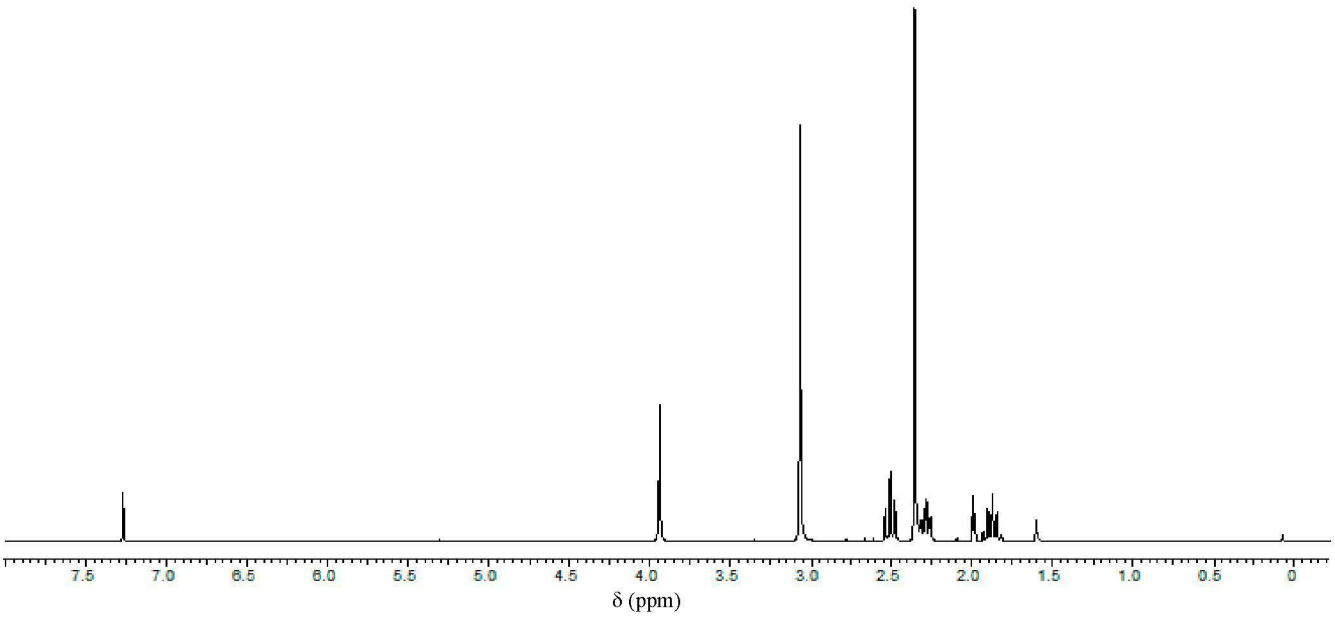

^{1}H NMR of **4a** in $CDCl_3$.

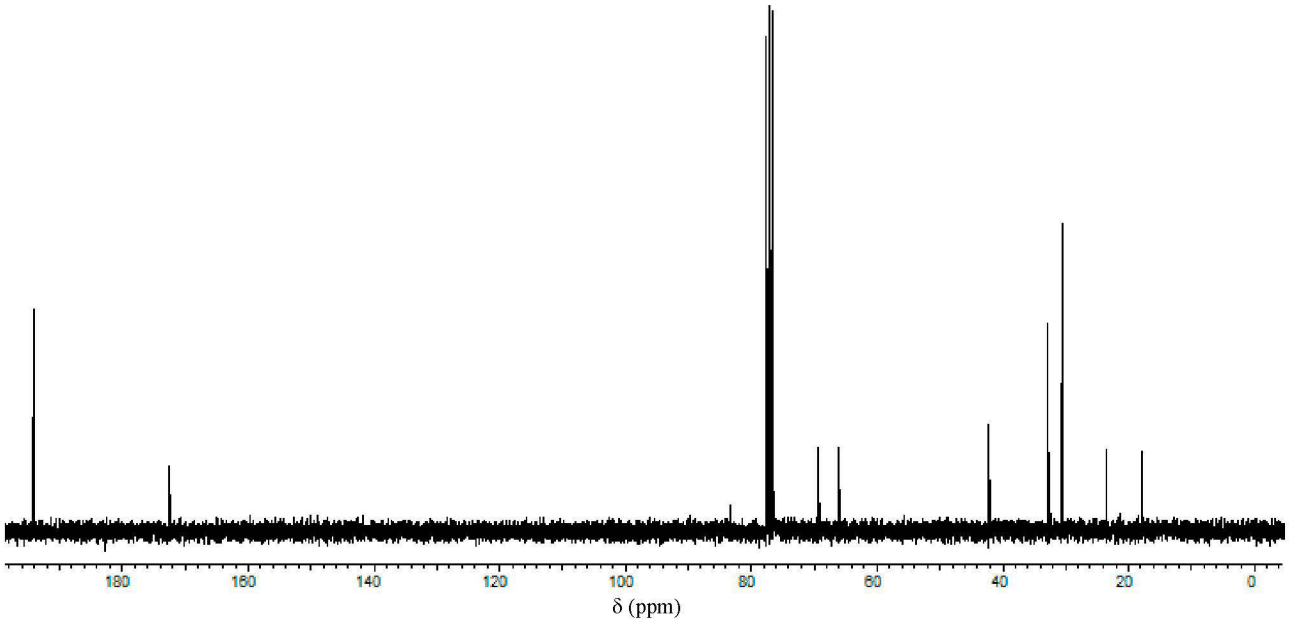

^{13}C NMR of **4a** in $CDCl_3$.

Compound **4b**:

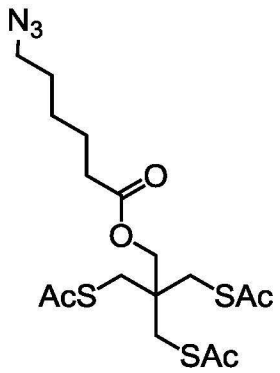

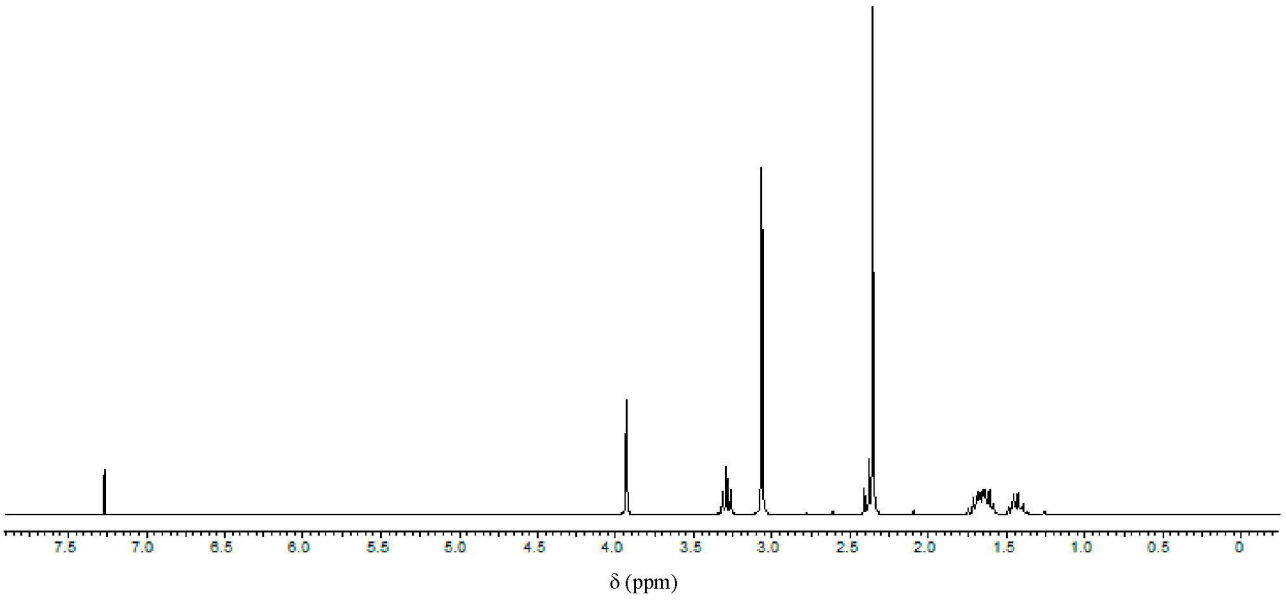

^{1}H NMR of **4b** in $CDCl_3$.

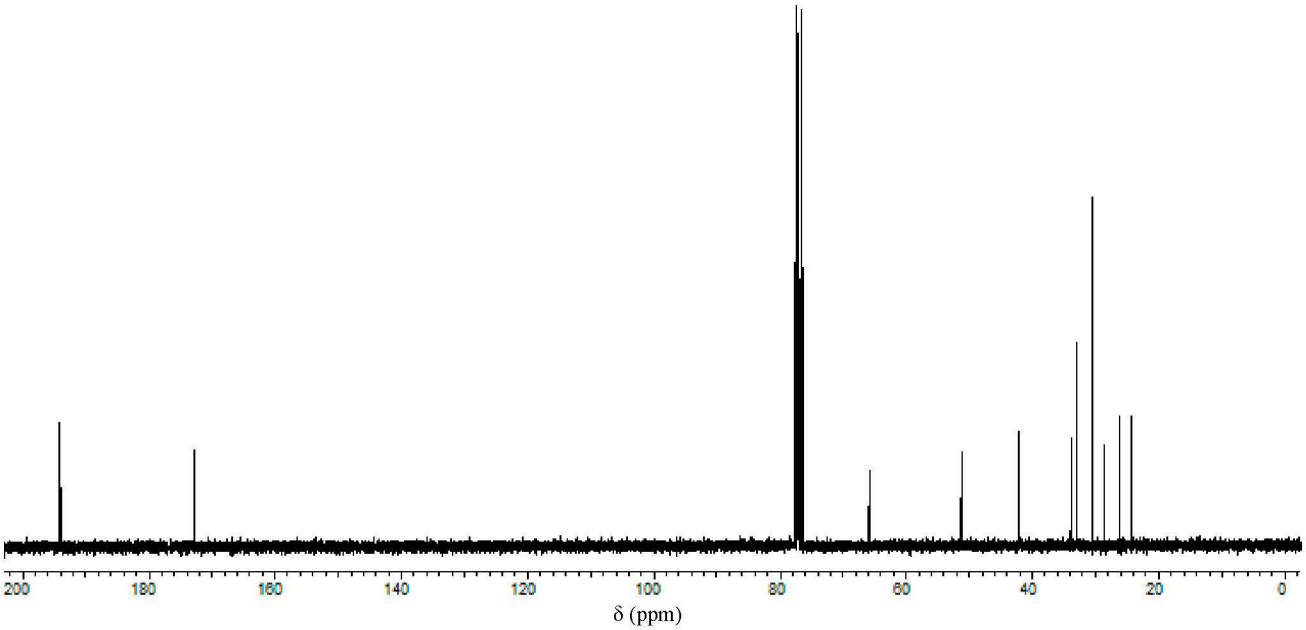

^{13}C NMR of **4b** in $CDCl_3$.

Compound **4c**:

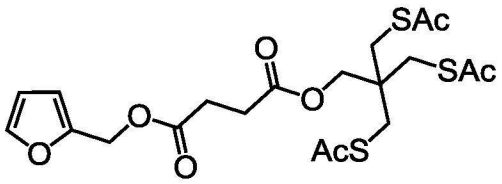

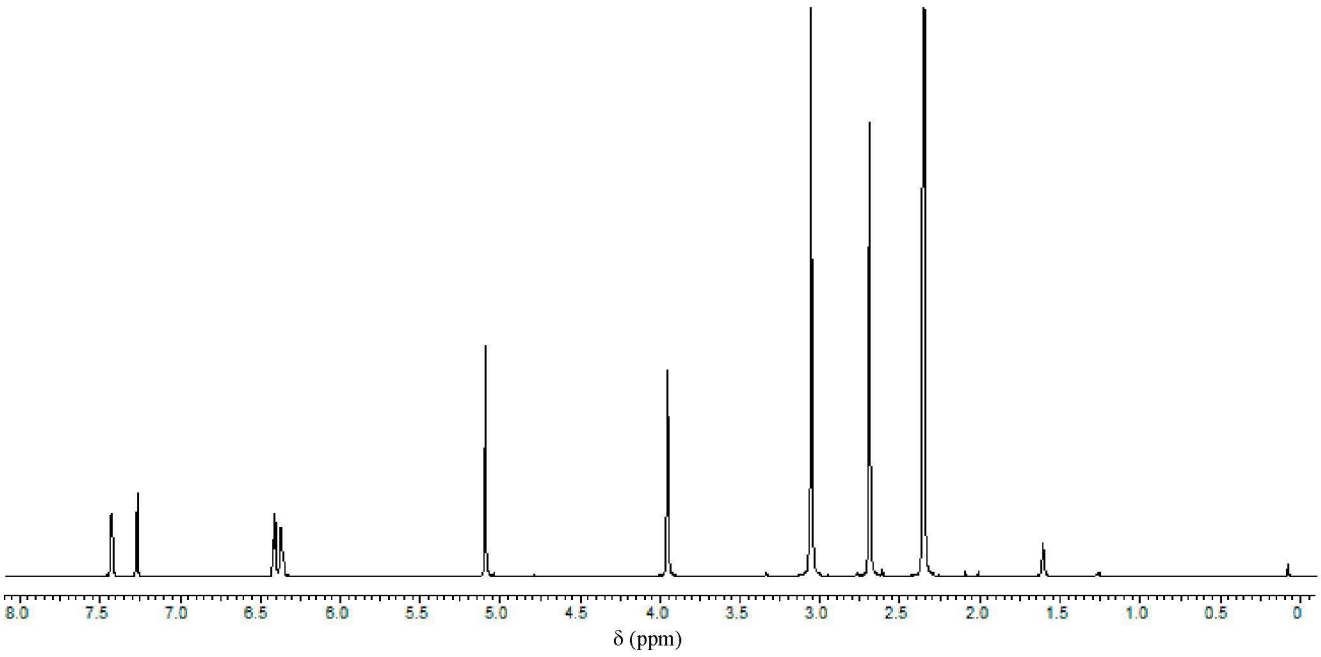

^{1}H NMR of **4c** in $CDCl_3$.

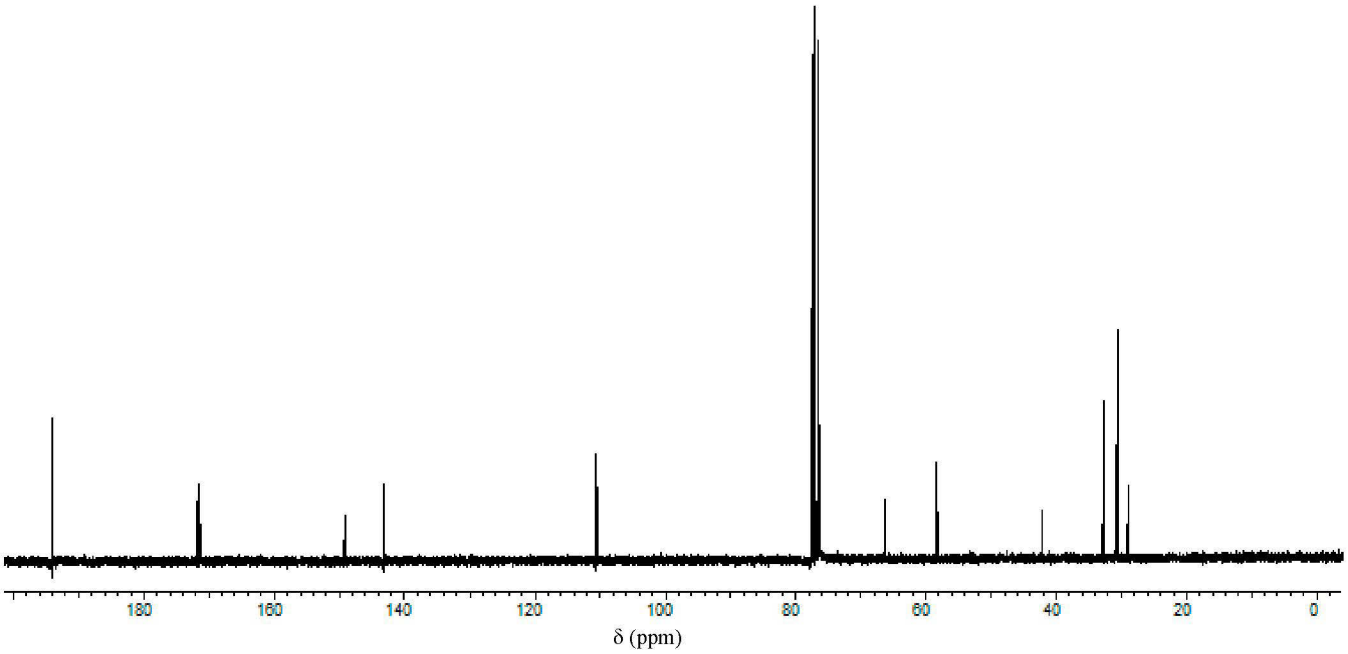

^{13}C NMR of **4c** in $CDCl_3$.

Publication P5

Poly(2-vinyl pyridine)-*block*-poly(ethylene oxide) Featuring a Furan Group at the Block Junction – Synthesis and Functionalization

T. Rudolph, M. J. Barthel, F. Kretschmer, U. Mansfeld, S. Hoeppener, M. D. Hager, U. S. Schubert, F. H. Schacher

Macromol. Rapid Commun. **2014**, *35*, 916-921.

Poly(2-vinyl pyridine)-*block*-Poly(ethylene oxide) Featuring a Furan Group at the Block Junction—Synthesis and Functionalization

Tobias Rudolph, Markus J. Barthel, Florian Kretschmer, Ulrich Mansfeld, Stephanie Hoeppener, Martin D. Hager, Ulrich S. Schubert, Felix H. Schacher*

Furfuryl glycidyl ether (FGE) represents a highly versatile monomer for the preparation of reversibly cross-linkable nanostructured materials via Diels–Alder reactions. Here, the use of FGE for the mid-chain functionalization of a P2VP-*b*-PEO diblock copolymer is reported. The material features one furan moiety at the block junction, $P2VP_{68}$-FGE-*b*-PEO_{390}, which can be subsequently addressed in Diels–Alder reactions using maleimide-functionalized counterparts. The presence of the FGE moiety enables the introduction of dyes as model labels or the formation of hetero-grafted brushes as shell on hybrid Au@Polymer nanoparticles. This renders $P2VP_{68}$-FGE-*b*-PEO_{390}, a powerful tool for selective functionalization reactions, including the modification of surfaces.

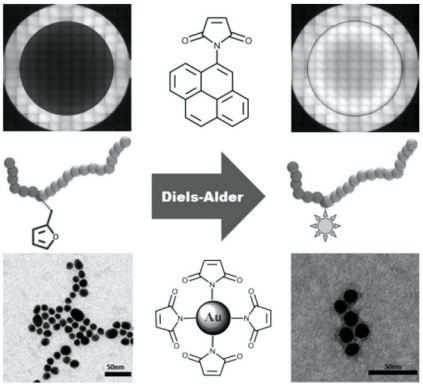

1. Introduction

During the last decades, well-defined block copolymers revealed high potential for a broad range of applications, mainly driven by the possibility to combine different properties within one single material and to introduce the ability to undergo self-assembly into nanostructured materials in various environments.[1–5] The preparation of block copolymers is usually achieved by sequential polymerization of different monomers or via post-polymerization modification using suitable macromolecular conjugation reactions [e.g., 1,3-dipolar cycloadditions or (hetero) Diels–Alder (DA) reactions].[6–10] Thereby, the precise positioning of functional groups within polymer chains is crucial for the synthesis of linear block copolymers or materials of different architectures, e.g., star-shaped structures.[11–13] Although more and more examples are found where polymeric building blocks are functionalized at one or both chain ends, examples for addressing the mid-chain junction point, i.e., the covalent linkage of blocks A and B of diblock copolymers, are scarce.[14–17] Such functional mid-chain junctions can be introduced by functional initiators[18–20] or end-capping of an active polymer chain and the subsequent polymerization of the second block.[21] The resulting functionalized polymers were used in surface coatings (e.g., on glass)[22] as well as for the preparation

T. Rudolph,[+] M. J. Barthel,[+] F. Kretschmer, U. Mansfeld, Dr. S. Hoeppener, Dr. M. D. Hager, Prof. U. S. Schubert, Prof. F. H. Schacher
Laboratory of Organic and Macromolecular Chemistry, Friedrich Schiller University Jena, Humboldtstr. 10, 07743 Jena, Germany
E-mail: felix.schacher@uni-jena.de
T. Rudolph,[+] M. J. Barthel,[+] F. Kretschmer, U. Mansfeld, Dr. S. Hoeppener, Dr. M. D. Hager, Prof. U. S. Schubert, Prof. F. H. Schacher
Jena Center for Soft Matter (JCSM), Friedrich Schiller University Jena, Philosophenweg 7, 07743 Jena, Germany
M. J. Barthel,[+] Prof. U. S. Schubert
Dutch Polymer Institute, P.O. Box 902, Eindhoven 5600 AX, The Netherlands
[+]These authors contributed equally to this work.

DOI: 10.1002/marc.201300875

of different architectures (e.g., H-shaped polymers[23] and miktoarm stars).[14] Current examples most commonly feature a new initiating group or a clickable moiety. In that respect, epoxides can be used as straightforward and highly efficient end-capping agents during living anionic polymerization using lithium counter ions. Here, due to the strong coordination of lithium toward the alkoxide chain-end, further polymerization of epoxides is prevented and the attachment of one single molecule can be realized. Potential functionalized epoxides such as allyl glycidyl ether (AGE) or ethoxy ethyl glycidyl ether (EEGE) are commercially available and transform this substance class into an interesting tool for the selective mid-chain functionalization of polymer chains.

Recently, furfuryl glycidyl ether (FGE) has been established as a versatile and functional monomer for anionic ring-opening polymerization (AROP) and the subsequent use of the furan moiety for controlled and reversible crosslinking of micellar cores or individual domains within nanostructured films via the DA reaction using a bismaleimide.[24,25] In the latter case, the potential application of poly(ethylene oxide)-*block*-poly(furfuryl glycidyl ether) (PEO-*b*-PFGE) diblock copolymers as self-healing coatings was proposed.

Here, we use FGE as functional end-capping agent for the living anionic polymerization of poly(2-vinyl pyridine) (P2VP), followed by the subsequent polymerization of ethylene oxide (EO) and the formation of mid-chain-functionalized P2VP-*b*-PEO. After characterization via size-exclusion chromatography (SEC), nuclear magnetic resonance (NMR) spectroscopy, and MALDI-TOF MS, the furan moiety in between the two blocks was used for selective DA reactions with maleimide-functionalized model dyes and gold nanoparticles (AuNPs).

2. Results and Discussion

Mid-chain-functionalized block copolymers represent interesting materials when it comes to the modification of surfaces such as on planar substrates or on (nano) particles. The introduction of a furan group at the junction point of diblock copolymers in turn is motivated by the broad accessibility of functional groups and architectures by the DA chemistry. Therefore, the synthesis of poly(2-vinyl pyridine)-*block*-poly(ethylene oxide) (P2VP-FGE-*b*-PEO), featuring a FGE moiety in between the P2VP and the PEO segment, was carried out in two steps. First, 2-vinylpyridine was polymerized after initiation via *sec*-butyl lithium (*sec*-BuLi). After full conversion, 1,1-diphenylethylene was added to the reaction mixture to decrease the nucleophilicity of the active chain end,[16] and the living P2VP chains were end-capped with FGE (Figure 1A). Afterward, the reaction was quenched by the addition of methanol and the crude product was precipitated into cold hexane. P2VP-FGE-OH was characterized via SEC, ^{1}H NMR, and MALDI-TOF MS (Figure 1; Table S1 and Figure S2, Supporting Information). The degree of polymerization (DP) was determined to be 68, resulting in P2VP$_{68}$-FGE-OH. The end-group fidelity was assessed via MALDI-TOF MS and NMR and was found to be 100% within the error of the measurement. MALDI-TOF MS also revealed the presence of the lithium counterion (Figure S2, Supporting Information), which however had to be removed prior to the polymerization of ethylene oxide. For this purpose, the material was intensively washed with water and precipitated into cold hexane several times (Figure S3, Supporting Information). As second step, P2VP$_{68}$-FGE-OH was dissolved in THF and the hydroxyl end-group was activated by the addition of an excess of diphenylmethyl potassium (DPMK), until a deep red color could be observed (Figure 1A). Under vigorous stirring, ethylene oxide was added to the reaction at −20 °C, the reaction mixture was slowly heated to 40 °C, and the polymerization was terminated via the addition of methanol after 24 h, followed by precipitation of the block copolymer into cold diethyl ether. The obtained material was again investigated via SEC, ^{1}H NMR, and MALDI-TOF MS (Figure S4, Supporting Information). The SEC trace shows a clear shift to lower elution volume in comparison to P2VP$_{68}$-FGE-OH (Figure 1B; Table S1, Supporting Information), and a new peak around 3.6 ppm for the PEO backbone appears in the ^{1}H NMR spectrum. The exact molar mass of the block copolymer was determined by MALDI-TOF MS, leading to 24 500 g mol^{-1}, and a composition of P2VP$_{68}$-FGE-PEO$_{390}$ (Figure S4, Supporting Information), which was also confirmed via ^{1}H NMR spectroscopy.

As a first proof of successful functionalization, P2VP$_{68}$-FGE-*b*-PEO$_{390}$ was used in DA reactions with two different maleimide-functionalized dyes [*N*-(1-pyrenyl)maleimide and 4-phenylazomaleinanil]. Therefore, the block copolymer and the respective dye (20 equiv.) were dissolved in 2 mL DMF separately in two vials and heated to 75 °C for 24 h. Afterward, the dye-functionalized materials were purified via size exclusion column chromatography (BioBeads SX1) to remove any excess of the dyes. In both cases, successful functionalization with the azobenzene-, P2VP$_{68}$-azo-*b*-PEO$_{390}$, and the pyrene-moiety, P2VP$_{68}$-pyr-*b*-PEO$_{390}$, was proven by UV–vis measurements (Figure 2B,C). The UV–vis spectra display that the initial P2VP$_{68}$-FGE-*b*-PEO$_{390}$ shows no characteristic absorption band (triangles), whereas the characteristic patterns of the individual molecules [spheres, 331 nm for 4-phenylazomaleinanil and 313, 326, and 342 nm for *N*-(1-pyrenyl) maleimide] can be found for the block copolymers after successful functionalization (squares).

Pyrene is known as a hydrophobic, fluorescent dye suitable for the determination of the critical

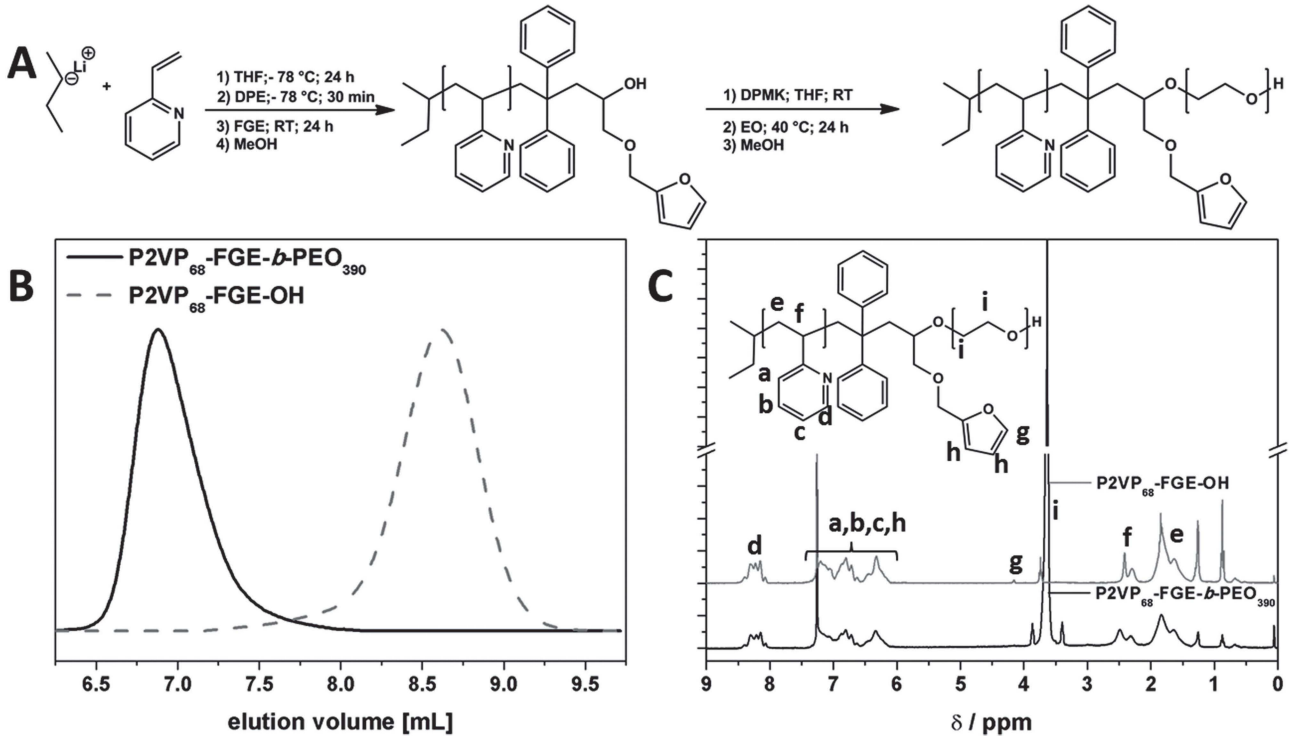

Figure 1. A) Block copolymer synthesis via sequential polymerization of 2-vinylpyridine and ethylene oxide, B) comparison of SEC traces for $P2VP_{68}$-FGE-OH (dashed gray line) and $P2VP_{68}$-FGE-*b*-PEO_{390} (black straight line), and C) the NMR spectra for $P2VP_{68}$-FGE-OH (gray line) and $P2VP_{68}$-FGE-*b*-PEO_{390} (black line).

micellization concentration (cmc) of amphiphilic block copolymers.[26–29] In case of *N*-(1-pyrenyl)maleimide, no fluorescence is described in the literature for the pristine dye in water, only after nucleophilic attack by thiols.[30] This can also be observed for our system after functionalization with *N*-(1-pyrenyl)maleimide and this was investigated via fluorescence microscopy (excitation wavelength = 357 nm; emission filter = 460 nm, Figure 3). Using this setup, no fluorescence could be detected for the pure dye in MilliQ water, whereas pyrene itself showed clear fluorescence under these conditions (Figure S6C, Supporting Information). Both $P2VP_{68}$-pyr-*b*-PEO_{390} and $P2VP_{68}$-FGE-*b*-PEO_{390} were transferred from THF into MilliQ water (pH7) by evaporation of the organic solvent (concentration was 5 mg mL^{-1} in both cases). In Figure 3, the circle originates from the fluorescence of the well-plate itself, while in the center the sample solution is located. As P2VP is known to exhibit a weak autofluorescence,[31] some fluorescence was also observed for $P2VP_{68}$-FGE-*b*-PEO_{390}, whereas $P2VP_{68}$-pyr-*b*-PEO_{390} shows a twofold increase in fluorescence in comparison to the pristine block copolymer (Figure 3; Figures S6 and S7, Supporting Information). This strong increase in fluorescence can be explained by electronic changes after the covalent attachment to the block copolymer chain by DA chemistry.

We were also interested in using $P2VP_{68}$-FGE-*b*-PEO_{390} for the functionalization of AuNPs. In that way, a hetero-brush could be generated in analogy to poly(styrene)-*block*-poly(ethylene oxide) (PS-*b*-PEO) brushes on planar surfaces.[22] Therefore, a maleimide-functionalized tri-thioacetate was synthesized (Figure S1, Supporting Information) and used for the synthesis of maleimide-functionalized AuNPs.[32–35] Possible excess of the maleimide-linker was removed by centrifugation of the particles (60 min at 5000 rpm), followed by resuspension in DMF (three cycles). The protective group was removed by heating the functionalized NP for 1 h at 140 °C. Both size and shape of the NPs were confirmed via DLS, TEM, and UV–vis (Figure 4). Spherical AuNPs with a $\langle R_h \rangle_{z,app}$ of 8 nm were obtained according to DLS (Figure 4D) and TEM (Figure 4A). For the attachment of $P2VP_{68}$-FGE-*b*-PEO_{390} to the NP surface, AuNP and $P2VP_{68}$-FGE-*b*-PEO_{390} were suspended together in DMF and heated for 2 d at 75 °C. After this treatment, the solution was centrifuged and washed with DMF to remove any unreacted $P2VP_{68}$-FGE-*b*-PEO_{390}. After resuspension, the particles ($P2VP_{68}$-DA_{Au}-*b*-PEO_{390}) were investigated using UV–vis spectroscopy and DLS, showing a slight red-shift in the UV–vis spectra from 527 to 538 nm (Figure 4C) and an increase in hydrodynamic radius ($\langle R_h \rangle_{z,app}$ = 12 nm)

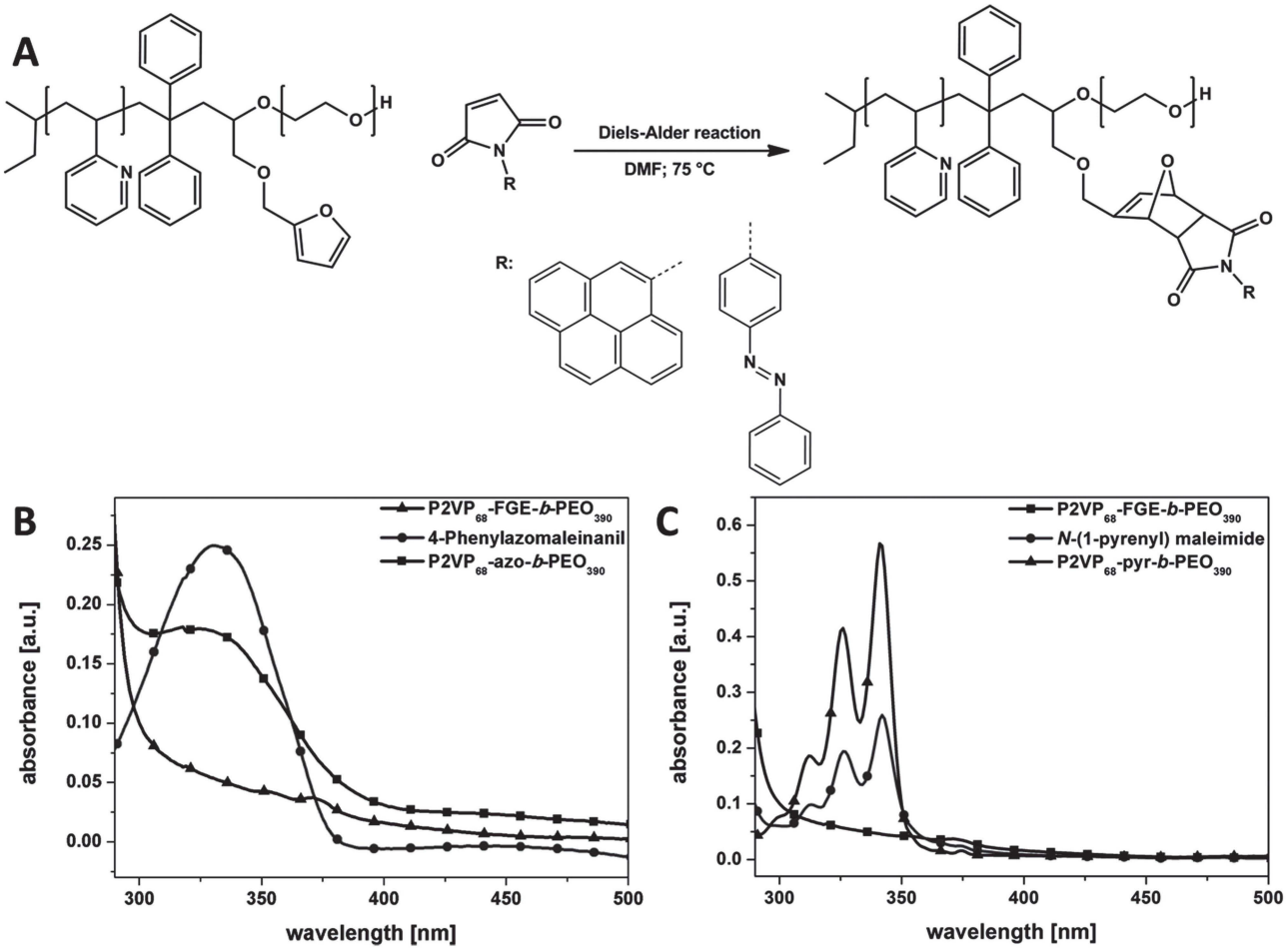

Figure 2. A) DA reaction between $P2VP_{68}$-FGE-*b*-PEO_{390} and maleimide-functionalized dyes; comparison of UV–vis spectra for B) $P2VP_{68}$-FGE-*b*-PEO_{390} (triangles), 4-phenylazomaleinanil (spheres), and $P2VP_{68}$-azo-*b*-PEO_{390} (squares); C) $P2VP_{68}$-FGE-*b*-PEO_{390} (squares), *N*-(1-pyrenyl) maleimide (spheres), and $P2VP_{68}$-azo-*b*-PEO_{390} (triangles) in THF.

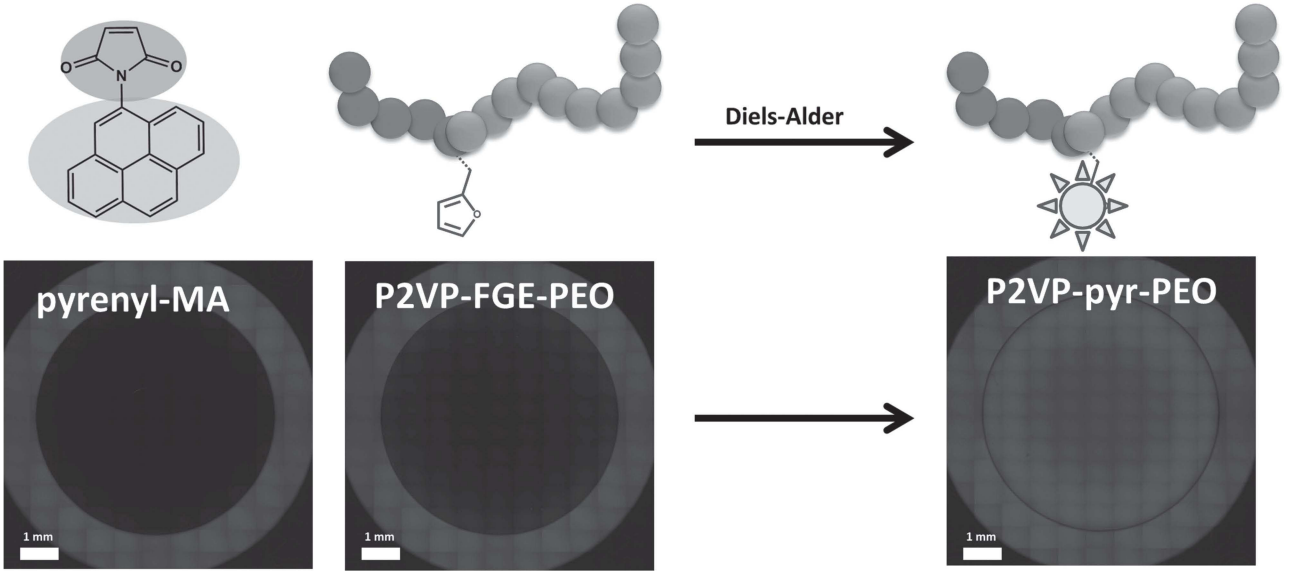

Figure 3. Functionalization of $P2VP_{68}$-FGE-*b*-PEO_{390}; comparison of fluorescence microscope images of *N*-(1-pyrenyl)maleimide (left), $P2VP_{68}$-FGE-*b*-PEO_{390} (5 mg mL^{-1}, middle), and $P2VP_{68}$-pyr-*b*-PEO_{390} (5 mg mL^{-1}, right) in water.

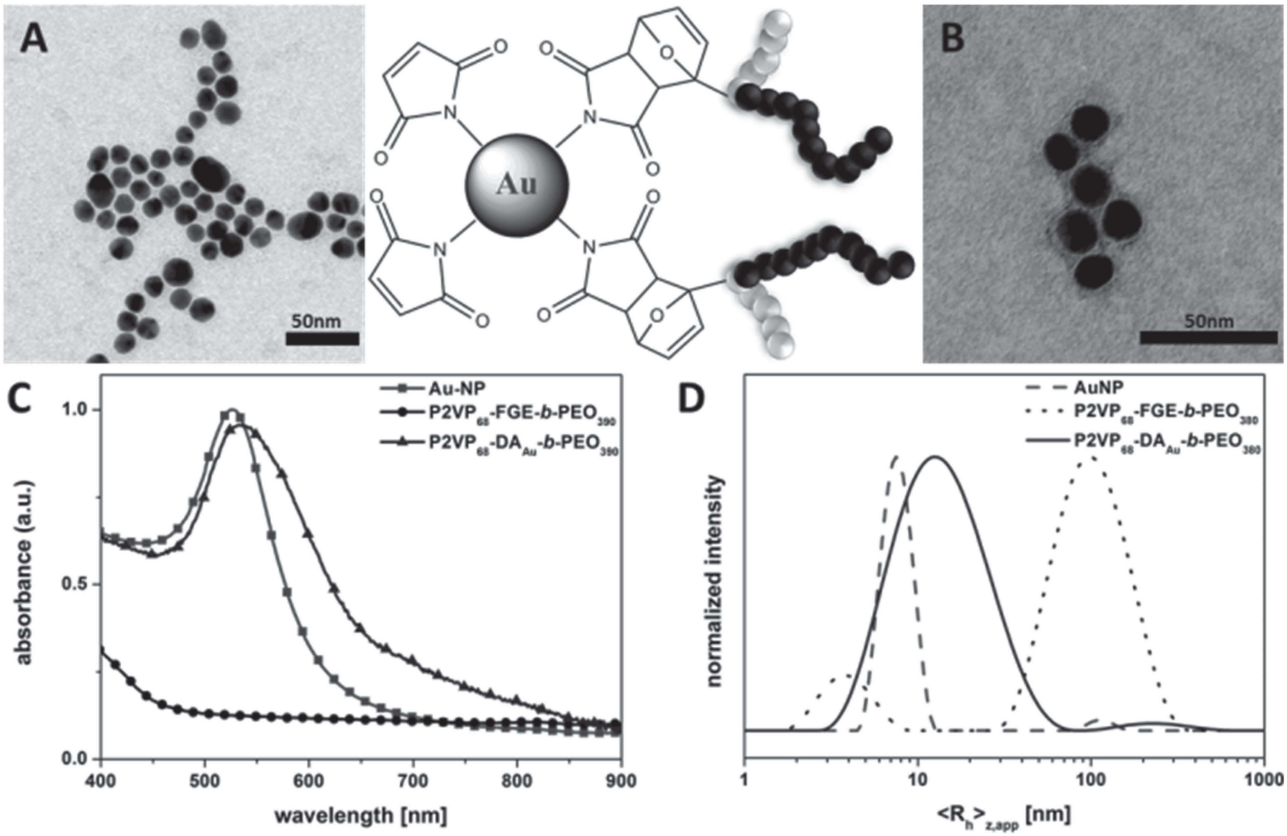

Figure 4. Comparison of TEM images for the pristine (A, unstained) and block copolymer-coated AuNP (B, stained with uranyl acetate); C) comparison of UV–vis spectra for $P2VP_{68}$-FGE-*b*-PEO_{390} (spheres), maleimide-functionalized AuNP (squares), and $P2VP_{68}$-DA_{Au}-*b*-PEO_{390} (triangles); D) comparison of intensity-weighted DLS CONTIN plots for $P2VP_{68}$-FGE-*b*-PEO_{390} (dotted curve; $\langle R_h \rangle_{z,app}$ = 4 nm and 100 nm; 2 mg mL^{-1}), maleimide-functionalized AuNP (dashed curve; $\langle R_h \rangle_{z,app}$ = 8 nm; 1 mg mL^{-1}), and $P2VP_{68}$-DA_{Au}-*b*-PEO_{390} (straight curve; $\langle R_h \rangle_{z,app}$ = 12 nm; 1 mg mL^{-1}) in DMF.

compared with the pristine block copolymer ($\langle R_h \rangle_{z,app}$ = 4 nm), and the maleimide-functionalized AuNP ($\langle R_h \rangle_{z,app}$ = 8 nm, Figure 4D).

According to DLS, the size distribution of $P2VP_{68}$-DA_{Au}-*b*-PEO_{390} slightly broadens, which might be due to a certain amount of aggregation of the hybrid particles in solution. If the structures are subjected to TEM analysis, the freshly prepared AuNPs feature sharp edges whereas this seems not to be the case after DA reaction with $P2VP_{68}$-FGE-*b*-PEO_{390}, indicating the attachment of a polymeric shell (Figure S8, Supporting Information). Staining with uranyl acetate was applied to the NP both before and after surface modification. As expected, no changes were observed for the pristine AuNP, except for a slight decrease of the overall contrast within the corresponding TEM images due to an increase of the electron density on the underlying carbon support on the whole TEM grid (Figure S8, Supporting Information). For $P2VP_{68}$-DA_{Au}-*b*-PEO_{390}, a continuous dark ring of a few nanometers thickness is observed and this further supports the assumption of the successful formation of a P2VP/PEO shell. $P2VP_{68}$-DA_{Au}-*b*-PEO_{390} was also transferred into DMF-d_7 and was investigated via ^{1}H NMR, but the signal intensity of the obtained spectrum was rather low (Figure S9, Supporting Information). However, both the characteristic signals for P2VP and PEO could be assigned.

As a further proof for the successful particle coating, both $P2VP_{68}$-DA_{Au}-*b*-PEO_{390} and the pristine AuNP were transferred from DMF into water (pH 7). While the solution containing $P2VP_{68}$-DA_{Au}-*b*-PEO_{390} showed a red color (hinting toward well-dispersed hybrid particles), the pristine NP aggregated, indicated by a bluish color (Figure S10A, Supporting Information). Under acidic conditions (pH ≤ 4), P2VP becomes protonated and positively charged. Therefore, zeta-potential measurements were performed for the block copolymer and the NPs, respectively (Figure S10B, Supporting Information). While the pristine AuNP show a zeta potential of ≈−33 mV at pH 7, precipitation was observed at pH 4. After coating, a zeta potential of −3 mV at pH 7 and +22 mV at pH 4 was found, following the trend observed for

$P2VP_{68}$-FGE-*b*-PEO_{390} under this conditions (Figure S10B, Supporting Information).

3. Conclusion

We successfully synthesized a mid-chain-functionalized block copolymer featuring one furan moiety, $P2VP_{68}$-FGE-*b*-PEO_{390}, by sequential living anionic polymerization. The furan moiety was subsequently used in DA reactions with maleimide-functionalized counterparts to introduce dyes as model labels to the block copolymer or to create a hetero-grafted shell on AuNP. Our results convincingly demonstrate that $P2VP_{68}$-FGE-*b*-PEO_{390} is a versatile example for (surface) functionalization and the introduction of hetero-brushes. Our results may also be used in the future for the stabilization of carbon nanotubes via $P2VP_{68}$-pyr-*b*-PEO_{390}, surface modification of NPs different from Au, or the preparation of ABC miktoarm star terpolymers.

Supporting Information

Supporting Information is available from the Wiley Online Library or from the author.

Acknowledgements: The authors thank Sarah Crotty for MALDI-TOF MS, Ulrike Günther for zeta-potential measurements, David Pretzel for fluorescence microscopy measurements, and Jürgen Vitz for technical support regarding the ethylene oxide polymerization. F.H.S. thanks the VCI for an independent researcher fellowship, and T.R. acknowledges the Carl-Zeiss foundation for a PhD scholarship. The work of M.J.B. forms part of the research program of the Dutch Polymer Institute (DPI), project #690. The authors also acknowledge the Thuringian Ministry for Education, Science and Culture (grants #B514–09051, NanoConSens, #B515–10065, ChaPoNano, #B515–11028, BASIS, and #B515–07008) for financial support of this study. U.S.S., M.D.H., F.K. and S.H. thank the Federal Ministry of Education and Research (Spitzencluster PHONA) for financial support.

Received: November 27, 2013; Revised: December 30, 2013; Published online: February 24, 2014; DOI: 10.1002/marc.201300875

Keywords: anionic polymerization; block copolymer; Diels–Alder reaction; furfuryl glycidyl ether; mid-chain junction; poly(ethylene oxide)

[1] F. H. Schacher, P. A. Rupar, I. Manners, *Angew. Chem Int. Ed.* **2012**, *51*, 7898.
[2] A. H. Gröschel, F. H. Schacher, H. Schmalz, O. V. Borisov, E. B. Zhulina, A. Walther, A. H. E. Müller, *Nat. Commun.* **2012**, *3*, 710.
[3] H.-C. Kim, S.-M. Park, W. D. Hinsberg, *Chem. Rev.* **2009**, *110*, 146.
[4] A. Nunns, J. Gwyther, I. Manners, *Polymer* **2013**, *54*, 1269.
[5] S. B. Darling, *Prog. Polym. Sci.* **2007**, *32*, 1152.
[6] M. A. Tasdelen, M. U. Kahveci, Y. Yagci, *Prog. Polym. Sci.* **2011**, *36*, 455.
[7] C. Barner-Kowollik, F. E. Du Prez, P. Espeel, C. J. Hawker, T. Junkers, H. Schlaad, W. Van Camp, *Angew. Chem Int. Ed.* **2011**, *50*, 60.
[8] K. Kempe, A. Krieg, C. R. Becer, U. S. Schubert, *Chem. Soc. Rev.* **2012**, *41*, 176.
[9] A. S. Goldmann, M. Glassner, A. J. Inglis, C. Barner-Kowollik, *Macromol. Rapid Commun.* **2013**, *34*, 810.
[10] T. T. T. N'Guyen, H. T. T. Duong, J. Basuki, V. Montembault, S. Pascual, C. Guibert, J. Fresnais, C. Boyer, M. R. Whittaker, T. P. Davis, L. Fontaine, *Angew. Chem Int. Ed.* **2013**, *52*, 14152.
[11] T. Rudolph, S. Crotty, M. v. d. Lühe, D. Pretzel, U. S. Schubert, F. Schacher, *Polymers* **2013**, *5*, 1081.
[12] D. Fournier, R. Hoogenboom, U. S. Schubert, *Chem. Soc. Rev.* **2007**, *36*, 1369.
[13] H. Durmaz, A. Sanyal, G. Hizal, U. Tunca, *Polym. Chem.* **2012**, *3*, 825.
[14] A. Hanisch, H. Schmalz, A. H. E. Müller, *Macromolecules* **2012**, *45*, 8300.
[15] C. Tonhauser, H. Frey, *Macromol. Rapid Commun.* **2010**, *31*, 1938.
[16] A. Natalello, C. Tonhauser, E. Berger-Nicoletti, H. Frey, *Macromolecules* **2011**, *44*, 9887.
[17] X.-S. Feng, C.-Y. Pan, *Macromolecules* **2002**, *35*, 4888.
[18] O. Altintas, U. Tunca, C. Barner-Kowollik, *Polym. Chem.* **2011**, *2*, 1146.
[19] O. Altintas, B. Yankul, G. Hizal, U. Tunca, *J. Polym. Sci., Part A: Polym. Chem.* **2007**, *45*, 3588.
[20] Z. L. Wang, J. T. Xu, B. Y. Du, Z. Q. Fan, *J. Colloid Interface Sci.* **2011**, *360*, 350.
[21] C. Tonhauser, B. Obermeier, C. Mangold, H. Lowe, H. Frey, *Chem. Commun.* **2011**, *47*, 8964.
[22] C. Tonhauser, A. A. Golriz, C. Moers, R. Klein, H. J. Butt, H. Frey, *Adv. Mater.* **2012**, *24*, 5559.
[23] O. Altintas, D. Schulze-Suenninghausen, B. Luy, C. Barner-Kowollik, *ACS Macro Lett.* **2013**, *2*, 211.
[24] M. J. Barthel, T. Rudolph, S. Crotty, F. H. Schacher, U. S. Schubert, *J. Polym. Sci., Part A: Polym. Chem.* **2012**, *50*, 4958.
[25] M. J. Barthel, T. Rudolph, A. Teichler, R. M. Paulus, J. Vitz, S. Hoeppener, M. D. Hager, F. H. Schacher, U. S. Schubert, *Adv. Funct. Mater.* **2013**, *23*, 4921.
[26] K. Knop, G. M. Pavlov, T. Rudolph, K. Martin, D. Pretzel, B. O. Jahn, D. H. Scharf, A. A. Brakhage, V. Makarov, U. Mollmann, F. H. Schacher, U. S. Schubert, *Soft Matter* **2013**, *9*, 715.
[27] K. Kalyanasundaram, J. K. Thomas, *J. Am. Chem. Soc.* **1977**, *99*, 2039.
[28] M. Wilhelm, C. L. Zhao, Y. Wang, R. Xu, M. A. Winnik, J. L. Mura, G. Riess, M. D. Croucher, *Macromolecules* **1991**, *24*, 1033.
[29] G. Kwon, M. Naito, M. Yokoyama, T. Okano, Y. Sakurai, K. Kataoka, *Langmuir* **1993**, *9*, 945.
[30] C.-W. Wu, L. R. Yarbrough, F. Y. H. Wu, *Biochemistry* **1976**, *15*, 2863.
[31] D. Vyprachtický, K. W. Sung, Y. Okamoto, *J. Polym. Sci., Part A: Polym. Chem.* **1999**, *37*, 1341.
[32] F. Kretschmer, U. Mansfeld, S. Hoeppener, M. Hager, U. S. Schubert, *Chem. Commun.* **2013**, *50*, 88.
[33] H. Y. Song, M. H. Ngai, Z. Y. Song, P. A. MacAry, J. Hobley, M. J. Lear, *Org. Biomol. Chem.* **2009**, *7*, 3400.
[34] M. G. Badin, A. Bashir, S. Krakert, T. Strunskus, A. Terfort, C. Woll, *Angew. Chem Int. Ed.* **2007**, *46*, 3762.
[35] Y. K. Kang, D. J. Won, S. R. Kim, K. J. Seo, H. S. Choi, G. H. Lee, Z. S. Noh, T. S. Lee, C. J. Lee, *Mater. Sci. Eng. C* **2004**, *24*, 43.

Supporting Information

for *Macromol. Rapid Commun.,* DOI: 10.1002/marc.201300875

Poly(2-vinyl pyridine)-*block*-Poly(ethylene oxide) Featuring a Furan Group at the Block Junction—Synthesis and Functionalization

*Tobias Rudolph, Markus J. Barthel, Florian Kretschmer, Ulrich Mansfeld, Stephanie Hoeppener, Martin D. Hager, Ulrich S. Schubert, and Felix H. Schacher**

Supporting Information

Poly(2-vinyl pyridine)-*block*-Poly(ethylene oxide) featuring a Furan Group at the Block Junction – Synthesis and Functionalization

Tobias Rudolph,[1,2,#] Markus J. Barthel,[1,2,3,#] Florian Kretschmer,[1,2] Ulrich Mannsfeld,[1,2] Stephanie Hoeppener,[1,2] Martin D. Hager,[1,2] Ulrich S. Schubert,[1,2,3] and Felix H. Schacher[1,2,*]

[1] Laboratory of Organic and Macromolecular Chemistry, Friedrich Schiller University Jena, Humboldtstr. 10, 07743 Jena, Germany

E-mail: felix.schacher@uni-jena.de

[2] Jena Center for Soft Matter (JCSM), Friedrich Schiller University Jena, Philosophenweg 7, 07743 Jena, Germany

[3] Dutch Polymer Institute, P.O. Box 902, Eindhoven 5600 AX, The Netherlands

# These authors contributed equally to this work.

Instruments

NMR: Proton nuclear magnetic resonance (^{1}H-NMR) spectra were recorded in $CDCl_3$ on a Bruker AC 300 MHz spectrometer at 298 K. Chemical shifts are given in parts per million (ppm, δ scale) relative to the residual signal of the deuterated solvent.

SEC: Size exclusion chromatography was measured on a system equipped with a SCL-10A system controller, a LC-10AD pump and a RID-10A refractive index detector using a solvent mixture containing chloroform ($CHCl_3$), triethylamine (TEA) and *iso*-propanol (*i*-PrOH) (94:4:2) at a flow rate of 1 mL min^{-1} on a PSS SDV linear M 5 μm column. The system was calibrated using PS (100 to 100,000 g mol^{-1}) and PEO (440 to 44,700 g mol^{-1}) standards.

MALDI-ToF MS: Matrix-assisted laser desorption/ionization time of flight mass spectrometry was performed on an Ultraflex III TOF/TOF (Bruker Daltonics, Bremen, Germany), equipped with a Nd:YAG laser and with *trans*-2-[3-(4-*tert*-butylphenyl)-2-methyl-2-propenylidene] malononitrile (DCTB) as the matrix and NaCl as the doping agent in reflector and linear mode. The instrument was calibrated prior to each measurement with an external poly(methyl methacrylate) (PMMA) standard from PSS Polymer Standards Services GmbH (Mainz, Germany).

DLS: Dynamic light scattering was performed at a scattering angle of 90° on an ALV CGS-3 instrument equipped with a He-Ne laser operating at a wavelength of 633 nm at 25 °C. The CONTIN algorithm was applied to analyze the obtained correlation functions. For temperature control, the DLS is equipped with a Lauda thermostat. Apparent hydrodynamic radii were calculated according to the Stokes-Einstein equation.

Transmission electron microscopy (TEM): TEM measurements were performed on a Philips CM-120. 15 μL of the sample solution were blotted onto clean carbon coated TEM

grids (Mesh 400, Quantifoil, Jena) and excess material was removed by a filter paper (Whatman No. 1); the samples were allowed to dry prior to the transfer to the microscope. Grid cleaning was performed by UV-ozone treatment for 40 s. For staining purpose a drop of uranyl acetate (3 mg ml^{-1}) was applied to the grid, the supernatant solution was removed via filter paper and the sample washed with water to remove the excess of uranyl acetate.

Centrifugation was performed with a Heraeus Biofuge Primo with a fixed angle rotor in 1.5 mL Eppendorf tubes.

UV-Vis spectroscopy: UV-Vis absorption spectra were recorded with a Specord 250 spectrometer (Analytik Jena) or a Lambda 750 UV/VIS/NIR spectrometer (PerkinElmer) in Suprasil quartz glass cuvettes 104-QS (Hellma Analytics) with a thickness of 10 mm at room temperature.

Fluorescence microscope: Fluorescence images were measured on a fluorescence microscope (Cell Observer Z1, Carl Zeiss, Jena, Germany) equipped with a mercury arc UV lamp and the appropriate filter combinations for excitation and detection of emission. In this case the sample was irradiated with 357 nm and an emission filter of 460 nm. All images were measured using identical instrument settings (e.g. UV lamp power, integration time, camera gain) and spots of the well plate were addressed using an automated XY table.

Zeta Potential Measurements: The ζ-potentials were measured on a ZetaSizer Nano ZS from Malvern *via* the M3-PALS technique with a laser beam at 633 nm. The detection angle was 13°. The electrophoretic mobilities (u) were converted into ζ –potentials *via* the Henry equation in the Smoluchowski approximation, $z = u\,\eta/\varepsilon_0\,\varepsilon$, where η denotes the viscosity and $\varepsilon_0\,\varepsilon$ the permittivity of the solution.

Experimental section

Materials

Sec-butyl lithium, tetrahydrofuran, dimethylformamide, 2-vinyl pyridine, ethylene oxide, DPMK was synthesized as described in the literature.[1] Furfuryl glycidyl ether was purified *via* column chromatography as described in literature.[2] 4-Phenylazomaleinanil and N-(1-pyrenyl)-maleimide were purchased from Sigma Aldrich and used as received. DMF (anhydrous, amine free, 99.9%) was purchased from Alfa Aesar. Dicylcohexylcarbodiimide (DCC), furane, 4-dimethylaminopyridine (DMAP) and potassium thioacetate were purchased from Sigma-Aldrich. Pentaerythritol tribromide was received from TCI Europe. Water (< 0.1µS/cm) was purchased from ELGA Purelab Prima. All chemicals were used as received.

Compound **1**[3] and citrate stabilized nanoparticles[4] were synthesized as reported in the literature.

Anionic polymerization of 2-vinylpyridine and end-capping with furfuryl glycidyl ether

In a Schlenk flask 80 mL freshly prepared THF were cooled to –78 °C with an *iso*-propanol/dry ice bath and 0.71 mL (1 mmol) of *s*-BuLi was added and stirred for 10 min. Afterwards 5.1 mL (47 mmol) of freshly distilled 2-vinyl pyridine were added quickly to the reaction solution and stirred for 1 hours. Afterwards, 0.4 mL diphenylethylene (2.3 mmol) were added to the reaction mixture to decrease the nucleophilicity of the active chain end. After addition of 0.27 mL of furfuryl glycidyl ether (2.3 mmol) the solution was allowed to warm to RT and stirred overnight at 25 °C. The reaction was terminated afterwards by the addition of methanol.

The polymer was precipitated in cold hexane and the crude product was purified by dissolving in chloroform and washing with water. The solvent was removed under reduced pressure and the product was dried under vacuum.

SEC ($CHCl_3$/*i*-PrOH/Et_3N): M_n = 8 700 g mol^{-1}; Đ = 1.08 (PS-calibration); **^{1}H NMR** (300 MHz, $CDCl_3$, δ): 8.5-8.0 (br, arom. *H*), 7.4-7.1 (br, arom. *H*), 4.15 (s, C*H*$_2$-furan), 3.74 (t, C*H*$_2$), 2.55-2.15 (br, -C*H*-P2VP); **MALDI-TOF MS**: M_p = 7 200 g mol^{-1}.

Anionic polymerization of ethylene oxide (EO) via P2VP$_{68}$-FGE-OH-macro initiator

2.0 g of P2VP$_{68}$-FGE-OH (0.28 mmol) were dissolved in 100 mL freshly distilled THF and transferred into a Büchi GlasUster PicoClave reactor. The hydroxyl-end group was activated *via* the addition of an excess of DPMK (~10 eq.) until a black color was observed. The reaction mixture was cooled to –20 °C and ethylene oxide (EO; 5.3 mL; 107 mmol) were introduced into the reaction vessel. The solution was slowly heated to 40 °C and stirred for 24 hours. The remaining pressure was released from the reactor system and the polymerization was terminated by the addition of methanol.

The desired block copolymer was obtained after precipitation into cold ether, filtering, and drying under vacuum.

SEC ($CHCl_3$/*i*-PrOH/Et_3N): M_n = 20 000 g mol^{-1}; Đ = 1.11 (-calibration); **^{1}H NMR** (300 MHz, $CDCl_3$, δ): 8.5-8.0 (br, arom. *H*), 7.4-7.1 (br, arom. *H*), 3.8-3.4 (PEO-backbone), 2.55-2.15 (br, -C*H*-P2VP); **MALDI-TOF MS**: M_p= 24 500 g mol^{-1}.

Synthesis of the thiol-linker

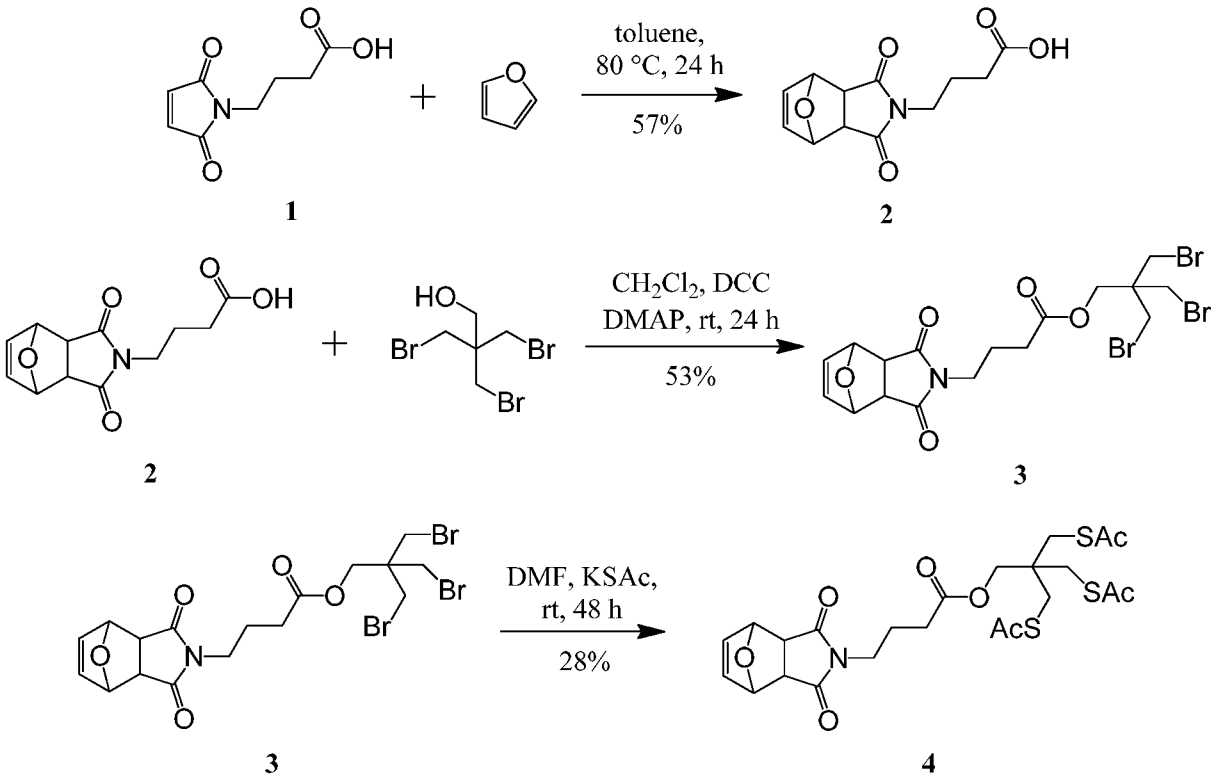

Figure S1: Synthetic strategy for the preparation of the maleimide-functionalized thiol-linker.

4-(1,3-Dioxo-3a,4,7,7a-tetrahydro-1H-4,7-epoxyisoindol-2(3H)-yl)butanoic acid (2)

1 (1.4 g, 7.64 mmol) and furane (5.2 g, 76.40 mmol) were dissolved in 20 mL toluene and the solution was heated to 80 °C for 24 h. Subsequently, the reaction was cooled to 4 °C in the fridge. The formed precipitated was filtered off and dried to obtain **2** as white crystals. Yield 1.1 g (57% of theory).

^{1}H NMR (300 MHz, $CDCl_3$): δ = 6.52 (s, 2 H, 2 CH), 5.28 (s, 2 H, 2 CH), 3.58 (t, J = 6.8 Hz, 2 H, CH_2), 2.86 (s, 2 H, 2 CH), 2.37 (t, J = 7.42 Hz, 2 H, CH_2), 1.93 (m, J = 7.22 Hz, 2 H,

CH_2) ppm. **^{13}C NMR** (250 MHz, $CDCl_3$): *d* = 177.31, 176.28, 136.50, 80.94, 47.40, 37.95, 30.78, 22.59 ppm.

3-Bromo-2,2-bis(bromomethyl)propyl-4-(1,3-dioxo-3a,4,7,7a-tetrahydro-1H-4,7-epoxy-isoindol-2(3H)-yl)butanoate (3)

2 (1.1 g, 4.38 mmol), pentaerythritol tribromide (1.7 g, 5.23 mmol), DCC (1.36 g, 6.59 mmol) and DMAP (82 mg, 0.67 mmol) were dissolved in 50 mL methylene chloride and stirred at room temperature under nitrogen for 24 h. Afterwards the mixture was filtered and the clear solution was washed with 50 mL water. The organic phase was dried over sodium sulfate and the solvent was removed under reduced pressure. Subsequently the crude product was purified *via* column chromatography (silica gel 60, methylene chloride: ethyl acetate 95:5) and **3** was obtained as a colorless solid. Yield 1.3g (53% of theory).

^{1}H NMR (300 MHz, $CDCl_3$): δ = 6.52 (s, 2 H, 2 CH), 5.27 (s, 2 H, 2 CH), 4.21 (s, 2 H, CH_2), 3.56 (s, 6 H, 3 CH_2), 3.55 (t, 2 H, CH_2), 2.86 (s, 2 H, 2 CH), 2.35 (t, *J* = 7.31 Hz, 2 H, CH_2), 1.92 (m, *J* = 7.08 Hz, 2 H, CH_2) ppm. **^{13}C NMR** (75 MHz, $CDCl_3$): δ = 176.22, 171.53, 136.49, 80.94, 63.71, 47.39, 42.73, 37.88, 34.11, 30.89, 22.71 ppm. **MS (HR-ESI)**: *m/z* calculated for $[C_{17}H_{20}Br_3NO_5]^{Na+}$: 577.8784; found: 577.8776 [M + Na].

3-(Acetylthio)-2,2-bis((acetylthio)methyl)propyl 4-(1,3-dioxo-3a,4,7,7a-tetrahydro-1H-4,7-epoxyisoindol-2(3H)-yl)butanoate (4)

3 (1 g, 1.79 mmol) and potassium thioacetate (1.22 g, 10.68 mmol) were dissolved in 10 mL DMF and stirred in a closed vial at room temperature for 48 h. Subsequently, 50 mL diethyl ether were added and the formed precipitate was filtered off. The organic solution was washed five times with 50 mL water followed by drying over sodium sulfate. Afterwards the solvent was removed under reduced pressure. The crude product was purified *via* column

chromatography (silica gel 60, methylene chloride: acetonitrile 38:2) to obtain **4** as a yellow oil which solidifies upon standing. Yield 290 mg (28% of theory).

^{1}H NMR (300 MHz, $CDCl_3$): δ = 6.52 (s, 2 H, 2 CH), 5.29 (s, 2 H, 2 CH), 3.95 (s, 2 H, CH_2), 3.57 (t, J = 6.85, 2 H, CH_2), 3.07 (s, 6 H, 3 CH_2), 2.86 (s, 2 H, CH_2) 2.36 (s, 9 H, 3 CH_3), 2.35 (t, 2 H, CH_2), 1.93 (m, J = 7.08 Hz, 2 H, CH_2) ppm. **^{13}C NMR** (75 MHz, $CDCl_3$): δ = 194.14, 176.20, 171.97, 136.53, 80.94, 66.09, 47.43, 42.16, 37.99, 32.94, 30.99, 30.58, 22.68 ppm. **MS (HR-ESI)**: *m/z* calculated for $[C_{23}H_{29}NO_8S_3]^{Na+}$: 566.0948; found: 566.0900 [M + Na].

Synthesis of maleimide stabilized gold nanoparticles (Au-NP)

10 × 1 mL citrate stabilized gold nanoparticles were pipetted in Eppendorf tubes and centrifuged at 5000 rpm for 90 minutes. Respectively, 950 µL of the supernatant solution were taken off, subsequently, a solution of **4** (100 µL, 1 mg/mL DMF) and 850 µL DMF were added. The particles were redispersed by simple shaking. The solution was centrifuged at 5000 rpm for 90 minutes, afterwards, 900 µL of the supernatant solution were taken off and the remaining 100 µL solution of the ten tubes were combined and pipetted in a glass vial. Finally, a solution of **4** (46 µL, 1 mg/mL DMF) was added and the mixture was heated to 130 °C for 1 h in order to cleave off the furan unit.

Diels-Alder reaction with maleimide-functionalized gold-nanoparticle

$P2VP_{68}$-FGE-*b*-PEO_{390} (5 mg) and 1 mg AuNP (46 µg of **4**) were dissolved in 1.5 mL DMF and heated to 75 °C for 2 days. The excess of block copolymer was removed by centrifugation at 5000 rpm for 90 minutes. The supernatant solution was removed and the particles re-suspended in DMF.

Diels-Alder reaction $P2VP_{68}$-FGE-b-PEO_{390} and N-(1-pyrenyl)maleimide

$P2VP_{68}$-FGE-*b*-PEO_{390} (100 mg; 4 µmol) and *N*-(1-pyrenyl)maleimide (24 mg; 0.08 mmol) were dissolved in 2 mL DMF. The solution was heated to 75 °C overnight. The desired product was received after size exclusion column chromatography (BioBeads SX1) with THF as eluent.

SEC ($CHCl_3$/*i*-PrOH/Et_3N): M_n = 17 000 g mol^{-1}; Đ = 1.22 (PEO-calibration)

Diels-Alder reaction $P2VP_{68}$-FGE-b-PEO_{390} and 4-phenylazomaleinanil

$P2VP_{68}$-FGE-*b*-PEO_{390} (100 mg; 4 µmol) and 4-phenylazomaleinanil (24 mg; 0.08 mmol) were dissolved in 2 mL DMF. The solution was heated to 75 °C overnight. The desired product was received after size exclusion column chromatography (BioBeads SX1) with THF as eluent.

SEC ($CHCl_3$/*i*-PrOH/Et_3N): M_n = 16 000 g mol^{-1}; Đ = 1.24 (PEO-calibration)

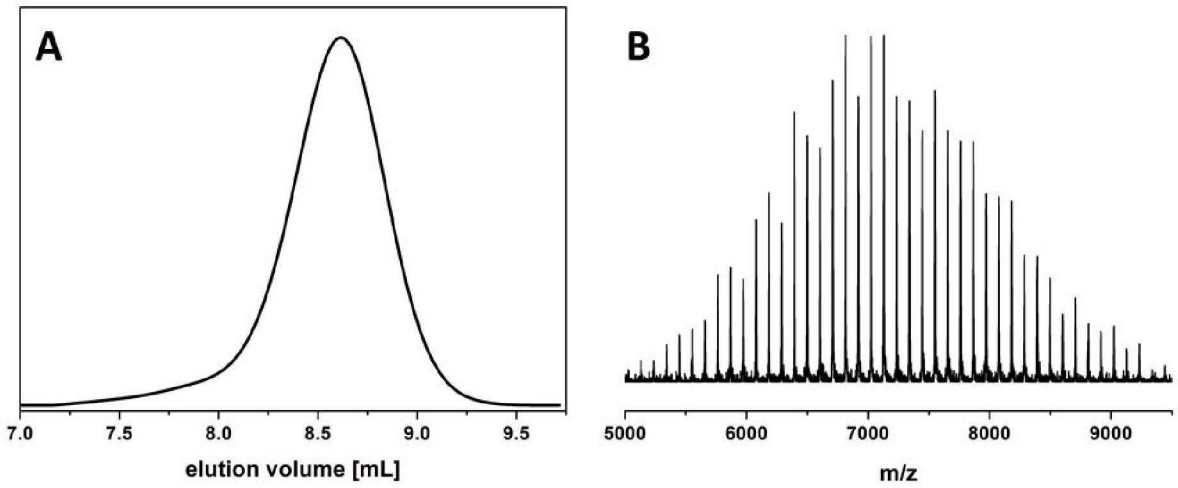

Figure S2: SEC trace (A) and MALDI-TOF MS spectra (B) for P2VP$_{68}$-FGE-OH.

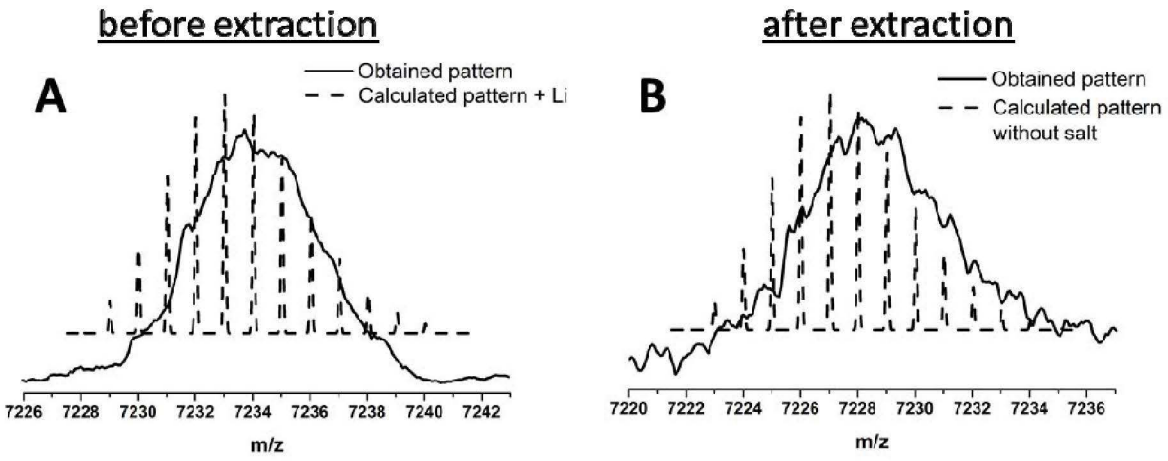

Figure S3: Comparison of the measured and the calculated MALDI-TOF MS spectra for P2VP$_{68}$-FGE-OH before (A) and after (B) extraction to remove the lithium counterion.

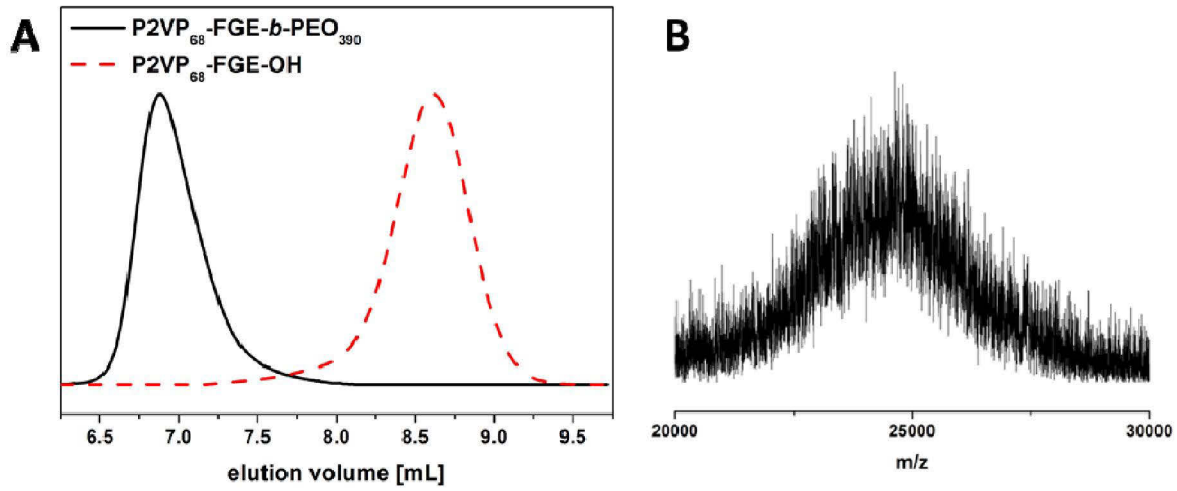

Figure S4: Comparison of the SEC traces for for $P2VP_{68}$-FGE-OH (dashed line) and for $P2VP_{68}$-FGE-*b*-PEO_{390} (A) and MALDI-TOF MS spectra of $P2VP_{68}$-FGE-*b*-PEO_{390}.

Table S1: Characterization of the functionalized homopolymer ($P2VP_{68}$-FGE-OH), block copolymer ($P2VP_{68}$-FGE-*b*-PEO_{390}) and the functionalized $P2VP_{68}$-FGE-*b*-PEO_{390}.

Polymer	M_n[a] [g mol^{-1}]	PDI[a]	M_p[d] [g mol^{-1}]
$P2VP_{68}$-FGE-OH[b]	8 700[c]	1.08[c]	7 200
$P2VP_{68}$-FGE-*b*-PEO_{390}[b]	19 000	1.11	24 500
$P2VP_{68}$-azo-*b*-PEO_{390}	16 000	1.24	-
$P2VP_{68}$-pyr-*b*-PEO_{390}	17 000	1.22	-

a) SEC ($CHCl_3$/*iso*-propanol/triethylamine) (PEO-calibration)
b) Determination by a combination of ^{1}H-NMR and MALDI-TOF MS
c) SEC ($CHCl_3$/*iso*-propanol/triethylamine) (PS-calibration)
d) MALDI-TOF MS

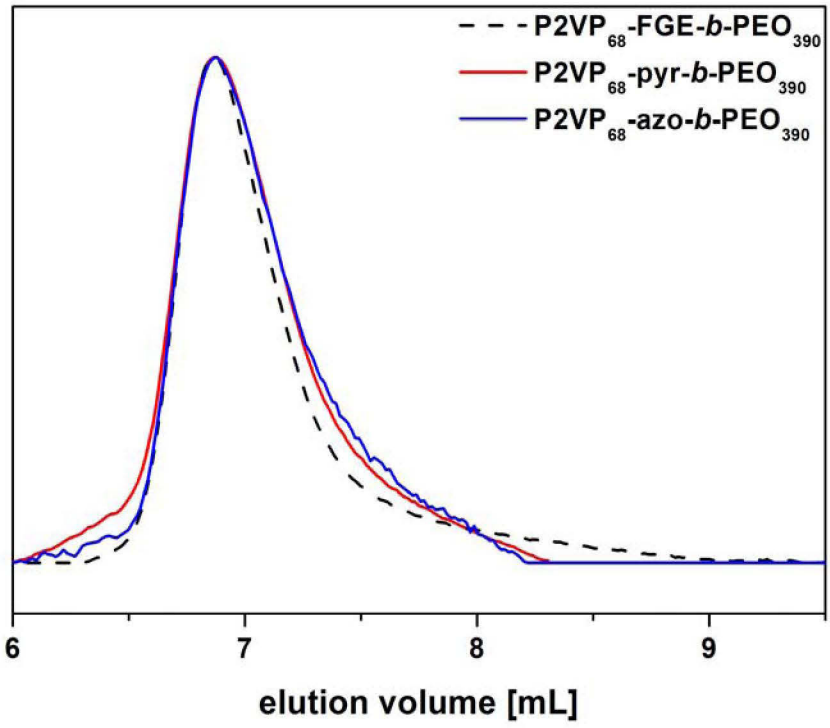

Figure S5: Comparison of SEC traces for the $P2VP_{68}$-FGE-*b*-PEO_{390} (black dashed curve), $P2VP_{68}$-pyr-*b*-PEO_{390} (red curve), and $P2VP_{68}$-azo-*b*-PEO_{390} (blue curve).

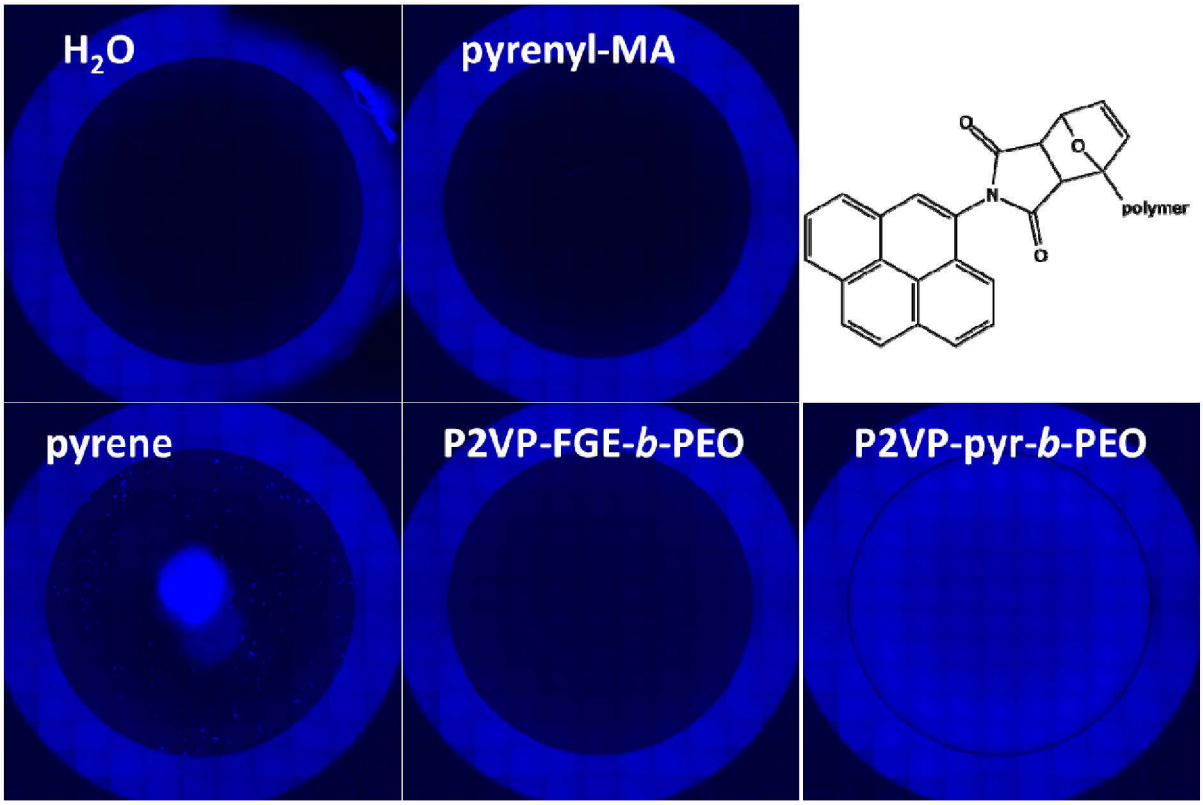

Figure S6: Comparison of fluorescence micrographs for water (A), pristine *N*-(1-pyrenyl)maleimide (B), pyrene (C), $P2VP_{70}$-FGE-*b*-PEO_{380} (5 mg mL^{-1}), and $P2VP_{70}$-pyr-*b*-PEO_{380} (5 mg mL^{-1}) in water (at pH 7) under comparable conditions (same gain, excitation 357 nm; emission filter 460 nm).

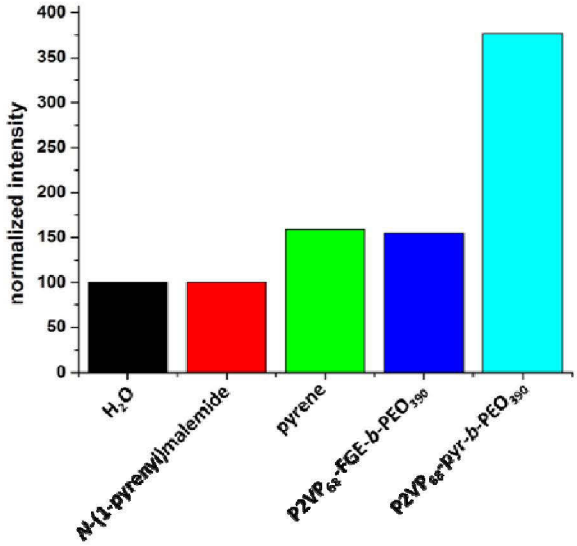

Figure S7: Comparison of the fluorescence measurements normalized in comparison to H_2O (black) for *N*-(1-pyrenyl)-maleimide (red), pyrene (green), $P2VP_{68}$-FGE-*b*-PEO_{390} (blue, 5 mg mL^{-1}) and $P2VP_{68}$-pyr-*b*-PEO_{390} (cyan, 5 mg mL^{-1}) in water (at pH 7) under comparable conditions (same gain, excitation 357 nm; emission filter 460 nm).

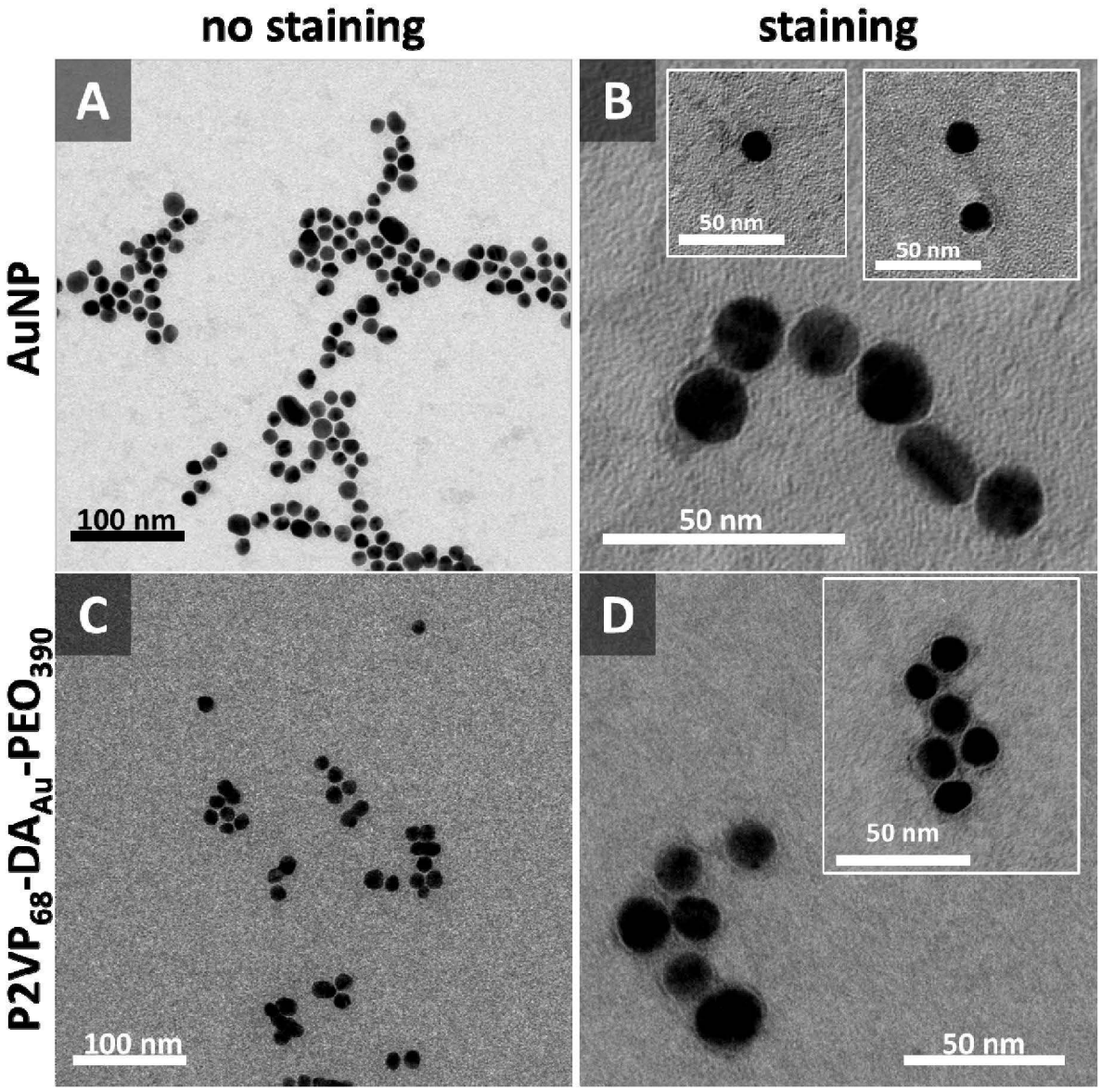

Figure S8: Comparison of TEM micrographs of the maleimide-coated AuNPs (A and B) and $P2VP_{68}$-DA_{Au}-*b*-PEO_{390} (C and D): before (A and C) and after (B and D) staining with uranyl acetate.

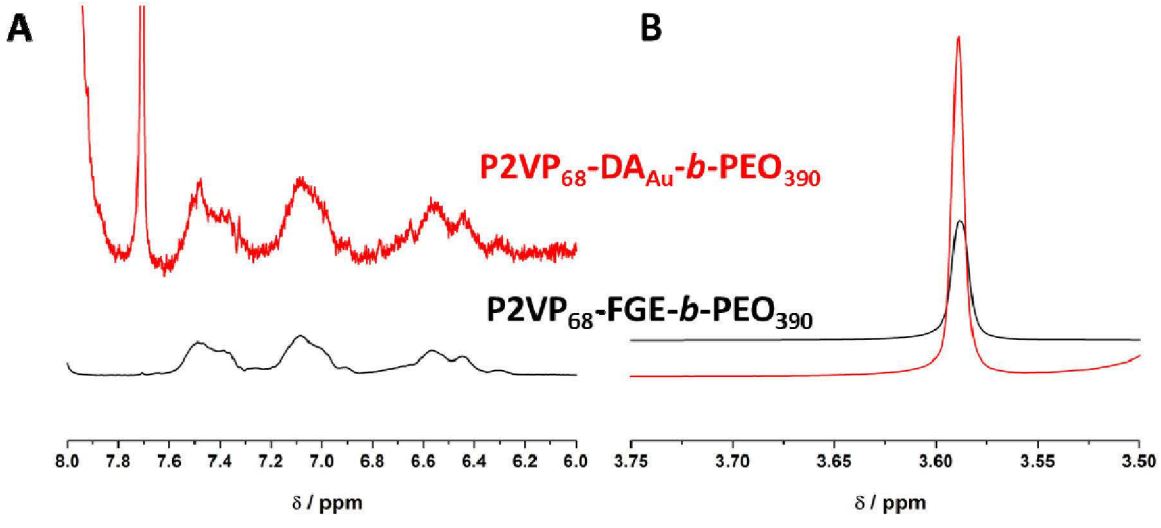

Figure S9: Comparison of NMR spectra for $P2VP_{68}$-FGE-*b*-PEO_{390} (black curve) and $P2VP_{68}$-DA_{Au}-*b*-PEO_{390} (black curve) in the characteristic regions for P2VP (A) and PEO (B).

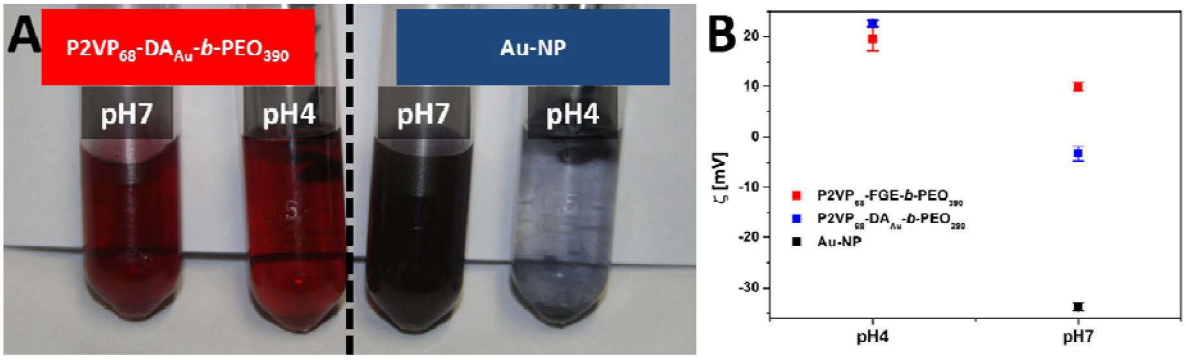

Figure S10: A) Comparison of images for $P2VP_{68}$-DA_{Au}-*b*-PEO_{390} (left) and AuNP (right); B) Zeta potential measurements for $P2VP_{68}$-DA_{Au}-*b*-PEO_{390} (blue dots; ~0.2 mg mL^{-1} polymer), $P2VP_{68}$-FGE-*b*-PEO_{390} (red dots; 0.5 mg mL^{-1}) and Au-NP (black dot) after transfer into water at different pH 4 and 7.

References

1 H. Normant, B. Angelo; *B. Soc. Chim. Fr.*, 1960, 354.

2 M. J. Barthel, T. Rudolph, S. Crotty, F. H. Schacher, U. S. Schubert; *J. Polym. Sci. Part A: Polym. Chem.*, 2012, 50, 4958-4965.

3 H. Y. Song, M. H. Ngai, Z. Y. Song, P. A. MacAry, J. Hobley, M. J. Lear, *Org. Biomol. Chem.*, 2009, 7, 3400-3406.

4 F. Kretschmer, U. Mansfeld, S. Hoeppener, M. Hager and U. S. Schubert, *Chem. Commun.*, 2013, **50**, 88-90.

Publication P6

Tunable Synthesis of Poly(ethylene imine)-gold Nanoparticle Clusters

F. Kretschmer, U. Mansfeld, S. Hoeppener, M. D. Hager, U. S. Schubert

Chem. Commun. **2014**, *50,* 88-90.

ChemComm

COMMUNICATION

View Article Online
View Journal | View Issue

Tunable synthesis of poly(ethylene imine)–gold nanoparticle clusters†

Cite this: *Chem. Commun.*, 2014, 50, 88

Received 6th July 2013,
Accepted 5th August 2013

DOI: 10.1039/c3cc45090b

www.rsc.org/chemcomm

Florian Kretschmer,[ab] Ulrich Mansfeld,[ab] Stephanie Hoeppener,[ab] Martin D. Hager[abc] and Ulrich S. Schubert*[abc]

The reaction of tetrachloroauric acid in DMF with poly(ethylene imine) (PEI) as a reducing agent yields spherical nanoparticles. Depending on the reaction conditions single gold nanoparticles or gold–PEI clusters with tunable size up to 200 nm in diameter were obtained which could serve as potential building blocks for metamaterials.

Directing the assembly of noble metal nanoparticles has attracted considerable interest in recent years as a source for potential analytical, medical and optoelectronic applications.[1,2] Among the most intriguing materials that can be obtained in this way are metamaterials due to their unique properties not found in nature.[3] Being able to manipulate electromagnetic waves in a defined way enables the creation of novel devices like superlenses[4] or cloaking devices.[5] Meta-atoms are the building blocks of such materials. Structures, which can serve as building blocks, can be obtained *via* spherical cluster formation or satellite assemblies of plasmonic nanoparticles.[6] One strategy to synthesize these structures is to employ spherical templates usually consisting of silica,[7] polymers[8] or micelles[9] and the subsequent synthesis of nanoparticles in their interior. Moreover, already formed nanoparticles can be assembled on their outer surface *via* electrostatic or strong sulfur–metal particle interactions.[10] A second approach is the synthesis of particles, followed by their encapsulation in a spherical shell.[11] The approach described herein involves the simultaneous synthesis of the nanoparticles and cluster formation.[12] Our strategy involves cheap commercial reagents and requires only one reaction step to create size-tunable gold nanoparticle clusters.

The proposed mechanism for the formation of gold nanoparticle–polymer clusters is depicted in Scheme 1. In general a solution of branched poly(ethylene imine) (bPEI) (25 kDa) and $HAuCl_4$ in DMF is heated, which results in the formation of nanoparticles encapsulated by the polymer. Mixing the solutions leads immediately to a large bathochromic shift (Fig. 1, Fig. S1 and S2, ESI†). The first step in this process is the protonation of the primary, secondary and tertiary amine groups of the polymer. The Au^{3+} ions are colored yellow in solution and the color change indicates the complex formation between the gold ions and bPEI. It is also possible for one gold ion to complex multiple polymer chains which can facilitate crosslinking. Upon heating, Au^{3+} ions are first reduced to colorless Au^{+} ions and

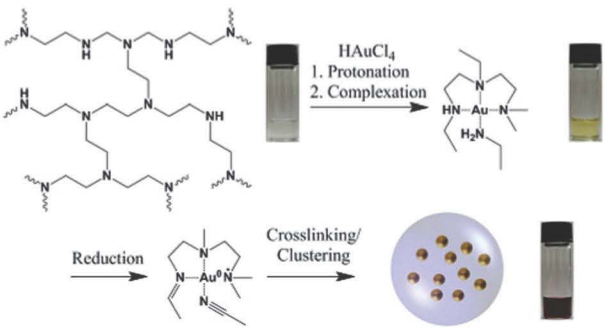

Scheme 1 Schematic representation of the cluster formation. Photographs depict the solutions at the different stages of the synthesis.

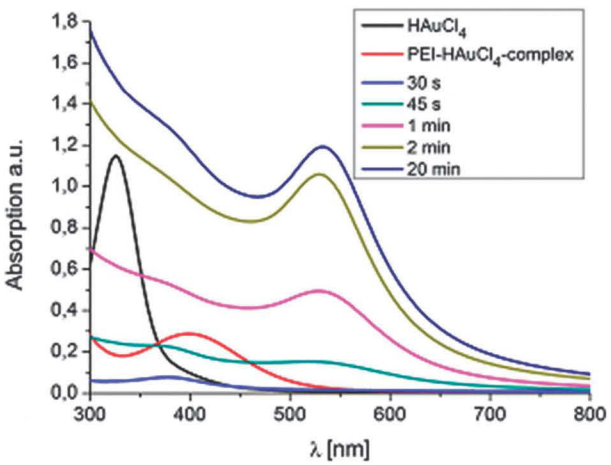

Fig. 1 UV-vis spectra of the solutions at the different stages of the synthesis (in DMF).

[a] *Laboratory of Organic and Macromolecular Chemistry (IOMC), Friedrich Schiller University Jena, Humboldtstr. 10, 07743 Jena, Germany. E-mail: ulrich.schubert@uni-jena.de; Fax: +49 3641 948202*
[b] *Jena Center for Soft Matter (JCSM), Friedrich Schiller University Jena, Philosophenweg 7, 07743 Jena, Germany*
[c] *Dutch Polymer Institute (DPI), P.O. Box 902, 5600 AX Eindhoven, The Netherlands*

† Electronic supplementary information (ESI) available. See DOI: 10.1039/c3cc45090b

then to elemental gold. This can also be followed by UV-vis spectroscopy which shows at first a decrease in absorption due to the formation of Au^+ but over time the plasmon band of the nanoparticles evolves and increases in intensity. Metal centers are frequently used in dehydrogenation reactions,[13] and organic amines are commonly used for the synthesis of gold nanoparticles.[14] Dehydrogenative oxidation of primary and secondary amine groups leads first to imine formation and, depending on the reaction time and temperature, in a second step the formation of nitrile groups in the case of primary amines is possible. For the tertiary amines, transformation to an imine can take place, in addition, formation of radical species can occur which is also a known mechanism in photocatalytic processes in which, *e.g.*, triethylamine acts as an electron donor.[15]

To gather further insights into the cluster formation process we first started investigating the effect of the PEI : $HAuCl_4$ mass ratio on the formation of nanoparticles (Fig. S3 and S5, ESI†). At a 1 : 4 ratio a blue solution with an absorption maximum at 622 nm could be obtained which is an indication of the formation of nanoparticles. In this case the amount of reducing agent might be too low to reduce all gold ions to elemental gold. Besides this, the stabilization of the formed particles by the polymer shell could be insufficient, resulting in larger aggregates of nanoparticles. Increasing the ratio to 1 : 2 results in a stable nanoparticle solution with an absorption maximum at 544 nm. TEM imaging showed spherical nanoparticles with a rather large size distribution and the formation of a polymer film around the particles. However, there is no distinct segregation between the clusters, and most of them appear to be fused together. Increasing the ratio to 1 : 1 led to the formation of clearly separated gold–polymer clusters without aggregated gold particles as evidenced by a plasmon band at 532 nm. It is worth noting that the polymer shell shows considerable stability against water. It is possible to perform three times a centrifugation–redispersion cycle without dissolution of the polymer shell or release of gold nanoparticles (Fig. S6, ESI†). This supports the hypothesis of a crosslinking mechanism as pure bPEI is readily soluble in water. The nanoparticles can be etched by addition of cyanide which, however, also results in aggregation of the empty polymer shells.

Motivated by these initial results, we sought to explore the effect of changing concentrations of bPEI and $HAuCl_4$ at a fixed ratio of 1 : 1. Surprisingly, increasing or decreasing the amount of the compounds in solution does not result in more or less clusters in solution but, in fact, causes a significant change in the cluster size (Fig. 2 and 3). Decreasing the concentration of each of the reactants to 1 mg mL^{-1} leads to the formation of single nanoparticles with an average size of

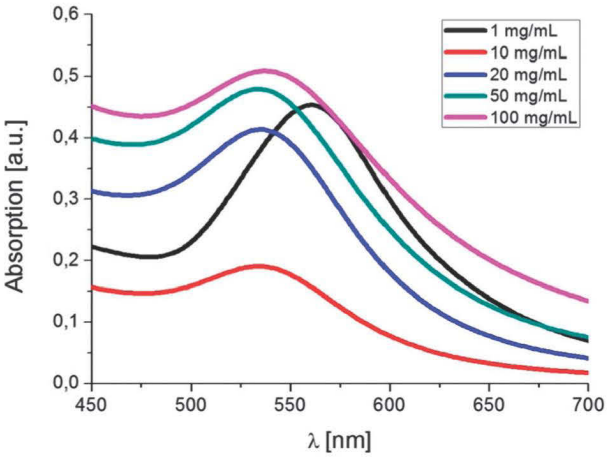

Fig. 3 UV-vis spectra of single particles and clusters synthesized at different concentrations of the reactants (in DMF).

33 nm. There is no obvious cluster formation and only occasionally a thin polymer shell is visible. UV-vis spectroscopy indicates a bathochromic shift of the absorption to 561 nm. Increasing the concentrations to 10, 20, 50 and 100 mg mL^{-1} yielded polymer shells with sizes of 40, 60, 120 and 230 nm, respectively, with small encapsulated gold nanoparticles (~3 to 8 nm). The maximum of the absorption changes only insignificantly except for the highest concentration. To address the effect of the polymer size and shape on the formation of nanoparticles we investigated branched PEIs with different molar masses and one linear PEI (lPEI, 25 kDa) (Fig. S4 and S5, ESI†). Application of low molar mass bPEI (0.6 kDa) resulted in the formation of nanoparticles; however, precipitation with simultaneous color change to blue occurred during the reaction. Hence, it was concluded that the polymer might simply be too short to stabilize the particles against aggregation. After increasing the molar mass to 1.8 kDa TEM imaging showed the formation of clusters. However, it should be noted that still some precipitation was observed due to incomplete stabilization, which can also be visualized by the UV-vis spectrum that showed a small broadening of the surface plasmon resonance. Increasing the molar mass to 10 kDa (bPEI) resulted in a stable solution and cluster formation without any evidence of aggregation. Synthesis of clusters with lPEI gave similar results to the ones with the low molar mass bPEI; nanoparticles were formed, but aggregation occurred during the synthesis. Even though the size of the lPEI should be sufficient to stabilize the nanoparticles, the linear structure could compromise the crosslinking of the PEI chains,

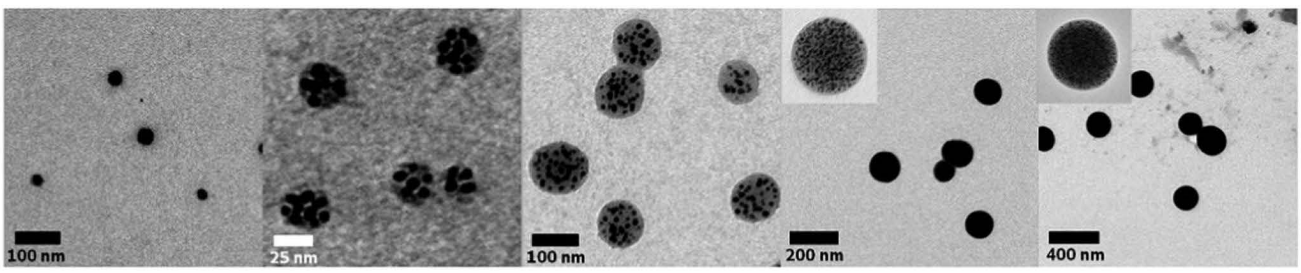

Fig. 2 TEM images of single particles and clusters synthesized from bPEI 25 kDa and $HAuCl_4$ at a fixed ratio of 1 : 1. Concentrations of the reactants: 1, 10, 20, 50, 100 mg mL^{-1} (from left to right).

resulting only in a small or no polymer layer around the nanoparticles. This is, however, not corroborated by experiments conducted with polyallylamine (PAAm). The main difference is the nature of the amine unit, which is primary in the case of PAAm. While the overall polymer structure still corresponds to a linear chain, PAAm was also able to generate particle clusters.

As the formation of metal nanoparticles in water *via* PEI is well known,[16,17] though, without formation of a polymer shell, we suggest that the solvent might also contribute to the shell formation. To elucidate this issue we investigated the impact of the solvent on the cluster formation (Fig. S7 and S8, ESI†). It turned out to be difficult to identify a solvent in which bPEI and $HAuCl_4$ are soluble at the same time. At first we performed similar experiments reported in the literature with water as the solvent and a 1 : 1 ratio of the compounds which resulted in single spherical particles. Due to the aforementioned difficulties ethanol was used as the solvent yielding also no clusters. As ethanol and many other organic solvents are also capable of reducing gold ions to elemental gold, the formation of nanoparticles might merely be attributed to the reducing properties of the organic solvent while the polymer acts only as a capping agent. DMF is also reported to be a reducing agent for gold salts;[18] however, the reduction proceeds only at high temperature or over a prolonged period of time. To exclude this effect we conducted the reaction in DMF at room temperature. In contrast to the reactions performed at 130 °C the reaction was complete only after several days. Cluster formation takes place, but as is evident from the TEM image, the clusters are less defined and the polymer shell is considerably thinner (Fig. S8, ESI†). In addition, occasionally rather large nanoparticles are formed and the particles appear more aggregated. This is in agreement with the UV-vis spectrum of the solution which shows a slight bathochromic shift in conjunction with an overall broadening of the plasmon resonance compared to the samples prepared at elevated temperature.

Next to gold, silver is the most interesting material for plasmonic applications due to its more favorable optical properties and lower costs.[19] In case the reaction is conducted with an equivalent amount of silver nitrate instead of $HAuCl_4$ a yellow solution is formed. TEM imaging and UV-vis spectroscopy showed the formation of silver nanoparticles with a broad size distribution, however, no cluster formation could be observed. Two factors could contribute to this result: on the one side, in contrast to gold, DMF is a good reducing agent for silver ions which results in a similar combination to the aforementioned ethanol : $HAuCl_4$: PEI system. On the other hand, the counter ion might contribute to the formation of the polymer shell. While bPEI is soluble in water and some polar organic solvents, bPEI hydrochloride is soluble only in water but not in DMF. No formation of clusters is evident directly after mixing the reactants, however, as hydrochloric acid evolves during complexation and reduction of $HAuCl_4$, more protonation of the polymer takes place, resulting in the formation of clusters. In order to confirm this hypothesis we conducted a control experiment with NH_4Cl. Upon heating NH_3 is driven off and HCl is formed. This resulted in the formation of polymer nanoparticles as evidenced by TEM imaging, however, devoid of gold particles (Fig. S2, ESI†).

The optical properties of nanoparticle assemblies are also dependent on the size of the gold particles in the cluster and the filling fraction of gold. While the size of the gold particles cannot be increased by increasing the gold concentration it turned out to be possible to utilize pre-synthesized gold particles which are encapsulated during the synthesis. Citrate-stabilized Au nanoparticles were transferred into DMF, and, in a similar way as introduced before, small or large clusters can be synthesized. TEM imaging showed for a low concentration of initial particles concomitantly present small and large particles (Fig. S9 and S10, ESI†). However, the fraction of small particles is significantly lower compared to the synthesis without initial particles. In addition, empty clusters can also be observed. In the case of a high initial particle concentration no secondary nucleation is found. This observation indicates that the formation mechanism of these clusters remains essentially the same as previously described, except that in addition the seeded growth of the initial particles takes place. In accordance with theoretical predictions[6] an increased filling fraction leads to a more pronounced broadening of the localized surface plasmon resonance as indicated by UV-vis spectroscopy.

In conclusion, we synthesized tuneable gold nanoparticle–PEI clusters and investigated the effects of the polymer structure, solvent and concentration of the reactants. The mechanism relies on the reducing properties of the amine moieties with concomitant insolubilization of the polymer *via* HCl and crosslinking of the polymer chains. The filling fraction and size can be increased *via* encapsulation of pre-synthesized gold nanoparticles. The introduced approach presents a versatile route to synthesize cluster systems with good control and potentially promising properties for further research, *e.g.*, for application in metamaterials or the design of functional polyamine–plasmonic particle composites.

Financial support by the Federal Ministry of Education and Research (Spitzencluster PHONA) is acknowledged.

Notes and references

1 N. J. Halas, S. Lal, W. S. Chang, S. Link and P. Nordlander, *Chem. Rev.*, 2011, **111**, 3913–3961.
2 Y. Jin, *Adv. Mater.*, 2012, **24**, 5153–5165.
3 Y. Liu and X. Zhang, *Chem. Soc. Rev.*, 2011, **40**, 2494–2507.
4 N. Fang, H. Lee, C. Sun and X. Zhang, *Science*, 2005, **308**, 534–537.
5 L. H. Gabrielli, J. Cardenas, C. B. Poitras and M. Lipson, *Nat. Photonics*, 2009, **3**, 461–463.
6 J. Dintinger, S. Mühlig, C. Rockstuhl and T. Scharf, *Opt. Mater. Express*, 2012, **2**, 269–278.
7 M. Xiao, C. Zhao, H. Chen, B. Yang and J. Wang, *Adv. Funct. Mater.*, 2012, **22**, 4526–4532.
8 J. Cho and F. Caruso, *Chem. Mater.*, 2005, **17**, 4547–4553.
9 X. Chen, Y. An, D. Zhao, Z. He, Y. Zhang, J. Cheng and L. Shi, *Langmuir*, 2008, **24**, 8198–8204.
10 S. Mühlig, A. Cunningham, S. Scheeler, C. Pacholski, T. Burgi, C. Rockstuhl and F. Lederer, *ACS Nano*, 2011, **5**, 6586–6592.
11 M. Grzelczak, A. Sanchez-Iglesias, H. H. Mezerji, S. Bals, J. Perez-Juste and L. M. Liz-Marzán, *Nano Lett.*, 2012, **12**, 4380–4384.
12 J. Kim, M. J. Sadowsky and H. G. Hur, *Biomacromolecules*, 2011, **12**, 2518–2523.
13 F. Richard Keene, *Coord. Chem. Rev.*, 1999, **187**, 121–149.
14 J. D. Newman and G. J. Blanchard, *Langmuir*, 2006, **22**, 5882–5887.
15 S. Rau, B. Schäfer, D. Gleich, E. Anders, M. Rudolph, M. Friedrich, H. Görls, W. Henry and J. G. Vos, *Angew. Chem., Int. Ed.*, 2006, **45**, 6215–6218.
16 X. Sun, S. Dong and E. Wang, *Langmuir*, 2005, **21**, 4710–4712.
17 K.-S. Shin, J.-H. Kim, I.-H. Kim and K. Kim, *Bull. Korean Chem. Soc.*, 2012, **33**, 906–910.
18 I. Pastoriza-Santos and L. M. Liz-Marzán, *Langmuir*, 2002, **18**, 2888–2894.
19 N.-H. Shen, T. Koschny, M. Kafesaki and C. Soukoulis, *Phys. Rev. B*, 2012, **85**, 075120–075124.

Supplementary information for:

Tunable synthesis of poly(ethylene imine)-gold-nanoparticle clusters

Florian Kretschmer,[a,b] Ulrich Mansfeld,[a,b] Stephanie Hoeppener,[a,b] Martin D. Hager,[a,b] Ulrich S. Schubert[a,b]*

[a] Laboratory of Organic and Macromolecular Chemistry (IOMC), Friedrich Schiller University Jena, Humboldtstr. 10, 07743 Jena, Germany. E-mail: ulrich.schubert@uni-jena.de; Fax: +49 3641 948202
[b] Jena Center for Soft Matter (JCSM), Friedrich Schiller University Jena, Philosophenweg 7, 07743 Jena, Germany

Materials and Instrumentation:

DMF (anhydrous, amine free, 99.9%) and hydrogen tetrachloroaurate(III) trihydrate (99.99%) were purchased from Alfa Aesar. Silver nitrate (>99.8%), ethanol, branched PEI (bPEI; 25 kDa), PAAm (17 kDa, 20 wt% aqueous solution) and sodium citrate dihydrate (>99%) were purchased from Sigma-Aldrich. Linear PEI (lPEI; 25 kDa), bPEI (0.6, 1.8 and 10 kDa) was purchased from Polysciences Inc.. Potassium cyanide (techn.) was obtained from Riedel De Haen. Ammonium chloride (>99%) was purchased from Roth. Water (< 0.1µS/cm) was purchased from an ELGA Purelab Prima. All chemicals were used as received.

UV-vis absorption spectra were recorded on a Perkin Elmer Lambda 750 spectrometer in 1 cm quartz cuvettes at room temperature. TEM measurements were performed on a Philips CM-120. 15 µL of the sample solution were blotted onto clean carbon coated TEM grids (Mesh 400, Quantifoil, Jena) and excess material was removed by a filter paper (Whatman No. 1); the samples were allowed to dry prior to the transfer to the microscope. Grid cleaning was performed by UV-ozone treatment for 40 s. Particle sizes were determined from the TEM

images utilizing ImageJ. Centrifugation was performed with a Heraeus Biofuge Primo with a fixed angle rotor in 1.5 mL Eppendorf tubes.

Synthesis of the clusters with different PEI/$HAuCl_4$ ratios and different PEIs:

A solution of bPEI (25 kDa 2.5; 3.3; 5; and 10 mg/mL DMF) and a solution of $HAuCl_4 \times 3$ H_2O (10 mg/mL DMF) were prepared. To 1 mL DMF in a small glass vial 40 µL of each solution were added and the mixture was immersed in an oil bath at 150 °C (corresponding to an internal temperature of ~130 °C after 20 min) and stirred for 20 min at 700 rpm and afterwards cooled to room temperature. In the same way particles with bPEI 0.6; 1.8; 10 kDa and lPEI 25 kDa were prepared (10 mg/mL of the reactants, 1:1 ratio).

Synthesis of PEI clusters with NH_4Cl:

To 1 mL of a solution of bPEI (25 kDa, 4 mg/mL DMF) 100 µL NH_4Cl (10 mg/mL H_2O) was added and the solution immersed in an oil bath at 150 °C and stirred for 20 min at 700 rpm and then cooled to room temperature.

Synthesis of gold nanoparticle–PAAm clusters:

A solution of PAAm (66.5 mg/mL water) and a solution of $HAuCl_4 \times 3H_2O$ (10 mg/mL DMF) were prepared. To 1 mL DMF in a small glass vial 40 µL of each solution were added. The mixture was immersed in an oil bath at 150 °C and stirred for 20 min at 700 rpm and then cooled to room temperature.

Synthesis of single gold particles and differently sized gold nanoparticle–PEI clusters:

Solutions of 1 mg/mL, 10 mg/mL, 20 mg/mL, 50 mg/mL, 100 mg/mL of bPEI (25 kDa) and $HAuCl_4 \times 3$ H_2O were prepared. To 1 mL DMF 40 µL of each solution were added under

stirring and the mixtures were immersed in an oil bath at 150 °C. After stirring for 20 min at 700 rpm the mixtures were cooled to room temperature.

Transfer into water, etching of the particles and synthesis in water/ethanol:

All experiments were conducted with the solutions synthesized with bPEI 25 kDa at a 1:1 ratio. 40 µL of each solution were added to 1 mL DMF (concentration of 10 mg/mL for each reactant).

To transfer the clusters into water 1 mL of the solution was centrifuged at 5.000 rpm for 90 min, afterwards 950 µL of the supernatant solution was taken off, 950 µL of water were added and the procedure was repeated two more times. Etching of the gold cores was accomplished by addition of 100 µL of a KCN solution (10 mg/mL H_2O) to 1 mL of the cluster solution.

In case of water and ethanol as the solvents the reaction was conducted at 95 °C and 70 °C oil bath temperature, respectively, for 20 min. The synthesis of the clusters at room temperature was conducted by stirring the reaction for one week.

Synthesis of silver nanoparticles:

The synthesis was performed with a fresh solution of $AgNO_3$ (4.3 mg/mL DMF) and bPEI (25 kDa, 10 mg/mL). 40 µL of each solution were added to 1 mL DMF and the mixture was immersed in an oil bath (temperature 150 °C) and stirred for 20 min at 700 rpm. Subsequently, the mixture was cooled to room temperature.

Synthesis of citrate stabilized gold nanoparticles:

In a 250 mL round bottom flask 200 mL of a $HAuCl_4 \times 3H_2O$ (1 mM) solution was heated to 100 °C while stirring at 700 rpm. To the refluxing solution 1 mL of a sodium citrate solution (0.78 mM) was added at once. The color of the solution turned red after ~ 30 seconds.

Heating was continued for 30 minutes, afterwards the solution was cooled down and stored in the dark at 4 °C.

Synthesis of clusters with increased gold particle size and filling fraction:

For clusters with a low concentration of initial nanoparticles, 1 mL of the citrate nanoparticles were centrifuged in a plastic vial at 5000 rpm for 90 min and 950 µL of the supernatant solution was taken off. Afterwards 100 µL of a PVP solution (10 mg/mL DMF) and 850 µL DMF were added and the particles were redispersed by simple shaking. The solution was centrifuged two times at 5000 rpm for 2.5 h and each time 950 µL supernatant was taken off and the particles were redispersed in 950 µL DMF. For solutions with a high concentration of initial gold particles ten 1 mL solutions were processed in the same way. As an additional step the solutions were centrifuged again, 900 µL of the supernatant was taken off, and all the solutions were combined.

For the synthesis of small clusters, to 1 mL of the low or high concentrated particle solution 40 µL PEI (10 mg/mL DMF) and 40 µL $HAuCl_4 \times 3H_2O$ (10 mg/mL DMF) were added under stirring at 1200 rpm. The solution was then immersed in an oil bath at 150 °C and stirred for 5 minutes at 700 rpm; afterwards it was cooled to room temperature.

For the synthesis of large clusters, to 1 mL of the low or high concentrated particle solution 40 µL PEI (50 mg/mL DMF) and 40 µL $HAuCl_4 \times 3H_2O$ (50 mg/mL DMF) were added under stirring at 1200 rpm. The solution was then immersed in an oil bath at 150 °C and stirred for 5 minutes at 700 rpm; afterwards it was cooled to room temperature.

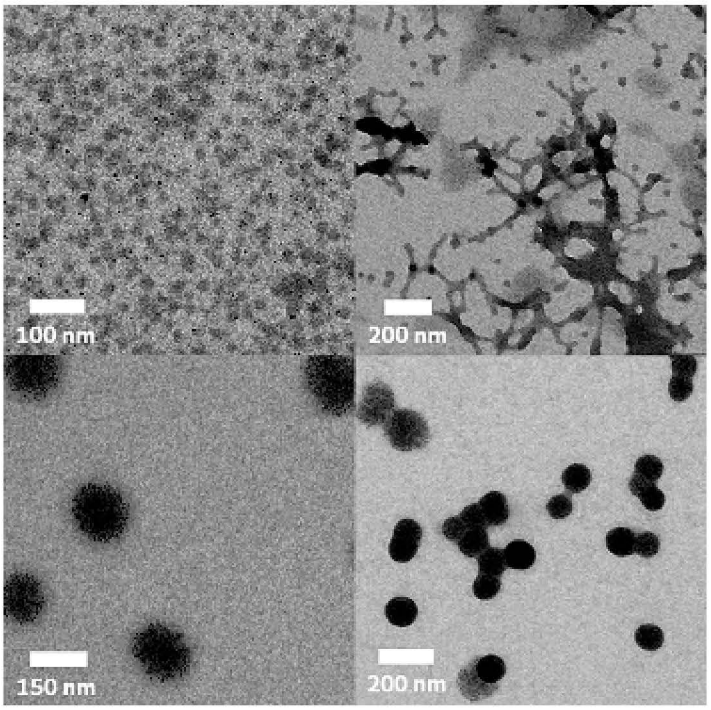

Figure S1. TEM images at different stages of the nanoparticle synthesis. After 30 sec (top left), 45 sec (top right), 1 min (bottom left) and 2 min (bottom right).

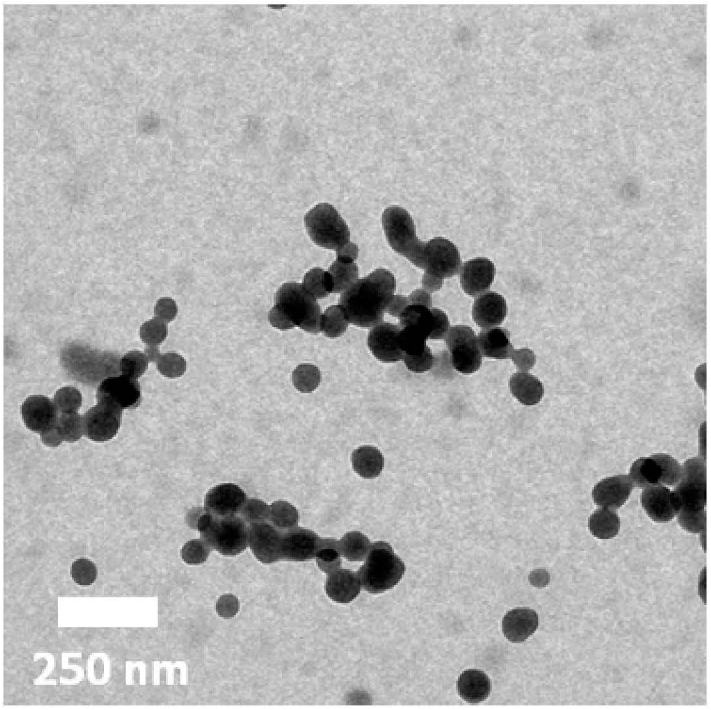

Figure S2. TEM image of the control solution with NH_4Cl instead of $HAuCl_4$.

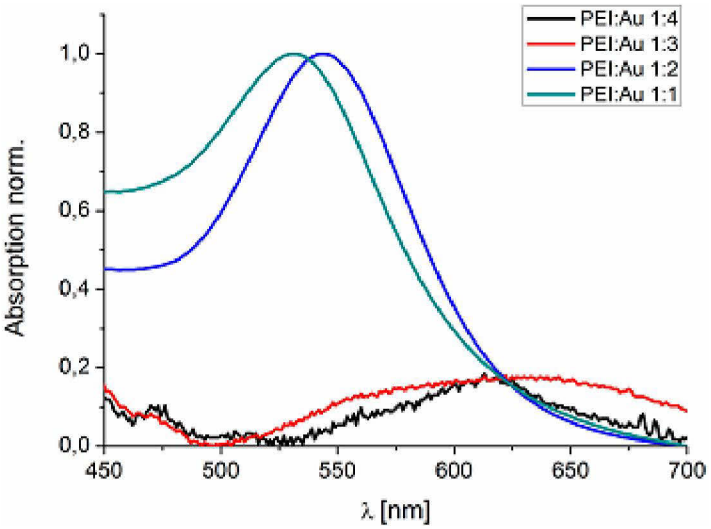

Figure S3. UV-vis spectra of particles synthesized with different PEI/$HAuCl_4$ ratios (in DMF).

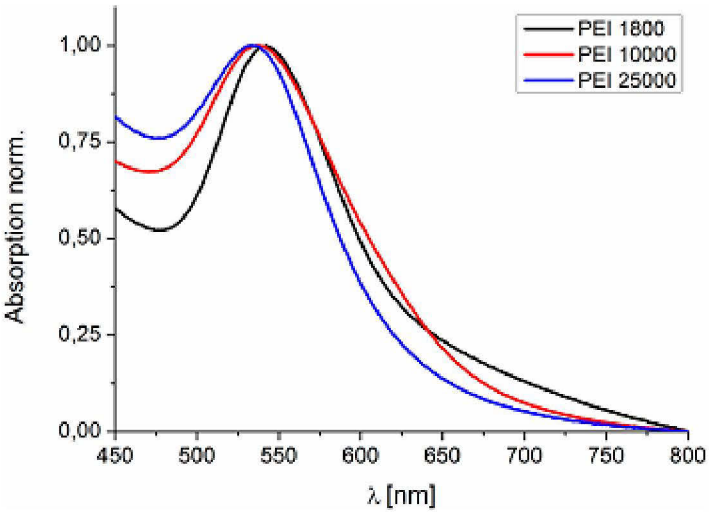

Figure S4. UV-vis spectra of clusters synthesized with PEIs of different molar masses (in DMF).

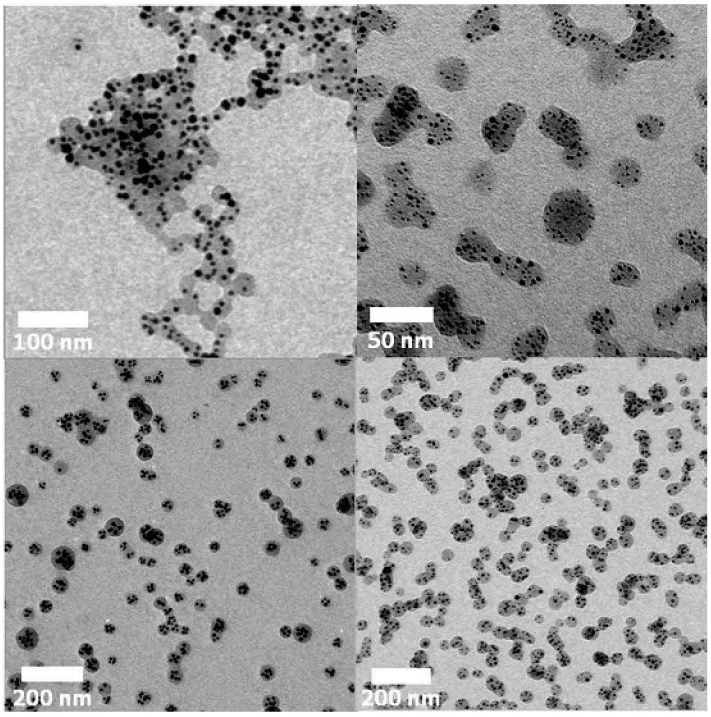

Figure S5. TEM images of particles synthesized with a 1:2 ratio (top left), with PAAm (top right), bPEI 1.8 kDa (bottom left) and bPEI 10 kDa (bottom right).

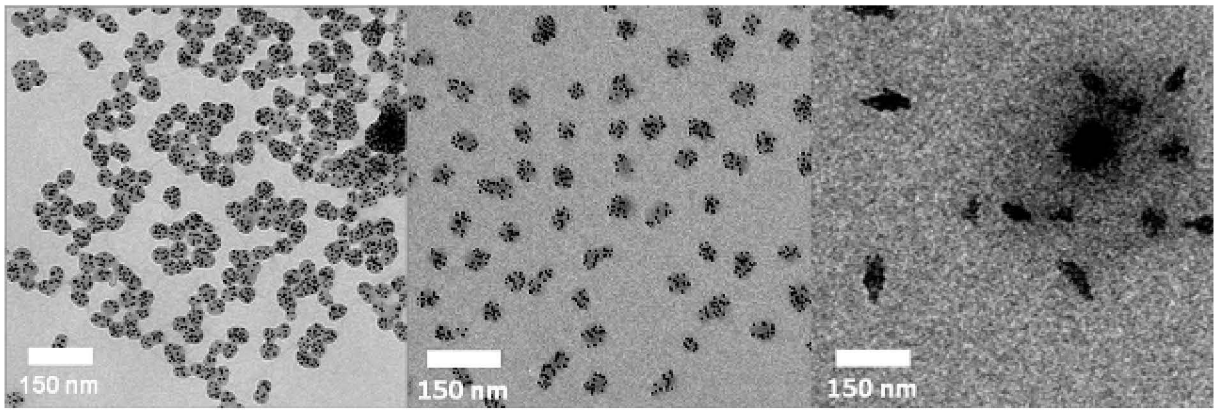

Figure S6. TEM images of as synthesized particles with bPEI 25 kDA and a 1:1 ratio, after three times centrifugation and redispersion in water and after etching with KCN (left to right).

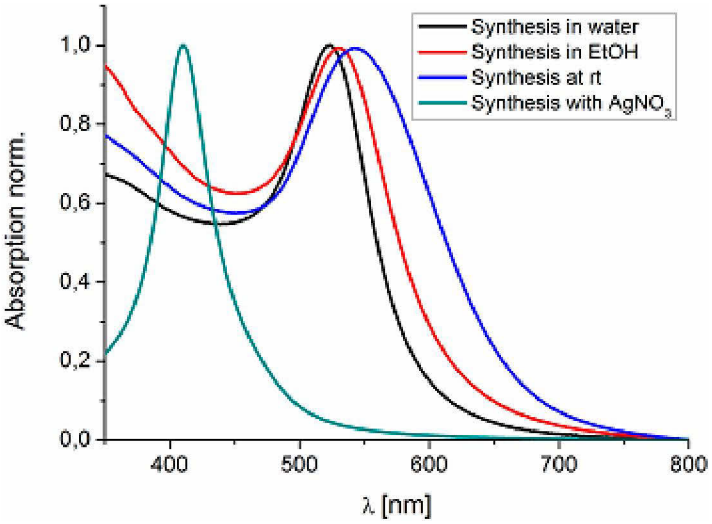

Figure S7. UV-vis spectra of particles synthesized in water, ethanol, at room temperature (in DMF) and with silver nitrate (in DMF).

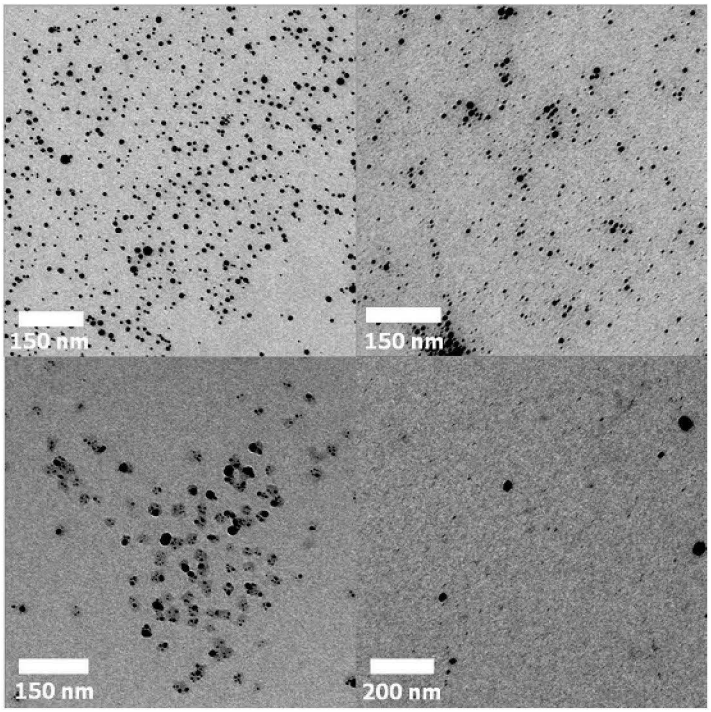

Figure S8. TEM images of particles synthesized in water (top left), ethanol (top right), at room temperature (bottom left) and with silver nitrate (bottom right).

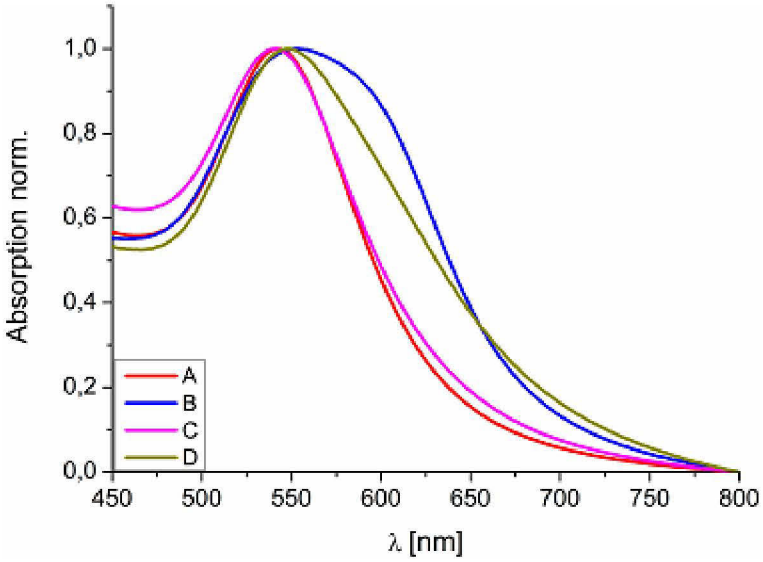

Figure S9. UV-vis spectra of clusters of different size and filling fractions: A - small clusters, low filling fraction; B - small clusters, high filling fraction; C - large clusters, low filling fraction; D - large clusters, high filling fraction (in DMF).

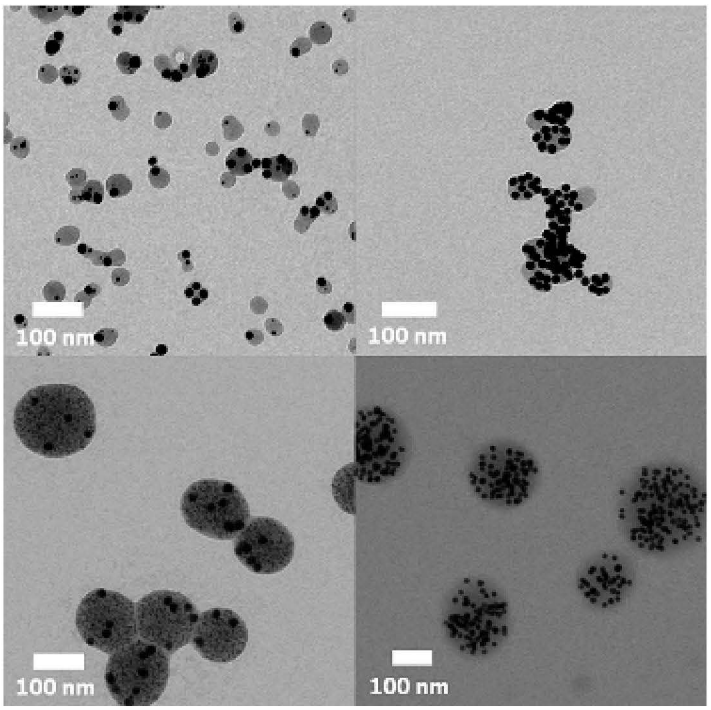

Figure S10. TEM images of clusters of different size and filling fractions: top left - small clusters, low filling fraction; top right - small clusters, high filling fraction; bottom left - large clusters, low filling fraction; bottom right - large clusters, high filling fraction.

Publication P7

Plasmonic Nanoparticle Clusters with Tunable Plasmonic Resonances in the Visible Spectral Region

F. Kretschmer, M. Fruhnert, R. Geiss, U. Mansfeld, C. Höppener, S. Hoeppener, C. Rockstuhl, T. Pertsch, U. S. Schubert

J. Mater. Chem. C **2014**, *2*, 6415-6422.

Journal of Materials Chemistry C

PAPER

Plasmonic nanoparticle clusters with tunable plasmonic resonances in the visible spectral region

Cite this: DOI: 10.1039/c4tc01018c

Florian Kretschmer,[ab] Martin Fruhnert,[c] Reinhard Geiss,[d] Ulrich Mansfeld,[ab] Christiane Höppener,[e] Stephanie Hoeppener,*[ab] Carsten Rockstuhl,[f] Thomas Pertsch[d] and Ulrich S. Schubert*[ab]

Received 16th May 2014
Accepted 20th June 2014

DOI: 10.1039/c4tc01018c

www.rsc.org/MaterialsC

The seeded growth of poly(ethylene imine) – gold nanoparticle clusters enables the formation of particle assemblies with tunable optical properties. Clusters with increasing particle sizes, filling factors and assemblies consisting of PEI–gold–silver core shell particles can be synthesized in this way. Profound structural characterization is carried out *via* TEM imaging and FIB milling which allows visualizing the cross-section of the clusters. Determination of the optical properties was performed *via* UV-Vis spectroscopy and spectral dark-field microscopy of individual particles. Additionally, numerical calculations were carried out based on the Mie theory. The results are in good agreement with the experimental findings and reveal the contribution of different multipoles to the spectra which cannot be resolved by UV-Vis spectroscopy in solution. The isotropic nature and adjustable properties of these clusters could render them versatile building blocks for metamaterials.

Introduction

The controlled fabrication of noble metal nanostructures has become a major driving force for the implementation of uncountable potential applications in fields like medicinal therapy,[1,2] sensors,[3] energy conversion,[4–5] catalysis[6] and optical devices.[7,8] Up to now, most interest was gathered by gold and silver nanoparticles as they feature a localized surface plasmon resonances (LSPRs) in the visible and near infrared (IR) region, as well as they provide a high environmental stability. Light-matter interactions of these particles can be tuned *via* different parameters, *i.e.*, their sizes or shapes but also by the assembly of such particles into superstructures.[9,10]

Due to the ability to create completely tunable and artificial properties, metamaterials are certainly the most exciting applications as they could potentially be utilized to fabricate perfect lenses or cloaking devices.[11] Bottom-up approaches for the synthesis of plasmonic nanoparticle assemblies can serve as an excellent starting point for the fabrication of metamaterials since they can be formed by *meta*-atoms in the nanometer range. Next to the synthesis of individual nanoparticles the utilization of colloidal superstructures promises a wider range of possibilities to manipulate the optical properties of assemblies.[10,12] However, it is obvious that for the time being the focus of such nanostructures has mostly not been primarily on the synthesis of potential *meta*-atoms. While a considerable amount of work has been conducted to elaborate the theoretical aspects of these superstructures, practical approaches to synthesize them, in particular, with complex architectures, have been scarce. Mediated by block copolymers, small clusters with a defined particle number can be synthesized.[13,14] These clusters can be utilized for analytical applications, *e.g.*, SERS; however, also metamaterials[15] could be potentially created in this way. Yet, an undesired property of these clusters is their highly anisotropic behavior, *i.e.* their electric and magnetic response is dependent on the angle and polarization of the irradiated light. Exceptions are tetrahedral clusters due to their isotropic nature but the current methods allow their preparation only in low yields. Moreover, purification from other cluster structures is necessary. Here we introduce a conceivable method to synthesize plasmonic superstructures consisting of hundreds of individual plasmonic nanoparticles embedded into polymeric spherical assemblies, introduce a model to predict their optical properties and compare the obtained results with spectroscopically resolved dark field microscopy investigations on the level of individual superstructures. The spherical superstructure of these clusters renders them isotropic by design. Additionally, changing the particle number will have a negligible

[a]*Laboratory of Organic and Macromolecular Chemistry (IOMC), Friedrich Schiller University, Jena, Humboldtstr. 10, 07743 Jena, Germany. E-mail: s.hoeppener@uni-jena.de; ulrich.schubert@uni-jena.de; Fax: +49 3641 948202*

[b]*Jena Center for Soft Matter (JCSM), Friedrich Schiller University Jena, Philosophenweg 7, 07743 Jena, Germany*

[c]*Institute of Condensed Matter Theory and Solid State Optics, Abbe Center of Photonics, Friedrich Schiller University Jena, Max-Wien-Platz 1, 07743 Jena, Germany*

[d]*Institute of Applied Physics, Abbe Center of Photonics, Friedrich Schiller Universität Jena, Max-Wien-Platz 1, 07743 Jena, Germany*

[e]*NanoBio Photonics, Physical Institute, Universtity of Münster, Wilhelm-Klemm Str. 3, 48149 Münster, Germany*

[f]*Institute of Theoretical Solid State Physics, Karlsruhe Institute of Technology, Wolfgang-Gaede-Strasse 1, 76131 Karlsruhe, Germany*

influence on their optical properties, in contrast to clusters with a low amount of particles. The optical response of spherical assemblies of plasmonic nanoparticles depends on several parameters, *i.e.*, the chosen metal, the filling factor of the metal, the size of the metal particle as well as of the overall architecture of the superstructure. For example the UV-Vis spectrum of an assembly of small gold nanoparticles into a spherical superstructure with a low filling fraction will be hardly different from the spectrum of nonassembled individual gold particles. However, if, *e.g.*, the particle size and/or the filling factor is increased new material properties arise, which change the optical response of the assemblies.[16–19]

In literature different strategies were reported to create colloidal superstructures. A suitable approach is the synthesis of satellite type structures by the assembly of plasmonic nanoparticles onto a spherical template. Organic or inorganic nanoparticles consisting of polystyrene or silica can be applied as templates.[20–22] For example, Mühlig and co-workers assembled larger gold nanoparticles on the surface of functionalized silica particles *via* electrostatic attraction as well as by strong thiol–gold interactions.[23] In this way the authors were able to establish structures generating a magnetic dipole moment in the visible region of the spectrum.

Clusters on the one hand can be prepared by first synthesizing plasmonic nanoparticles which are subsequently encapsulated.[24–26] Dintinger and coworkers demonstrated the fabrication of silver nanoparticle clusters *via* an emulsification technique and their optical response could be associated with a magnetic dipole resonance.[19] An alternative approach was utilized by Xiao *et al.* The authors demonstrated an approach that involves the synthesis of mesoporous hollow silica particles.[27] A gold salt as well as a reducing agent solution can enter these particles and, *via* heating, gold nanoparticles are formed inside the cluster. The most striking feature of this approach is that the gold particles can be used also to grow other structures inside the particles.

Another strategy to form colloidal superstructures consisting of clusters relies on the preparation of plasmonic nanoparticles and the simultaneous formation of larger clusters at the same time.[28] Recently, we reported such an approach to form poly(ethylene imine)–gold nanoparticle clusters.[29] Branched PEI and $HAuCl_4$ were heated in DMF, which results in differently sized polymer particles with small encapsulated gold nanoparticles. Depending on the overall concentration of the reactants the size of the clusters could be reliably tuned.

Here we introduce a number of additional considerations based on theoretical predictions, which are verified experimentally. In particular the seeded growth of the particles inside the clusters to increase the filling factor is introduced. Further, the first synthesis of clusters consisting of gold–silver core–shell nanoparticles is demonstrated. The structure of the clusters was characterized by TEM as well as FIB milling/SEM imaging. Optical characterization was performed by UV-Vis spectroscopy of the solutions as well as by spectroscopically resolved dark-field microscopy on the individual nanoparticle level. These results were compared to numerically predicted plasmonic spectra. The easily tunable optical properties as well as the isotropic nature of the clusters renders the described approach a versatile way for the creation of *meta*-atoms.

Results and discussion

Branched PEI and $HAuCl_4$ are heated in DMF which results in differently sized polymer particles with tiny encapsulated gold nanoparticles.[29] Depending on the overall concentration of the reactants the size of the clusters can be tuned. Based on the size of the particles and the amount of PEI and $HAuCl_4$ used, an initial filling factor of 2.7% of gold was calculated. For clusters with small gold particle sizes and only a low filling factor the UV-Vis spectra are dominated by the plasmon resonances of the individual nanoparticles and no effect from their incorporation into a superstructure could be observed.

However, simulations based on the Mie theory on superstructures with higher filling factor, particle/cluster size or utilization of silver instead of gold promised the occurrence of new optical properties, *e.g.*, magnetic dipole moments. Possible strategies to access the cooperative coupling of the nanoparticles within the cluster include, *e.g.*, the simple increase of the size of the clusters. Moreover, it is possible to increase the size of the encapsulated nanoparticles by utilizing pre-synthesized gold nanoparticles, which are concomitantly encapsulated during the synthesis. However, the transfer of the pre-synthesized particles into DMF is challenging due to their protection with additional polymer in order to prevent aggregation. Hence, several time consuming centrifugation cycles are required. Furthermore, to achieve high filling factors and to avoid secondary nucleation a high initial particle concentration is required. As a result the concentration of citrate stabilized particles, *e.g.*, to tenfold of their initial concentration, leads approximately only to a doubling of the filling factor for the largest polymer particles.[29]

To overcome these restrictions we propose to utilize alternatively the seeded growth of already encapsulated gold nanoparticles (Scheme 1). For all seeded growth experiments discussed in this contribution, clusters of 120 nm diameter were used (Fig. 1) as initial PEI–NP aggregates. In literature there are several protocols available to increase the size of gold particles *via* seeded growth.[30–32] Hydroxylamine is a commonly utilized reducing agent for this approach.[33] In the first step of the reaction Au^{3+} is reduced to Au^{+}, subsequently, it can be reduced to Au^{0} if elemental gold is already present. This straightforward method, however, cannot be directly applied for PEI–NP clusters as it results to a large extend in the destruction of the clusters as well as a large size and shape distribution of the final particles. On the other hand, a combination of ascorbic acid (AA) and cetyltrimethylammonium bromide (CTAB)[34] lead to the successful growth of larger spherical particles inside the clusters. In order to further finetune the particle size and the filling factor the amount of growth solution was kept constant and different volumes of the cluster solution were added. In this way the size of the gold particles could be increased by concomitantly decreasing the seed concentration. By adding 20, 10 and 5 μL of the clusters to 1 mL of the growth solution the size of the gold particles increased respectively (Fig. 2). The

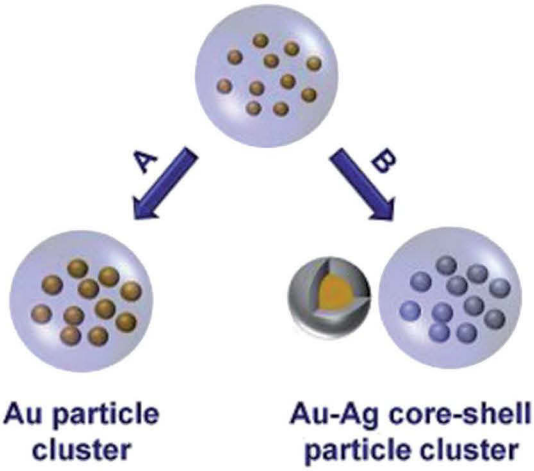

Scheme 1 Schematic representation of the nanoparticle growth inside of the clusters mediated by $HAuCl_4$/AA/CTAB (A) or $AgNO_3$, $NH_{3(aq)}$, $HCHO_{(aq)}$ (B).

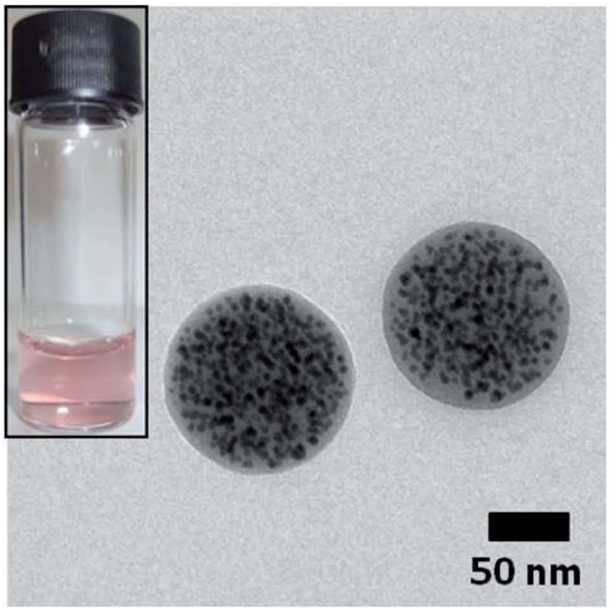

Fig. 1 TEM image of the cluster seeds prior to the seeded growth.

process could also easily be followed by the characteristic color change of the solution. The initial, slightly red color of the seed solution, changes to a dark purple, violet and finally dark blue. UV-Vis spectroscopy indicates furthermore an increased intensity of the LSPR band with increasing particles size, additionally the band is red-shifted and broadened. For the lowest seed concentration a clear shoulder can be observed at 600 nm. An average seed number of 300 small gold particles in one cluster was determined by manually counting the particles in a cluster of average size. Due to the large extend of overlapping of the internal metal particles, in particular for clusters with higher filling factors, the particle size could not be reliably determined experimentally. Hence, an initial particle diameter of 5.4 nm was calculated based on the seed number and amount of PEI as well as gold used. Upon growth, the gold particle size changes to 8.1, 9.6 and 11.8 nm, respectively.

Next to the increase of the size of the nanoparticles inside the aggregate structures also the incorporation of silver into the cluster structure is regarded as another efficient method to further tune the plasmonic properties. While the direct synthesis of PEI–Ag clusters could not be successfully established[29] the formation of silver shells around the incorporated gold particles could be implemented which resulted in spherical clusters consisting of Au–Ag core–shell particles. This system is rather sensitive towards the applied chemical routes; *e.g.*, for the CTAB/AA system it was observed that the bromide ions led to the precipitation of silver bromide. Despite the fact that DMF is known as a versatile reducing agent for silver ions[35] a simple addition of silver nitrate to a solution of clusters dissolved in DMF did not result in the formation of silver particles but resulted in the destruction of the clusters. The choice of the reducing agents is, thus, generally critical. The addition of, hydroquinone, sodium citrate, glucose or AA alone, resulted only in the aggregation of the clusters or secondary nucleation.

Finally, Tollens reagent was identified as a suitable way to circumvent these issues. Similar to the growth of gold nanoparticles, the size of the silver shell could be tuned by variation of the seed volume. No secondary nucleation was observed by TEM. For a low amount of seeds larger particles may occur also on the outside, supposedly due to the fact that particles on the outside grow faster since the growth solution has to diffuse into the clusters. This effect might be further amplified by the different nucleation and growth kinetics of silver.[36,37] In addition, it is also reasonable to assume that the particles, as soon as they penetrate the polymer shell, grow significantly faster.

In case a high amount of seeds is used the color of the solution changes to yellow, and a shoulder occurs in the UV-Vis spectra at ~400 nm which stems from the contribution of the silver LSPR. For decreasing amounts of seeds the color changes to violet and blue and a distinct shoulder at higher wavelengths arises accompanied by a large broadening of the plasmon resonance which extends into the NIR region for the lowest amount of seeds. Upon growth, the initial gold cores are decorated with a silver shell of 2.2, 3.3 and 4.7 nm thickness yielding core–shell particles of 9.8, 12 and 14.8 nm diameter, respectively.

While most of the cluster solutions settle within several hours, they could easily be redispersed by shaking. In case of the core–shell clusters this was not possible and control experiments showed that the ammonia solution was the reason for their irreversible aggregation. However, it was found that poly(acrylic acid) represents a suitable reagent to stabilize the solutions.

The initial filling factor of 2.7% increases to 9.2, 15.4 and 28.5% for decreasing amounts of seeds when treated with the gold growth solution. In case of the seeded growth with silver filling factors of 16.3, 29.3 and 56.3% were obtained, respectively.

To further evaluate the structural properties of the clusters a cross-section was prepared using focussed ion beam (FIB)

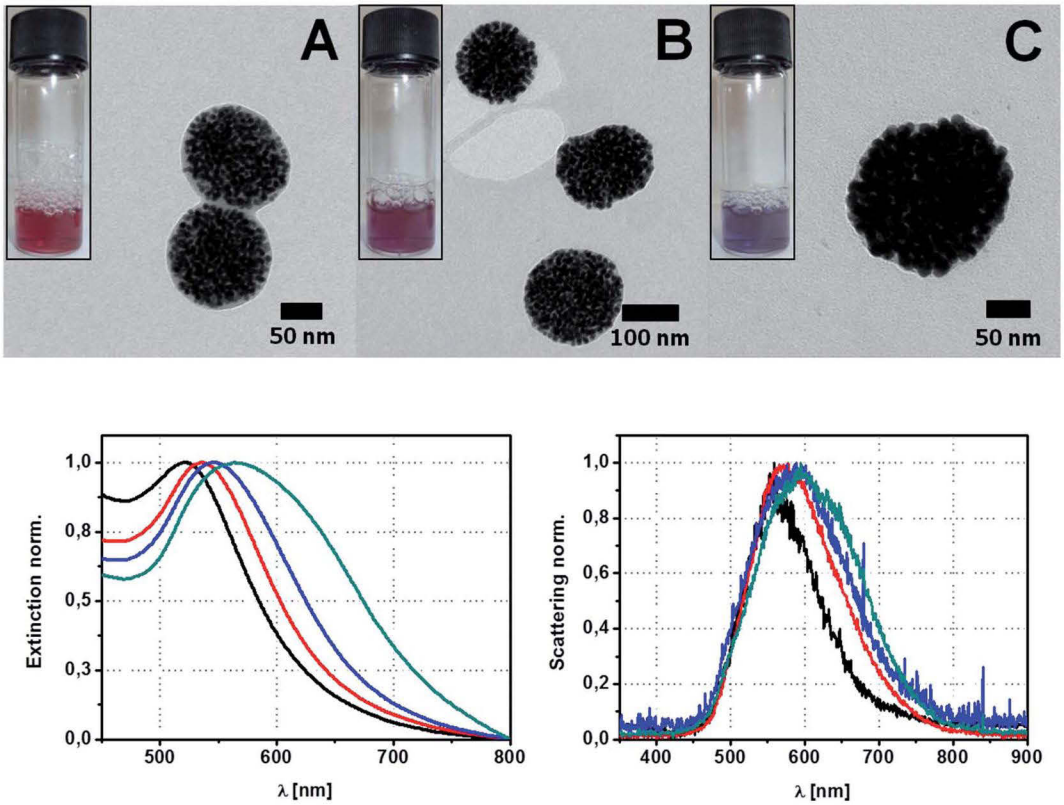

Fig. 2 TEM images of the gold clusters synthesized with decreasing volumes of the seed solution (A 20 μL, B 10 μL, C 5 μL) (Top). UV-Vis spectra of the gold cluster solutions (bottom left) and scattering spectra of individual clusters (bottom right): black – original clusters; red, blue, green – gold cluster solutions with increasing gold particle sizes/filling fractions. The seed concentration decreases from red to green.

milling.[38] In contrast to TEM imaging that merely records projections of the entity of particles constituting the cluster, the FIB preparation displays an actual cross-section image at a specific position inside the particle. To avoid charging of the sample during FIB/SEM operation the clusters were prepared onto a conductive substrate. A platinum layer was deposited on top of the particles which protects the top edge of the particle from rounding and increases the visibility of the particle by introducing a solid interface with the metal layer. Gallium ions were subsequently used for cross-sectioning. The results obtained from the SEM imaging are shown in Fig. 4. Inside the large outer shell of the particle smaller bright areas are clearly visible representing the gold nanoparticles.

For small particle sizes or for molecules (*e.g.* dyes) the UV-Vis spectrum corresponds in good approximation to the extinction spectrum of the sample. With increasing particle size, however, the proportion of the scattering to the UV-Vis spectrum increases and contributes to a significant amount to the extinction. For very large particles it can even exceed the contribution of the absorption to the extinction spectrum. In this way, UV-Vis spectroscopy of large clusters solutions only allows to determine the sum of scattering and absorption. Moreover, no conclusions can be drawn on the optical features of individual particles as UV-Vis spectroscopy determines the bulk properties of a sample and represents a sum spectrum of contributions from the absorption and scattering of the solution. Moreover, averaging over a large number of particles occurs by utilizing conventional UV-Vis spectroscopy.

Dark field microscopy (Fig. 5) represents a versatile tool to analyze the LSPRs of nanoparticles and is been increasingly used, *e.g.*, for tracking of nanoparticles in biological tissue or orientation determination of anisotropic nanoparticles.[39,40] Depending on the size, structure and metal the scattering contributions change in intensity and wavelength which is reflected by differently colored dots on the dark field image.[41–45] We investigated the scattering behavior of selected individual clusters of all prepared samples. The dark-field spectra were recorded with the setup described in the materials and instrumentation section. The noise in the data stems largely from the small numerical aperture of the collection objective chosen to suppress efficiently the direct background light, short integration times and read out noise. The dark field images of the original clusters as well as gold and gold–silver core–shell particle clusters grown with a medium amount of seeds are depicted in Fig. 6. Clearly, individual dots of yellow, greenish and blue color are present. Since the synthesized clusters are mostly of spherical shape it is unlikely that the different colors arise from different particle structures. However, the scattering wavelength redshifts with increasing cluster size indicating that yellow dots correspond to larger clusters whereas blue dots correspond to small cluster. The scattered light of individual dots reflects the scattering spectrum which can be recorded by a

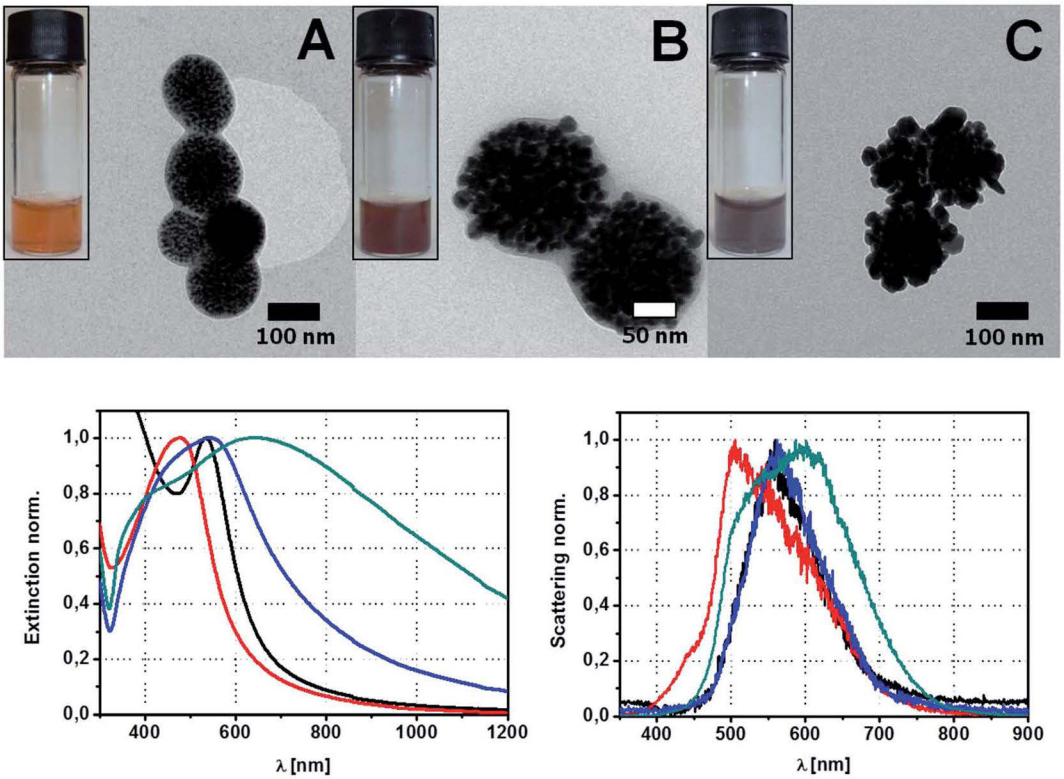

Fig. 3 TEM images of the gold–silver core–shell clusters synthesized with decreasing volumes of the seed solution (A 20 μL, B 10 μL, C 5 μL) (Top). UV-Vis spectra of the gold–silver core–shell cluster solutions (bottom left) and scattering spectra of individual clusters (bottom right): black – original clusters; red, blue, green – gold cluster solutions with increasing gold particle sizes/filling fractions. The seed concentration decreases from red to green.

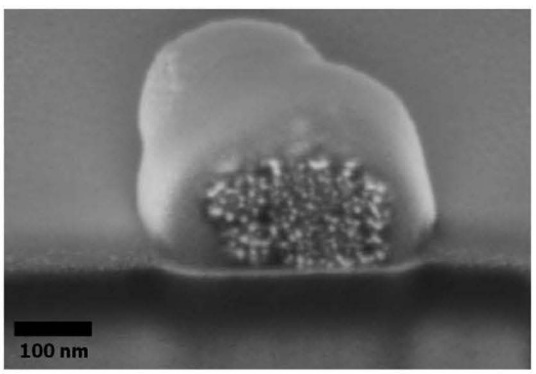

Fig. 4 SEM image of a FIB prepared cross-section from a "gold-only" cluster with the highest filling factor. The area is covered by 40 nm platinum layer, the substrate material is SiO_2 with a conductive layer of 10 nm ITO.

spectrometer. In order to perform a selected evaluation, multiple spectra of different dots were recorded for each sample. For the original seed clusters a scattering maximum at 559 nm arises. In comparison, the UV-Vis spectrum showed the maximum at 521 nm. The maximum of the gold cluster solutions increases in wavelength to 578 nm, 588 nm and 595 nm for solutions synthesized with decreasing seed concentrations (Fig. 2). For gold–silver core–shell clusters at first a bathochromic shift to 505 nm occurs due to the scattering

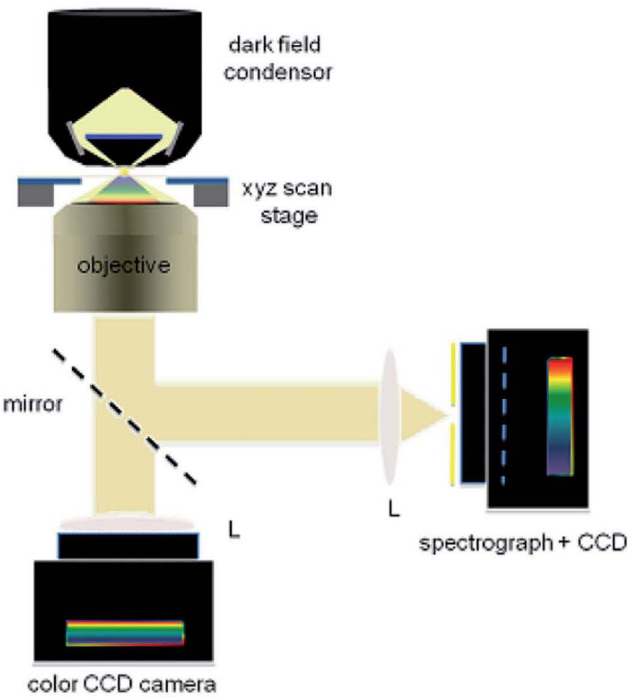

Fig. 5 Schematic representation of the setup for the dark field microscopy experiments.

Fig. 6 Dark field images of the seed solution (left), after gold growth with a medium amount of seeds (middle) and after silver growth with a medium amount of seeds (right).

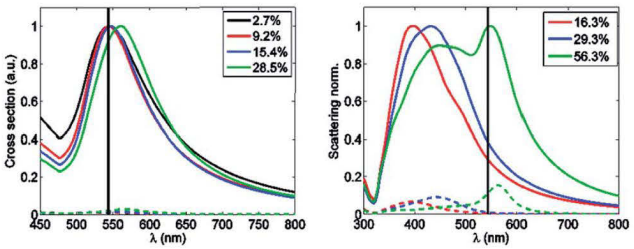

Fig. 7 Simulated scattering cross-sections of gold nanospheres (left) and gold nanospheres with silver shells (right). Black – original particles; red, blue, green – gold particles with increasing diameter or silver shell thickness, respectively, where the colors correspond to different filling fractions of the cluster. Solid lines – total scattering cross-section; dashed lines – magnetic dipole contribution to the scattering cross-section. Black vertical line – resonance position of an isolated gold particle.

contribution of silver (Fig. 3). Afterwards the increase in particle size and filling factor again leads to a redshift of the scattering maximum to 562 nm and 587 nm, respectively.

To support the experimental measurements the scattering response from clusters of gold nanoparticles of different sizes and gold particles with silver shells according to the experimental situation was simulated. The calculations are based on a rigorous solution of Maxwell's equations and were performed with an in-house software.[46,47] We made use of the extended Mie-Theory for multiple spheres in a self-consistent manner. The electromagnetic fields are expanded into vector-spherical-harmonics and the obtained coefficients can be used to attribute Cartesian dipole and, depending on the expansion order, higher order multipole moments to the individual spheres. Furthermore we can calculate the scattering and absorption cross sections of the whole structure from the coefficients. In the present case we used an expansion order of two, which gave us the dipole and quadrupole moments, this is sufficient for small spheres. This full-wave simulation method provides essentially the scattering response of an arbitrary but finite cluster made from an ensemble of spherical particles for a given illumination. This is implemented by expanding the incident, the internal and the scattered fields from each spherical particle in the ensemble into Eigenmodes. These Eigenmodes are vector spherical harmonic functions. By enforcing the usual boundary conditions at the surface of the spheres, the amplitudes of all modes can be calculated in a self-consistent manner from which all further properties can be derived. The considered clusters consist of 300 isolated nanoparticles that group to form a spherical object. The surrounding medium consists of water for which we assume a nondispersive permittivity of $\varepsilon = 1.7$. The initial gold spheres have a diameter of 5.4 nm and the cluster has always a total diameter of 120 nm. The initial cluster exhibits a resonance at a wavelength of approximately 540 nm, as can be clearly seen from Fig. 7. This resonance wavelength coincides with the resonance wavelength of an isolated gold nanosphere. This is not surprising since eventually the nanospheres do not experience the existence of neighboring objects for such large dilution. Therefore, the single particle spectrum emerges from the cluster. However, when the diameters of the constituents increases while maintaining the total diameter of the cluster, the filling fraction rises too. This effectively lowers the nearest-neighbor distance of the nanospheres. The emerging onset of coupling causes the resonance to shift to higher wavelengths like it has been observed in the experiments. This can be clearly seen in the simulations as shown in the left of Fig. 7. The simulations of the silver covered gold particles yield a picture similar to the experimental results. The respective results are shown in the right of Fig. 7. At first, the introduced silver shells cause a strong blue shift of the resonance with respect to the resonance wavelength of the pristine and strongly diluted gold cluster. This is not surprising since the plasmonic resonance of an isolated silver sphere occurs due to the higher plasma frequency of the material at shorter wavelengths. The resonance of the gold nanosphere in the core can be weakly seen as a shoulder in the spectra. However, the silver shell shields the gold core and prevents the electromagnetic field to penetrate the object. Therefore, the interaction strength is much reduced and the resonance is very weak. By increasing the shell size, the same coupling effects as observed for the gold clusters cause again a strong red-shift of the resonance wavelength; in full agreement with the experimental results.

One advantage of the numerical method at hand is the possibility to investigate the scattering cross-section in more detail, *e.g.*, by calculating the contributions of different multipole moments to the scattering cross-sections. The main contribution of the resonance comes from the electric dipole moments. This can be easily understood because an isolated metallic sphere can be sufficiently approximated by an electric dipole. But as the size of the particles increases, and therefore the coupling of the individual spheres, a magnetic dipole moment contribution (dashed line) evolves. This magnetic dipolar scattering response is very important since it is at the heart of many unprecedented optical effects as described in the introduction. This effect is even stronger when considering the gold particles with silver shells. Silver, in general, is often preferred since the intrinsic absorption is smaller which causes plasmonic resonances to be much stronger. This eventually translates also to a stronger magnetic dipole moment for the cluster made from gold particles covered with a silver shell. Deviations of the exact resonance position from experimental results are likely due to uncertainties in the particle sizes, shapes and distributions of the particles in the clusters, *e.g.*, some particles may be in very close proximity or even merged

during the growth process. However, the important properties are very well reflected in the simulations.

Conclusion

Summarizing, we have synthesized plasmonic nanoparticle clusters with tunable optical properties. *Via* a seeded growth approach small gold particles inside the clusters could be grown to either larger gold particles or into gold–silver core–shell particles as evidenced by TEM imaging. This was confirmed by FIB sectioning which enabled to visualize the cross-section of the clusters. UV-Vis spectroscopy revealed stronger coupling between the particles with increasing filling factor leading to a bathochromic shift in case of the gold clusters. In contrast, a hypsochromic shift first occurs for the gold–silver clusters, however, for higher filling factors also a broadening at longer wavelengths takes place. Scattering spectra were obtained from individual clusters which correlate well with the trends obtained from UV-Vis spectroscopy. Simulated spectra showed to be in good agreement with the experimental results. Moreover, multipole analysis revealed in particular for the gold–silver core–shell clusters a significant contribution of a magnetic dipole moment. Hence, such cluster structures might serve as versatile building blocks for future meta materials.

Materials and instrumentation

DMF (anhydrous, amine free, 99.9%) poly(acrylic acid) 25%, 240.000 g mol^{-1} and hydrogen tetrachloroaurate(III) trihydrate (99.99%) were purchased from Alfa Aesar. Silver nitrate (>99.8%) and branched PEI (bPEI; 25 kDa) were purchased from Sigma-Aldrich. Polyvinylpyrrolidone K25 and formaldehyde solution 36% was purchased from Carl Roth. CTAB (p.a. >99%) was purchased from Merck. Ammonia solution 25% was purchased from VWR. Water (<0.1 μS cm^{-1}) was purchased from an ELGA Purelab Prima. All chemicals were used as received.

UV-Vis spectra were recorded on a Perkin Elmer Lambda 750 spectrometer in 1 cm quartz cuvettes at room temperature. TEM measurements were performed on a Philips CM-120 at 120 kV. 15 μL of the sample solution were blotted onto carbon supported TEM grids (Mesh 400, Quantifoil) and excess material was removed by a filter paper (Whatman no. 1) under ambient conditions. The samples were allowed to dry prior to the transfer to the microscope. Grid cleaning was performed by argon plasma treatment for 1 min prior to the preparation of the solutions. Synthesis of the clusters and growth reactions were performed in standard glass vials. Dark field microscopy measurements were conducted on a Nikon Ti-U inverted microscope equipped with a Nikon dark-field condenser (NA 1-1.4) and a Plan Fluor 100× objective (NA 0.5-1.3). Images were taken with a Nikon FIXXX color CCD camera. Scattering spectra were recorded on an Acton 300i spectrograph with nitrogen cooled Pylon CCD sensor. A common 20 W halogen lamp was used as light source. Dark field spectra were acquired with an integration time of 10 s. Background signals were acquired in the same way. Correction of the dark field spectra was performed by using the background signal of the light source as reference. Filling factors and particle sizes of the clusters after seeded growth were determined *via* calculations based on the amount of metal added to the corresponding seed solutions. The number of seed particles in an individual cluster was determined by manually counting the particles inside a cluster of average size (120 nm). For the FIB/SEM measurements a ZEISS NEON60 CrossBeam System was used. The sample was dried on a SiO_2 substrate with a 10 nm ITO coating. Directly before FIB sectioning a 40 nm layer of platinum was locally deposited on top of the particle by FIB-assisted chemical vapour deposition. The cross-section patterning was performed with 30 kV gallium ions at a current of 2 pA.

Particle synthesis

For the seeded growth approach, clusters of an average diameter of 120 nm were prepared as reported in literature.[29] A growth solution was prepared in the following way: 12 mg CTAB were dissolved in 1 mL water and to this solution 40 μL $HAuCl_4 \times 3H_2O$ (10 mg mL^{-1} H_2O) were added. The solution was sonicated and heated in order to dissolve all the CTAB. After cooling to room temperature, 250 μL of the clear solution was added to 750 μL water. Subsequently, 25 μL ascorbic acid (12 mg mL^{-1} H_2O) were added under gentle shaking and the yellow solution immediately turned colorless. To this solution 20, 10 or 5 μL of the seed solution was added, respectively.

For the growth of the silver shell a solution consisting of 1 mL water, 20 μL $AgNO_3$ (4.3 mg mL^{-1} H_2O) and 20 μL NH_{3aq} (2.5% H_2O) was prepared. To this solution 20, 10 or 5 μL of the seed solution was added, respectively. Finally, the reaction was initiated *via* addition of 20 μL formaldehyde (3.6% H_2O). After 10 minutes the solutions were stabilized by adding 20 μL PAA (100 mg mL^{-1} H_2O).

Acknowledgements

Financial support from the research initiative PhoNa (Photonic nanomaterials), which is supported by the German Federal Ministry of Education and Research in the program "Spitzenforschung und Innovation in den Neuen Ländern" (support code 03IS2101A), is acknowledged.

References

1 T. L. Doane and C. Burda, *Chem. Soc. Rev.*, 2012, **41**, 2885–2911.
2 X. Huang, P. K. Jain, I. H. El-Sayed and M. A. El-Sayed, *Lasers. Med. Sci.*, 2008, **23**, 217–228.
3 Y. Jin, *Adv. Mater.*, 2012, **24**, 5153–5165.
4 H. A. Atwater and A. Polman, *Nat. Mater.*, 2010, **9**, 205–213.
5 S. Linic, P. Christopher and D. B. Ingram, *Nat. Mater.*, 2011, **10**, 911–921.
6 T. Mallat and A. Baiker, *Annu. Rev. Chem. Biomol. Eng.*, 2012, **3**, 11–28.
7 C. M. Soukoulis and M. Wegener, *Nat. Photonics*, 2011, **5**, 523–530.

8 H. Chen, *J. Mater. Chem.*, 2011, **21**, 6452–6463.
9 A. Moores and F. Goettmann, *New J. Chem.*, 2006, **30**, 1121–1132.
10 N. J. Halas, S. Lal, W. S. Chang, S. Link and P. Nordlander, *Chem. Rev.*, 2011, **111**, 3913–3961.
11 W. Cai, U. K. Chettiar, A. V. Kildishev and V. M. Shalaev, *Nat. Photonics*, 2007, **1**, 224–227.
12 X. Ye, J. Chen, B. T. Diroll and C. B. Murray, *Nano Lett.*, 2013, **13**, 1291–1297.
13 N. Pazos-Perez, C. S. Wagner, J. M. Romo-Herrera, L. M. Liz-Marzán, F. J. García de Abajo, A. Wittemann, A. Fery and R. A. Alvarez-Puebla, *Angew. Chem.*, 2012, **51**, 12688–12693.
14 A. S. Urban, X. Shen, Y. Wang, N. Large, H. Wang, M. W. Knight, P. Nordlander, H. Chen and N. J. Halas, *Nano Lett.*, 2013, **13**, 4399–4403.
15 Y. A. Urzhumov, G. Shvets, J. A. Fan, F. Capasso, D. Brandl and P. Nordlander, *Opt. Express*, 2007, **15**, 14129–14145.
16 C. Rockstuhl, F. Lederer, C. Etrich, T. Pertsch and T. Scharf, *Phys. Rev. Lett.*, 2007, **99**, 017401–017404.
17 V. Yannopapas and A. Vanakaras, *Phys. Rev. B: Condens. Matter Mater. Phys.*, 2011, **84**, 045128–045132.
18 S. Mühlig, C. Rockstuhl, V. Yannopapas, T. Bürgi, N. Shalkevich and F. Lederer, *Opt. Express*, 2011, **19**, 9607–9616.
19 J. Dintinger, S. Mühlig, C. Rockstuhl and T. Scharf, *Opt. Mater. Express*, 2012, **2**, 269–278.
20 D. I. Gittins, A. S. Susha, B. Schoeler and F. Caruso, *Adv. Mater.*, 2002, **14**, 508–512.
21 M. Xie, L. Ding, Z. You, D. Gao, G. Yang and H. Han, *J. Mater. Chem.*, 2012, **22**, 14108–14118.
22 T. Wu, Q. Zhang, J. Hu, G. Zhang and S. Liu, *J. Mater. Chem.*, 2012, **22**, 5155–5163.
23 S. Mühlig, A. Cunningham, S. Scheeler, C. Pacholski, T. Bürgi, C. Rockstuhl and F. Lederer, *ACS Nano*, 2011, **5**, 6586–6592.
24 K. Y. van Berkel and C. J. Hawker, *J. Polym. Sci., Part A: Polym. Chem.*, 2010, **48**, 1594–1606.
25 S. Mühlig, C. Rockstuhl, V. Yannopapas, T. Bürgi, N. Shalkevich and F. Lederer, *Opt. Express*, 2011, **19**, 9607–9616.
26 A. S. Kumbhar and G. Chumanov, *Chem. Mater.*, 2009, **21**, 2835–2839.
27 M. Xiao, C. Zhao, H. Chen, B. Yang and J. Wang, *Adv. Funct. Mater.*, 2012, **22**, 4526–4532.
28 Q. Liang, C. Li, G. Chen and M. Jiang, *J. Colloid Interface Sci.*, 2012, **383**, 82–88.
29 F. Kretschmer, U. Mansfeld, S. Hoeppener, M. D. Hager and U. S. Schubert, *Chem. Commun.*, 2014, **50**, 88–90.
30 C. Ziegler and A. Eychmüller, *J. Phys. Chem. C*, 2011, **115**, 4502–4506.
31 S. D. Perrault and W. C. Chan, *J. Am. Chem. Soc.*, 2009, **131**, 17042–17043.
32 N. R. Jana, L. Gearheart and C. J. Murphy, *Chem. Mater.*, 2001, **13**, 2313–2322.
33 K. R. Brown, D. G. Walter and M. J. Natan, *Chem. Mater.*, 2000, **12**, 306–313.
34 J. Rodriguez-Fernandez, J. Perez-Juste, F. J. Garcia de Abajo and L. M. Liz-Marzán, *Langmuir*, 2006, **22**, 7007–7010.
35 I. Pastoriza-Santos and L. M. Liz-Marzán, *Adv. Funct. Mater.*, 2009, **19**, 679–688.
36 X. Dong, X. Ji, H. Wu, L. Zhao, J. Li and W. Yang, *J. Phys. Chem. C*, 2009, **113**, 6573–6576.
37 H. Li, H. Xia, D. Wang and X. Tao, *Langmuir*, 2013, **29**, 5074–5079.
38 J. Orloff, S. Lynwood and M. Utlaut, *High Resolution Focused Ion Beams: FIB and its Applications*, Springer Press, 2003.
39 K. J. Lee, P. D. Nallathamby, L. M. Browning, T. Desai, P. K. Cherukuri and X. H. Xu, *Analyst*, 2012, **137**, 2973–2986.
40 S. Biswas, D. Nepal, K. Park and R. A. Vaia, *J. Phys. Chem. Lett.*, 2012, **3**, 2568–2574.
41 C. Jing, Z. Gu, Y. L. Ying, D. W. Li, L. Zhang and Y. T. Long, *Anal. Chem.*, 2012, **84**, 4284–4291.
42 J. R. Navarro and M. H. Werts, *Analyst*, 2013, **138**, 583–592.
43 R. Jin, Y. Cao, C. A. Mirkin, K. L. Kelly, G. C. Schatz and J. G. Zheng, *Science*, 2001, **294**, 1901–1903.
44 J. J. Mock, M. Barbic, D. R. Smith, D. A. Schultz and S. Schultz, *J. Phys. Chem.*, 2002, **116**, 6755–6759.
45 T. Huang and X. H. Nancy Xu, *J. Mater. Chem.*, 2010, **20**, 9867–9876.
46 S. Mühlig, C. Rockstuhl, J. Pniewski, C. R. Simovski, S. A. Tretyakov and F. Lederer, *Phys. Rev. B: Condens. Matter Mater. Phys.*, 2010, **81**, 075317–075324.
47 Y.-l. Xu, *Appl. Opt.*, 1997, **36**, 9496–9508.

Publication P8

Tunable PS-*b*-P2VP Plasmonic Nanostructures *via* a Cyclic Complexation-Reduction Approach

F. Kretschmer, S. Stumpf, U. Mansfeld, F. H. Schacher, S. Hoeppener, U. S. Schubert

J. Mater. Chem. C, submitted

Tunable PS-*b*-P2VP plasmonic nanostructures *via* a cyclic complexation-reduction approach

Florian Kretschmer,[a,b] Steffi Stumpf,[a,b] Ulrich Mansfeld,[a,b] Felix Schacher,[b,c] Stephanie Hoeppener,[a,b*] Ulrich S. Schubert[a,b]

[a] Laboratory of Organic and Macromolecular Chemistry (IOMC), Friedrich Schiller University Jena, Humboldtstr. 10, 07743 Jena, Germany

[b] Jena Center for Soft Matter (JCSM), Friedrich Schiller University Jena, Philosophenweg 7, 07743 Jena, Germany

[c] Laboratory of Organic and Macromolecular Chemistry, Friedrich Schiller University Jena, Lessingstr. 8, 07743 Jena, Germany

Corresponding author: Dr. Stephanie Hoeppener, Tel.; 03641 948596, e-mail: s.hoeppener@uni-jena.de

Abstract

Block copolymers enable the formation of ordered nanostructures on large areas. In combination with silver or gold nanoparticles plasmonic assemblies can be created. In this contribution a polystyrene-*block*-poly(2-vinylpyridine) (PS-*b*-P2VP) block copolymer (BCP) was utilized, which can selectively complex metal ions in the P2VP phase. In order to increase the metal content a cyclic complexation-reduction approach was applied to reduce complexed ions to their elemental form and, thereby, to release the pyridine units for the next complexation step. In this way, ordered films with tunable optical properties could be synthesized. The structures were analyzed *via* UV-Vis spectroscopy, atomic force microscopy and transmission electron microscopy.

Introduction

Ultrathin layers or nanoparticles of certain metals feature a collective resonance of their electron cloud under electromagnetic irradiation.[1] Gold and silver nanoparticles gathered particular attention due to their high environmental stability, in comparison, *e.g.*, to copper or alkali metals. Another important

feature of these metals is the spectral region of the surface plasmon resonance, which can be tuned from the visible to the near IR region depending on the size and shape of the nanoparticles.[2-3] When brought into close vicinity, additional resonances may occur due to electromagnetic coupling between the particles.[4] The fabrication of plasmonic nanoparticle assemblies, hence, allows to further tune the optical properties of these materials. This results in a wide range of applications in analytics,[5] medicinal therapy[6] and optics.[7] In this way, even materials with completely artificial properties (*e.g.* negative refractive indices) could potentially be created.

Bottom-up strategies to synthesize nanoparticle assemblies involve, for instance, DNA[8] or electrostatic interactions[9] as well as chemical reactions between surface modified particles.[10] In addition, also (oligo)thiols[11] and polymers[12] can be utilized to guide the formation of nanoparticle assemblies. These strategies, however, result mostly in the formation of rather small metal clusters, while for potential applications large area plasmonic structures are required. Top-down approaches, *e.g.*, through application of different lithography methods[13-17] can be used for the fabrication of extended structures, however, these methods suffer from long fabrication times and high costs. In contrast, block copolymers (BCPs) enable the formation of ordered nanostructures on a macroscopic scale.[18-20] Different strategies can be employed to create plasmonic nanostructures *via* BCPs.[21] Assemblies can be created, *e.g.*, by the incorporation of nanoparticles into the BCP phases.[22] This, however, requires the functionalization of the nanoparticles with one of the polymer blocks to enhance their miscibility with one of the phases, otherwise demixing will occur. The filling fraction of the metal in the BCP phase can be tuned by varying the concentrations of the functionalized nanoparticles.[22] Another approach utilizes phase-separated BCP films where nanoparticles can be incorporated into the voids, formed by etching one of the blocks, *via* capillary forces.[23] An alternative approach involves the incorporation of metal salts into one of the blocks.[24] This strategy can be applied either to solutions, where the formed micelles are spin-coated onto a substrate and are afterwards reduced forming a hexagonal lattice, or to BCP films with an already formed phase separation, which can be immersed in a metal precursor solution followed by reduction.[24] This approach enables an easier formation of large ordered plasmonic

nanostructures, however, a pivotal point for such structures is the metal content/filling fraction, which is rather low for this metal-precursor-approach. A thermal evaporation approach has been described by Lopes *et al.*, which, however, requires a rather complicated setup.[25] Seeded growth in the BCP structures has been also reported.[26-28]

In this contribution we report a versatile approach to synthesize plasmonic nanostructures facilitated by BCPs which allows to easily tune the filling factor (Scheme 1). PS-*b*-P2VP films were spin-coated onto glass substrates and AFM measurements were utilized to investigate the nanostructures formed under different annealing conditions. Repeated immersion in a metal salt solution, followed by reduction with hydrazine vapor, enabled to increase the metal content. The optical properties and the overall morphology of the hybrid films were investigated using UV-Vis spectroscopy as well as transmission electron microscopy (TEM) after each cycle.

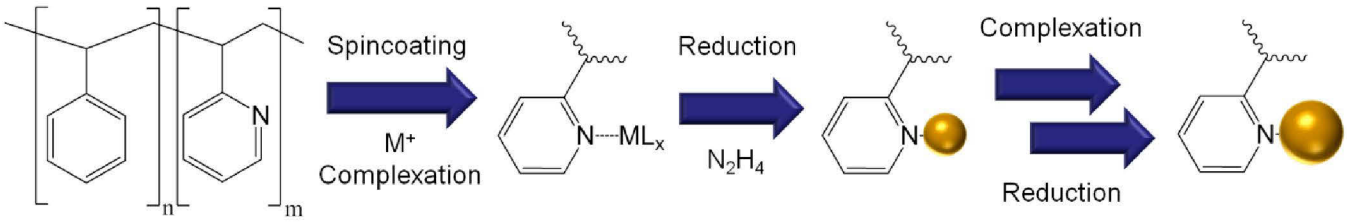

Scheme 1. Schematic representation of the cyclic complexation-reduction approach in a PS-*b*-P2VP block copolymer.

Results and discussion

A 1 wt% solution of PS-*b*-P2VP (M_n = 230,000 g/mol, PS:P2VP 65:35, PDI 1.03, synthesized *via* sequential living anionic polymerization[29]) in chloroform was prepared.

Based on the phase diagram, predicted by the self-consistent mean field theory, both a hexagonal or lamellar phase separation can be expected for this block copolymer composition.[30-31] Films were prepared by spin-coating the BCP solution onto glass substrates. Directly after the film formation phase-

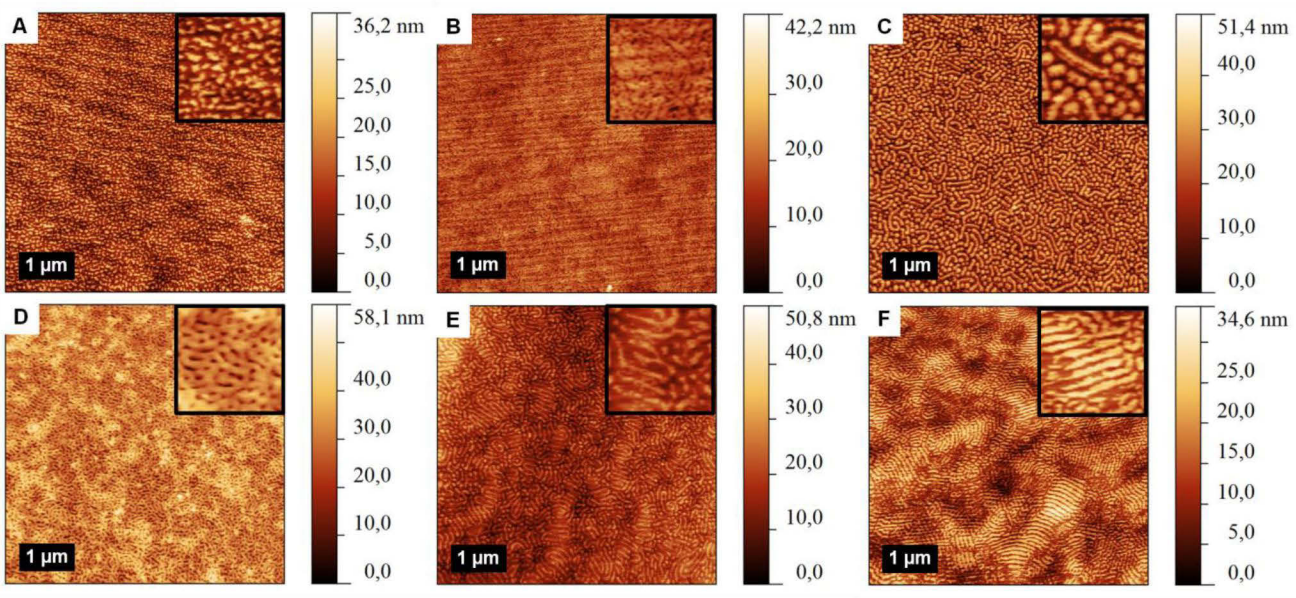

Figure 1. AFM height micrographs of PS-*b*-P2VP films annealed for 1 h in solvent vapor. A - as-cast, B - hexane, C - toluene, D - ethanol, E - tetrahydrofuran, F - chloroform. Images were acquired under hard-tapping conditions. Inset width is 630 nm in all cases.

Finally, by annealing with dichloromethane for 1 to 2 hours the most promising results could be obtained (Figure 2). For shorter annealing times less ordered or mixed structures between hexagonal and lamellar phases were found. Prolonged annealing resulted only in deterioration of the ordered nanostructure, a similar behavior was also observed by Li *et al.*.[35] A height profile revealed only small differences of 1 to 2 nm in height between the respective phases resulting from the hard-tapping conditions. The thickness of the PS phase corresponds to approximately 30 nm, whereas the respective P2VP domain has around half the size.

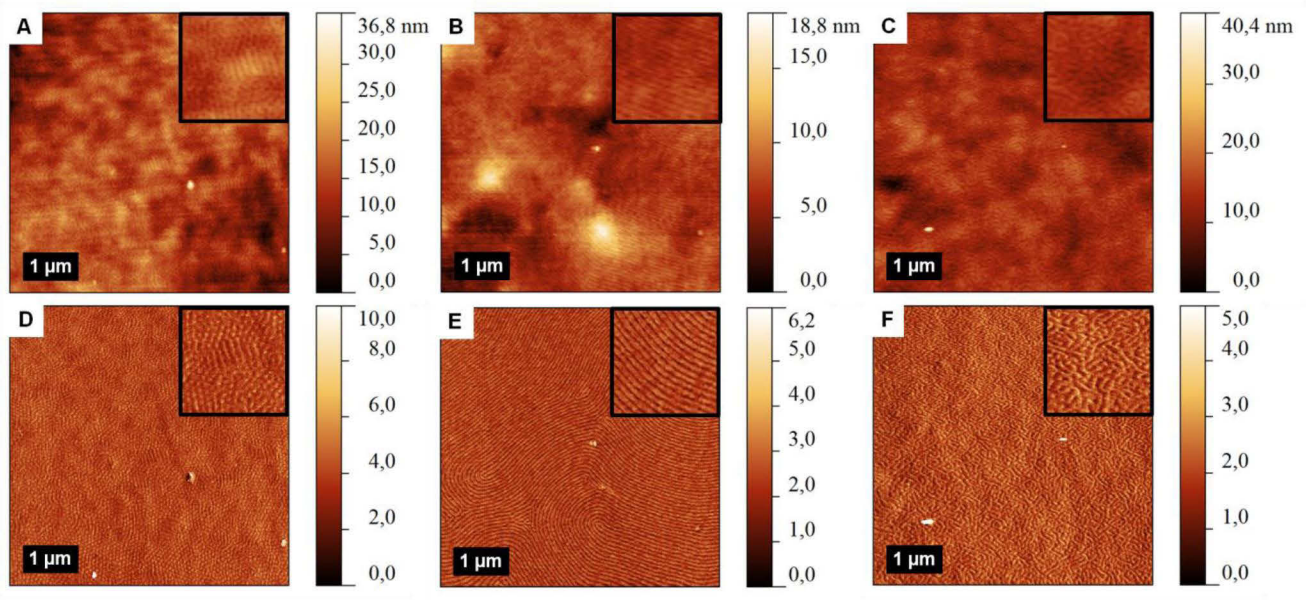

Figure 2. AFM height (A-C) and phase (D-F) micrographs of PS-*b*-P2VP films annealed for different times in dichlormethane vapor. A/D - 5 min, B/E - 1 h, C/F - 4 h. Inset width is 630 nm in all cases.

In order to introduce metal ions, the annealed films were immersed in a solution of silver nitrate or tetrachloroauric acid, respectively. In literature, primary and secondary amines are commonly used to synthesize gold or silver nanoparticles.[12, 36] Also the reduction with tertiary amines has been reported,[37] however, in our case no reaction was observed within the PS-*b*-P2VP films. Therefore, after a short washing step and drying of the film, the complexed metal ions were reduced to their elemental form *via* hydrazine vapor. The success of the reaction was clearly visible by the naked eye *via* a color change of the films from colorless to a slight purple color in case of gold or yellow-brown in case of silver (Figure 3). TEM imaging of the films revealed lamellar structures with small embedded nanoparticles in one phase corresponding to the P2VP block. In general, high filling factors are desired for optical applications of the ordered nanoparticles, since additional plasmon resonances can arise when nanoparticles are in close proximity and form ordered assemblies. In order to increase the filling factor the amount of metal was enhanced *via* seeded growth. For the reduced Au-BCP films a mixture of ascorbic acid, cetyl trimethylammonium bromide and $HAuCl_4$ or a combination of hydroxylammonium chloride with $HAuCl_4$ was applied. In the case of silver a commercial enhancer kit consisting of a silver salt as well as a reducing agent solution was utilized for growth. Preferred growth on the metal seeds

was occasionally visible, but secondary nucleation on the whole film led to the formation of large particles or even complete overgrowth on the films. Hence, a different strategy had to be applied in order to increase the amount of metal nanoparticles in the film. In principle, only a limited amount of metal ions can be complexed in one step. But reduction to the elemental form releases the pyridine units, which subsequently are capable of again coordinating metal ions in a subsequent step. Consequently, an approach based on multiple complexation-reduction cycles was developed and applied. This successfully led to an increase of the metal content with increasing cycle number; overall up to five cycles could be applied. The progress is easily visible by the changing color of the samples. Films with gold turn dark purple and finally blue, whereas silver films mostly show a more intensive yellowish/brownish color.

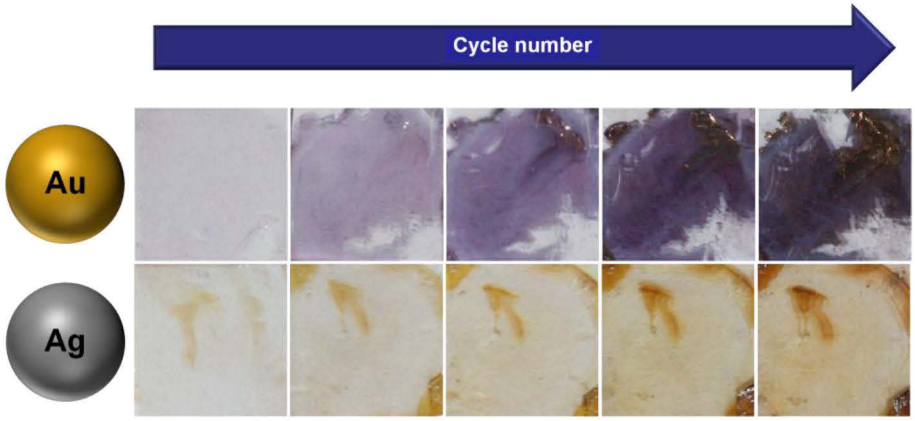

Figure 3. Photographs (~ 1×1 cm) of PS-*b*-P2VP films with increasing metal content after different complexation-reduction cycles.

In case of gold, TEM imaging revealed single particles (14.3 ± 2.5 nm diameter) for the first reduction step (Figure 4A). Afterwards, larger particles (18.1 ± 4.9 nm) occurred which already show a tendency to fuse into larger aggregates (Figure 4B). This trend continues with increasing cycle number until only a small amount of single spherical particles is present. Instead, elongated rod-like structures from dozens up to several hundred nanometers in length form along the P2VP phase (Figure 4C-E).

For silver a slightly different behavior was observed. In the beginning also single particles (12.5 ± 2.5 nm) are formed (Figure 4F). By increasing the cycle number the amount of particles in the P2VP block

increases and also larger particles (14 ± 3.3 nm, 16.2 ± 3.8 nm, 18.7 ± 4.4 nm, 22 ± 4.8 nm, respectively; Figure 4G-J) are formed. Yet, the amount of fused structures is lower compared to the respective films containing Au-NPs. It was initially assumed that the amount of silver should be higher in the films because silver(I) ions usually form divalent complexes[38] whereas gold(III) prefers a tetravalent coordination.[39] As a consequence, on a simple molar basis, already double the amount of silver could be potentially complexed which approximately transfers to double the volume compared to gold. However, this applies for solutions and might not hold true for strongly confined BCP films.

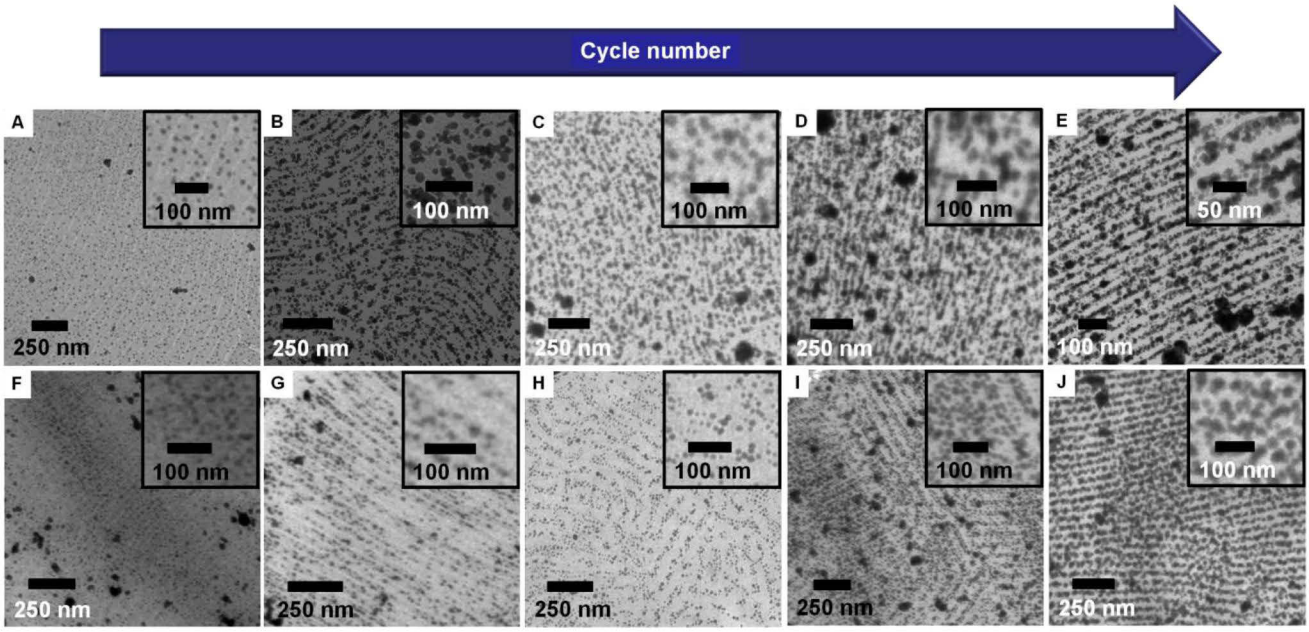

Figure 4. TEM images of PS-*b*-P2VP films with increasing metal content. Top - gold. Bottom - silver.

Additionally, UV-Vis spectroscopy was applied to prove the increase of the metal content as well as to evaluate the optical properties of the composite materials (Figure 5). The original gold films after the first reduction step revealed only a very small surface plasmon resonance at ~550 nm. Compared to a plasmon peak at 520 nm for single particles of the same size in solution[40] this corresponds to a significant bathochromic shift. Several factors could contribute to this behavior. At first the LSPR is dependent on the direct environment of the particles. In solution, adsorption of, *e.g.*, a polymer on the particle surface leads to a small red shift. In addition, the particles already form assemblies and are sometimes in close vicinity leading to additional plasmon resonances. Furthermore, also nonspherical

particles and larger particles can occur on the surface of the film which feature a similar optical behavior. With increasing metal content, the plasmon resonance shows a small red shift and an increase in intensity. After the 3rd cycle, a small shoulder arises, probably caused by coupling of multimer structures within the films. Moreover, also a strong absorption beyond the main plasmon peak emerges extending into the near-IR region. The fusion of particles into elongated structures probably is the reason for this phenomenon, since nanorods feature two plasmon resonances.[41] The position of the resonance strongly depends on the aspect ratio of the rods. For long rods, the resonance along the longer axis is strongly bathochromically shifted by several hundred nanometers to the NIR region. However, in the present case these rod-like particles have different lengths leading to an overlapping of all possible resonances which causes one broad band extending to the NIR region.

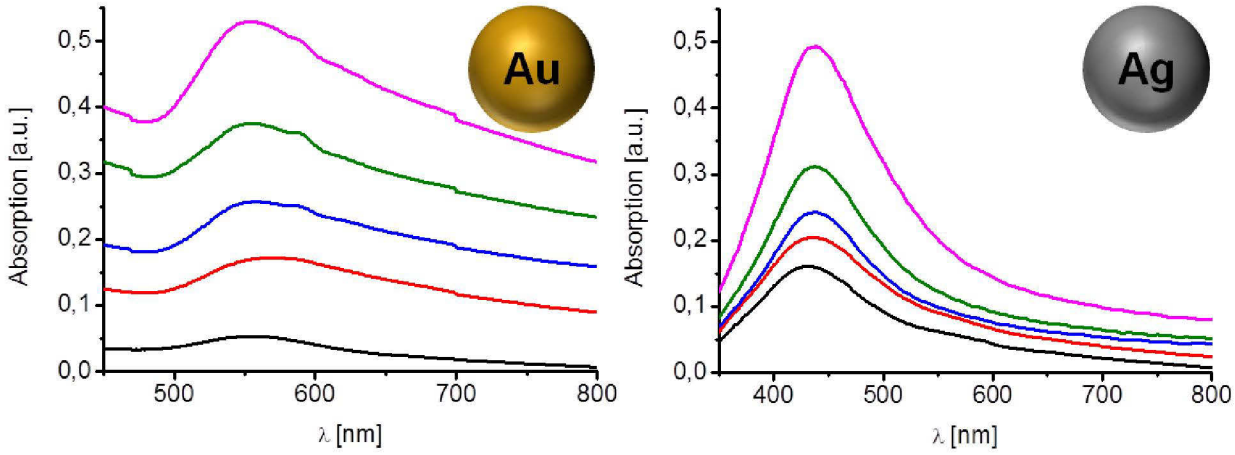

Figure 5. UV-Vis spectra of PS-*b*-P2VP films with increasing metal content. Black - cycle 1, red - cycle 2, blue - cycle 3, green - cycle 4, violet - cycle 5.

The structures containing silver NPs show a prominent absorption peak at ~ 440 nm. The lower wavelength of the resonance is caused by the higher plasma frequency of silver. In addition, a bathochromic shift as well as an increase in intensity could be observed with increasing cycle number, however, the absorption in the NIR region is rather low compared to gold. The overall intensity of the absorption after the fifth cycle is also lower compared to the respective sample with gold. This intriguing behavior could be caused by the susceptibility of silver against oxidation or by a different

complexation in solution compared to a solid P2VP phase. Thereby, the absence of rod-like structures as well as the overall lower absorption could be explained. The deterioration of the silver-BCP films was also visible after prolonged storage by a slight discoloration over time.

Conclusion

In summary, we have introduced a novel approach for synthesizing block copolymer / plasmonic nanoparticle assemblies. Annealing of PS-*b*-P2VP in dichloromethane vapor led to the formation of lamellar structures. The repetitive complexation and reduction of metal ions in the P2VP phase of PS-*b*-P2VP created ordered nanostructures with a tunable metal content. TEM imaging of films with gold nanoparticles revealed a transition from single particles to rod-like structures with increasing cycle number. In contrast, samples prepared with silver formed mostly larger particles and showed a lower tendency to form rods. In either case UV-Vis spectroscopy revealed both an increase of the surface plasmon resonance and a red shift or broadening at higher wavelengths as well as the appearance of additional peaks in the case of Au.

Materials and instrumentation

Hydrogen tetrachloroaurate(III) trihydrate (99.99%) was purchased from Alfa Aesar. Silver nitrate (>99.8%), hydrazine monohydrate (N_2H_4 64-65%, reagent grade, 98%) and the silver enhancer kit were received from Sigma-Aldrich. Solvents were purchased from VWR. PS-*b*-P2VP was prepared according to the literature by a sequential anionic polymerization.[29]

UV-Vis spectra were recorded on a Perkin Elmer Lambda 750 spectrometer in 1 cm quartz cuvettes at room temperature. Spin coating was performed with a WS-400B-6NPP/LITE (Laurell Technologies Corporation). AFM measurements were performed in tapping mode with a NTegra Aura (NT-MDT) with non-contact cantilevers (NSC35, MicroMash) under hard tapping conditions. TEM measurements were performed on a FEI Technai G2 20 cryo-Transmission Electron Microscope at 200 kV. The carbon

supported TEM grids (Mesh 400, Quantifoil) were cleaned by argon plasma treatment for 30 seconds prior to the preparation of the samples. Determination of the particle size was performed with the software ImageJ by measuring 100 particles per sample.

Experimental part

Glass substrates (~1×1 cm) were cleaned by washing with water and acetone followed by plasma cleaning (argon plasma, 10 min, Diener Electronics). Immediately afterwards, 20 µL of a PS-*b*-P2VP solution (1 wt%, $CHCl_3$) was pipetted onto the substrates followed by spin coating (1000 rpm, 30 sec). Solvent vapor annealing was performed by placing a support inside a petri dish. The sample was placed on the support and 2 mL of the respective solvents were added into the dish. A lid was placed onto the dish and the whole assembly was placed in a desiccator for the indicated times referred to in the text. Afterwards, the samples were immersed in a $HAuCl_4 \times 3H_2O$ (10 mg/mL) or $AgNO_3$ (4.3 mg/mL) solution for at least one hour. The samples were taken out and rinsed with water for two seconds followed by drying with compressed air. The substrates were placed in a petri dish and 10 µL of a hydrazine hydrate solution was placed next to the samples. Reduction was performed for one hour followed by removal of the hydrazine. The samples were dried for 2 h under ambient conditions. Samples with increased metal content were prepared by repeating the immersion and reduction process. For TEM preparation the glass substrate with the polymer film was immersed in aqua dest. in a petri dish. Afterwards a small piece of thin polymer film was scraped off the glass under water with a razor blade. The scraped film was transferred to the air/water interface and deposited onto the TEM grid with a wire loop.

Acknowledgement

Financial support from the research initiative PhoNa (Photonic nanomaterials), which is supported by the German Federal Ministry of Education and Research in the program "Spitzenforschung und Innovation in den Neuen Ländern" (support code 03IS2101A), is acknowledged. Holger Schmalz is acknowledged for the synthesis of the PS-*b*-P2VP block copolymer. The cryo-TEM facilities of the Jena Center for Soft Matter (JCSM) were established by a grant from the German Research Council (DFG) and the European Fonds for Regional Development (EFRE).

References

[1] N. J. Halas, S. Lal, W. S. Chang, S. Link, P. Nordlander, *Chem. Rev.* **2011**, *111*, 3913-3961.
[2] M. Rycenga, C. M. Cobley, J. Zeng, W. Li, C. H. Moran, Q. Zhang, D. Qin, Y. Xia, *Chem. Rev.* **2011**, *111*, 3669-3712.
[3] P. Zhao, N. Li, D. Astruc, *Coord. Chem. Rev.* **2013**, *257*, 638-665.
[4] J. Gong, G. Li, Z. Tang, *Nano Today* **2012**, *7*, 564-585.
[5] Y. Jin, *Adv. Mater.* **2012**, *24*, 5153-5165.
[6] J. Chen, M. Yang, Q. Zhang, E. C. Cho, C. M. Cobley, C. Kim, C. Glaus, L. V. Wang, M. J. Welch, Y. Xia, *Adv. Funct. Mater.* **2010**, *20*, 3684-3694.
[7] N. I. Zheludev, Y. S. Kivshar, *Nat. Mater.* **2012**, *11*, 917-924.
[8] M. P. Busson, B. Rolly, B. Stout, N. Bonod, E. Larquet, A. Polman, S. Bidault, *Nano Lett.* **2011**, *11*, 5060-5065.
[9] I. Y. Goon, L. M. H. Lai, M. Lim, P. Munroe, J. J. Gooding, R. Amal, *Chem. Mater.* **2009**, *21*, 673-681.
[10] J. P. Hermes, F. Sander, U. Fluch, T. Peterle, D. Thompson, R. Urbani, T. Pfohl, M. Mayor, *J. Am. Chem. Soc.* **2012**, *134*, 14674-14677.
[11] J. M. Wessels, H. G. Nothofer, W. E. Ford, F. von Wrochem, F. Scholz, T. Vossmeyer, A. Schroedter, H. Weller, A. Yasuda, *J. Am. Chem. Soc.* **2004**, *126*, 3349-3356.
[12] F. Kretschmer, U. Mansfeld, S. Hoeppener, M. D. Hager, U. S. Schubert, *Chem. Commun.* **2014**, *50*, 88-90.
[13] S. Sun, K. Y. Yang, C. M. Wang, T. K. Juan, W. T. Chen, C. Y. Liao, Q. He, S. Xiao, W. T. Kung, G. Y. Guo, L. Zhou, D. P. Tsai, *Nano Lett.* **2012**, *12*, 6223-6229.
[14] L. Johnson, D. A. Walsh, *J. Mater. Chem.* **2011**, *21*, 7555-7559.
[15] K. Liu, C. L. Ho, S. Aouba, Y. Q. Zhao, Z. H. Lu, S. Petrov, N. Coombs, P. Dube, H. E. Ruda, W. Y. Wong, I. Manners, *Angew. Chem. Int. Ed.* **2008**, *47*, 1255-1259.
[16] Q. Dong, G. Li, C. L. Ho, M. Faisal, C. W. Leung, P. W. Pong, K. Liu, B. Z. Tang, I. Manners, W. Y. Wong, *Adv. Mater.* **2012**, *24*, 1034-1040.
[17] Q. Dong, G. Li, C.-L. Ho, C.-W. Leung, P. W.-T. Pong, I. Manners, W.-Y. Wong, *Adv. Funct. Mater.* **2014**, *24*, 857-862.
[18] S. Krishnamoorthy, C. Hinderling, H. Heinzelmann, *Mater. Today* **2006**, *9*, 40-47.
[19] V. V. Terekhin, O. V. Dement'eva, V. M. Rudoy, *Russ. Chem. Rev.* **2011**, *80*, 453-472.
[20] S. Förster, M. Antonietti, *Adv. Mater.* **1998**, *10*, 195-217.
[21] S. Mehdizadeh Taheri, S. Fischer, S. Förster, *Polymers* **2011**, *3*, 662-673.

[22] A. Horechyy, B. Nandan, N. E. Zafeiropoulos, P. Formanek, U. Oertel, N. C. Bigall, A. Eychmüller, M. Stamm, *Adv. Funct. Mater.* **2013**, *23*, 483-490.
[23] Z. Liu, H. Huang, T. He, *Small* **2013**, *9*, 505-510.
[24] S. Mössmer, J. P. Spatz, M. Möller, T. Aberle, J. Schmidt, W. Burchard, *Macromolecules* **2000**, *33*, 4791-4798.
[25] W. A. Lopes, H. M. Jaeger, *Nature* **2001**, *414*, 735-738.
[26] J. Yuan, A. Hajebifard, C. George, P. Berini, S. Zou, *J. Colloid Interface Sci.* **2013**, *410*, 1-10.
[27] T. Lohmueller, E. Bock, J. P. Spatz, *Adv. Mater.* **2008**, *20*, 2297-2302.
[28] A. Sánchez-Iglesias, P. Aldeanueva-Potel, W. Ni, J. Pérez-Juste, I. Pastoriza-Santos, R. A. Alvarez-Puebla, B. N. Mbenkum, L. M. Liz-Marzán, *Nano Today* **2010**, *5*, 21-27.
[29] M. Bräutigam, P. Weyell, T. Rudolph, J. Dellith, S. Krieck, H. Schmalz, F. H. Schacher, B. Dietzek, *J. Mater. Chem. A* **2014**, *2*, 6158-6166.
[30] F. S. Bates, G. H. Fredrickson, *Phys. Today* **1999**, *52*, 32-38.
[31] M. W. Matsen, F. S. Bates, *Macromolecules* **1996**, *29*, 1091-1098.
[32] E. Bhoje Gowd, B. Nandan, M. K. Vyas, N. C. Bigall, A. Eychmuller, H. Schlorb, M. Stamm, *Nanotechnology* **2009**, *20*, 415302-415311.
[33] A. del Campo, E. Arzt, *Chem. Rev.* **2008**, *108*, 911-945.
[34] Y. Wang, U. Gosele, M. Steinhart, *Nano Lett.* **2008**, *8*, 3548-3553.
[35] X. Li, J. Peng, Y. Wen, D. H. Kim, W. Knoll, *Polymer* **2007**, *48*, 2434-2443.
[36] T. Mishra, R. K. Sahu, S. H. Lim, L. G. Salamanca-Riba, S. Bhattacharjee, *Mater. Chem. Phys.* **2010**, *123*, 540-545.
[37] P. L. Kuo, C. C. Chen, *Langmuir* **2006**, *22*, 7902-7906.
[38] W. C. Vosburgh, S. A. Cogswell, *J. Am. Chem. Soc.* **1943**, *65*, 2412-2413.
[39] Y. Nagel, W. Beck, *Z. Anorg. Allg. Chem.* **1985**, *529*, 57-60.
[40] N. G. Bastus, J. Comenge, V. Puntes, *Langmuir* **2011**, *27*, 11098-11105.
[41] L. Vigderman, B. P. Khanal, E. R. Zubarev, *Adv. Mater.* **2012**, *24*, 4811-4841.

TOC:

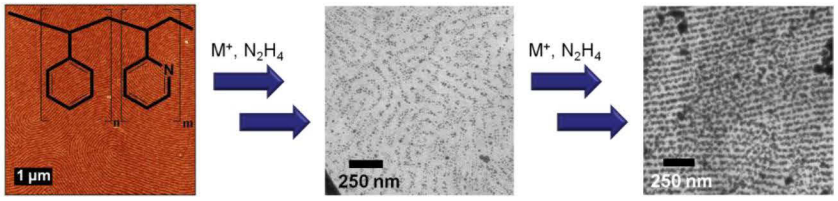

A cyclic complexation-reduction approach of PS-P2VP films yields nanoparticle assemblies with tunable filling factors and structures.